From protoplanetary disks to planets: demographic constraints from observations

Enrique Sanchis Melchor

München 2021

From protoplanetary disks to planets: demographic constraints from observations

Enrique Sanchis Melchor

Dissertation
an der Fakultät für Physik
der Ludwig–Maximilians–Universität
München

vorgelegt von
Enrique Sanchis Melchor
aus Valencia, Spanien

München, den 26. Januar 2021

Erstgutachter: Prof. Dr. Barbara Ercolano
Zweitgutachter: Prof. Dr. Til Birnstiel
Tag der mündlichen Prüfung: 11. März 2021

This project has been carried out at the European Southern Observatory (ESO, Garching) under the supervision of Leonardo Testi, and co-supervision of Anna Miotello, Carlo F. Manara, Stefano Facchini, and Barbara Ercolano.

Contents

Zusammenfassung **xv**

Abstract **xvii**

1 Introduction **1**
1.1 Disk and planet formation 2
1.1.1 Disk formation 2
1.1.2 Disk classification 3
1.1.3 Planet formation 5
1.2 Protoplanetary disk's evolution and dispersal 8
1.2.1 Dust evolution 10
1.2.2 Observations of protoplanetary disks 12
1.3 Early stages of newborn planets 16
1.3.1 Evolutionary tracks of protoplanets 17
1.3.2 Detection techniques 19
1.4 Role of the Thesis 25

2 (Sub-)mm interferometric observations of protoplanetary disks **29**
2.1 Interferometric observations 29
2.1.1 Antenna power and primary beam 30
2.1.2 Two antennas interferometry 31
2.1.3 Antenna arrays and imaging 32
2.1.4 Atacama Large Millimeter/submillimeter Array 34
2.2 Modeling the emission from (sub)millimeter interferometry 35
2.2.1 Modeling in the *uv*-plane 36
2.2.2 Modeling in the image plane 38
2.2.3 Total mass and extent of the disk from interferometric observations 39

3 Demographics of the dust content in protoplanetary disks **43**
3.1 Introduction 43
3.2 Sample selection 45
3.3 Observations 46
3.4 Modeling 51

3.4.1 Size definition . . . 52
3.4.2 Dust disk masses . . . 53
3.4.3 Modeling results . . . 53
3.4.4 Disk size results . . . 56
3.4.5 Total dust mass results . . . 58
3.5 Discussion . . . 59
3.5.1 Comparison to disks around T Tauri stars . . . 59
3.5.2 Planet formation around BDs . . . 67
3.6 Conclusions . . . 68

4 Demographics of the gas content in protoplanetary disks 71
4.1 Introduction . . . 71
4.2 Sample selection . . . 73
4.2.1 Observations . . . 74
4.3 Modeling . . . 75
4.3.1 CO modeling . . . 75
4.3.2 Dust modeling . . . 78
4.4 Disk size results . . . 78
4.4.1 CO size results . . . 78
4.4.2 Dust size results . . . 81
4.4.3 Gas/dust size ratio results . . . 82
4.5 Discussion . . . 86
4.5.1 Disk evolution: Gas size relative to dust size . . . 86
4.5.2 Possible correlations between the size ratio and other stellar and disk properties . . . 87
4.5.3 CO optical depth . . . 90
4.6 Conclusions . . . 91

5 Search for protoplanets 95
5.1 High contrast imaging . . . 96
5.1.1 ADI and PDI techniques . . . 96
5.1.2 Present and future observations . . . 97
5.2 Detectability of planets embedded in protoplanetary disks . . . 99
5.2.1 Effects of resolution on the disk-planet interaction . . . 100
5.2.2 Gap opening analysis . . . 102
5.2.3 Prescription of the extinction curve . . . 103
5.2.4 Effects of dust composition on extinction . . . 104
5.2.5 Search for protoplanets in PDS 70, HL Tau, and HD 163296 . . . 104
5.2.6 Conclusions . . . 110

6 Conclusions & outlook 113

A Tests comparing $R_{68\%}$ and $R_{95\%}$ 117

B Disk properties relations using other dust temperature prescriptions 119
B.1 Dust temperature from Andrews et al. (2013) . . . 119
B.2 Dust temperature from van der Plas et al. (2016) . . . 119

C Results from fits in the continuum 123
C.1 Results for Sz 102 . . . 123
C.2 Results for V 1094 Sco . . . 123
C.3 Results for GQ Lup . . . 123
C.4 Results for Sz 76 . . . 123
C.5 Results for RXJ 1556.1-3655 . . . 123
C.6 Results for EX Lup . . . 123

D Accretion luminosity versus scaled continuum flux 131

E Interferometric modeling of line emission from DSHARP 133

F Results of CO sizes using different methodology 139

G Criterion to model CO in the image plane based on the residuals 143

H Best fit parameters for CO disks modeled with a Nuker function 147

I Observed, model and residual CO maps of the Lupus disk population 149

J Singular disks in Lupus 157
J.1 Sz 75 . . . 157
J.2 Sz 83 . . . 158
J.3 Sz 131 . . . 158
J.4 Sz 111 . . . 158
J.5 Sz 69 . . . 159
J.6 Sz 65 . . . 159
J.7 Sz 82 . . . 159
J.8 Brown dwarfs/very low-mass stars . . . 160

Danksagung 182

List of Figures

1.1 Classification of young stellar objects by classes 4
1.2 Schematic view of accretion onto a young star 9
1.3 SED of a classic T Tauri star 14
1.4 Light curve of a star due to a planet transit 20
1.5 Population of confirmed exoplanets 24

2.1 Interference in a two-antennas interferometer 30
2.2 Frequency coverage of ALMA Bands 35
2.3 Dust continuum maps from an ALMA survey on Lupus disks 41
2.4 Schematic view of steps to obtain the visibilities of a model 42

3.1 Hertzsprung–Russell diagram for the studied disk population in Lupus . . 48
3.2 Dust continuum images of the new Lupus BDs disks survey 49
3.3 Fitting of the visibilities of a BD disk 54
3.4 Corner plot from the modeling of a BD dust emission 55
3.5 Modeled brightness profile of a dusty disk 56
3.6 Probability density function of the $R_{68\%}$ for a dusty disk 58
3.7 Reconstructed observed/modeled/residual map of a dusty disk 59
3.8 Relation between the stellar luminosity and flux at 890 μm in the Lupus population 60
3.9 Histogram of the total dust mass in the Lupus population 61
3.10 Stellar mass vs. total dust mass in the Lupus population 62
3.11 Size vs. continuum flux in the Lupus population 63
3.12 Mass accretion rate vs. disk mass in the Lupus population 65
3.13 Histogram of the accretion depletion timescale in the Lupus population . . 67

4.1 Comparison of CO and dust size with previous studies 81
4.2 Histograms of CO and dust sizes in the Lupus population 83
4.3 Comparison between CO and dust sizes in the Lupus population 84
4.4 Size ratio vs. various stellar and disk properties in the Lupus population . 93
4.5 CO size vs. CO flux in the Lupus population 94

5.1 Direct detection of planet in PDS 70 97
5.2 Contrast curves from observations searching for planets 98

5.3 Vertical density stratification near the planet from HD simulations 102
5.4 Gap depth for each planet from HD simulations 103
5.5 Extinction coefficients and expected planet magnitudes in IR 105
5.6 PDS 70 contrast curves in H- K, and L-bands 107
5.7 HL Tau contrast curves in J-, H- K, and L-bands 108
5.8 HD 163296 contrast curves in J-, H- K, and L-bands 110

A.1 Cumulative distribution function of various empirical models 118
A.2 Comparison of dust sizes with previous work 118

B.1 Stellar mass vs. total dust mass using Andrews et al. (2013) temperatures 120
B.2 Mass accretion rate vs. disk mass using Andrews et al. (2013) temperatures 120
B.3 Stellar mass vs. total dust mass using van der Plas et al. (2016) temperatures 121
B.4 Mass accretion rate vs. disk mass using van der Plas et al. (2016) temperatures 121

C.1 Modeling results of the Sz 102 continuum emission 124
C.2 Modeling results of the V 1094 Sco continuum emission 125
C.3 Modeling results of the GQ Lup continuum emission 126
C.4 Modeling results of the Sz 76 continuum emission 127
C.5 Modeling results of the RXJ 1556.1-3655 continuum emission 128
C.6 Modeling results of the EX Lup continuum emission 129

D.1 Accretion luminosity vs. continuum flux in the Lupus population 132
D.2 Histogram of ratio between accretion luminosity and continuum flux in Lupus population 132

E.1 Fitting of the visibilities of CO emission 134
E.2 Corner plot from the interferometric modeling of CO 135
E.3 Reconstructed observed/modeled/residuals map of two different CO models 136
E.4 Modeled brightness profile of a CO disk 137

F.1 Comparison of the CO size from two different datasets 141

G.1 Residuals of Gaussian CO models by comparing two datasets 144
G.2 Residuals of Nuker CO models by comparing two datasets 145

I.1 Modeling results of CO disks in Lupus (#1) 149
I.2 Modeling results of CO disks in Lupus (#1) 150
I.3 Modeling results of CO disks in Lupus (#2) 151
I.4 Modeling results of CO disks in Lupus (#3) 152
I.5 Modeling results of CO disks in Lupus (#4) 153
I.6 Modeling results of CO disks in Lupus (#5) 154
I.7 Modeling results of CO disks in Lupus (#6) 155

List of Tables

3.1 Stellar properties of the new Lupus sources modeled 47
3.2 Continuum fluxes of the new Lupus sources modeled 50
3.3 Results of the continuum models of the new Lupus sources 57
3.4 Linear regression correlations between dust disk properties 66

4.1 Summary of the archival ALMA projects used for the gas and dust modeling 74
4.2 Results of the CO and dust sizes in the Lupus population 80
4.3 Statistical tests of possible correlations with size ratio 89

5.1 Properties of new simulations with doubled resolution 101

F.1 CO sizes using different models 140

H.1 Results of the CO Nuker models 148

Zusammenfassung

Planeten bilden sich in scheibenförmigen Strukturen aus Gas und Staub, die junge Sterne umkreisen. Diese sogenannten protoplanetaren Scheiben sind Überreste des stellaren Kernkollapses und als solche anfangs dick und dicht; sie verlieren kontinuierlich an Material, bis sie vollständig verschwunden sind. Planeten können nur entstehen, bevor das Scheibenmaterial sich zu sehr zerstreut hat. Somit hängen die Planetenbildung und die Auflösung der Scheibe von den physikalischen Prozessen innerhalb der Scheibe ab.

Fortschritte bei der Beobachtungsinstrumentierung haben in den letzten Jahren zu einem überwältigenden Durchbruch beim direkten Nachweis von Exoplaneten geführt – und damit unser Verständnis von protoplanetaren Scheiben und ihrer Fähigkeit zur Bildung von Planeten revolutioniert. Einerseits haben Interferometer wie das Atacama Large Millimeter Array (ALMA) es ermöglicht, protoplanetare Scheiben in verschiedenen atmosphärischen Schichten und bis hinunter zur Mittelebene abzubilden. Diese Beobachtungen – insbesondere die von ALMA – können dazu verwendet werden, eine große Anzahl von Scheiben detailliert zu charakterisieren und ihre Entwicklung statistisch einzugrenzen. Andererseits ist es dank Verbesserungen bei der Detektionstechnologie jetzt möglich, exoplanetare Systeme durch eine Kombination verschiedener Techniken routinemäßig zu detektieren.

Die direkte Beobachtung von protoplanetaren Scheiben und Exoplaneten bietet außergewöhnliche Möglichkeiten, die Entstehung von Planeten einzugrenzen und die Planetensysteme zu charakterisieren, die überhaupt entstehen können. Die vorliegende Arbeit liegt zwischen den beiden Bereichen; ihr Ziel ist es, die physikalischen Prozesse einzugrenzen, die das Schicksal protoplanetarer Scheiben bestimmen, und abzuschätzen, ob kürzlich entstandene Planeten erkannt werden können, während sie noch in der Scheibe eingebettet sind.

Die Scheibeneigenschaften werden mittels einer hochgradig vollständigen, auf ALMA-Beobachtungen basierenden Sammlung von Scheiben charakterisiert. Hierbei werden im Rahmen einer homogenen Methodik Staub- und Gasbeobachtungen getrennt, um entscheidende Parameter wie Scheibenmasse und Staub- und Gasausdehnung abzuleiten. Die Ergebnisse werden aus einer demografischen Perspektive untersucht; dies ermöglicht eine Eingrenzung des wahren Verhaltens der Scheibenpopulation.

In dieser Dissertation wird außerdem ein Modell zur Untersuchung der Wechselwirkung zwischen Planet und Scheibe entwickelt; das Ziel ist es, die Infrarot-Extinktion aufgrund des Materials zu quantifizieren, das einen in die Scheibe eingebetteten Planeten umgibt.

Dieses erweiterte Modell wird dann auf reale Systeme angewendet. Die Ergebnisse liefern erstens wichtige Beschränkungen für die Häufigkeit, mit der Planeten in sehr jungen Systemen direkt beobachtet werden können, und zweitens eine Richtlinie, um für zukünftige Beobachtungen protoplanetare Scheiben mit idealen Bedingungen für die direkte Erkennung von Planeten auszuwählen.

Abstract

Planets form in disk-shaped structures of gas and dust that orbit young stars. The so-called protoplanetary disks, remnants of the core collapse process, start as thick and dense structures that continuously lose material until they completely vanish. Planets need to form before the disk material is dispersed. In such framework, planet formation and disk dispersal depend on the physical processes that take place within the disk.

In recent years, thanks to the advancements in observational instrumentation, our understanding of protoplanetary disks, their ability to form planets, and the direct detection of planets has experienced an overwhelming breakthrough. On the one hand, interferometers like the Atacama Large Millimeter Array (ALMA) have allowed to resolve protoplanetary disks at different atmospheric layers and down to the mid-plane. These observations, and in particular those from ALMA, can be used to characterize in great detail large samples of disks, and to constrain the evolution of disks from a statistical approach. On the other hand, thanks to the improvements on detection technology, it is now possible to detect exoplanetary systems routinely by using various techniques.

The intersection between protoplanetary disk and exoplanetary fields offers extraordinary potential to constrain planet formation and to characterize the planetary systems that might form. This Thesis lays in between the two fields, aiming to constrain the physical processes that shape the fate of protoplanetary disks, and assess whether recently formed planets can be detected when still embedded in the disk.

The characterization of the disk properties is accomplished by studying a highly complete population of disks based on ALMA observations. I perform an homogeneous methodology, separating dust and gas observations, to infer crucial properties such as the disk mass, the dust and the gas extent. I study the results from a demographic perspective, which allows me to constrain the true behavior of the disk population.

In this Thesis I further develop a model to study the planet-disk interaction in order to quantify the infrared extinction, due to surrounding material, that affects the detection of a planet embedded in the disk. The enhanced model is then applied to real systems. The results pose important limitations on how often planets can be directly observed in very young systems, and provide a guidance for future observations to target those protoplanetary disks with the ideal conditions for the direct detection of planets.

Chapter 1

Introduction

The observation of the sky has played a fundamental role in the development of humankind. From spiritual beliefs in the prehistoric ages, through discoveries in ancient civilizations that set the foundations of science, up to the modern world, where state-of-the-art technology allows not only to observe but to routinely interact with the 'sky', and hundreds of unmanned and manned spacecrafts provide essential services to humankind. Advancements in the study of the sky and the celestial bodies contributed to colossal progress in our knowledge. These advancements were decisive to switching to a scientific interpretation of the universe, key to the progress attained in the contemporary age.

Of particular relevance has been the evolution of the role that humankind and the Earth has played with respect to the Sun and the other planets of the Solar System. The change from a geocentric to a heliocentric paradigm shifted the Earth's role from being central to the universe to a secondary one. Further discoveries on the true scale of the galaxy and the universe continued to shift humankind to an even more trivial role within the universe. At the same time, the shift in how humankind intertwines with the Sun, the planets and the universe brought new questions that only science can fully address. Questions about the origin of life, the uniqueness of the Earth and its living creatures. With perhaps one question that summarizes them all: *is there life elsewhere in the Universe?*

To answer this question, we looked at the Solar System to try finding answers. Astronomers focused on the Moon, Mars and the other planets of the Solar System. In the late 19th century, astronomers such as Giovanni Schiaparelli studied the Mars surface, and misinterpreted its features as indications of a declining Martian civilization. Besides the pedagogical lesson on how to interpret scientific experiments and observations, this story exemplifies how the search for life beyond Earth became inherent to the study of other planets. Contemporary missions from space agencies have a major focus on the search for life in other planets and moons, and the quest to understand life's origin. It is by the study of planets, and especially how they form, that we can investigate the origin of life and address how common in the universe life is.

Planet formation theories were already developed in the late modern period thanks to eminent thinkers such as Immanuel Kant or Pierre-Simon Laplace (Kant 1755; Laplace 1796). Their nebular hypothesis was already able to explain planets of the Solar System

being formed from a flattened structure of material orbiting the Sun. In the 1960s, astronomers like Viktor Safronov greatly expanded on the nebular hypothesis and settled the basic formulation of the planet formation processes (e.g., Safronov 1969), still latent in the field today. In the late 20th century, the field of planet formation was further developed, primarily thanks to the construction and operation of modern ground- and space-based telescopes, such as the InfraRed Astronomical Satellite (IRAS), the Hubble Space Telescope (HST), or interferometers such as the Very Large Array (VLA). But is specially from the 1990s, with the first discoveries of planets outside the Solar System (commonly referred as exoplanets), when the field of planet formation gained immense traction and experienced colossal progress.

Protoplanetary disks and planets are intrinsically constrained by each other: on one hand, the formation of a planet is only possible if the disk evolution processes allow material to conveniently assemble a planet-like body, and on the other hand, the fate of protoplanetary disks are greatly shaped by the presence of embedded planets. It is at the present time where the astonishing progress on both protoplanetary disk and exoplanetary fields allow to study the conjunction of the two fields.

My Thesis lays on the interconnection of the two fields. In this first chapter, I introduce the main concepts governing planet formation (Chapter 1.1), disk evolution (Chapter 1.2), and early planet evolution (Chapter 1.3), from a theoretical and observational perspective. Once the major physical processes and the basics of observations are set, I summarize the open questions and the key goals that this thesis addresses (Chapter 1.4).

1.1 Disk and planet formation

The formation of planets takes place around young stars, and is deeply connected to the star formation process. Planets form within the so-called protoplanetary disks, defined as disk-shape structures that orbit around young stars, and are essentially composed by – atomic and molecular – gas and dust grains of varying size and composition.

1.1.1 Disk formation

Disks are a byproduct of the star formation process. More specifically, disks are the result of the molecular cloud collapse that also produces the cores that would become protostars. Indistinctly of how exactly the collapse of the cloud operates (different collapse models either explain an inside-out collapse or the collapse of the entire cloud, see, e.g., Shu 1977; Whitworth & Summers 1985; André et al. 2003), a disk is expected to form rapidly.

A way to understand how a disk forms is to view the cloud as a solid body that is rotating slowly and in hydrostatic equilibrium. During the cloud collapse, a gas parcel will tend to infall towards the cloud center. Depending on its specific angular momentum, the gas parcel will either accrete directly onto the central core, or reach the equatorial plane of the rotating cloud following a parabolic trajectory (e.g., Dominik 2015). Assuming for simplicity that the cloud is spherically symmetric, another parcel of gas from the opposite

side of the equatorial plane will follow an analogous trajectory. Thus both gas parcels would meet at the equatorial plane and collide. This collision produces a heat excess, and a thin disk forms if the heat excess is radiated away (e.g., McKee & Ostriker 2007; Maury 2011; Dominik 2015). Thus, a thin disk at the equatorial plane is expected to form at the early stage of the cloud collapse. Once this initial disk has formed, other parcels of gas follow similar trajectories depending on their respective angular momentum: if low enough, the parcel directly infalls to the center and become part of the growing protostellar core; if high enough, the gas parcel follows a parabolic trajectory, reaching the thin disk, and eventually becoming part of the disk. Material from the disk is also accreted onto the central core but at a slower pace. Accretion regulates the disk, which is relatively stable and increases in radius (defined by the centrifugal radius, Terebey et al. 1984) at this early stage.

Even though clouds aren't perfectly spherical, and magnetic fields have a contribution to the collapse process (for detailed discussion of the effects on magnetic fields, see, e.g., Shu et al. 1994; Stahler & Palla 2004), this simplified view provides a basic understanding of how cloud collapse produces, besides a central protostellar core, an equatorial disk.

1.1.2 Disk classification

The moment in which the stellar embryo develops is generally designated as the starting time of the star's lifetime. This time also sets a distinction between the prestellar and the protostellar phases (e.g., Maury 2011).

These objects are designated by classes (from class 0 to III) following the general classification of pre-main sequence stars introduced by Lada (1987). This classification is based on the different Spectral Energy Distribution (SED) between these objects and stars in the Main Sequence (MS). A young object, compared to a MS star, has a larger InfraRed (IR) emission, which is known as IR excess. The distinction between classes I, II, and III from Lada (1987) is in fact based on the IR slope in the SED of each object. The class 0 was introduced shortly after by André et al. (1993). The IR excess is quantified by the SED slope ($\alpha_{\rm IR}$) between 2 and 25 μm, defined as:

$$\alpha_{\rm IR} = \frac{d\log \nu F_\nu}{d\log \nu} = \frac{d\log \lambda F_\lambda}{d\log \lambda}. \tag{1.1}$$

Based on the value of $\alpha_{\rm IR}$, the objects are classified as: class I if $\alpha_{\rm IR} > 0$, class II if $-1.6 < \alpha_{\rm IR} < 0$, and class III for values of $\alpha_{\rm IR} < -1.6$.

Each class can be understood as a different evolutionary stage of these pre-MS objects. In Figure 1.1, the temporal evolution of such objects is summarized. Each class is represented in a different panel, the left sub-panels show the simplified morphology and main ongoing processes at each stage, while the right sub-panels show a representative SED of the different classes. In the prestellar phase (top panel in Figure 1.1), the cloud is emitting at long wavelengths as a blackbody at a very low temperature. The remaining panels represent the classes 0-III:

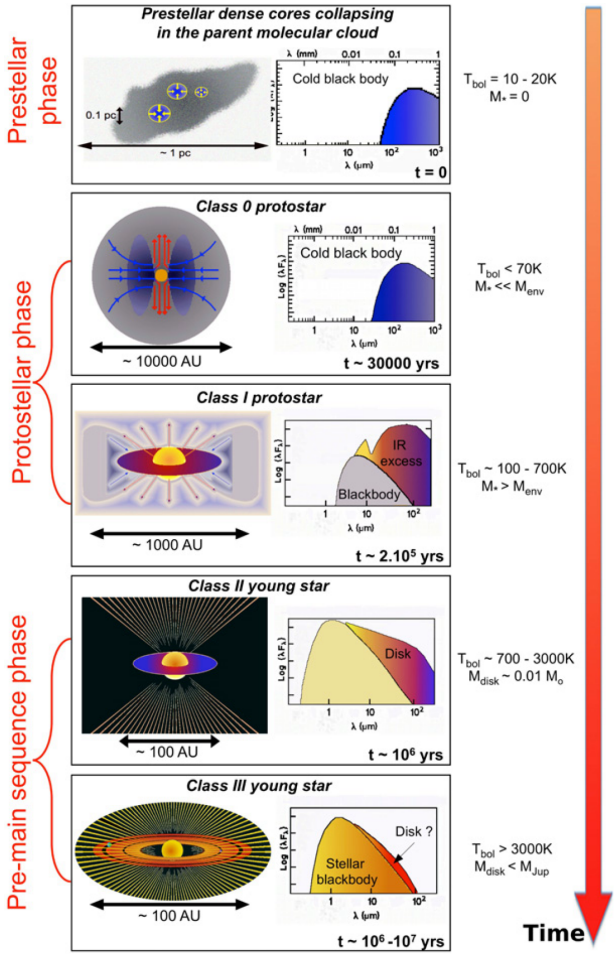

Figure 1.1: Classification of young stellar objects by classes (0, I, II and III). Adapted from André et al. (2000); André (2002); Maury (2011). Each class shows a distinctive SED, and relates to a particular phase of the YSO evolution before starting the main sequence star.

- **Class O**: at this stage, a dense envelope completely hides the protostellar core. The SED appears similar to the prestellar phase, but slightly shifted to shorter wavelengths since the envelope is at higher temperatures. Disks are expected to be present already at this very early stage, although observational evidence of disks in class 0 objects has been traditionally very difficult. However, recent studies conducted with the Atacama Large Millimeter/submillimeter Array (ALMA), have suggested the presence of compact disk emission on these objects (e.g., Maury et al. 2019; Tychoniec et al. 2020).

- **Class I**: the envelope loses material in a continuous rate, and at the same time, the central core becomes more massive and hotter. In the class I phase, the radiation of the protostar is no longer hidden by the envelope. At this stage, the protostar is

surrounded by an envelope and accretion disk in its equatorial plane. The disk is dense and thick, and its material is at much lower temperatures than the protostar, thus it emits at longer wavelengths. At this stage, the IR excess is very bright, primarily due to the disk.

- **Class II**: in this phase, the envelope has disappeared. The central object is now bigger and hotter, it continues to accrete material but only from the disk, which is now less massive. The SED is dominated by the emission of the hot central object. There is still IR excess but less bright than in the class I phase. Class II are often referred as the classic T Tauri stars.

- **Class III**: the clearing of disk material has continued, and the disk becomes extremely thin and faint. In the class III phase, SED is completely dominated by the central object, which is now close to start the MS phase, and the IR excess due to the disk emission is now very small.

Additional physical processes take place at every phase of the aforementioned classification: both the central object and the disk suffers different processes that affect the evolution, the structure and the dynamics of the system. The main processes that regulate the evolution and dispersal of the protoplanetary disk are discussed in Section 1.2.

1.1.3 Planet formation

A planet is assembled from the material available in the protoplanetary disk that orbits around the central object. To understand how planets form, it is important to take into account the large diversity of planets based on the Solar System and exoplanet surveys. The main distinction can be done between rocky planets and giant planets (see, e.g., Armitage 2011; Raymond & Morbidelli 2020), which is based on the mass of the planet, also connected to the planet composition (i.e., the fraction of gas). Rocky planets are essentially composed of silicates, and if gas is present (as an outer atmospheric layer), it only accounts for a small fraction of the total planet mass. On the other hand, giant planets are mainly made of gas. They may or may not have an inner rocky core, which would only be a small fraction of the total planet mass.

For rocky planets and giant planets with a rocky core, the first and essential step is the formation of the core itself. Once the rocky core is formed, the accretion of gas would typically define the final outcome: a rocky planet if no or little amount of gas is accreted; or a giant planet if a considerable amount of gas is accreted. The addition of gas depends on whether there is available gas in the vicinity of the planet core, thus it is only possible if the protoplanetary disk hasn't completely vanished (e.g., Howard et al. 2012; Alexander et al. 2014). The formation of planets without a rocky core is also possible, the main mechanism to form such planet is via gravitational instability. In this case, the end product is a giant planet composed of only gas. I now summarize the process to form a rocky core, and the gravitational instability process to form gas giants.

Formation of the planet core

The formation of the rocky core requires that dust from the protoplanetary disk, initially of sizes below microns, grow many orders of magnitude, first as kilometer-sized bodies (i.e., the so-called planetesimals) and up to the final size of the core. Small dust grains typically grow via grain-grain collisions (see Section 1.2.1 for a more detailed description). Collisions are very frequent due to the large gradient of velocities, sizes and trajectories of the dust population in disks, and are typically thought to be the major process to grow dust up to millimeter/centimeter sizes. There is plenty of evidence of grain growth in protoplanetary disks (e.g., Testi et al. 2003; Natta et al. 2004b; Ricci et al. 2010a,b). Beyond these sizes, the so-called bouncing barrier and other effects such as erosion and fragmentation prevent the grains to grow further (e.g., Blum & Münch 1993; Dullemond & Dominik 2005; Windmark et al. 2012).

An additional process or mechanism is needed for grains to grow further. Streaming instability can circumvent this cm-size barrier (Youdin & Goodman 2005). This process requires of a local over-density in the disk. The difference in the velocity between dust grains and gas causes a drag force to be exerted onto the grain. If the grain traverses an over-density, this drag force is diminished. The grain slows down and ultimately adheres to the over-density. An initially small over-density may become substantial with time, ending up as a large over-density where dust grains pile up. This over-density may become large enough to self-gravitate, forming a large body, namely, a planetesimal (e.g., Johansen et al. 2015; Simon et al. 2016, 2017). Streaming instability is the most likely and favored process to trespass the cm-size barrier, and it provides a robust mechanism to form planetesimals (Raymond & Morbidelli 2020).

Once a planetesimal is formed, gravity plays an important role since the planetesimal is large enough to attract dust, gas, and/or other planetesimals. The planetesimal should grow further in order to form a planet core. In the classical view, collisions between planetesimals were the preferred mechanism in order to form protoplanets (e.g., Wetherill 1992; Lissauer 1987, 1993). However this mechanism suffers from various limitations, such as the difficulty of keeping alive a population of planetesimals for enough time, or the difficulty of explaining the variety of planets in the Solar System (e.g., Morbidelli et al. 2015). Pebble accretion is a more favored mechanism to form a core. In this scenario, a planetesimal accretes small grains or pebbles from the surrounding material of the protoplanetary disk (Ormel & Klahr 2010). This scenario is in general more efficient, since the cross section between the planetesimal and a pebble is larger than between two planetesimals, and is favored by the ongoing evolution of the disk that allows the local disk to be continuously replenished with new material (e.g., Lambrechts & Johansen 2012, 2014; Johansen & Lambrechts 2017).

Therefore, a rocky core can form from a planetesimal thanks to pebble accretion. The amount of disk material left in the vicinity of the rocky core determines the end result of the planet. If gas is still present near the core, it might be accreted. If the core can accrete a large amount of gas, it will end up as a giant gaseous planet (e.g., Jupiter); if there is no available gas to be accreted, the core will end up as a planet of only rocky composition.

These are opposite outcomes, intermediate results are perfectly viable as well: the core might accrete a small fraction of gas that would then become the planet's atmosphere (e.g., the Earth), or a larger amount of gas to end up as a Neptune-like planet.

Gravitational instability

An alternative formation mechanism of giant planets is by disk fragmentation via gravitational instability (e.g., Boss 1997, 1998; Mayer et al. 2002). This requires of very massive disks, with masses of the order of the central protostar, so the self-gravity of the disk becomes important. Since the disk losses material with time, gravitational instabilities would typically occur at the very early stage of the disk's lifetime. Instabilities occur at a local scale, and are expected if the Toomre parameter Q (Toomre 1964), which quantifies the degree of self-gravitation, approximates to unity:

$$Q = \frac{c_s \kappa}{\pi G \Sigma}, \tag{1.2}$$

where c_s is the sound speed, κ is the epicyclic frequency (if disk follows Keplerian rotation, κ is equal to the keplerian orbital frequency Ω), G is the gravitational constant and Σ the disk surface density. Gravitational instability is thought to be feasible only in the outermost regions of the disk (Armitage 2011; Meru & Bate 2011). The instabilities will lead to self-gravitating clumps, that would then be able to contract further and become protoplanets. Studies have shown that these self-gravitating clumps will most often form objects more massive than planets, and likely beyond the deuterium burning limit (e.g., Kratter & Matzner 2006; Stamatellos & Whitworth 2009; Kratter et al. 2010; Forgan & Rice 2013). It is nevertheless possible to form giant planets such as Jupiter. To form such planet, particular requirements of the clumps must be met, such as the initial conditions, migration, survival of the clump and their cooling (see Kratter & Lodato 2016, and references therein). In a very particular scenario of gravitational instability with tidal stripping, it might also be possible to form a rocky planet (Nayakshin 2010).

The processes explained above provide a simplified view of planet formation. Additional aspects might have a considerable impact, as for instance the presence of other planets, resonances, migration, and the ongoing disk evolution processes. Planets are often found in multiple systems, that is, several planets orbiting the same star. The presence of other planets can help or prevent the formation of additional planets. Resonances between the location of the various planets likely affect the formation process, since there are favored orbital distances to arrange the planets (e.g., Terquem & Papaloizou 2007; Pierens & Nelson 2008; Izidoro et al. 2017). Migration of planetesimals and planets will most certainly take place at any stage of the planet formation process, and this will change the local disk and the available material that the planet accretes (Kley & Nelson 2012, and references therein). Lastly, the physical processes that take place in the disk pose many constraints

on the formation of the core and the addition of gas. In the next Section (1.2), I summarize the main physical processes and possible evolution of protoplanetary disks, which can help, limit or even prohibit planets to form.

1.2 Protoplanetary disk's evolution and dispersal

A protoplanetary disk, which starts as a very massive object, loses material with time due to various evolution processes until the disk becomes a debris disk or completely vanishes. Processes such as accretion, disk winds, and different dust evolution processes shape the disk structure and composition, and ultimately affects the disk's ability to form planets. Gas is the major component in protoplanetary disks, with a gas-to-dust ratio that is generally considered to be 100 based on the interstellar medium (although this ratio might be in some cases lower, see, e.g., Miotello et al. 2017).

Therefore, the gas component dominates the overall evolution and dispersal of the disk. The major processes to remove material from the disk are accretion onto the central star (or secondarily onto protoplanets that might form) and disk winds that typically remove material of the atmospheric layers of the disk. Dust evolution processes are crucial, on the other hand, to form planets as explained in Section 1.1.3. Dust can also interact with gas, thus affecting (and being affected by) gas evolution. In this section, I first describe the major mechanisms of gas evolution that leads to disk dispersal (namely, accretion, photoevaporative, and magnetohydrodynamical winds), and later I focus on the major dust evolution processes.

Accretion

Accretion of material from the protoplanetary disk onto the central star is the most widely accepted mechanism for angular momentum transport. The large mass difference between the original prestellar cores and MS stars provides a strong evidence that an important fraction of the stellar mass was accreted from a rotationally supported disk (Hartmann et al. 2016). Additionally, ongoing accretion in young systems have been widely observed (e.g., Bertout et al. 1988; Basri & Bertout 1989; Basri & Batalha 1990; Hartmann et al. 1998), especially in Class II objects where the central star and the innermost parts of the disks are less affected by extinction (e.g., Alcalá et al. 2014, 2017; Manara et al. 2016a; Mulders et al. 2017).

In an accreting disk, the central protostar is fed by a relatively continuous inflow of material from the innermost region of the disk. The origin of accretion is, however, still open to debate, yet the most accepted mechanism is via viscosity, typically formulated with the α prescription (Shakura & Sunyaev 1973), α being a parameter that quantifies the viscosity in the disk. The cause of viscosity in disks is also unclear, however, magneto-rotational instability (MRI) producing magnetohydrodynamical (MHD) turbulence in the disk is the most accepted mechanism to explain viscosity (Balbus & Hawley 1991). MRI requires gas in the disk to be sufficiently ionized and the presence of a weak magnetic

field in the disk (Ercolano & Pascucci 2017). In Figure 1.2 a representative diagram of the accretion onto the central star is shown. Material of the disk is transported inwards, thus there is an effective angular momentum transport. The innermost part of the disk is truncated by the stellar magnetosphere at around 0.1 AU from the center. Accretion flows launch from this innermost region and transport the material from the disk onto the protostar following the magnetic field of the star.

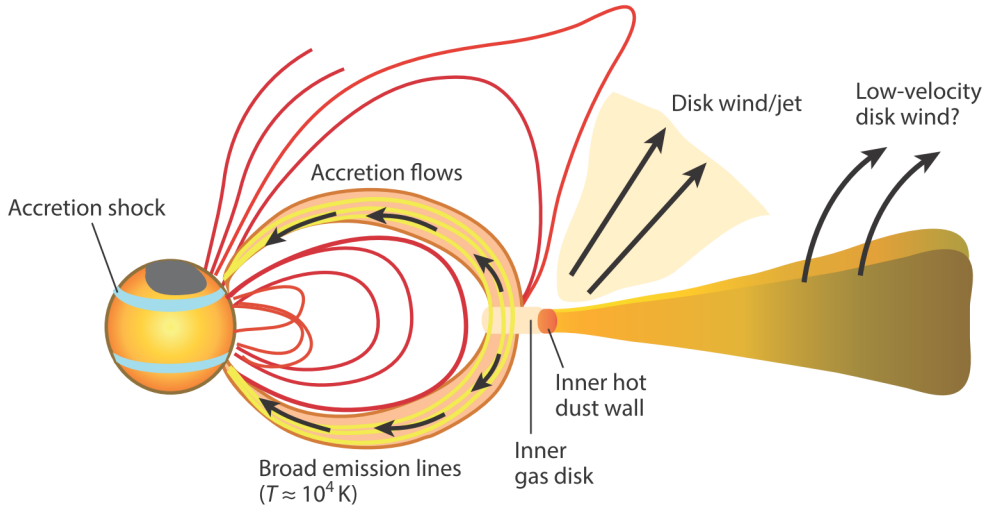

Figure 1.2: Schematic view of the main angular momentum transport and dispersal mechanisms of a protoplanetary disk. Adapted from Hartmann et al. (2016).

In a viscously evolving disk, the gas surface density decreases with time, but increases its extent to larger radii (Dullemond et al. 2006; Natta et al. 2007; Lodato et al. 2017), until the disk is finally dispersed or too faint to be detected. Accretion, typically measured as the mass accretion rate $\dot{M}_{\rm acc}$, is strong in an earlier stage and decreases with time. Accretion is, nevertheless, a variable process, with sporadic episodes of strong accretion onto the central object.

Photoevaporative winds

The strong radiation from the central star has a big impact on the evolution of the protoplanetary disk. This radiation reaches the atmospheric layer of the disk, heating up the material at these upper layers, and causing gas to escape if a critical temperature is exceeded. This escape of gas generates a photoevaporative wind, which provides a steady mass loss of the disk, thus it contributes to the disk depletion (e.g., Armitage 2011; Alexander et al. 2014; Gorti et al. 2016). Irradiation from far-UltraViolet (UV), extreme-UV and X-ray is effective at heating up the atmospheric layer of the disk, and consequently generating such winds. The penetration depth depends largely on the photon energy, and this influences the mass loss rate due to the wind. There is a critical radius in which irradiation hitting this or larger radii will produce most of the mass loss (Ercolano & Pascucci 2017).

The evolution due to photoevaporative winds in a viscous disk is dominated by the accretion onto the central object in the early stages, since the mass accretion rate is initially larger than the mass loss rate due to photoevaporation. The accretion rate decreases with time while the mass loss from winds is relatively steady. Once the accretion rate becomes low enough, accretion cannot replenish the mass loss due to photoevaporation, and a gap (typically at $\lesssim$ 10 AU) appears (Clarke et al. 2001). The material between the central object and the gap is then rapidly depleted, resulting in a transition disk with a large cavity. In this latest stage, the inner edge of the disk is completely exposed to the stellar radiation and the disk material is removed from this to outer radii until the entire disk is depleted.

Photoevaporation can also occur due to external irradiation of neighboring stars. If external photoevaporation is important, the strength of the external irradiation, and the particular morphology of the system will largely alter the disk evolution as described above.

MHD winds

The presence of magnetic fields can explain the existence of accretion and viscosity in disks. Additionally, it has been shown that vertical magnetic fields may produce magnetic winds that will remove material from the atmospheric layers. The vertical field is motivated by the environment of the disk, where the magnetic field lines of the molecular cloud traverse the entire disk. Studies investigating MRI and winds from MHD simulations suggest that magnetic winds can indeed be very effective at removing material from the disk, with results varying from extreme winds able to deplete the disk in less than 1 Myr (Miller & Stone 2000), to more gentle effects that would cause a similar disk evolution to what photoevaporative winds cause (Armitage et al. 2013). Other studies have also shown that strong MHD winds can account for accretion in disks even without MRI (Bai & Stone 2013, 2017). Further studies and advancements in our understanding of the true magnetic fields in protoplanetary disks are crucial in order to better constrain the importance and effects of MHD winds.

1.2.1 Dust evolution

The dust component of a protoplanetary disk, although certainly affected by the overall disk evolution, suffers from different forces and processes. This causes the evolution of dust to differ from the evolution of the gaseous component of the disk. Furthermore, dust evolution is the essential condition to form cores of planets. Therefore, understanding the main physical processes that affect dust is necessary in order to constrain the ability of the protoplanetary disk to form planets, and also the main properties of the assembled planet. In this section I describe the main physical processes that affect dust grains and shape the dust evolution in protoplanetary disks.

Grain growth

The initial population of dust grains in a disk is below micron sizes. Growth is required in order to form the rocky cores of planets, as described in Section 1.1.3. The initial growth is possible primarily thanks grain-grain collisions, but also via condensation. In grain-grain collisions. the main parameters that determine the final outcome are the relative velocity, the composition, size, and shape of the grains, and other properties such as porosity and internal structure. The frequency of the collisions, on the other hand, depends on factors such as the collision cross section, the number density of the particles and the relative velocity (detailed description in Testi et al. 2014). Based on laboratory experiments and the expected collision frequency, grain growth up to mm/cm sizes is generally expected by grain-grain collisions.

Growth via condensation occurs when the temperature of the gas surrounding the dust grain decreases below the gas condensation temperature. The gas then settles onto the dust grain surface, and eventually an iced mantle forms, effectively increasing the size of the dust particle (Goldreich & Ward 1973). This mechanism requires of large supplies of material in the gas phase close to the dust grains, which is often unavailable. Condensation is generally more effective on small grains, as it depends on surface area and small grains greatly outnumber large grains (Testi et al. 2014). Consequently, condensation would typically account for only a fraction of the total grain growth.

Radial drift

Dust particles in the protoplanetary disk can suffer friction with gas. This occurs to particles larger than the mean free path of the gas molecules. A drag force has a perceptible influence on the dynamics of these particles. The Stokes number (St) is used to quantify whether the particle motion is coupled to the fluid dynamics or not, defined as:

$$\mathrm{St} = \frac{\Omega_\mathrm{K}\ m\ v}{F_\mathrm{drag}}, \tag{1.3}$$

where Ω_K, m, and v are the orbital period, mass and speed of the dust grain, and F_drag the exerted drag force. If the Stokes number is small (< 1) the particle follows the motion of the fluid (i.e., the gas component), while if large, the particle follows its own inertia, thus effectively being dynamically decoupled from the gas.

The gas motion is slightly sub-keplerian as a result of the forces balance between the gravitational, centrifugal, and pressure forces. Small grains, since they typically have low values of the Stokes number, follow this gas motion. On the other hand, grains with high Stokes number (typically large grains) move freely, do not feel the pressure force, and therefore have a keplerian orbit that differs from the gas motion. This causes friction with the surrounding gas, resulting in a reduction of the particle's speed that pulls the particle towards the gradient pressure maxima. In a smooth standard disk without sub-structure, the pressure maxima is at the innermost region of the disk, thus the dynamically decoupled grain will effectively move inwards. This process is known as radial drift (Whipple 1972; Adachi et al. 1976; Weidenschilling 1977).

Radial drift is generally very effective at drifting large particles towards the pressure maxima. This drift halts at some inner region of the disk, resulting in a pile up of large grains. This over-density of large grains can boost the formation of planetesimals through pebble accretion, as described in Section 1.1.3. The presence of disk sub-structure like gaps, dead zones, radial an/or azimuthal inhomogeneities can modify the location of the pressure maxima, changing the direction of the drift, and the location of the piled-up grains that drift. Lastly, the gas-to-dust ratio has an impact on radial drift and the particle's motion (e.g., Testi et al. 2014). For the common value of 100 of the gas-to-dust ratio, radial drift behaves as explained, but with low enough values of the gas-to-dust ratio, the behavior might be reversed (Youdin & Goodman 2005), and could lead to other effects (e.g., streaming instability).

Turbulence, Brownian motion and vertical mixing

Turbulence in viscously accreting disks may cause stirring and turbulent motion of grains if the Reynolds number is large enough (e.g., Voelk et al. 1980; Markiewicz et al. 1991; Ormel & Cuzzi 2007). Additionally, grains are subject to Brownian motion, that is, random motion of particles that are suspended in a fluid (e.g., Testi et al. 2014). On the other hand, the vertical component of the particle's position and velocity should not be forgotten. If a particle is at a certain height above the disk mid-plane, it will move towards the mid-plane. This motion can be either damped oscillations until settling on the mid-plane if the Stokes number of the particle is large, or damped within one orbit if St is low (e.g., Dubrulle et al. 1995; Fromang & Nelson 2009). Turbulence and Brownian motion ensures vertical (and radial) mixing of particles, thus the different atmospheric layers of the disk continue to be replenished by a new population of dust grains. Vertical mixing is more effective on small grains, since large grains are heavier thus once settled at the mid-plane, it becomes more difficult to transport them vertically.

All these types of motion affect the dust component of the disk and contribute to the large variety of speeds and directions of the dust grains in protoplanetary disks, increasing the frequency of grain-grain collisions that help grains to grow up to mm/cm sizes.

1.2.2 Observations of protoplanetary disks

The field of protoplanetary disks experienced a drastic evolution in the 20th century, and most notably on the second half, thanks, to a great extent, to the advances on technology and astronomical instrumentation. The discoveries of T Tauri and Herbig AeBe young star types (Joy 1945, 1949; Herbig 1960, 1962), were the first step on the extraordinary breakthrough that followed.

In the 1960-70s, features such as the blue and IR excess emission in these young objects were first seen as evidence of shells or envelopes as remnants of the cloud collapse (e.g., Mendoza V. 1966, 1968; Strom et al. 1971). Both features were soon after explained as hot (blue) emission from the stellar surface and accretion shocks, and as IR emission from cool dust further from the star (e.g., Lynden-Bell & Pringle 1974a; Cohen 1983;

Lada & Wilking 1984; Uchida & Shibata 1984). By the 1980s, the view of these young objects as circumstellar disks accreting material onto the central protostar was set. Further characterization followed thanks to the discovery of features such as collimated outflows, winds, disk instabilities due to outbursts, polarized and scattered light from the disk (e.g., Elsasser & Staude 1978; Vrba et al. 1979; Lada 1985; Hartmann & Kenyon 1985; Edwards et al. 1987; Cabrit et al. 1990). These advances were accompanied by the first spatially resolved observations of disks in the 1990s, thanks to the Hubble Space Telescope (HST) (e.g., O'dell et al. 1993; McCaughrean & O'dell 1996) and the first radio interferometers in the millimeter (e.g., Sargent & Beckwith 1987; Koerner et al. 1993; Dutrey et al. 1994).

The progress in the field continued to speed up with the beginning of the 21st century. Instruments such as the Spitzer Space Telescope (Werner et al. 2004) greatly contributed to the field, allowing the identification and classification of young stars with IR excess. As result, large catalogs of protoplanetary disks were assembled (e.g., Evans et al. 2009; Furlan et al. 2009, 2011). More recently, the study of protoplanetary disks has been dramatically improved thanks to the exquisite sensitivity and angular resolution that ALMA offers at (sub-)mm wavelengths. This radio telescope provides interferometric observations with resolutions down to ~ 0.02 arcsec that allow to fully resolve the emission of nearby protoplanetary disks. In this section, I summarize the main types of observations that allows us to characterize the dust and gas components of protoplanetary disks.

Unresolved observations

As introduced in Section 1.1.2, the SED allowed to classify protoplanetary disks around young stars thanks to the IR excess with respect to a MS star. The object's class provides a first idea of the evolutionary stage of the disk. Other features in the SED can also help constraining other processes and properties of protoplanetary disks, such as accretion, composition, morphology, or their lifetime.

In a classic T Tauri star (a class II object), the SED is essentially the sum of the SED of a star and of a disk (example in Figure 1.3). At micron wavelengths, the contribution of the star radiation dominates the SED. The contribution of the disks is noticeable from near-IR wavelengths, with emission of the disk typically peaking at mid- and far-IR. The SED of the disk is dominated by the thermal emission of the dust continuum. The emission at different wavelengths typically originate from dust at different regions of the disk with different temperatures and optical depths. Emission at near- and mid-IR traces warm dust heated by the central object irradiation that is found in the inner regions of the disk at the atmospheric layers. The optical depth at these wavelengths is very large (e.g., Adams et al. 1987; Kenyon & Hartmann 1987). At longer wavelengths (e.g., far-IR), the emission is less optically thick, and mostly originates by dust at lower temperatures that extends over larger distances in the disk (from ~ 1 to ~ 50 AU) and at intermediate atmospheric layers (e.g., Andrews 2015). At (sub-)mm wavelengths, the emission is mostly optically thin and traces the cold dust at the disk mid-plane (e.g., Beckwith & Sargent 1991; Henning & Stognienko 1996). On the other hand, the gas component of the disk produces emission and absorption lines along the SED; these lines provide insightful information of the gas

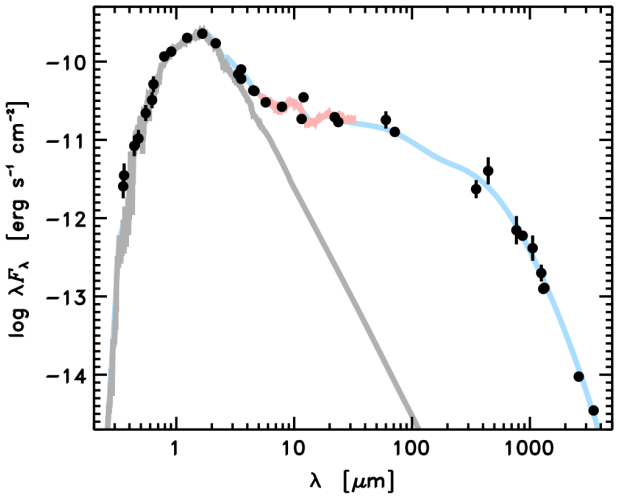

Figure 1.3: SED of GO Tau system. Black dots represent observed emission at different wavelengths, from Andrews (2015) and originally assembled by Andrews et al. (2013). The gray curve represents stellar photospheric models, while blue curve represents radiative model of the protoplanetary disk orbiting the central object. Red curve shows the observed IR spectrum from Furlan et al. (2009).

species near and far from the star, and at different atmospheric layers of the disk.

However, the study of the SED has many limitations since the disk emission is not resolved. Many of the disk processes can't be fully addressed from only the SED, due to the degeneracy of solutions (e.g., Thamm et al. 1994). In order to further study the different regions and processes of the disk, it is necessary to resolve the emission.

Resolved thermal emission

In order to resolve the disk thermal emission, interferometers are necessary, since even the closest disks are smaller than the diffraction limit of single telescopes. By combining several telescopes together, interferometry allows to increase the resolution of the observations. Interferometric observations measure the emission of a source in the frequency domain instead of the spatial domain. In Section 2.1, I provide a detailed description of the main formulation and principled of interferometry.

Depending on the wavelength used, interferometric observations probe different regions of the disk. On the one hand, IR interferometry, with resolutions that can go well below 1 AU, probe the inner disk and its boundary with the outer disk. At around 1 AU, a rounded dust rim sets the start of the outer disk, composed of dust and gas. In the inner disk, free of dust, atomic and molecular gas at a high temperature is present (Dullemond & Monnier 2010). This inner disk gets very close to the star, usually only a few stellar radii distance from the center. At its innermost region, vertical flows originate from the mid-plane and are accreted onto the central object (see Figure 1.2). Therefore, IR interferometry allows for very valuable studies of the stellar accretion, the accretion flows, the inner disk, the

dust rim separating inner and outer disk, and even the first AU of the outer disk (e.g., Millan-Gabet et al. 2007; Dullemond & Monnier 2010).

On the other hand, (sub-)mm interferometers capture the cold thermal emission from the outer disk, which typically extends over tens or even hundreds of AU (Testi et al. 2014; Andrews 2015). Since it is where the bulk of the disk mass is, the study of the outer disk at these wavelengths provide unique insights of the disk and the planet formation mechanisms. Both dust and gas can be studied at these wavelengths. In Chapter 2, I discuss in more detail these observations and how to model the emission of the dust and gas component at these wavelengths.

Scattered light

These observations allow to resolve the disk by studying the light that is scattered by the atmospheric layers of the outer disk (e.g., Watson et al. 2007). The central star radiates in every direction, thus some of this radiation reaches the disk. A fraction of this radiation is reflected by the small dust grains present in the upper-most atmospheric layers of the disk, while the remaining radiation will travel to deeper layers of the disk, heating up these layers. The light scattered by the disk is typically observed in optical and IR wavelengths. These observations are extremely valuable for the study of the vertical structure of disks, since the light is scattered by the uppermost layers of the disk atmosphere.

Scattered light observations are limited by the high contrast brightness between the central star and the reflected light. There are a number of strategies that help reducing this limitation, as for instance, the use of adaptive optics, coronagraphs, and other methods. Techniques like the Polarimetric Differential Imaging (PDI) are nowadays frequently used to improve the signal of the disk. These techniques can also be used to search for planetary companions, as discussed in more detail in Chapter 5.

Gas observations

Observations of the gas component in protoplanetary disks are accomplished by studying specific wavelengths at which the transitions between excitation states of each gas species take place. Therefore, these observations require higher spectral resolutions than dust continuum observations. Each species has its own characteristic energy levels, and consequently emission and absorption lines of the gaseous component of the disk can be found throughout the SED of the system. Observations at short wavelengths (UV, optical, IR) generally trace the hot gas close to the star and in the inner disk, with temperatures $\gtrsim$ 100-2500 K, while longer wavelengths (e.g., mm) trace the cold gas in the outer disk, with temperatures typically below 100 K (Carmona 2010). The main element in protoplanetary disks is hydrogen, and the primary gaseous species is H_2. Heavier elements and molecules are present but with much lower abundances. H_2 is difficult to detect since it is a symmetric molecule and consequently has no electric dipole moment. Other transitions of this molecule, like ro-vibrational and fluorescent electronic lines can be found in near-IR and UV respectively (e.g., Herczeg et al. 2006; Najita et al. 2007).

Transition lines of other atomic and molecular species are often easier to detect, and are therefore used to characterize the gas component in disks. In optical and IR wavelengths, atomic lines (e.g., oxygen and neon, Acke et al. 2005; Güdel et al. 2010) and ro-vibrational lines of organic molecules (e.g., C_2H_2, HCN, CO_2) are extensively detected (e.g., Lahuis et al. 2006; Carr & Najita 2008). These lines are emitted from the inner disk and close to the central object.

At (sub-)mm, rotational transition lines of many molecules are detectable, and trace the cold gas in the atmosphere of the outer disk. Molecules observed frequently at these wavelengths (with varying abundances) are CO, HCO^+, H_2CO, CN, and complex molecules (e.g., Guilloteau & Dutrey 1998; Dutrey et al. 1997; van Zadelhoff et al. 2001; Thi et al. 2004; Henning et al. 2010). Even species at very low temperatures emitting from the mid-plane, like H_2D^+ or N_2H^+, can be observed thanks to their very low condensation temperatures (e.g., Ceccarelli et al. 2004; Dutrey et al. 2007).

CO is one of the most abundant and frequently detected species at (sub-)mm wavelengths thanks to modern interferometers like ALMA, and it allows to study the outer disk structure and dynamical behavior. Isotopologues that are often observed are ^{12}CO, ^{13}CO and C^{18}O (e.g., Guilloteau & Dutrey 1998; Dartois et al. 2003). The last two isotopologues are less abundant and optically thinner than ^{12}CO, thus typically trace colder layers of the disk. By observing various transitions with different optical depths, we can probe different atmospheric layers of the disk, and is therefore possible to characterize the vertical structure of the disk.

CO has, nonetheless, some limitations. The CO abundance is, in a first order, determined by two main processes, namely photodissociation and freeze-out. Photodissociation of CO is the process of separating the two atoms from absorption of a UV photon (the binding energy of the CO molecule being 11.09 eV). This occurs at the higher layers of the disk atmosphere where the molecules are radiated by the central star. At deeper layers, the CO column density becomes large enough to self-shield from the absorption of UV photons. For ^{12}CO, self-shielding occurs at around $\sim 10^{15}$ cm^{-2} (van Dishoeck & Black 1988). For rarer isotopologues, the column density is typically lower, thus self-shielding occurs at deeper layers in the disk. On the other hand, in the coldest regions of the disk (i.e., in the mid-plane) the molecule may freeze-out at the surface of dust grains if the temperature is low enough. This effectively reduces the abundance of the molecule in gas phase, thus no longer emitting. The freeze-out temperature of CO is typically of 20 K, although it can be slightly higher or lower depending on factors such as density and ice's composition (Bisschop et al. 2006; Harsono et al. 2015). Another caveat of studying CO is the possibility of CO being less abundant than expected compared to ISM abundances, as suggested by recent studies (e.g., Miotello et al. 2017).

1.3 Early stages of newborn planets

Planets, once formed, continue to evolve during their lifetime. At very early ages, a planet is typically very hot, and with time, becomes colder. At the beginning of this section I

focus on the early evolution of planets. I then discuss the main methods used to detect planets, with special interest on young systems where disks are still present.

1.3.1 Evolutionary tracks of protoplanets

Once a planet has formed, as described in Section 1.1, its evolution is dominated by its entropy, assumed that there are no drastic events as impacts with other large bodies. The main two mechanisms to form planets, core formation with subsequent accretion (often referred as core accretion) and gravitational instability, can produce very different properties of the planet.

Planets formed following the core accretion scenario are expected to have higher metallicity than planets formed by disk instability. A higher metallicity causes the radius to be smaller when comparing two planets with the same entropy formed by the two mechanisms (e.g., Burrows et al. 2000; Guillot et al. 2006). It also increases the opacity of the atmosphere, which slows down the rate at which the planet loses heat (Burrows et al. 2007). Another difference between the planets formed by the two mechanisms is the time required to form each planet. Gravitational instability is a very fast process that would typically occur at the very early stages of the disk. Planets by this mechanism can form in only a few orbits (Boss 2000). Core accretion, on the other hand, takes about 1 Myr (with variations of about an order of magnitude) since processes such as grain growth and the formation of planetesimals are typically slow (e.g., Pollack et al. 1996; Spiegel & Burrows 2012).

A final key difference between the planets formed via the two main mechanisms is the disparity in the initial entropy. A planet formed from gravitational instability keeps most of the entropy from the disk, while if formed from core accretion, the entropy is highly reduced by the accretion shocks generated in the formation process (e.g., Hubickyj et al. 2005; Spiegel & Burrows 2012). This difference in the expected initial entropy is used to model the early evolution of planets, distinguishing between *hot-start* and *cold-start* models of planets. In reality, the *hot* and *cold-start* models are likely extreme opposites, accretion shocks can also occur during the formation of gravitational instability planets (thus losing entropy), and also the efficiency of removing entropy by accretion shocks is rather variable (Mordasini et al. 2011; Bromley & Kenyon 2011). However, it is very useful to study the early planet evolution based on the two opposing scenarios (*hot* and *cold start* models), keeping in mind that a real planet has likely an initial entropy in between the two scenarios.

Based on these considerations of the initial entropy, and by studying the evolution of the cooling process for a variety of planets with initial entropies and properties, the early evolution of planets can be modeled (e.g., Spiegel & Burrows 2012). These models typically focus on the first Myr of the planets, providing estimates on main planet properties such as entropy, temperature and radius. These models show that more massive planets are able to keep heat for longer times, this is a consequence of the virial equilibrium, in which the thermal energy scales with the gravitational energy, and the gravitational energy $\propto M_{\rm pl}^2$ (Spiegel & Burrows 2012).

Entropy, planet radius and effective temperature decrease with time, this is valid independent of the formation mechanism, initial entropy or mass. When considering different initial entropies for the same planet mass, the evolution of the planet properties converges with time (within the first 100 Myr - 1 Gyr). From that point forward, the initial conditions do not have any incidence on the planet evolution.

It is possible to study the absolute magnitude of the planets by modeling the early evolution of the planet's SED. A planet typically peaks at IR wavelengths given the typical range of effective temperature ($\sim$ 200 - 1000 K). The planet atmosphere, in particular its composition, is crucial in order to model the planet SED in detail. The composition of the atmosphere determines the emission and absorption features that characterize the SED of the planet. The existence of clouds and the metallicity are often considered when modeling the time evolution of the planet emission. A way to model the SED of the planet as a function of time is by using various SED templates that consider different planet atmospheres (e.g., Burrows et al. 2011; Spiegel & Burrows 2012).

In accordance with the evolution of entropy and effective temperature of the planets, the evolution of the SED decreases with time. At the very early ages (<100 Myr), planets formed by gravitational instability are considerably brighter than those formed via core accretion. The difference in the SED between the two scenarios decrease with time, until a time where the SED of the two models coincide (e.g., Spiegel & Burrows 2012).

The evolution explained above is an ideal scenario where changes in the environment of the planet are not considered, and where the planet does not encounter major unexpected or disruptive events (e.g., collisions). Such events can have dramatic consequences on the planet, its properties and its temporal evolution. In a more realistic evolution scenario, the environment also plays a role on the cooling and composition of the planet, and it is plausible to think that the planet will indeed encounter drastic events with unpredictable consequences. A major consideration is the radiation variability from the environment, predominantly from the central star (Güdel 2007).

For instance, in the solar System, the early Sun was hotter than today, and consequently it was also much brighter (about 10-30 times). The Earth formed in a warmer environment and most likely in a region without water. Besides, by the time the proto-Earth was formed and on its early phases, the Sun was extremely variable, and generated extreme winds. Due to the strong winds, most volatile elements in the initial Earth's atmosphere could have evaporated and escaped. Other environmental agents, such as meteorites can also have an incidence, for instance in the planet composition. Lastly the formation of moons should be considered as well. In the case of the Moon, it is thought that it formed as a consequence of an impact with a large body (e.g., Canup & Asphaug 2001; Canup 2004). The release of gravitational energy from such impact would heat the protoplanet surface, altering its main properties, and likely evaporating a large fraction of its atmosphere.

1.3.2 Detection techniques

I now focus on the methods that can be used to detect planets outside the Solar System. From early in the 1990s with the detection of the first exoplanets, the field experienced and astounding development, with up to 4379 confirmed planets discovered up to date (Dec 1st 2020, from http://exoplanet.eu). The first detection of an exoplanetary system was accomplished by studying time delays of the radio pulses of PSR1257 + 12 pulsar, which in fact confirmed the existence of at least 2 planets (Wolszczan & Frail 1992). Velocity variations of stars caused by orbiting planets were detected previously, but misinterpreted as either stellar activity (Campbell et al. 1988) or as a likely brown dwarf companion (Latham et al. 1989), and only later on it was confirmed to be due to planets.

Many techniques have been successful in detecting exoplanets. I summarize the main techniques that have been used so far:

Radial velocity

A planet orbiting a star exerts a gravitational force that causes the star to rotate around the barycenter of the two bodies. This relative motion of the star induced by the planet produces a Doppler shift in the signal of the star, and can be therefore identified as oscillations in the star's radial velocity. The amplitude of this oscillation increases for more massive planets and shorter orbital periods (e.g., Fischer et al. 2014). Only a minimum mass of the orbiting planet can be measured (i.e., $M_{\rm pl} \sin i$, i being the orbital inclination). This method usually requires to study the radial velocity variations for a few orbital periods at least, in order robustly determine the oscillations caused by the planet (e.g., Lovis & Fischer 2010).

The radial velocity method became the most fruitful technique to detect exoplanets until 2011. From then, its discovery pace has slowed down due to the required high precision and due to the larger orbital period of the still to be detected planets (Fischer et al. 2014). The precision has indeed improved from around 10 m s^{-1}, down to $\lesssim$ 50 cm s^{-1} thanks to the advancements in instrumentation. On the other hand, since the exoplanets with shortest orbital periods could be detected already, to continue with new discoveries it is now necessary to monitor stars for long periods of time, and a detection can even take several years (Dumusque et al. 2012).

The amplitude of the oscillations is also increased for lower stellar masses (e.g., M dwarfs). These stars are indeed ideal targets to study, since the habitable zone of these stars appear at closer orbits. Many radial velocity surveys have therefore focused on M dwarfs (e.g., Bonfils et al. 2013). In these surveys, The most limiting factor is the fainter stellar emission. In order to ease their radial velocity measurements, surveys targeting these stars are typically designed to study red optical and near-IR, since is at these wavelengths where the emission of these low mass stars peaks.

Transits

A planet orbiting a star might result in a transit if, due to its orbital motion, the planet crosses the line-of-sight between star and observer. In such scenario, while the planet is transiting the star, the emission of the star is partly covered by the planet, causing a dip in the stellar emission. The light curve of the star is used to identify a transiting planet, as Figure 1.4 shows for the first transiting planet ever found (Charbonneau et al. 2000; Henry et al. 2000). Transit events can only occur when the orbit of the planet is nearly edge-on. The dip in the light curve of the star is more accentuated when the planet radius is larger (thus generally more massive planets), and when the orbit's inclination is closer to 90°. The probability to encounter a transit depends on the particular geometry of the system, but primarily the radius and the orbital period of the planet are the parameters with a higher impact (e.g., Fischer et al. 2014). A transit event alone doesn't provide a measurement of the planet mass, this greatly limits how many planets can be confirmed by this method, especially the larger planets, whose transit signatures can easily be confused with very low mass stars or brown dwarfs.

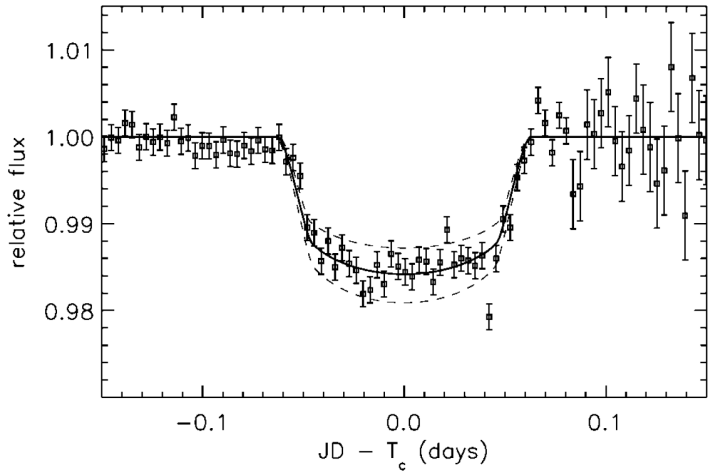

Figure 1.4: Light curve of star HD 209458, that shows the dip due to a transiting planet (Charbonneau et al. 2000). The solid line represents the best fit model of the transit, with planet radius of 1.27 R_J and inclination of 87.1°. Upper and lower dashed lines represent models with planet radii 10% smaller and larger respectively.

The number of exoplanets discoveries using this method has grown exponentially after the first detection. The earlier discoveries were done thanks to ground-based observations (e.g., Bakos et al. 2007; Collier Cameron et al. 2007). But, undoubtedly, the space-based telescopes have been the agents that revolutionized the field of exoplanets. The major contributor to the detection of exoplanets has been NASA's Kepler mission (Borucki et al. 2010), designed to search for transiting planets in the habitable zone around sun-like stars. It allowed the discovery of more than 2500 exoplanets and more than 5000 exoplanet candidates, and after 9 years collecting data, it ceased operations in October 2018. Following

Kepler, the Transiting Exoplanet Survey Satellite (TESS), and the CHaracterising ExOPlanets Satellite (CHEOPS) launched respectively in 2018 and 2019, will continue to increase the number of confirmed exoplanets and exoplanet candidates in the following years.

Transit events can even be used to study the atmosphere of the transiting exoplanet (e.g., Charbonneau et al. 2002). And, in combination with radial velocity measurements, the density of the transiting planet can be measured, which can be used to constrain the composition of the planet (Lithwick et al. 2012).

Pulsar timing

The first confirmation of an exoplanetary system was accomplished by this method (Wolszczan & Frail 1992). The radiation of pulsars (which are fast rotating neutron stars), is detected as pulses that are more regular than atomic clocks. These pulses are typically of the order of millisecond to second, set by the star's rotation. The presence of planets in the system causes the neutron star to orbit the barycenter of the system. This causes slight variations of the pulses that can be modeled to confirm the presence of the planet. This method can be used to detect planets with masses of only a fraction of the Earth's mass (Fischer et al. 2014). The main limitation of detecting planets by this method is that pulsars are relatively rare events, therefore, only a few dozens exoplanets has been detected by pulsar timing thus far.

Gravitational microlensing

This technique is based on the event of gravitational lensing, that occurs when the path of light emitted by a background source is bent by the gravitational potential of a second body located between light source and observer (Chwolson 1924; Einstein 1936). If the background source and lens are two stars, the event is referred as microlensing. Depending on the specific geometry of the lensing event, the observer can see different patterns in the sky. If the lens is perfectly aligned between light source and observer, the last one will see a ring of emission; if the lens is slightly offset, the observer will see two images of the source. More peculiar geometries can produce very complicated deformation patterns in the sky.

This phenomenon can be used to search for exoplanets orbiting the star that acts as the lens (e.g., Mao & Paczynski 1991; Gould & Loeb 1992; Griest & Safizadeh 1998). The presence of a planet might cause perturbations on the original microlens image in the sky. This can only occur if the planet is timely located near one of the images that the lensing event generates. To identify the presence of an exoplanet by this method, a very peculiar arrangement of source, lens, planet and observer is required. Consequently, millions of stars need to be monitored in order to detect a microlensing event.

Astrometry

This method consists on studying the motion of a star relative to the background sky. If a planet is orbiting the star, the star rotates around the barycenter of the system. The variation in the star's position is typically very small, and the further the star is from the observer, the smaller the displacement caused by the planet. Therefore, the precision required to detect exoplanets by this method is very high. For ground-based observations, the atmosphere's turbulence limits the precision of the telescope and needs to be addressed with the use of adaptive optics (Cameron et al. 2009), with appropriate modeling (e.g., Lazorenko & Lazorenko 2004), or by other means (e.g., Shao & Colavita 1992).

At the moment, only a few exoplanets have been discovered using this technique due to the required precision. However, astrometry is extremely helpful as a complementary method of radial velocity and other methods, since the planetary mass can be inferred from astrometric detections (if the stellar mass is known), and also inclination of the planet's orbit can be determined (e.g., Gatewood 1976; Black & Scargle 1982).

Direct imaging

The direct detection of the planet's emission is the most advantageous method to study exoplanets. It unambiguously confirms the presence of a planet, and, additionally, allows for a very detailed characterization of the planet.

However, the most limiting factor is the sensitivity required to directly observe the planet, which emission is many orders of magnitude lower than the star. In order to mitigate the emission difference between planet and parent star, a number of strategies should be taken. Since the peak emission of planets is typically in the near-IR, telescopes at these wavelengths are the most suitable for directly imaging the planets. And, by targeting young systems (< 100 Myr), planets are, in principle, easier to detect, since young planets are hotter and brighter. Adaptive optics, and coronagraphs are common methods to improve sensitivity and reduce residual emission from the parent star (e.g., Guyon et al. 2006; Lyot 1939). Other high contrast imaging techniques, such as Angular Differential Imaging (ADI, Marois et al. 2004, 2006), and Polarimetric Differential Imaging (PDI, Kuhn et al. 2001), are now employed on the most advanced imagers, such as the Spectro-Polarimetric High-contrast Exoplanet REsearch (SPHERE) at the Very Large Telescope (VLT) array. In Section 5.1, I discuss high contrast imaging observations in more detail.

There have been a number of exoplanets successfully detected by direct imaging techniques (e.g., Lagrange et al. 2010; Lafrenière et al. 2010; Kuzuhara et al. 2013). The first discovery was of a 5 M_J planet orbiting the 2MASSWJ 1207334-393254 young brown dwarf (Chauvin et al. 2004). Most of the discoveries have been accomplished on systems with ages of around 10-500 Myr old, but whose protoplanetary disk being already depleted, or with only a debris disk remaining. However the recent discovery of two young planets around PDS 70 (Keppler et al. 2018), a ~ 5 Myr old star with a protoplanetary disk, has perhaps the biggest impact. This discovery has tremendous significance since it allows the study of planet formation, the planet-disk interaction and the effect of a planet in the

evolution and dispersal of the disk.

Other indirect methods

There are a number of alternative techniques that have either been proven to successfully detect exoplanets, or that can potentially become powerful techniques in the future. For instance, the level of polarization of light from a star can tell about the existence of a planet, since starlight is unpolarized but becomes polarized when scattered by a planet atmosphere (Berdyugina et al. 2008). Other techniques involve eclipses from X-ray observations, or time variations from eclipsing binaries (Di Stefano et al. 2020; Doyle et al. 2011).

On the other hand, by studying protoplanetary disks and the imprint that an embedded planet could have on the disk, a number of indirect techniques can reveal the presence of a planet. Thanks to the advancements of the past years, protoplanetary disks are now being fully resolved, and many different features at the sub-structure level are now seen with relatively high frequency. Some of these features are often interpreted as the outcome of an embedded planet interacting with its surrounding disk material. The existence of gaps in protoplanetary disks, as the famous ALMA observation of HL Tau (ALMA Partnership et al. 2015a), have been commonly attributed to planets depleting the disk material around themselves. Similarly, spirals in protoplanetary disks have been also observed (e.g., Benisty et al. 2017; Huang et al. 2020; Wölfer et al. 2020), and an interpretation might be that material from the disk is infalling and being accreted onto an embedded protoplanet.

Another indirect method that may be used to infer the presence of protoplanets is by searching for the circumplanetary disk that would form around a planet that is still accreting material. As a matter of fact, the circumplanetary disk around PDS 70 b has been recently detected based on (sub-)mm continuum observations (Isella et al. 2019), with an estimated dust disk mass of $\sim$ 2-4 $\times$ 10^{-3} $M_{\oplus}$.

Lastly, a promising method to unveil the presence of planets embedded in disks is the study of the kinematics of the protoplanetary disk (Pinte et al. 2018b; Teague et al. 2018). If a planet is present, the motion of the surrounding material would be perturbed by the planet. By studying velocity maps of disks that are now frequently produced from (sub-)mm observations, small-scale perturbations can be understood as the outcome of planet-disk interaction. However, gaps, spirals, and other sub-structure features in protoplanetary disks do not unambiguously confirm the presence of planets. Therefore the interpretation of disk features to detect young planets should be taken with a lot of precaution.

Exoplanet population

There is now a rich population of confirmed exoplanets, showing a great diversity of planet masses, orbits, and architecture of the systems. In Figure 1.5, the mass and orbital period of the population of $\sim$ 4300 confirmed exoplanets is shown, distinguishing by discovery method, and including the planets from the Solar System (Gaudi et al. 2020). The most successful methods up to date have been radial velocity and transit techniques, specially the later method during the 2010s thanks to the enormous dataset that the Kepler mission

yielded.

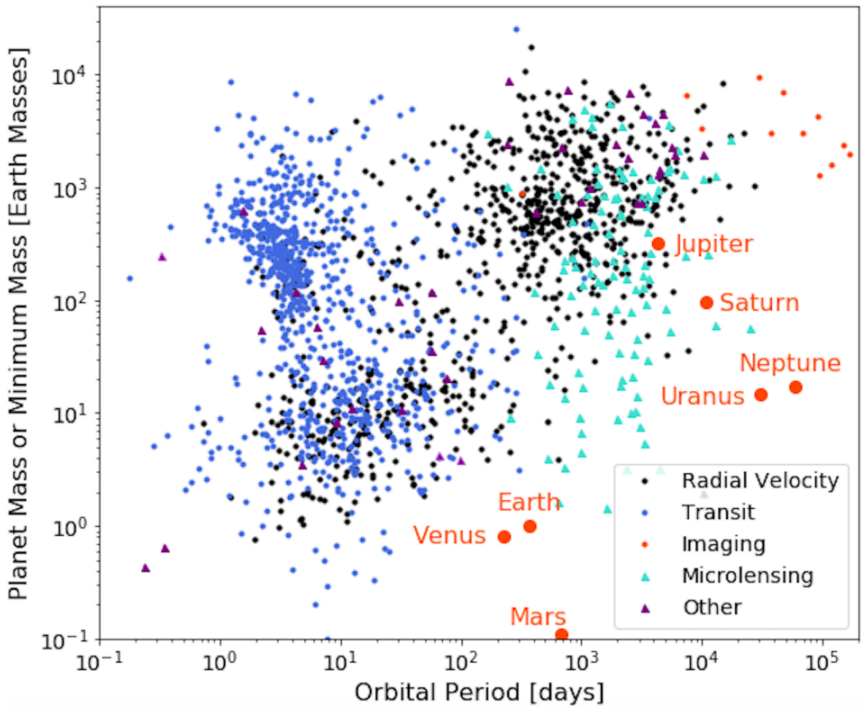

Figure 1.5: Confirmed exoplanet population, represented as a function of planet mass (or minimum planet mass if the exoplanet was discovered by the radial velocity method) and orbital period. From Gaudi et al. (2020). Different symbols represent the technique employed for its discovery: black dots for radial velocity, blue dots for transits, orange dots from direct imaging (large orange dots representing the planets from the Solar System), turquoise triangles are exoplanets discovered by microlensing, purple triangles represent the remaining techniques.

The figure clearly shows, on the other hand, which are the major archetypes of the confirmed exoplanet population: hot gas giants at very close distances to the parent star ($\lesssim$ 0.1 AU), cold gas giants (at distances of $\gtrsim$ 1 AU) and sub-Neptune planets at orbits smaller than 1 AU. These results show as well the current bias of the various detection techniques, favoring the detection of planets with specific properties: sub-Neptunes and (hot) gas giants with short orbital periods are easily detected by the transit method, while cold gas giants are easier to detect from the radial velocity method. The current population of exoplanets is therefore highly incomplete and the true population might be weighted differently from what can be seen in Figure 1.5.

A way to reduce the biases from the sample selection is by binning the exoplanetary population by specific planet properties (e.g., planet mass, planet radius, orbital period) and by stellar properties (typically spectral type or stellar mass). The occurrence rate is broadly used in the exoplanetary field for this regard; it is defined as the mean number of planets of a specific property range that is expected by a star. These rates are extracted

from the total population of exoplanets, and it alleviates the problem of the sample selection bias since one can restrict the analysis to well sampled bins. Due to our interest on finding Solar System analogs, stars with masses within the [0.5-1.2] $M_{\odot}$ range have been targeted the most in exoplanetary surveys. Therefore, occurrence rates are better constrained for these stars. The occurrence rate of small planets (with radius between 1 to 4 $R_{\oplus}$) orbiting Sun-like stars is around 0.5. This value can be understood as half of Sun-like stars are hosting a planet with a radius within [1-4] $R_{\oplus}$. For the same type of stars, the occurrence rate of gas giants is lower, around 0.1 (Winn & Fabrycky 2015). Future surveys will continue to expand the range of stellar types, radii and mass ranges of planets, and will help constraining occurrence rates further.

The exoplanetary system can also be studied with the current datasets. The number of stars that host two or more confirmed planets is indeed very significant: from the $\sim$ 3200 exoplanetary systems known to date, more than 700 are multiple systems (more than 20%). Taking into account the reduced sample of planets that can be detected due to the biases introduced by each technique, the fraction of multiple systems is considerable, and the true fraction is most likely higher. For systems with multiple planets, the study of the orbits and the relative separation within planets is an important property that characterizes the system, and more importantly, can be used to understand how planet formation proceeded in the system. Although resonant distances are more frequent, the full histogram of planet pairs do cover the full range of relative distances (e.g., Burke et al. 2014)

1.4 Role of the Thesis

The major goal of this thesis is to constrain disk evolution and planet formation processes, primarily by providing robust measurements of the dust and gas properties in a homogeneous population of protoplanetary disks, and secondly by assessing the possibility of detecting young planets that might be present within the disks.

The importance of measuring disk properties is paramount for constraining the disk evolution and the major physical processes that take place in protoplanetary disks. Moreover, these processes are intimately linked to the ability of the disk to form planets. Planets with a rocky core are assembled from the available dust in the protoplanetary disk. In an initial stage, dust grains are of very small sizes ($\lesssim 1$ μm). Growth of dust grains is required to form the rocky core of planets, first to mm/cm size grains, and continuing the growth up to km-sizes to become planetesimals. When the dust grains are of the order of mm/cm size, they become (dynamically) separate bodies from the gas, and experience radial drift (see Section 1.2.1). In a standard disk without sub-structural features, radial drift would typically result in a pile-up of large grains in the inner region of the disk. This over-density of dust can facilitate further growth, first to planetesimals, and up to the final planet core (see Section 1.1.3).

Although there is observational evidence of grain growth and radial drift in protoplanetary disks, it has been limited to a narrow and heterogeneous sample of sources. There is at the moment no systematic study of an homogeneous and large sample of disks

where these processes have been studied accurately. This greatly limits our knowledge on protoplanetary disk evolution and planet formation processes. It is necessary to perform a demographic analysis of these processes based on an homogeneous sample with a high completeness fraction, in order to fully understand how the bulk of the disks truly behaves.

The first part of this thesis aims at providing a statistical analysis of the evolutionary stage of protoplanetary disks observed with ALMA, the state-of-art interferometer that has revolutionized the field in the last years. This approach provides an unbiased and rich understanding of the true behavior of disks, in particular the evolution of dust, which is necessary for the formation of planet's cores. In order to accomplish this goal, I focus on the Lupus star-forming region, located at a median distance of 158.5 parsec (from parallaxes of Gaia Collaboration et al. 2018), and with an estimated age of around 1-3 Myr (Comerón 2008; Alcalá et al. 2017). Since Lupus is one of the closest star-forming regions and is particularly well suited in the sky for ALMA observations, it is one of the regions with the richest ALMA dataset. It is therefore an ideal target to constrain dust evolution and the possibility of planet formation. For this first goal of the Thesis, I describe and employ a robust methodology to determine crucial disk properties such as dust mass, dust disk and gas disk extent. These properties are used to constrain planet formation, and to assess the dust evolution on this highly complete sample of protoplanetary disks.

There are, on the other hand, indications that the planet formation process might occur at a faster pace than originally thought (e.g., Greaves & Rice 2010; Williams 2012; Najita & Kenyon 2014). A strong evidence of planets being present within protoplanetary disks is the recent detection of two planetary companions in PDS 70 (Keppler et al. 2018; Haffert et al. 2019). This system, which is about 5.4 Myr old and has a central star of about $0.76 M_\star$ (Müller et al. 2018), has a cavity of around 0.4 arcsec where the companions have been observed in infra-red and H_α emission. The discovery of the exoplanets embedded in the PDS 70 disk opens an exciting period for exoplanet detection, in which the goal is to find other protoplanetary disks that host young planets. This search has thus far failed in finding robust detections of planets embedded in disks. The most likely explanation of a lack of detections is that the disk has enough material to obscure the planet flux. Even in protoplanetary disks with low surface densities, the column density of material might be large enough to hide emission of a young embedded planet.

In the last part of this thesis I deepen on the study of the extinction of an already formed planet that is still within the disk. The planet-disk interaction is the key aspect governing the local disk densities and distribution of material. In order to determine the level of extinction that is expected for such a young planet, an accurate representation of the planet-disk interaction is necessary. In the last part of the thesis I expand over previous initial work in which high resolution 3D hydrodynamical simulations were performed in order to study the planet-disk interaction. My goal is to assess how the extinction suffered by a young planet due to surrounding disk material changes with dust composition, the resolution of the simulations and other factors. I then apply the results to high contrast imaging observations to understand whether planets can be detected in a handful of real systems.

Therefore, in my PhD I have focused on performing an homogeneous demographic

study of disk and dust evolution in protoplanetary disks to constrain planet formation, and additionally I investigated how different factors such as the dust properties and the disk architectures affect the detection of planets that might be embedded in disks. The Thesis is organized as follows:

Chapter 2 – I present the methodology employed to analyze interferometric observations of protoplanetary disks in (sub-)mm wavelengths. Firstly, I describe the essential concepts of interferometric and ALMA observations. This is followed by a detailed explanation of the methodology to model dust continuum and gas rotational lines emission from ALMA observations, necessary to infer crucial disk properties.

Chapter 3 – I apply the methodology to model interferometric observations of ALMA to the dust continuum emission of the highly complete sample of protoplanetary disks in the Lupus clouds. By gathering a large and homogeneous population of disks, properties such as the dust mass and the dust extent can be inferred. This allows for an unbiased determination of the dust properties in an archetypal disk population. These properties are crucial to understand the ability of the disk to form planets, and also to constrain dust evolution processes such as radial drift.

Chapter 4 – Here I focus on the gas component of the same sample of protoplanetary disks studied in Chapter 3. I model the gas emission of interferometric observations covering the ^{12}CO rotational line. This allows me to measure the gas extent of these disks. The relative extent between gas and dust, key to understand dust and disk evolution, is investigated in detail from a statistical approach in order to constrain dust evolution.

Chapter 5 – I focus on the possibility of detecting planets already formed in protoplanetary disks. At the beginning of this chapter I describe in detail high contrast imaging techniques that allows for direct detections of planets embedded in disks. I then expand over previous initial study that I conducted in my Master Thesis, where 3D hydrodynamical simulations were performed to study the expected extinction in the IR of a planet still surrounded by disk material. This chapter further develops the basic initial study by improving on the prescription of the extinction curves, and by studying the incidence that important factors have on the planet extinction. I investigate the effects of the resolution by performing new simulations with double resolution, the effects of dust composition, and how the results can be applied to high contrast observations to characterize the possible planets that might be present, including the companions of PDS 70.

Chapter 6 – The conclusions of this Thesis are outlined in this chapter. I summarize the major findings, what they entail, and how future work in line with this Thesis can further strengthen our knowledge in the field.

Chapter 2

(Sub-)mm interferometric observations of protoplanetary disks

In this Chapter I describe how interferometric observations of protoplanetary disks can be used to model the dust and gas emission and infer important disk properties. I first discuss the basic principles and considerations needed to understand how observations by interferometers are performed, with special focus on the ALMA interferometer (Section 2.1); this is followed by a description of the methodology that allows to model the dust and gas properties of disks based on ALMA observations (Section 2.2).

2.1 Interferometric observations

Interferometry is a technique that combines the signal from two or more separated antennas, allowing for observations of angular scales smaller than single antenna observations (e.g., SIW 1989). This is accomplished by the interference between the signals of the various antennas. In a single telescope, the minimum angular scale that can be recovered is defined by the wavelength (λ) and the diameter (d) of the telescope dish, $\theta_{\rm min} \approx \lambda/d$. By combining two or more antennas, the minimum angular scale depends instead on the distance between the antennas, i.e., the baseline (B), approximately as $\theta_{\rm min} \approx \lambda/B$ (e.g., Bradt 2004). The dependence of the minimum angular scale with wavelength implies that observations in the (sub-)mm with one single telescope have poor angular resolution. It is indeed at these wavelengths were interferometry has allowed for great improvements in our understanding of protoplanetary disks.

The basic idea of interference in an astronomical context can be understood as follows. The electromagnetic waves from a distant source can be approximated as incoming plane waves. In the case of two antennas, if the wavefront reaches the two antennas simultaneously (left sketch in Figure 2.1), the signals measured at each antenna interfere constructively to produce a sinusoidal signal of large amplitude. A non-zero angle between the source and the baseline defined by the two antennas ($\theta \neq 0$) causes the wavefront to reach the second antenna with a time delay with respect to the first one. When the angle

$\theta = (\frac{1}{2} + n)\frac{\lambda}{B}$ (with n being an integer, i.e., n = 1, 2, 3, ...), the time delay between the two antennas causes the respective detected signals to be in opposite phase, producing a destructive interference (central sketch in Figure 2.1). On the other hand, a constructive interference can be recovered when the two detected signals become in phase again (right sketch in Figure 2.1), that is, when the angle $\theta = n\frac{\lambda}{B}$ (with n as an integer).

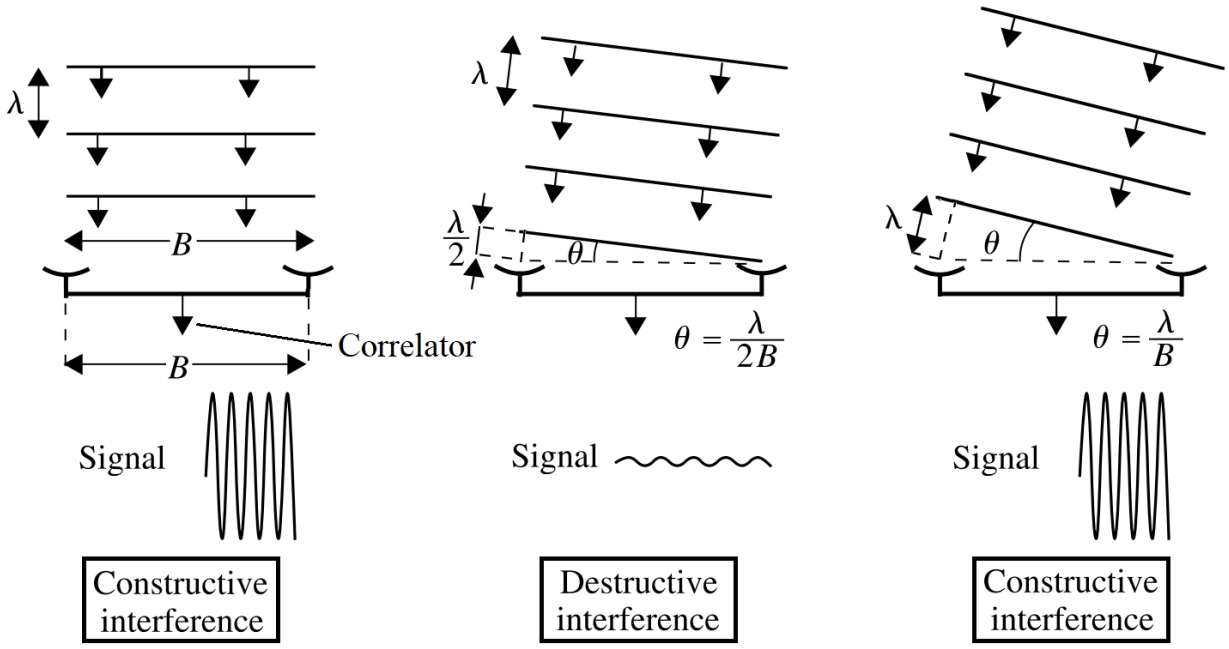

Figure 2.1: Schematic view of constructive and destructive interference from the detection of an astronomical source by a two-antennas interferometer. Each vignette represents the interference for different angles between the baseline between the two antennas and the sky position of the source (θ). Depending on θ, the baseline, and the wavelength, the interference of the two signals can be constructive (*left* and *right vignettes*) or destructive (*central vignette*). Adapted from Bradt (2004).

2.1.1 Antenna power and primary beam

For each antenna, the total power received from a solid angle $\delta\Omega$ depends on the intensity of the source I_ν and the effective area of the antenna A_e, following (e.g., ALMA Cycle 7 Technical Handbook, 2019):

$$P_{\rm rec} = \frac{1}{2} I_\nu A_e \delta\Omega. \tag{2.1}$$

This is valid for an antenna receiver where only one polarization mode can be detected simultaneously; in fact, ALMA antennas can measure the two polarization modes simultaneously, thus $P_{\rm rec}$ for an ALMA antenna is two times that one from Equation 2.1.

Equation 2.1 is an ideal case where the source is perfectly aligned with the antenna axis. Due to self-interference, the power received is affected by the antenna (or power) response, which primarily depends on the angle offset between the antenna axis and the source. At the focus of the antenna, the reflected signals between opposite sides of the dish cause a destructive interference if the offset angle is $\approx \frac{\lambda}{d}$ (d being the antenna diameter). The primary beam of an antenna is known as the angular scale between the antenna axis and the angle at which the first destructive interference occurs. Taking into account the angle dependence of the power response P_N, the total power received by an antenna can be described as:

$$P_{\text{rec}} = \frac{1}{2} \int_{4\pi} I_\nu P_N \delta\Omega. \tag{2.2}$$

2.1.2 Two antennas interferometry

I now provide a more robust mathematical description of the interferometric measurements for a pair of antennas. The received power by each antenna can be described as a function of the other antenna by the phase delay. The voltage V (such as $P \propto V^2$) of the second antenna can be described as:

$$V_2(l, m) = V_1(l, m)\, e^{2\pi i(ul+vm)}, \tag{2.3}$$

where l and m are the angles in the tangent plane with respect the E-W and N-S directions; and u and v are the components of the spatial frequency (spatial frequency being the inverse of the angular distance between constructive interference signals) in the two orthogonal E-W and N-S directions (ALMA Cycle 7 Technical Handbook, 2019).

The combination of the signals between the two antennas takes place in the so-called correlator. This device multiplies the two signals and time averages the combined signal, such as:

$$\langle V_1 V_2 \rangle = \langle \iint V_1(l, m)\, dl\, dm \iint V_2(l, m)\, dl\, dm \rangle. \tag{2.4}$$

By assuming that the signals from different regions of the sky are incoherent, by using Equation 2.3, that $P \propto V^2$ and that $P \propto I_\nu$ (from Equation 2.1), the correlator measurement is proportional to:

$$\langle V_1 V_2 \rangle \propto \iint I(l, m) e^{2\pi i(ul+vm)}\, dl\, dm. \tag{2.5}$$

This term is known as the complex visibility V, and is precisely the Fourier transform of the brightness distribution in the image plane (i.e., on the sky). The complex visibility is formulated as:

$$V(u, v) = \iint I(l, m) e^{2\pi i(ul+vm)}\, dl\, dm. \tag{2.6}$$

Equivalently, V can be mathematically described by an amplitude A and a phase θ, such as $V(u, v) = Ae^{i\theta}$. The brightness distribution, on the other hand, is the Fourier transform

of the complex visibility:

$$I(l,m) = \iint V(u,v) e^{-2\pi i(ul+vm)}\, du\, dv. \tag{2.7}$$

The relationship between the complex visibility and the brightness distribution is known as the van Cittert-Zernike theorem. It allows to determine the brightness distribution from the complex visibilities measured by the correlator.

2.1.3 Antenna arrays and imaging

In order to retrieve the true brightness distribution of the sky, it is necessary to Fourier-transform the distribution of complex visibilities across the *uv*-plane. A complete *uv* coverage (namely, the number of data points sampled in the *uv*-plane) is crucial in order to recover the true brightness distribution in the image plane. However, a pair of antennas provides only two visibilities (or two points) in the *uv*-plane, one at the (u, v) position, and the second being its complex conjugate at ($-u$, $-v$). By adding N number of antennas arranged at different positions, the total number of points sampled in the *uv*-plane increase to $N(N-1)$. In addition, the rotation of the Earth is used to improve the *uv* coverage (e.g., SIW 1989). From the perspective of an observer (i.e., an antenna), the astronomical source is continuously moving along the sky plane, thus the projected distances between each pair of antennas change at each position. Consequently, the longer the observing time, the higher number of points sampled in the *uv*-plane.

However, it is not possible to obtain visibilities from the entire *uv*-plane. This incomplete *uv* coverage limits the accuracy or fidelity between the recovered image and the true brightness distribution of the sky. The distribution of the all the measured visibilities $B(u,v)$ can be expressed as a sum of $2M$ Dirac (δ) functions (M being the total number of *uv* points sampled):

$$B(u,v) = \sum_{k=1}^{2M} \delta(u-u_k, v-v_k). \tag{2.8}$$

Using the van Cittert-Zernike and convolution theorems, the recovered image $I^D(l,m)$ can be formulated as (e.g., ALMA Cycle 7 Technical Handbook, 2019):

$$I^D(l,m) = b(l,m) * I(l,m)\, P_N(l,m), \tag{2.9}$$

where $b(l,m)$ is the point spread function (also named dirty or synthesized beam), the Fourier transform of the sampling distribution ($b(l,m) = FT^{-1}\{B(u,v)\}$); $I(l,m)$ is the true brightness distribution of the sky; and P_N is the antenna power response. Equation 2.9 states that the recovered image (known as dirty image) can be obtained by the convolution between the dirty beam and true brightness distribution multiplied by the antenna response.

There are a number of deconvolution techniques that can reduce the effect of the incomplete sampling in the *uv*-plane, and therefore improve the fidelity of the recovered image

(SIW 1999). The *cleaning* algorithm (Högbom 1974) is one of the most often used deconvolution techniques. It is an iterative process that allows to extract a model of the true brightness distribution of the sky from the dirty image. Once a sky model is subtracted, its convolution with a clean beam (usually of Gaussian shape) provides a clean image that lacks the artifacts due to the incomplete sampling. The extraction of the sky model is limited by the prior knowledge of the true brightness distribution, and is subjective to the individual application of the algorithm. Due to these limitations, artifacts might still be present in the cleaned image, and additionally, the cleaning process can introduce other artifacts if the extracted model of the sky is incorrect. Therefore, the model subtraction and the study of the cleaned image should be done carefully.

A convenient distribution of the *uv* points from the interferometric observation is important for a convenient study of the visibilities and the brightness distribution. In the image reconstruction process, the weighting scheme allows to correct for the imperfect uv sampling by prioritizing some visibility points over others (e.g., SIW 1999). For instance, it is possible to correct for a high concentration of points in a particular region in the *uv*-plane, most typically near the center of the plane. The two most common weighting schemes are the natural and uniform weightings. The former provides the same weighting to every visibility, therefore the high concentration of points in the central region of the plane remains dominant, and consequently the recovered image has typically higher sensitivity but lower angular resolution. The uniform weighting gives a lower weight to the visibilities in the central region of the *uv*-plane, thus the longer baselines are prioritized. This results on an improved angular resolution, at the expense of lower sensitivity. To ease the switch between weighting schemes, the robustness parameter was introduced by Briggs (1995). This parameter can be set to any value $\in [-2, 2]$; if it is set to 2 the scheme used is equivalent to the natural weighting, if set to -2, the uniform weighting is applied.

The weighting scheme has an impact on the angular resolution of the reconstructed image, which can be estimated from:

$$\theta_{\rm res} = \frac{k\lambda}{L_{\rm max}}, \tag{2.10}$$

where k is a factor that depends on the weighting scheme and typically ranges between $0.7 < k < 1.2$, and $L_{\rm max}$ is the longest baseline of the antenna array.

Lastly, interferometric observations cannot sample the central region of the *uv*-plane. This is due to the impossibility of covering baselines smaller than the summed radii of two antennas. This limitation is known as the zero-spacing problem. The lack of these *uv* points causes that the interferometer is insensitive to very large angular scales (e.g., ALMA Cycle 7 Technical Handbook, 2019). The maximum recoverable scale ($\theta_{\rm MRS}$) in an interferometric observation can be determined as:

$$\theta_{\rm MRS} \approx \frac{0.6\lambda}{L_{\rm min}}, \tag{2.11}$$

where $L_{\rm min}$ is the smallest baseline covered by the antenna configuration. Emission from scales larger than the $\theta_{\rm MRS}$ cannot be detected by the array.

2.1.4 Atacama Large Millimeter/submillimeter Array

ALMA is an array of 66 antennas that can detect radiation at mm and sub-mm wavelengths. It is located on the Chajnantor plateau in Chilean Andes at an elevation of around 5000 m above sea level. This location offers outstanding weather and sky conditions that allow extremely precise observations at these wavelengths. Due to the high elevation, the array and the associated instrumentation needed for appropriate operation are controlled from the Operation Support Facility at 2900 m altitude (Observing with ALMA – A Primer, 2019). ALMA is a partnership between different countries around the globe, in order to facilitate the communication between the instrument and the users, three ALMA regional centers are offered by each executive of the partnership (North American, European, and East Asian).

From the total of 66 antennas, 50 are part of the 12-m Array, each of them with a dish diameter of 12 m (ALMA Cycle 7 Technical Handbook, 2019). This array is designed for sensitive and high resolution observations thanks to the long baselines that the various array configurations cover. The 12-m Array is complemented by a second array of 16 antennas, known as the Atacama Compact Array (ACA): 12 of them being 7 m antennas at close separations (known as the 7-m Array), and 4 12 m antennas that can be used for single dish observations. The ACA is of great help to reduce the zero-spacing problem, covering the smallest possible baselines.

Each antenna is designed to integrate up to 10 different receiver bands (ALMA Bands 1 to 10; at the present time only Bands 3 to 10 are in operation). The ALMA Bands cover a wide range of wavelengths in the (sub-)mm, from Band 10 covering wavelengths as short as 0.32 mm ($\sim$950 GHz), up to 3.6 mm ($\sim$84 GHz) in Band 3. The frequency coverage of the different ALMA Bands are shown in Figure 2.2, where the transmission of the atmosphere on the ALMA site is also plotted for two different weather conditions. Other important factors such as the sensitivity that can be reached and the primary beam depend on the ALMA Band chosen for the observations.

ALMA allows for multiple (typically ten) configurations of the 12-m Array. The most compact configuration has only $\sim$ 150 m of maximum separation between antennas, while its most extended configuration has a maximum separation between antennas of $\sim$ 16 km (ALMA Cycle 7 Technical Handbook, 2019). Each configuration offers a different angular resolution and a maximum recoverable scale for the various ALMA Bands. Angular resolutions as low as $\sim 0.02''$ can be achieved at various ALMA bands in the most extended configuration available.

The study of protoplanetary disks is a top priority goal of the ALMA interferometer. The characterization of the dust and gas properties, together with their distribution and kinematics are key to achieve this ALMA scientific goal (Observing with ALMA – A Primer, 2019). The effort of the ALMA instrument on unveiling how planet formation takes place in protoplanetary disks has greatly contributed to improve our understanding on the field. The high resolution and sensitivity capabilities reached by ALMA allow for the first time to conduct surveys with high completeness fraction targeting and resolving protoplanetary disks from nearby star-forming regions. This allows for a demographic

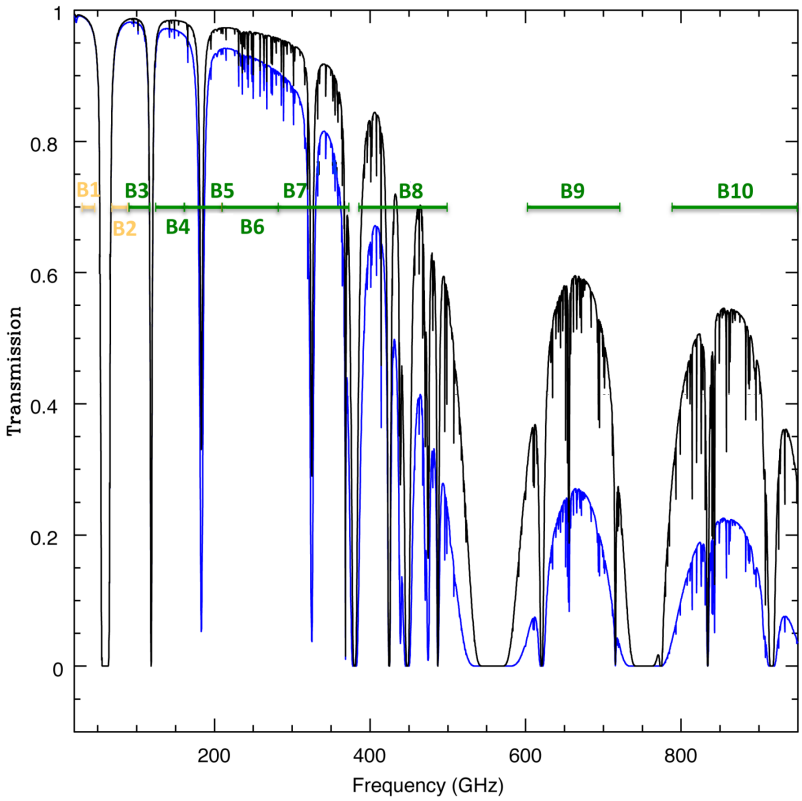

Figure 2.2: Frequency coverage of the current (Bands 3-10) and prospective (Bands 1 and 2) ALMA Bands. The transparency or transmission of the atmosphere on site is included for different weather conditions (blue line representing the 50th percentile over the year, the black line being the 12.5th percentile). From Observing with ALMA – A Primer, (2019).

(statistical) approach on determining disk properties, providing an unbiased study of the disk population of archetypal star-forming regions. In Chapters 3 and 4, I analyze and model observations from the ALMA interferometer in order to perform a demographic study of protoplanetary disks and its properties.

2.2 Modeling the emission from (sub)millimeter interferometry

ALMA has revolutionized the study of protoplanetary disks thanks to the high sensitivity and resolution observations in the (sub-)mm that it offers. Already with a very short integration time on a disk source, interferometric observations with ALMA provides very valuable measurements that allow to characterize important properties of protoplanetary disks. Moreover, ALMA has been proven exceptionally useful for the study and characterization of large populations of disks in nearby star-forming regions, such as Lupus,

Chamaeleon, Orion, Upper Scorpius (e.g., Ansdell et al. 2016; Pascucci et al. 2016; Eisner et al. 2018; Barenfeld et al. 2016). In Figure 2.3, the survey conducted with ALMA Band 7 targeting the known population of protoplanetary disks in the Lupus clouds is shown as an example of how diverse and rich the data from these surveys are. These surveys allow for the determination of dust and gas disk properties such as total mass and extent, that are crucial to understand disk evolution and planet formation.

Complementary to these large surveys, observations with longer integration times per target and using the most extended configurations of the ALMA antennas have been carried out recently (of particular importance, the DSHARP project; for a summary of the program, see Andrews et al. 2018a), providing studies of the dust and gas emission with extremely high angular resolution and sensitivity. These observations can resolve, not only the disk emission, but disk features of much smaller scales. Sub-structure such as rings, gaps, cavities, spirals and asymmetries can be seen in these observations (for a review of sub-structure in ALMA observations, see Andrews 2020).

In the remaining text of this chapter, I focus on the modeling of the disk emission based on interferometric observations. The methodology, although it is suitable and applicable to any observations from (sub-)mm interferometers, has been specifically tailored for ALMA observations with moderate angular resolution and sensitivity, since it is later used in Chapters 3 and 4 to determine the dust and gas disk properties for a large sample of disks in the Lupus star-forming region.

There are two main strategies in order to model the emission (i.e., brightness distribution) of the disk, depending on whether the fitting is performed in the *uv*-plane (namely, the Fourier space) or in the image plane. The former is accomplished by fitting the observed visibilities, which are the true measurements that interferometric observations yield. The later is a more straightforward and easy to apply approach, since the emission is fitted in the reconstructed image of the sky. It is on the other hand affected by the image reconstruction process and thus susceptible to higher uncertainties. These two different strategies can be used to model the dust and the gas emission indistinctly, although particularities on both cases apply.

2.2.1 Modeling in the *uv*-plane

In this approach, a brightness model of the disk is found by fitting the interferometric data in the *uv*-plane. The fit is accomplished by comparing the complex visibilities from the model and from the data. In order to perform this fitting, one should choose first a model that is suitable to describe the disk emission and that produces a brightness distribution model in the image plane. This brightness model can be either physically motivated, or an empirical function.

In the case of fitting the observations to a physical model, the chosen model would typically require to compute the thermal balance of the dust disk distribution (e.g., by approximating the disk to the two-layer model, see Chiang & Goldreich 1997; Dullemond et al. 2001; Tazzari et al. 2017), or the chemical composition and/or distribution in the case of modeling gas transition lines. The main disadvantages of using a physical model

are that it is typically more elaborated and more computationally expensive than using an empirical function; that a number of assumptions are needed in order to describe the physical processes of the disk and therefore it is only one possible solution to the observed emission, and the fact that the physical model chosen might not describe conveniently the brightness emission.

Therefore, in order to fit the observations in the most general way possible, it is preferable to choose an empirical function that simply fits the brightness distribution of the source without any assumptions of the disk physics. In the case of moderate resolution and sensitivity observations, the presence of sub-structure (e.g., gaps, asymmetries) is in most cases hidden, thus it is generally appropriate to describe the brightness distribution with a radial function, and assume that the emission of the disk is axi-symmetric. Functions commonly used to describe the disk emission are the so-called Nuker profile (see, e.g., Lauer et al. 1995; Tripathi et al. 2017) a power-law with exponential cut-off, or a Gaussian function. These functions are applicable to both dust continuum and gas line observations, and are well suited for both types of emission.

Once a suitable disk model is chosen, its brightness distribution in the image plane is Fourier transformed. This generates a set of synthetic complex visibilities that can be directly compared to the complex visibilities observed by the interferometer. The synthetic visibilities are estimated at the same *uv* points from the sampling distribution of the interferometric observation. The various steps applied to obtain the synthetic visibilities are shown in Figure 2.4: the starting point is an empirical function that describes the radial brightness distribution, which is then 2D-plotted in the image plane, and its Fourier transform is then computed to obtain the model visibilities in the *uv*-plane.

The model and observation are then compared with the estimation of the χ^2, using the synthetic and observed visibilities at each position in the *uv*-plane:

$$\chi^2 = \sum_{i=0}^{N} w_i \cdot |V^{\rm obs}(u_i, v_i) - V^{\rm mod}(u_i, v_i)|^2, \tag{2.12}$$

where N is the total number of *uv* points from the interferometric observation, w_i is the weight associated to each *uv* point, $V^{\rm obs}$ and $V^{\rm mod}$ are the observed and synthetic visibilities at the respective point.

The disk model is described by a set of free parameters (which are characteristic to the chosen model). In order to find the model that best describes the observation, a number of models should be computed and compared to the observation, and the one that provides the smallest value of the χ^2 would be the model that better describes the disk emission. A very efficient way to investigate the parameter space of a model is by using Markov chain Monte Carlo (MCMC) procedures. This allows to find the best values of each free parameter of the model by computing several thousands of different models and estimating their respective χ^2. This Bayesian approach has been proven very useful in modeling interferometric observations in samples with a considerable number of disks, particularly from dust continuum observations (e.g., Tazzari et al. 2017; Tripathi et al. 2017; Andrews et al. 2018b). I use this methodology to model the dust continuum emission of the full

population of disks in Lupus in Chapter 3, and I demonstrate how this modeling approach can be used in gas line observations in Chapter 4.

2.2.2 Modeling in the image plane

The modeling of interferometric observations of protoplanetary disks can also be performed directly in the image plane. In order to model the disk emission by this approach, the observed complex visibilities are Fourier transformed into emission in the image plane, following the image reconstruction process and deconvolution techniques described in Section 2.1. The advantage of this approach is that it is visually easier to understand the brightness distribution in the image plane than in the *uv*-plane. The main disadvantage is that, due to the image reconstruction process, the resulting image is more uncertain, and, if deconvolution techniques such as the cleaning algorithm are used, the image is affected by how one applies such algorithms (e.g., SIW 1989). However, this methodology provides useful results, specially when applied homogeneously to large samples of observed disks, since the relative differences between objects can be appropriately investigated.

A convenient approach to model the reconstructed emission in the image plane, is to azimuthally average the 2D emission of the source. In order to do so, the position angle and the inclination is used to de-project the brightness distribution on the sky. If the emission is azimuthally averaged, one ends up with an observed brightness profile as a function of radius, that can then be easily compared to a model brightness profile. Analogously to the interferometric fitting as in Section 2.2.1, it is possible to either use a physical or an empirical model that describes the brightness distribution of the disk (e.g., Guilloteau & Dutrey 1998; Tazzari et al. 2017; Boyden & Eisner 2020). In order to model the disk emission in the most general way possible, it is often preferable to fit an empirical function. Suitable functions such as the Nuker profile, a Gaussian distribution, or a power-law with exponential cut-off can be used on this approach as well, and it is also applicable to dust continuum and gas line emission. The azimuthally averaged brightness profile can then be fitted to the model brightness profile. Analogous to the interferometric fitting, by changing the values of the free parameters of the chosen model, one can investigate the parameter space, which allows to find the model that best fits the observed emission.

Both dust continuum and gas transition lines can be modeled with the two strategies described above. However, prior to modeling the emission, the interferometric data is handled differently, due to the differences between dust continuum and gas line observations. In ALMA observations, one needs to take into account the spectral resolution of the observations. Although the modeling can be performed at each frequency channel from the observation, the signal-to-noise (S/N) will generally be too low. Therefore, frequency averaging the interferometric data is often performed before the fitting, specially in observations with low or moderate sensitivity and resolution (e.g., Tazzari et al. 2017; Andrews et al. 2018b).

When fitting the gas line emission, the first step is to find the frequency channels where the line emission is detected. Once the line channels are found, the continuum emission should be subtracted from each channel. The most common approach to fit the line emission is to integrate all the channels that show line emission at the source location, analogous to computing the line moment zero map for the source (e.g., Ansdell et al. 2017; Long et al. 2017; Ubeira Gabellini et al. 2019; Boyden & Eisner 2020). The integrated emission can then be modeled following any of the two strategies described above. The handling and modeling of interferometric data from gas line observations is performed in Chapter 4, in order to study the CO emission of the disk population in the Lupus region.

2.2.3 Total mass and extent of the disk from interferometric observations

Interferometric observations in the (sub-)mm allows to determine important properties of the protoplanetary disk. Among other properties, the total disk mass and the size extent of the dust and gas components can be estimated from these observations, and are crucial to constrain planet formation and disk evolution. The disk mass tell us about the mass reservoir that is available in the disk to form planets (e.g., Testi et al. 2014; Manara et al. 2018a), while the dust and gas extent can be linked to the main physical processes that take place and dominate the evolution and fate of the disk (e.g., Facchini et al. 2017; Trapman et al. 2019).

The total disk mass is one of the most important disk properties that can be inferred from these observations, and provides insightful information on the evolutionary stage of the disk, and also on its ability to form planets. As introduced in Chapter 1, the disk is composed primarily by gas, thus the total disk mass is dominated by the gas mass. On the other hand, the dust mass would typically account for $\sim 1\%$ of the total disk mass based on the rough gas-to-dust ratio expected. However, measuring the total gas mass is in general limited to a handful of disks with a rich dataset, due to the difficulty on finding a reliable gas tracer of the mass that is also easily detected. Molecular lines from CO are commonly detected in disks in (sub-)mm wavelengths, and can be used to infer the total disk mass, as for instance by combining observations of various CO isotopologues and assuming molecular line ratios (e.g., Williams & Best 2014). Based on recent observations, there seems to be indications that the CO abundance might be lower than originally expected, and, furthermore, it could highly vary between disks (e.g., Miotello et al. 2017). Therefore, disk mass measurements based on these obsevations are uncertain. It is possible to obtain more accurate measurements of the total disk mass in disks where the H_2 abundance and the temperature structure is known. By combining the detection of hydrogen deuteride with CO isotopologues, more reliable measurements of the disk could be achieved (Bergin et al. 2013; Schwarz et al. 2016b). H_2 and deuteride species are however not detected frequently, thus this approach is unfortunately not feasible for large samples of disks.

The other approach to infer disk masses is by measuring the dust mass and then as-

suming a gas-to-dust ratio. The total dust mass can be determined in sources where dust continuum (sub-)mm emission is detected. Under the assumption that the emission is optically thin and in the Rayleigh-Jeans regime (Beckwith et al. 1990), the total dust mass $M_{\rm dust}$ can be estimated as:

$$M_{\rm dust} = \frac{F_\nu d^2}{\kappa_\nu B_\nu(T_{\rm dust})}, \tag{2.13}$$

where F_ν is the measured continuum flux at the specific frequency ν of the observation, d is the distance to the source, κ_ν is the opacity of the dust at the frequency ν, and B_ν is the Planck function at the specific temperature of the detected dust ($T_{\rm dust}$). By giving typical values of the dust opacity and temperature, the dust mass can be estimated, and by assuming a gas-to-dust ratio (typically of 100), the total disk mass becomes:

$$M_{\rm disk} \approx 100 \cdot M_{\rm dust}. \tag{2.14}$$

Due to its simplicity, this method is the most common approach to determine the total disk mass so far (e.g., Manara et al. 2016b; Miotello et al. 2017). It is particularly useful for the study of large samples of disks, since dust continuum is broadly detected in protoplanetary disks.

Another crucial property that tell us about the physical processes that the disk undergoes is the disk extent. More precisely, the extent of gas emission, dust emission, and the relative size ratio between gas and dust. From the interferometric modeling described in the previous sections, the brightness distribution profile for gas and dust can be determined from line and dust continuum observations. The model brightness profile can be used to obtain an observational size of the emission. A convenient metric of the size is the radius enclosing a certain fraction of the total modeled emission (e.g., Tripathi et al. 2017; Tazzari et al. 2017; Andrews et al. 2018b; Facchini et al. 2019). From the cumulative distribution associated to the model brightness profile, this size definition can be easily computed. This size can be used to determine the dust and gas extent respectively based on interferometric observations. When the dust and gas extent are determined for a large homogeneous sample of disks, it is possible to study the evolutionary stage of the disk population, particularly processes such as grain growth and radial drift (Facchini et al. 2017; Trapman et al. 2019, 2020). In the following Chapters 3 and 4, I determine the dust, gas and relative extent of the disk population of the Lupus clouds, and this allows me to draw important conclusions on the disk evolution of this archetypal sample of disks.

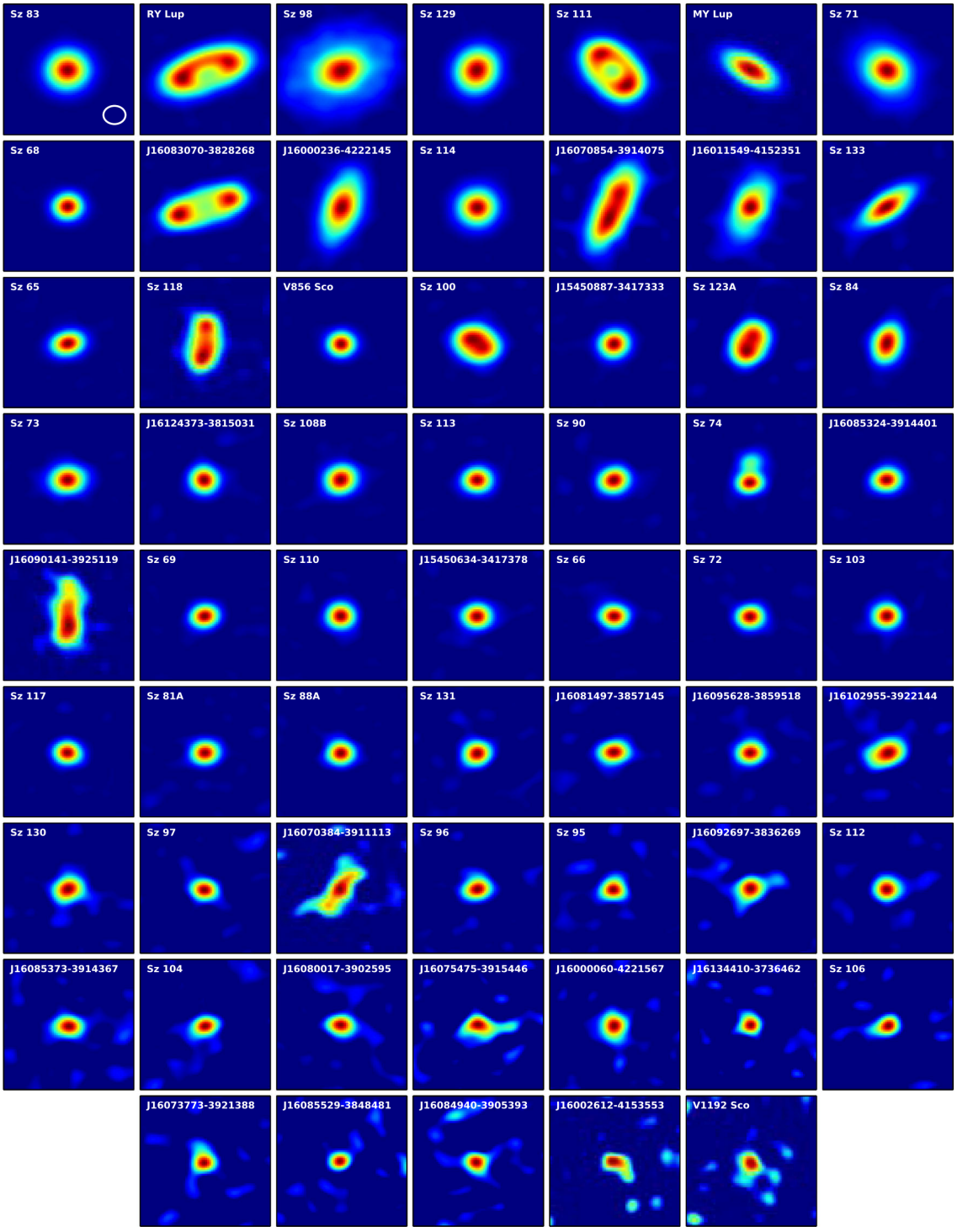

Figure 2.3: Dust continuum emission of protoplanetary disks in the Lupus star-forming region, conducted with ALMA in Band 7 (at $\sim 890\mu m$). The sub-panels show the reconstructed emission in the image plane of all the detected sources from the Lupus disk survey, from brighter to fainter. From Ansdell et al. (2016).

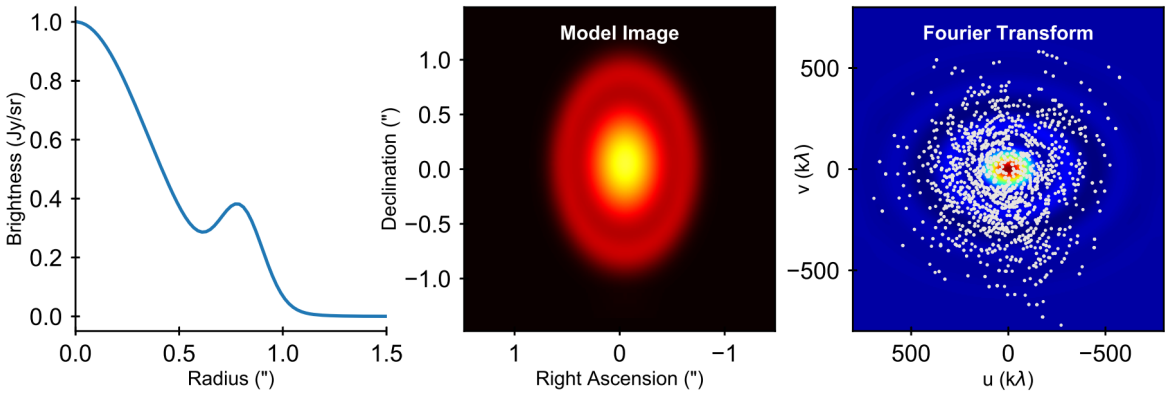

Figure 2.4: Visual representation of the various steps to apply to a disk model, prior to its comparison with the observed visibilities. The radial brightness profile (*left*) is plotted in the sky (i.e., image-) plane (*center*), which is then Fourier transformed (*right*) in order to obtain the model visibilities. Two common free parameters of the model are the position angle and the inclination of the disk, which are used in this example when plotting the model in the image plane. Adapted from Tazzari et al. (2018).

Chapter 3

Demographics of the dust content in protoplanetary disks

The content of this chapter has been published in:

> *" Demographics of disks around young very low-mass stars and brown dwarfs in Lupus "*
> **Sanchis, E.**, Testi, L., Natta, A., Manara, C., Ercolano, E., Preibisch, T., Henning, Th., Facchini, S., Miotello, A., de Gregorio-Monsalvo, I., López, C., Mužić, K., Pascucci, I., Santamaría-Miranda, A., Scholz, A., Tazzari, M., van Terwisga, S., and Williams, J., 2020, A&A, 633, 114.

3.1 Introduction

Millimeter (mm) and submillimeter (submm) wavelength observations are particularly useful to study dust properties in protoplanetary disks because the dust thermal emission of the outer disk, where the bulk of the dust mass resides, can be probed at these wavelengths (Testi et al. 2014; Andrews 2015). Demographic studies based on (sub-)mm wavelength surveys of the Class II population from nearby star-forming regions (Ansdell et al. 2016; Barenfeld et al. 2016; Pascucci et al. 2016; Cox et al. 2017; Cieza et al. 2018; Cazzoletti et al. 2019) have found positive correlations between various disk properties: disk mass with stellar mass ($M_{\rm disk}$-$M_\star$, Andrews et al. 2013; Ansdell et al. 2016; Pascucci et al. 2016), disk size with luminosity (Andrews et al. 2010; Tazzari et al. 2017; Tripathi et al. 2017; Andrews et al. 2018b), and mass accretion rate onto the central star with disk mass ($\dot{M}_{\rm acc}$-$M_{\rm disk}$, Manara et al. 2016b; Mulders et al. 2017; Rosotti et al. 2017).

These relations are poorly constrained in the brown dwarf (BD) and very low-mass (VLM) star regimes because these surveys focused primarily on disks around more massive stars. Therefore, observations at (sub-)mm wavelengths targeting BDs and VLM stars are necessary in order to extend these demographic studies and to investigate their formation mechanisms and ongoing physical processes in their disks.

General interest in BDs and VLM stars has increased substantially thanks to the recent exoplanet discoveries around VLM objects. The most thrilling cases are Trappist-1 (Gillon et al. 2017), a $\sim 0.085\ M_{\odot}$ VLM star that hosts seven rocky planets in a packed orbital configuration, and Proxima B (Anglada-Escudé et al. 2016), an Earth-like planet orbiting our closest neighboring star ($M_{\star} = 0.12\ M_{\odot}$), at a distance of only ~ 1.3 pc from Earth. These and other discoveries (e.g., 2M1207b and 2M J044144b, Chauvin et al. 2004; Todorov et al. 2010) suggest that planets orbiting BDs and VLMs may be a common outcome of their formation.

The study of the early stages of BDs and VLM stars is crucial to understanding the viability of planet formation around these objects and to determine the properties of the potential planetary systems that may form. In Klein et al. (2003), millimeter emission of dust from disks around BDs was detected for the first time. Like stars, BDs are often found surrounded by a protoplanetary disk in their early stages (Comeron et al. 1998; Natta & Testi 2001; Scholz 2008), where planet formation is expected to take place. The disk fraction for stellar and BD populations is found to be similar (Luhman 2012). Disk accretion (Jayawardhana et al. 2003; Scholz & Eislöffel 2004; Muzerolle et al. 2003, 2005) and outflows (Natta et al. 2004a; Whelan et al. 2005) also occur in the early stages of BDs, analogous to those around more massive stars.

In this study we conducted a systematic survey of BD disks in the Lupus star-forming region, observing the full known sample of BD disks from a single region with the Atacama Large Millimeter/submillimeter Array (ALMA) in the same band for the first time. Previous ALMA observations of BD disks studied incomplete samples of the known BD population of other regions (Testi et al. 2016; van der Plas et al. 2016; Ward-Duong et al. 2018).

Dust disk masses, dust emission distribution profiles, and dust disk characteristic sizes are determined from these observations. The last two properties are inferred from interferometric modeling of the dust disk emission. The characteristic size of the dusty disks is crucial to constraining the ongoing disk evolution processes (e.g., radial drift, grain growth). However, its determination is not straightforward. Firstly, the disk emission needs to be sufficiently resolved. For disks around BDs and VLM stars, this is only possible using state-of-art facilities, like ALMA, that provide the high resolution and sensitivity required at these wavelengths. In addition, a general size definition is needed for a reliable comparison between observations and theoretical models. In this work we use the radius enclosing 68% of the object's emission distribution; this definition is representative of the physical size of the object (Tripathi et al. 2017), and is independent of the model used to fit the observations. Another important disk property that can be derived from (sub-)mm observations is the disk mass. For the formation of rocky planets, the dust mass in disks should be larger than the mass of the resulting planets. However, comparing the mass derived from disk emission with the results from exoplanetary surveys, there is an apparent lack of material to produce the known planetary systems (Greaves & Rice 2010; Williams 2012; Najita & Kenyon 2014; Mulders et al. 2015; Pascucci et al. 2016; Testi et al. 2016; Manara et al. 2018a).

The inferred disk properties of the young BD population are compared to the properties

of disks around stars in the same region, with the aim of testing whether the known relations for stars hold for disks around BDs. In addition to the BD observations, a further seven T Tauri star (TTS) disks are characterized and modeled here for the first time.

The study is organized as follows: the target selection is described in Section 3.2. A summary of the observations and the data processing can be found in Section 3.3. Section 3.4 provides a description of the modeling employed for the determination of disk properties, together with the modeling results. The demographic comparison of the inferred properties between BD and stellar disks, and the planet formation implications from the measured dust masses of the BD disks are discussed in Section 3.5, and the main conclusions of this work are presented in Section 3.6.

3.2 Sample selection

The list of selected targets of the Lupus BD disks survey (Cycle 5; PI: L. Testi, Project ID: 2017.1.01243.S) encompasses all the known BDs in the Lupus region I-IV that were not observed previously with ALMA Band 7. Our population of BD disks in the Lupus star-forming region consists of all the known objects from the region census (Merín et al. 2008; Mužić et al. 2014, 2015) that show excess emission in at least two mid-infrared bands (Spitzer IRAC/MIPS). These objects have been spectroscopically classified as spectral type (SpT) M6 or later (excluding L type or later candidates), and with estimated masses of $\leq 0.09\ M_{\odot}$. L and later type candidates have been excluded. Eleven sources in Lupus satisfied these selection criteria; seven were the targets for the new observations and the remaining four had already been observed in the Lupus disks survey (Cycle 2; PI: J. Williams, Project ID: 2013.1.00220.S). Based on radial velocity analysis and X-shooter spectra, two sources in the sample, IRAS 15567-4141 and SSTc2d J160034.4-422540, were recently excluded from being Lupus members, and are likely background giants (Frasca et al. 2017; Alcalá et al. 2017), in agreement with the poorly constrained parallaxes from Gaia DR2 (Gaia Collaboration et al. 2018). Therefore, these will not be discussed further in this paper; only five new targets are discussed. All the studied BDs are isolated systems, except SONYC-Lup3-7, which might form a very wide ($\sim 7''$) binary system with SONYC-Lup3-6, but this last object has no confirmed membership to the region (Mužić et al. 2014).

In Table 3.1, we list all the sources analyzed in this work: the known BD population (five objects from the new observations and four from previous observations), together with the seven disks around stars observed in the Lupus completion survey (Cycle 5; PI: S.E. van Terwisga, Project ID: 2016.1.01239.S). The last two objects in the table are those that were observed but later excluded from the Lupus census (Frasca et al. 2017; Alcalá et al. 2017). The names, sky positions, and main stellar properties of the central stars are included in the Table 3.1. The stellar properties shown in the table (SpT, effective temperature $T_{\rm eff}$, extinction in V-band A_V, stellar luminosity $L_\star$ and $M_\star$) were reported by Alcalá et al. (2014, 2017) and Mužić et al. (2014). The methodology for the stellar luminosity derivation between these studies differs, but nevertheless the agreement between the two methods is very good, as shown in Manara et al. (2016a). Values for $L_\star$ have been

adjusted accounting for updated distances by Gaia DR2 (distance estimated as the inverse of the parallax, Gaia Collaboration et al. 2018). The stellar mass is derived from the pre-main sequence (MS) evolutionary models of Baraffe et al. (2015), estimated from the position in the Hertzsprung–Russell (HR) diagram. For objects with estimated mass >1.4 $M_{\odot}$ and objects laying above the 1 Myr isochrone, the tracks from Siess et al. (2000) are used instead. Stellar mass uncertainties are computed with a Monte Carlo approach (as described in Alcalá et al. 2017), which takes into account the associated uncertainties of the stellar properties $L_{\star}$ and $T_{\rm eff}$ used to infer the mass.

The BD disk population is compared to the sample of young stellar objects (YSOs) in Lupus that have a protoplanetary disk and estimated stellar mass >0.09 $M_{\odot}$. Thanks to the inclusion of the seven stellar disks from the Lupus completion survey, we have the largest sample of stellar disks in the Lupus clouds (I-IV) observed with ALMA in Band 7. The stellar disk population is assembled from different census of the region from 2MASS, Spitzer, and Herschel surveys (Hughes et al. 1994; Comerón 2008; Merín et al. 2008; Mortier et al. 2011; Dunham et al. 2015; Bustamante et al. 2015). Of these disks 82 were observed with ALMA in Band 7 in the original Lupus disks survey (ALMA Cycle 2; PI: J. Williams), IM Lup and Sz 91 were observed separately (Cycle 2; PI: I. Cleeves, Project ID: 2013.1.00226.S and Cycle 2; PI: H. Canovas, Project ID: 2013.1.00663.S), and the 7 remaining belong to the Lupus completion survey (Cycle 5; PI: S.E. van Terwisga).

Therefore, the BD and stellar disk samples of our demographic study consist of 9 and 91 sources respectively. The HR-diagram for the studied disk population is shown in Figure 3.1 using the stellar properties from previous studies as described before. The BD disks are marked in red, and the stellar disk population in blue. Subluminous sources, those with luminosities lower than those expected for YSOs with an age of $\sim$ 3 Myr (likely due to gray obscuration Alcalá et al. 2014, 2017), are illustrated with square symbols. From the re-adjusted $L_{\star}$ using the more accurate Gaia DR2 parallaxes, two objects (J16081497-3857145 and J16085373-3914367) are now added to the list of subluminous objects of the region.

3.3 Observations

ALMA observed our targets on 2018 April 1 and April 2 with 44 and 42 antennas respectively, each of 12m in diameter. The baselines ranged between 15.1 and 704.1 m for the array configuration of the first day, and between 15.1 and 629.2 m for the configuration of the second day. Four spectral windows were set for the continuum observation of the targets, centered at 334.432, 336.321, 345.889 and 347.821 GHz and bandwidths of 2, 1.875, 1.875 and 0.938 GHz respectively (total receivers bandwidth of $\sim$ 6.688 GHz). The calibrators for the observations were J1517-2422 for flux and passband, and J1610-3958 for the complex gain calibration, the same in both executions. The flux density scale accuracy is expected to be of 10% for observations of the Lupus BD disks survey. Twelve scans of 60-62 seconds duration each were performed for every target, for a total integration time of more than 12 minutes per source.

Table 3.1: Protoplanetary disks from Lupus modeled in this study.

Object	α (J2000)	δ (J2000)	Lupus cloud	Distance [pc]	SpT	$T_{\rm eff}$ [K]	A_V [mag]	$L_\star$ [$L_\odot$]	$M_\star$ [$M_\odot$]	Notes
BDs from this survey:										
J154518.5-342125	15:45:18.53	-34:21:24.8	I	152 ± 4	M6.5	2935	0.0	0.04	0.09 ± 0.02	1
SONYC-Lup3-7	16:08:59.53	-38:56:27.6	III	150 ± 6	M8.5	2600	0.0	0.01	0.02 ± 0.01	1, 4
Lup706	16:08:37.30	-39:23:10.8	III	158.5	M7.5	2795	0.0	0.002	0.05 ± 0.01	1, 3, 5
AKC2006-18	15:41:40.82	-33:45:19.0	I	149 ± 8	M6.5	2935	0.0	0.01	0.07 ± 0.02	1
SONYC-Lup3-10	16:09:13.43	-38:58:04.9	III	158.5	M8.8	2650	1.5	0.003	0.03 ± 0.01	2, 3
BDs from Lupus disks survey (Ansdell et al. 2016):										
Lup818s	16:09:56.29	-38:59:51.7	III	157 ± 3	M6	2990	0.0	0.02	0.09 ± 0.02	1
J161019.8-383607	16:10:19.84	-38:36:06.8	III	159 ± 3	M6.5	2935	0.0	0.04	0.09 ± 0.02	1
J160855.3-384848	16:08:55.29	-38:48:48.1	III	158 ± 3	M6.5	2935	0.0	0.05	0.09 ± 0.02	1
Lup607	16:08:28.10	-39:13:10.0	III	175 ± 6	M6.5	2935	0.0	0.05	0.10 ± 0.02	1
Disks from Lupus completion survey:										
Sz102	16:08:29.71	-39:03:11.0	III	158.5	K2	4900	0.7	0.01	-	1, 3, 5, 6
V1094 Sco	16:08:36.18	-39:23:02.5	III	154 ± 1	K6	4205	1.7	1.15	0.86 ± 0.18	1
GQ Lup	15:49:12.10	-35:39:05.1	I	152 ± 1	K6	4205	0.7	1.48	0.85 ± 0.17	1
Sz76	15:49:30.74	-35:49:51.4	I	160 ± 1	M4	3270	0.2	0.18	0.23 ± 0.04	1
Sz77	15:51:46.96	-35:56:44.1	I	155 ± 1	K7	4060	0.0	0.59	0.75 ± 0.15	1
RXJ1556.1-3655	15:56:02.10	-36:55:28.3	II	158 ± 1	M1	3705	1.0	0.26	0.5 ± 0.14	1
EX Lup	16:03:05.49	-40:18:25.4	III	158 ± 1	M0	3850	1.1	0.76	0.56 ± 0.13	1
Observed objects rejected from being members of Lupus:										
IRAS 15567-4141	16:00:07.42	-41:49:48.4	-	-	-	-	-	-	-	7
J160034.4-422540	16:00:34.40	-42:25:38.6	-	-	-	-	-	-	-	7

Notes. (1) Stellar properties from Alcalá et al. (2014, 2017) and adjusted to the new Gaia DR2 parallaxes. (2) Stellar properties from Mužić et al. (2014), and adjusted to the Gaia DR2 parallaxes. (3) Gaia parallax unknown, mean distance of Lupus region considered. (4) Two sets of stellar properties (Alcalá et al. 2017; Mužić et al. 2014). (5) Subluminous object (see Alcalá et al. 2014, 2017). (6) No estimation of the stellar mass since it falls below the zero-age main sequence in the HR diagram (see Alcalá et al. 2017). (7) Categorized as background sources (Frasca et al. 2017; Alcalá et al. 2017).

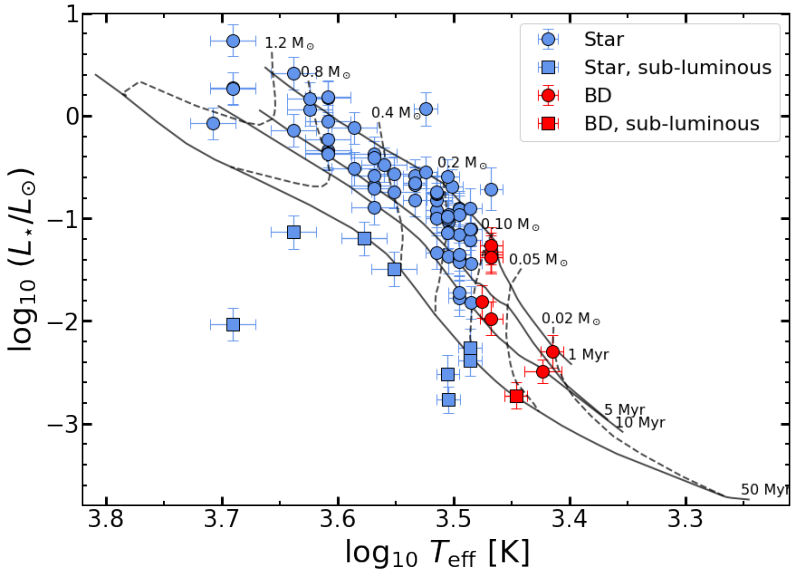

Figure 3.1: Hertzsprung–Russell diagram for the studied BD and stellar populations from Lupus. The stellar luminosity is taken from the literature and re-adjusted to the new distance associated to the parallaxes from Gaia DR2 (Gaia Collaboration et al. 2018). The BD population is shown in red, and the stellar population is indicated in blue. The pre-MS tracks of Baraffe et al. (2015) are overlaid in the figure. Objects with luminosities that would correspond to older ages than expected are considered subluminous and marked as squares. A number of points lay on top of each other (e.g., 4 BDs near the 1 Myr and the $0.1 M_{\odot}$ lines).

The CASA 5.3.0 software has been used for the interferometric visibilities calibration and imaging. The continuum maps are produced using the channels free from spectral line emission, with Briggs weighting of the visibilities (-1.0 and $+0.5$ robustness for resolved and unresolved objects respectively). None of the sources are bright enough to perform self-calibration. The full width at half maximum (FWHM) of the synthesized beam is $0.27'' \times 0.24''$ for robust parameter $= -1$, and $0.36'' \times 0.33''$ for robustness $= +0.5$, with average position angle (PA) of 28°. The continuum maps of the five BD disks observed are shown in Figure 3.2. The sensitivity for the BD disks survey is improved by a factor of about three with respect to the previous Lupus disk surveys, allowing us to detect fainter emission. Three BD disks are detected, J154518.5-342125, SONYC-Lup3-7, and Lup706, with respective signal-to-noise (S/N) of 42, 8, and 7. Emission is not detected from the two other disks (AKC2006-18 and SONYC-Lup3-10) or from the two background objects (IRAS 15567-4141 and J160034.4-422540).

The main results of the observations are reported in Table 3.2. This table includes the total disk flux, peak intensity, and the rms of the image. These values from the observations are obtained using identical methodology to the results presented in Ansdell et al. (2016) for the original Lupus disks survey. The continuum flux is inferred from the *uvmodelfit*

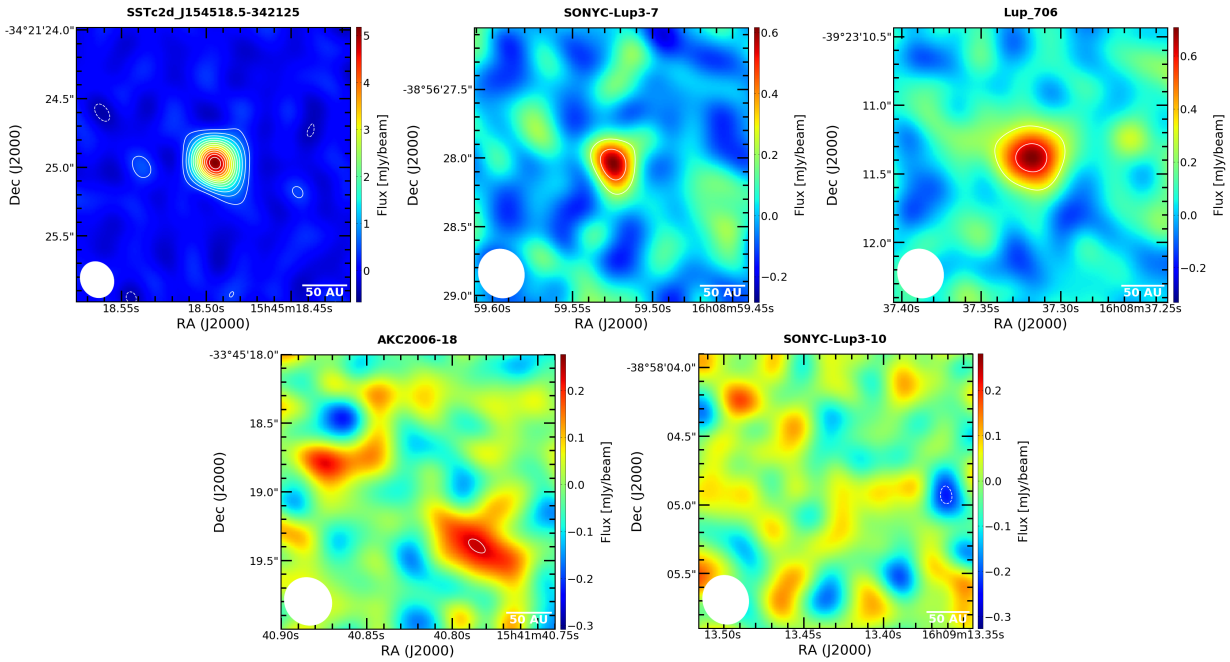

Figure 3.2: Dust continuum images at 890 μm of the Lupus BDs disks survey from ALMA Band 7 observations. The beam size FWHM is $0.27'' \times 0.24''$ for the J154518.5-342125 map (robust parameter of -1), and $0.36'' \times 0.33''$ for the rest of the maps (robustness $= +0.5$). The average beam position angle is $PA = 28°$. The contours are drawn at increasing (or decreasing) 3σ intervals as solid (dashed) lines.

task in CASA: emission is fitted with an elliptical Gaussian in cases where the resulting FWHM along the major axis from the fit is at least five times its uncertainty, otherwise the emission is fitted as a point source. For sources with resolved structure, the flux is obtained from a curve of growth method with increasing circular apertures centered at the peak emission of the object. The rms is computed from an annulus of 4-9radius centered on the detected emission, or on the expected source position if no disk emission is detected. The flux upper limits of the nondetected BD disks are displayed in the $F_{\rm cont}$ column of the table. In this work, upper limits of nondetected BD and stellar disks are computed as three times the rms level above the measured flux within the beam size (centered at the expected source position),which corresponds to a 99.87% confidence level. This differs slightly from the upper limits in Ansdell et al. (2016), considered to be 3σ.

We also derived the flux densities and image rms for the sources observed with ALMA in Band 7 in the Lupus completion survey (see also van Terwisga et al. 2018, 2019). For these sources we followed the same procedure as for the BDs disks. As reported by van Terwisga et al. (2018), the flux calibrator used for these disks in Band 7 was highly variable, and therefore the absolute flux densities are very uncertain. To alleviate this problem, van Terwisga et al. (2018) compared the flux of one of these sources (GQ Lup) to a previous observation with high S/N and reliable flux calibration (MacGregor et al. 2017), obtaining

Table 3.2: Inferred fluxes for all the studied disks. From top to bottom: the nine protoplanetary disks around BDs (five from the new Lupus BDs disks survey) and seven additional disks from the Lupus disks completion survey. The columns are the total disk flux ($F_{\rm cont}$), peak intensity ($I_{\rm peak}$) of each object, and the rms of their continuum maps.

Object	$F_{\rm cont}$ [mJy]	$I_{\rm peak}$ [mJy/beam]	rms [mJy/beam]
BDs from this survey:			
J154518.5-342125	5.75	5.39	0.12
SONYC-Lup3-7	0.52	0.59	0.07
Lup706	0.79	0.70	0.10
AKC2006-18	< 0.23	-	0.08
SONYC-Lup3-10	< 0.24	-	0.07
BDs from Lupus disks survey:			
Lup818s	7.44	7.40	0.24
J161019.8-383607	< 1.24	-	0.23
J160855.3-384848	1.81	1.81	0.26
Lup607	< 0.95	-	0.24
Disks from Lupus disks completion survey:			
Sz102	13.72	8.63	0.34
V1094 Sco	553.17	26.55	0.37
GQ Lup	78.43	44.91	0.34
Sz76	10.91	5.14	0.35
Sz77	4.88	3.73	0.20
RXJ1556.1-3655	56.39	18.93	0.35
EX Lup	43.47	11.11	0.35

a fluxes ratio of 1.3 ± 0.009 between both observations. Since GQ Lup and the rest of the disks of the Lupus completion survey were observed on the same day, we applied that factor to the measured fluxes of all these sources. The results are included in Table 3.2. For the observation results from the Lupus disks survey (ALMA Project ID: 2013.1.00220.S), we refer to Ansdell et al. (2016).

3.4 Modeling

Previous work characterizing interferometric observations of protoplanetary disks modeled the continuum emission with either physical or empirical models. A physical model commonly used is the two-layer approximation model (Ricci et al. 2014; Testi et al. 2016; Tazzari et al. 2017). Although this model can successfully describe the spectral energy distribution (SED) of TTS disks (Chiang & Goldreich 1997; Dullemond et al. 2001), the model assumes a simplified physical structure of the disk. In order to provide an observational characterization of the emission, we prefer to fit empirical analytical functions to the emission profile to allow a more straightforward comparison of the disk properties.

We model the extended disks around stars with the Nuker profile used in Andrews et al. (2018b) to characterize the Lupus disks observed with ALMA in Band 7 from Ansdell et al. (2016). By using the Nuker profile we ensure the homogeneity on the characterization of the Lupus disks sample, which is a key aspect of the demographic study discussed in the following section. We follow the modeling described in Tripathi et al. (2017), using the Lauer et al. (1995) formulation:

$$I_\nu(\rho) = I_0 \cdot \left(\frac{\rho}{\rho_t}\right)^{-\gamma} \cdot \left[1 + \left(\frac{\rho}{\rho_t}\right)^{\alpha}\right]^{(\gamma-\beta)/\alpha}, \tag{3.1}$$

where ρ_t is the transition radius that sets the boundary between the inner and outer regimes of the radial profile, γ and β are the inner and outer disk slopes and α is a factor that determines the smoothness of the transition between both regimes. The disk is assumed to be azimuthally symmetric. The total number of parameters used to model the extended disks with the Nuker profile are 9: ρ_t, γ, β, α, the total disk flux density $F_{\rm tot}$, and four additional geometrical parameters connected to the observation: inclination of the disk in the sky towards the observer (i, 0° face-on disk, 90° edge-on), the position angle in the sky plane (PA, defined east of north), and right ascension and declination off-sets to the phase center of the observations (ΔRA and ΔDec).

A simple parametrized Gaussian function has been used to fit the BD disks to reduce the number of free parameters because the emission maps of these objects are extremely compact; only one BD disk is marginally resolved. This function can be used to model moderate-resolution observations to characterize the disk brightness profile and its size, as shown in Appendix A (see Figure A.1) where the Gaussian profile together with other models were used to fit the disk emission around RXJ1556.1-3655: the resulting profiles are alike and the values of the chosen size definition are indistinguishable. The expression

of the Gaussian function used to model the BDs surface brightness profile is:

$$I_\nu(\rho) = I_0 \cdot \exp\left[-0.5 \cdot \left(\frac{\rho}{\sigma}\right)^2 \right], \tag{3.2}$$

where ρ is the projected radius in the sky in arcsec, I_0 is a normalization factor, and σ is the standard deviation of the Gaussian profile. The disk is assumed to be azimuthally symmetric. Six free parameters were used to model the BD disks: two from the Gaussian model (I_0 and σ), together with the observational parameters analogous to the Nuker model (i, PA, ΔRA and ΔDec).

To perform the fits, the `Galario` (Tazzari et al. 2018) and `emcee` (Foreman-Mackey et al. 2013) packages were used. For a detailed description of the methodology we refer to Tazzari et al. (2016, 2017). To run the affine invariant Markov chain Monte Carlo (MCMC) from Goodman & Weare (2010), 200 walkers were used in order to investigate the parameter space for each disk ($\gtrsim$ 20-30 walkers for each parameter); the computation ran for 20000 steps per walker, which guaranteed convergence in all fitted disks.

3.4.1 Size definition

An appropriate definition of the disk size is necessary for a proper characterization of disks from observations, and for comparison to theoretical models. An approach commonly used is to extract the radius from the models used to fit the emission. The transition radius ρ_t from the Nuker profile definition (Equation 3.1) provides misleading information on the disk size, since systems with very different architectures and extents might have similar values of ρ_t. When fitting to a power-law with an exponential cut-off, an analogous problem arises if the cut-off radius ρ_c from Guilloteau et al. (2011) parametrization is used. The outer radius $R_{\rm out}$ was used in Ricci et al. (2014) and in Testi et al. (2016) to fit BD disk observations, defined as the outermost radius of their modeled surface density.

All these definitions may be useful in specific studies, but are not suitable for a general characterization of disk sizes from their emission. A more convenient size definition is the radius enclosing a certain fraction of the total disk emission. This definition with a fraction of 68% of the total disk emission has been used in many recent works (e.g., Tripathi et al. 2017; Andrews et al. 2018b; Facchini et al. 2019; Long et al. 2019; Manara et al. 2019). In Tazzari et al. (2017), 95% of the total disk emission was used. To avoid confusion with the different terminology used in the literature, we simply refer to them as 68% ($R_{68\%}$) and 95% ($R_{95\%}$) flux radii. In the nomenclature used throughout this work, R refers to the radius in the system reference frame (typically in au), while ρ stands for the projected radius in the sky plane in arcsec.

We tested both $R_{68\%}$ and $R_{95\%}$ to determine the quality of each radius as the characteristic size for the disk emission (details in Appendix A). For this test we fitted the same disk to various models and inferred $R_{68\%}$ and $R_{95\%}$ for each model. This test shows that the dispersion on $R_{68\%}$ is much smaller than for $R_{95\%}$. Thus, we consider $R_{68\%}$ as the most reliable size definition for our sample. Nevertheless, in the modeling results of the disks (Table 3.3), we include both $R_{68\%}$ and $R_{95\%}$ for completeness.

Additionally, we fitted several disks that were previously modeled in Andrews et al. (2018b) in order to test the proper functioning of our modeling tool. This additional test is also included in Appendix A; the resulting $\rho_{68\%}$ from this work and from Andrews et al. (2018b) are in very good agreement.

3.4.2 Dust disk masses

To ease the comparison with the existing surveys of disks around stars in the Lupus clouds (Ansdell et al. 2016), we provide an estimate of the disk dust masses using the simplifying assumption of optically thin emission and using an average temperature of 20 K. We note that these assumptions may lead to underestimation of the disk mass in cases where the emission is optically thick or the average temperature is lower than the assumed value.

For the dust mass determination, assumptions on the dust temperature and opacity are needed. A dependence of the dust temperature with the stellar luminosity was first proposed on theoretical grounds (e.g., Yorke et al. 1993; Sonnhalter et al. 1995). More recently, from radiative transfer modeling of mm observations, Andrews et al. (2013) proposed a single-value mean temperature for each disk that could be used to estimate the disk mass for objects with $L_\star \in [0.1, 100]\ L_\odot$. Soon after, van der Plas et al. (2016) suggested a more flattened relation for VLM objects. In Ballering & Eisner (2019), the correlation of disk temperature with the stellar luminosity was derived using simplistic radiative transfer models from SED fitting of Taurus disks. Daemgen et al. (2016) and Tazzari et al. (2017) showed that depending on assumptions on disk size and vertical structure, similar $T_{\rm dust}$ even with very different luminosities are compatible with the data. From the different studies, it is unclear whether or not there is a simple and general relation between dust temperature and stellar properties. Using additional relations of the temperature with other stellar properties as proposed by Andrews et al. (2013), and van der Plas et al. (2016) might introduce spurious results in our analysis, or even erase possible relations between different disk properties.

We therefore compute the dust mass of each BD and stellar disk assuming a constant dust opacity of $\kappa_{890\mu m} = 2\ {\rm cm}^2\ {\rm g}^{-1}$, following previous ALMA Band 7 observations for VLMs and BDs (Ricci et al. 2014; Testi et al. 2016), and an averaged dust temperature of $T_{\rm dust} = 20$ K, as in Pascucci et al. (2016), Ansdell et al. (2016), and Ansdell et al. (2018). This value is the median temperature for protoplanetary disks in the Taurus region (Andrews & Williams 2005). Nevertheless, in Appendix B we show the main demographic results of this work using the dust temperature and stellar luminosity relations from Andrews et al. (2013), and van der Plas et al. (2016).

3.4.3 Modeling results

The results of the modeling and the derived properties of dust mass and disk size are presented in this section. The results for J154518.5-342125 are shown in Figures 3.3, 3.4, 3.5, and 3.7, while the results for the remaining disks whose fits converged are in Appendix C.

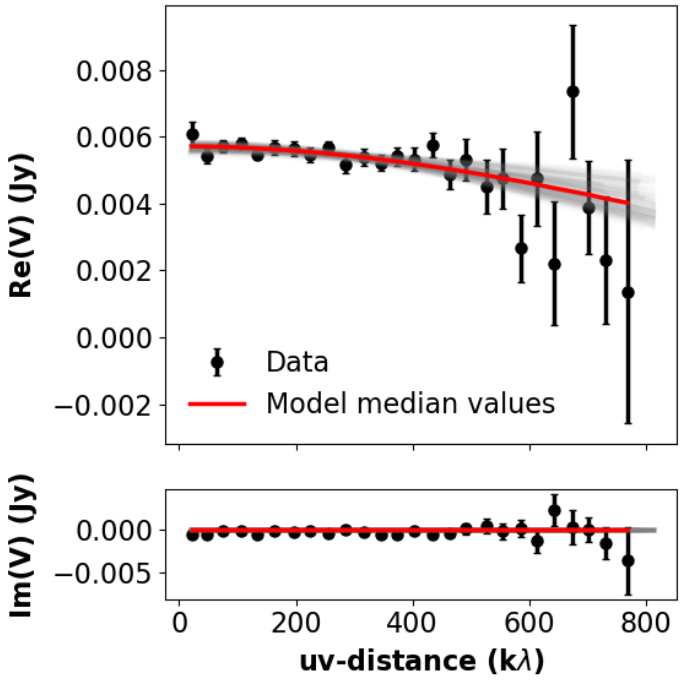

Figure 3.3: Observed and model visibilities of J154518.5-342125, plotted as real (*top*) and imaginary (*bottom*) parts as a function of the baseline (in kλ). The data from the observations are plotted as black data points with error bars, the model with the lowest χ^2 is shown as solid red curve, and a random set of models from the parameter space investigation are drawn as gray curves. This figure was made with the `uvplot` Python package Tazzari (2017).

In Figure 3.3 we show the real and imaginary part of the observed and modeled visibilities as a function of baseline. The visibilities were first centered using ΔRA and ΔDec from the model with lowest χ^2, and were then de-projected taking i and PA (for a detailed description, see Tazzari et al. 2017, 2018).

The posterior probability distribution functions (PDFs) of the free parameters (of the Gaussian model, or from the Nuker profile), are shown in the top panels of Figure 3.4. Vertical dashed lines represent the median values of each histogram, used as the best-fit parameter value, and the 16th and 84th percentiles, used to infer the lower and upper values of the uncertainties. From the figure, I_0, σ, and the sky plane off-sets are well determined, while the inclination and position angle are both degenerated, and their values are only poorly constrained. The remaining panels in the figure show the 2D histograms for the pairs of parameters, which indicate possible correlations between the different parameters. In a few disks of the Lupus completion survey, the smoothness parameter (α), and/or the inner and outer slopes (β, γ) of the Nuker profile cannot be appropriately constrained from moderate-resolution observations (see corner plots of the fits in Appendix C). This

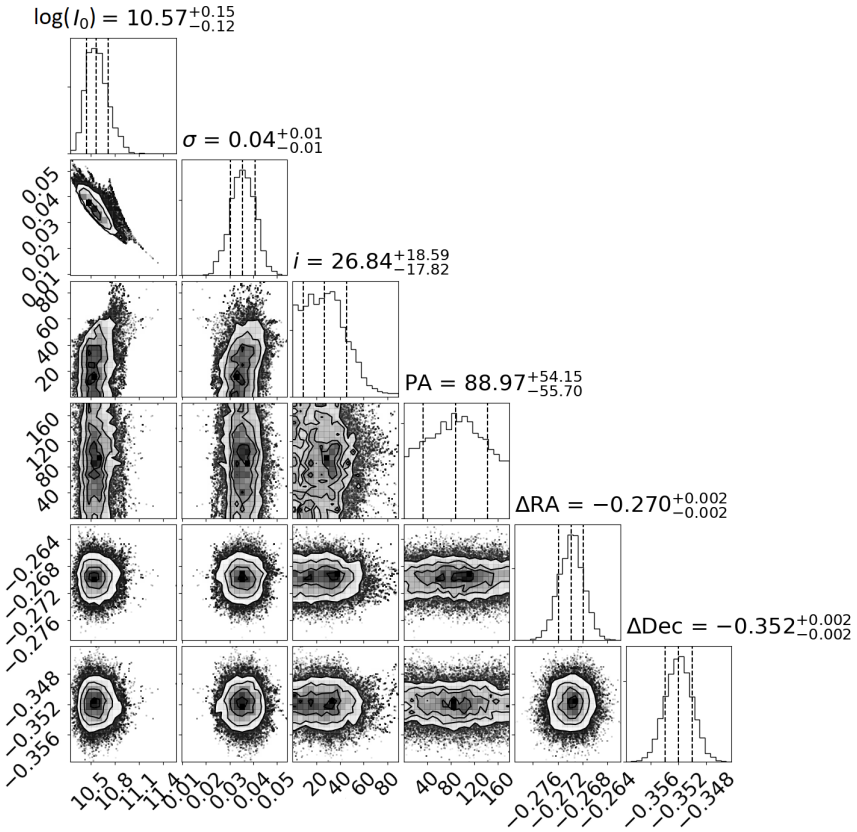

Figure 3.4: One- and two-dimensional histograms of the free parameters used to model J154518.5-342125 ALMA observations, resulting from the MCMC analysis. The marginalized PDFs of the parameters are plotted in the top panels, including the 16th, 50th, and 84th percentiles as vertical dashed lines. The I_0 and σ parameters are connected to the Gaussian model used, as defined in Equation 3.2; i, PA, ΔRA, and ΔDec are geometrical parameters linked to the observations.

limitation does not affect the characterization of their disk sizes.

The modeled emission distribution of the disk is shown in the top panel of Figure 3.5. The bottom panel shows the normalized cumulative flux $f_{\rm cumul}$ derived from Equation A.1 for the respective models of the top panel. In both plots, the inferred values of $R_{68\%}$ and $R_{95\%}$ radii are included as vertical dashed and dotted lines. These radii are computed for each model of the MCMC; the final values of $R_{68\%}$ and $R_{95\%}$ are the median of their respective PDFs, with upper and lower errors as the median $\pm 1\sigma$ (example of a $R_{68\%}$ PDF in Figure 3.6).

In Figure 3.7, we show the reconstructed (observed, modeled, and residuals) continuum emission of the source in the sky plane. Residuals are at noise level on all fitted disks, indicating that the model represents the observation faithfully.

The results of the free parameters from the fits and the derived disk properties can be found in Table 3.3. The values shown are the median of their respective PDF. Lower (up-

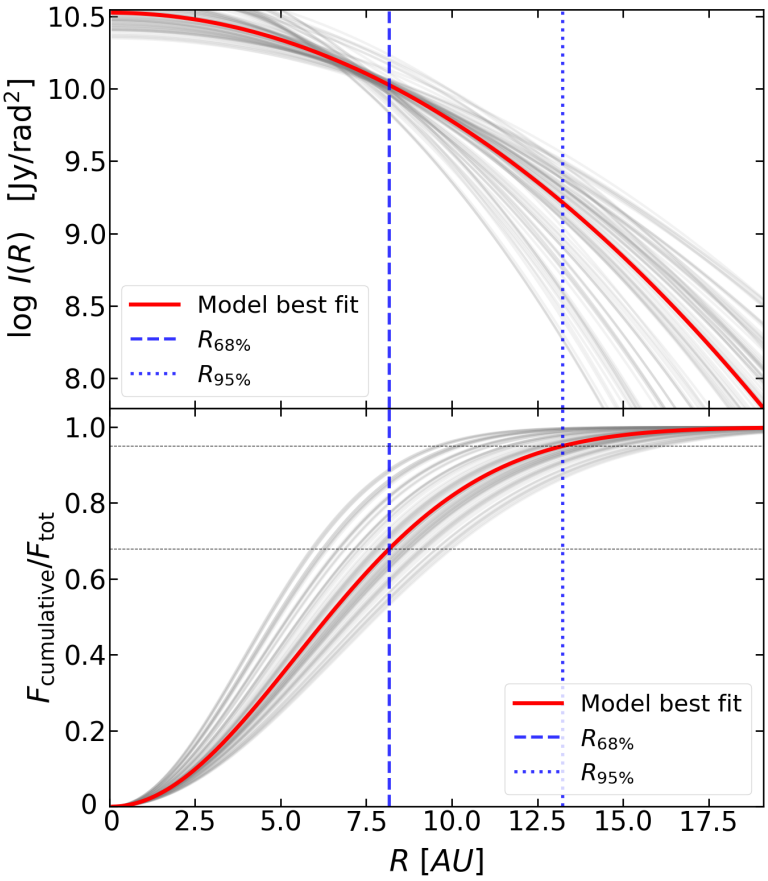

Figure 3.5: Radial brightness profile (*top panel*) and the associated cumulative flux (*bottom*) for the disk of J154518.5-342125 resulting from the Gaussian model used to fit the observed visibilities. The lowest χ^2 model and a random subset of models are drawn in both panels as a red and thin gray curves respectively.

per) uncertainties are obtained from the range between median and 16th (84th) percentiles of their posterior distribution. The missing values are for the cases in which the fit did not find a clear convergence. For source Sz 102, from our fit results, gray obscuration due to its inclination ($\sim 60°$) would not explain its subluminous nature. Strong episodic accretion as suggested by Baraffe & Chabrier (2010) could explain its luminosity: this effect reduces the radius of the star, increasing its temperature and resulting in different pre-MS path and a lower luminosity. Another viable explanation would be a misalignment of the inner and the outer disk.

3.4.4 Disk size results

The radii enclosing 68% and 95% of the total flux ($R_{68\%}$ and $R_{95\%}$) are specified in Table 3.3. The values are inferred from their respective PDFs (example in Figure 3.6), as

Table 3.3: Results from the modeling of the studied disks, together with inferred sizes ($R_{68\%}$ and $R_{95\%}$, in au), and total disk dust mass ($M_{\rm dust}$).

Object	$\log_{10}(I_0)$ [Jy/sr]	σ [arcsec]	i [deg]	PA [deg]	ΔRA [arcsec]	ΔDec [arcsec]	$R_{68\%}$ [au]	$R_{95\%}$ [au]	$M_{\rm dust}$ [$M_\oplus$]
BDs from this survey:									
J154518.5-342125	$10.56^{+0.16}_{-0.11}$	$0.035^{+0.005}_{-0.005}$	$25.8^{+18.7}_{-17.0}$	$90.2^{+54.7}_{-59.8}$	$-0.270^{+0.002}_{-0.002}$	$-0.352^{+0.002}_{-0.002}$	$8.2^{+1.0}_{-1.2}$	$13.2^{+1.7}_{-2.0}$	2.3 ± 0.2
SONYC-Lup3-7	$9.84^{+0.55}_{-0.49}$	$0.03^{+0.02}_{-0.01}$	-	-	$-0.07^{+0.02}_{-0.02}$	$-0.24^{+0.02}_{-0.02}$	< 17.5	< 28.3	0.21 ± 0.02
Lup706	$8.70^{+0.17}_{-0.15}$	$0.14^{+0.04}_{-0.03}$	-	$88.3^{+33.9}_{-38.5}$	$-0.12^{+0.02}_{-0.02}$	$-0.46^{+0.02}_{-0.02}$	< 56.4	< 91.4	0.35 ± 0.04
AKC2006-18	-	-	-	-	-	-	-	-	< 0.06
SONYC-Lup3-10	-	-	-	-	-	-	-	-	< 0.08
BDs from Lupus disks survey:									
Lup818s	$10.99^{+0.41}_{-0.36}$	$0.03^{+0.01}_{-0.01}$	-	-	$-0.06^{+0.01}_{-0.01}$	$-0.207^{+0.005}_{-0.005}$	< 12.1	< 19.7	3.2 ± 0.3
J161019.8-383607	-	-	-	-	-	-	-	-	< 0.45
J160855.3-384848	$10.15^{+0.59}_{-0.47}$	$0.04^{+0.03}_{-0.02}$	-	-	$-0.16^{+0.02}_{-0.02}$	$-0.43^{+0.02}_{-0.02}$	< 21.7	< 35.2	0.79 ± 0.08
Lup607	-	-	-	-	-	-	-	-	< 0.38

Object	ρ_t [arcsec]	γ [-]	β [-]	$\log_{10}\alpha$ [-]	$F_{\rm tot}$ [mJy]	i [deg]	PA [deg]	ΔRA [arcsec]	ΔDec [arcsec]	$R_{68\%}$ [au]	$R_{95\%}$ [au]	$M_{\rm dust}$ [$M_\oplus$]
Disks from Lupus disks completion survey:												
Sz102	$0.55^{+0.45}_{-0.26}$	$-1.2^{+1.2}_{-1.2}$	$15.2^{+3.3}_{-4.0}$	$-0.1^{+0.2}_{-0.2}$	$27.6^{+2.4}_{-2.0}$	$57.6^{+2.9}_{-2.9}$	$14.0^{+3.0}_{-2.9}$	$-0.134^{+0.001}_{-0.002}$	$0.130^{+0.002}_{-0.002}$	$20.1^{+1.1}_{-1.0}$	$43.6^{+4.9}_{-5.4}$	6.1 ± 0.6
V1094 Sco	$0.18^{+0.01}_{-0.01}$	$0.38^{+0.03}_{-0.03}$	$1.25^{+0.01}_{-0.01}$	$1.7^{+0.2}_{-0.3}$	1038^{+5}_{-4}	$56.2^{+0.3}_{-0.1}$	$110.9^{+0.2}_{-0.2}$	$-0.172^{+0.001}_{-0.001}$	$0.098^{+0.001}_{-0.001}$	$201.5^{+0.4}_{-0.4}$	301^{+1}_{-1}	230 ± 23
GQ Lup	$0.21^{+0.04}_{-0.04}$	$0.2^{+0.3}_{-0.4}$	$14.8^{+3.3}_{-4.5}$	$0.5^{+0.2}_{-0.1}$	$158.7^{+2.5}_{-2.5}$	$60.6^{+0.5}_{-0.4}$	$-11.6^{+0.5}_{-0.5}$	$0.0301^{+0.0003}_{-0.0002}$	$0.1284^{+0.0004}_{-0.0003}$	$18.4^{+0.3}_{-0.2}$	$29.2^{+0.8}_{-1.0}$	31.8 ± 3.2
Sz76	$0.45^{+0.12}_{-0.05}$	$1.38^{+0.04}_{-0.05}$	$12.6^{+5.1}_{-5.5}$	$1.2^{+0.5}_{-0.5}$	$17.2^{+2.4}_{-1.9}$	$38.9^{+7.6}_{-10.3}$	113^{+11}_{-12}	$0.001^{+0.003}_{-0.003}$	$0.003^{+0.003}_{-0.003}$	$40.9^{+4.4}_{-3.5}$	75^{+17}_{-8}	4.9 ± 0.5
Sz77	-	-	-	-	$11.1^{+4.0}_{-3.5}$	$61.7^{+10.3}_{-21.9}$	148^{+14}_{-17}	$0.008^{+0.004}_{-0.003}$	$-0.007^{+0.004}_{-0.004}$	< 55.5	< 136	2.1 ± 0.2
RXJ1556.1-3655	$0.30^{+0.03}_{-0.04}$	$0.4^{+0.1}_{-0.1}$	$15.9^{+2.8}_{-3.8}$	$0.6^{+0.1}_{-0.1}$	$85.5^{+1.3}_{-1.3}$	$49.4^{+0.7}_{-0.7}$	$58.1^{+0.8}_{-0.8}$	$-0.061^{+0.001}_{-0.001}$	$0.081^{+0.001}_{-0.001}$	$29.4^{+0.3}_{-0.3}$	$44.9^{+1.1}_{-1.1}$	24.8 ± 2.5
EX Lup	$0.23^{+0.01}_{-0.01}$	$0.38^{+0.05}_{-0.06}$	$14.4^{+3.9}_{-3.5}$	$1.4^{+0.4}_{-0.3}$	$50.0^{+0.9}_{-0.9}$	$30.8^{+1.5}_{-1.6}$	$69.2^{+2.9}_{-2.9}$	$-0.032^{+0.001}_{-0.001}$	$-0.007^{+0.001}_{-0.001}$	$29.8^{+0.4}_{-0.4}$	$39.0^{+1.4}_{-1.0}$	19.1 ± 1.9

Notes. The first 9 objects are the full list of known BDs in Lupus, fitted to a Gaussian model. The six free parameters are: normalization factor of the emission profile $\log I_0$, standard deviation of the Gaussian profile σ, inclination i, position angle PA, and right ascension and declination off-sets to the phase center of the observations ΔRA and ΔDec.
The last 7 disks were fitted to a Nuker profile. The nine free parameters of these fits are: transition radius ρ_t, inner and outer slopes γ and β, smoothness parameter α, total disk flux density $F_{\rm tot}$, and the geometrical parameters of the observation i, PA, ΔRA and ΔDec.

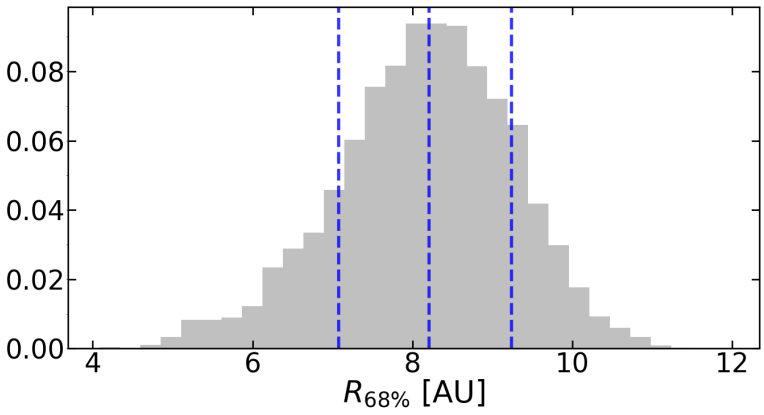

Figure 3.6: Probability density function of the $R_{68\%}$ radius for the disk around J154518.5-342125. Here, $R_{68\%}$ is computed for each model of the parameter space investigation, the value of the radius is taken as the median of the PDF, while upper and lower errors are the median $\pm 1\sigma$ of the distribution. The three values are represented as vertical dashed lines.

derived from the model parameter results. The radii of the detected BDs disks are unfortunately poorly determined due to the compactness of the sources combined with the low S/N of their continuum emission at this waveband. Only for J154518.5-342125 can we properly quantify its size, since its continuum emission is detected with enough S/N and is marginally resolved. We consider a disk to be marginally resolved if the disk emission is of similar spatial scale to the beam size in the image plane and the observed visibilities can be fitted by a Gaussian function with well constrained σ. For all the other BD sources we provide upper limits of their sizes as 95% confidence level, inferred from the PDF of $R_{68\%}$ and $R_{95\%}$. On the other hand, we determined the emission distribution size for six out of seven disks of the Lupus completion survey; for the remaining one (Sz77) we provide an upper limit.

Previous ALMA observations of BD disks in other regions showed that most of the objects were too compact to be resolved (van der Plas et al. 2016; Testi et al. 2016). Using different methodology to define and derive disk radii, Ricci et al. (2014) and Testi et al. (2016) showed that some BD disk radii (R) in Taurus may extend beyond $R \gtrsim 80$ au, while in ρ-Oph BD disks seem to all have $R \lesssim 25$ au.

Nevertheless, we should bear in mind that the few BD disks with well determined sizes are among the brightest and most massive of the BD population of their respective regions (Lupus, Taurus and Ophiuchus); they are likely not representative of the BD population.

3.4.5 Total dust mass results

The total disk dust mass (last column in Table 3.3) is computed from the assumptions detailed in Section 3.4.2. As all detections have good S/N (Table 3.2), the main uncertainty when comparing samples observed at different times is the flux calibrator uncertainty

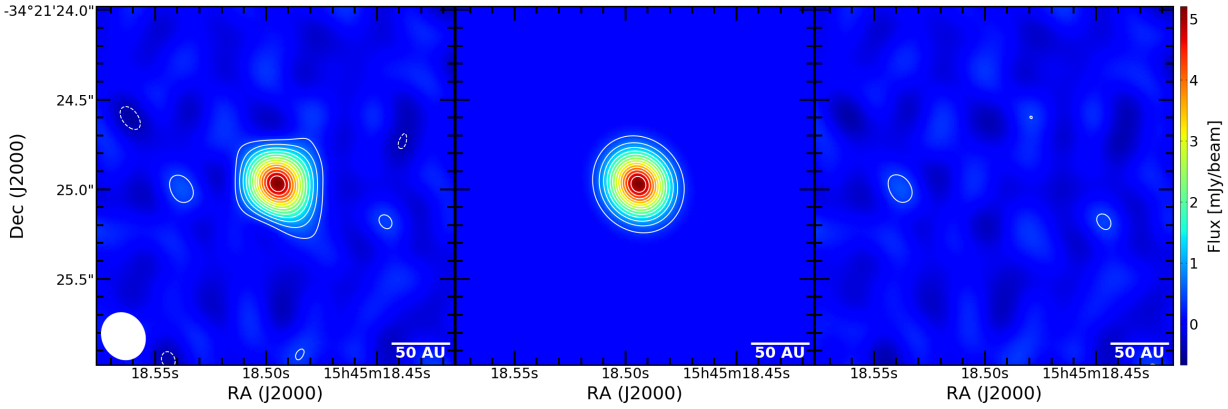

Figure 3.7: Observed (*left*), model (*center*), and respective (*right panel*) residuals for the continuum emission of J154518.5-342125 observed with ALMA. The modeled emission map is reconstructed from the synthetic visibilities with the lowest χ^2 from the interferometric modeling. The contours are drawn at increasing (or decreasing) 3σ intervals as solid (dashed) lines.

($\sim$ 10%, see Section 3.3). Dust mass upper limits for nondetected disks around BDs and stars are obtained from the respective continuum flux upper limits as described in Section 3.3.

The total dust mass for the detected BD disks range between 0.2 and 3.2 $M_{\oplus}$. This means that our sources are within the lightest protoplanetary disks known to date. In particular, SONYC-Lup3-7 is the BD disk with the lowest dust mass estimate, independent of the prescription used for the dust disk mass determination. Comparing our dust mass results of BD disks in Lupus to the results of BD disks in other regions, our results are found to be similar. In Testi et al. (2016), a sample of 17 BD disks in the ρ Ophiuchus region were observed and their dust mass estimates are within 0.5 and 6.3 $M_{\oplus}$, with the same assumptions of dust temperature and opacity as for our results. The dust masses of Taurus disks around BD and VLMs (Ward-Duong et al. 2018) range between $\sim$ 0.25 and $\sim$ 16.7 $M_{\oplus}$, using the same temperature and opacity values as in this work.

3.5 Discussion

3.5.1 Comparison to disks around T Tauri stars

We performed a demographic comparison between the BD and stellar disk populations of Lupus. For this analysis we use the derived disk properties to test whether the known relations for disks around stars are also relevant for BD disks. The observational datasets of both populations were obtained at the same facility (ALMA, Band 7), and the derivation of the properties has been conducted with homogeneous methodology for the entire disk population. In this manner we eradicate systematic errors due to the mixing of diverse datasets handled with different methods.

In addition, we updated the relations between disk properties in Lupus with the largest sample of disks in the region observed with ALMA in Band 7 thanks to the incorporation of the seven stellar disks from the Lupus completion survey to the stellar population. In Table 3.4 we summarize all the correlations discussed throughout this section.

Correlation between $M_\star$ and $M_{\rm dust}$

As a preliminary step, we show in Figure 3.8 the relation of the respective observables of $M_\star$ and $M_{\rm dust}$, that is, the stellar luminosities $L_\star$ and the fluxes at 890 μm wavelength (scaled to a distance of 158.5 pc). From the figure, there is a continuity of the correlation for any range of $L_\star$, and it holds for the BD population. The linear regression shown in the figure is for the entire population (stars and BDs), obtained following the Bayesian method described in Kelly (2007) [1]. Uncertainties and upper limits are taken into account, while subluminous objects are excluded for the fit.

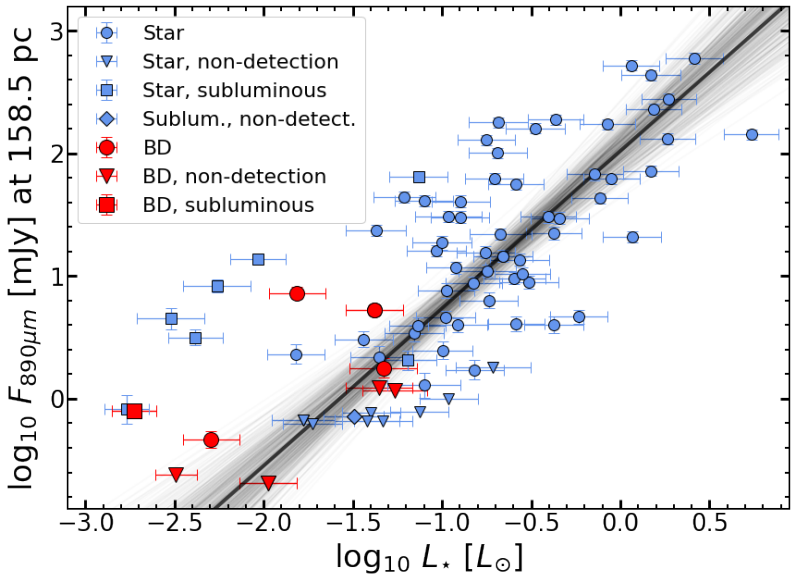

Figure 3.8: Here, 890 μm fluxes vs. stellar luminosity for the Lupus population. Stellar population is shown in blue; the BD disk population is plotted in red. Detected sources from ALMA observations are represented as circles; upper limits of nondetections are shown as triangles; subluminous objects as inferred from X-Shooter spectra are plotted as squares. The linear regression shown has been obtained from the entire population, excluding subluminous sources.

Testi et al. (2016) found potential evidence of BD disks being less massive than stellar disks, based on the analysis of an incomplete sample of BD disks in Ophiuchus. Our Lupus sample allows us to check whether similar results hold in this star forming region. In Figure 3.8, there is no obvious trend for BDs to have very significantly smaller 890

[1] implemented with the `linmix` Python package, `https://linmix.readthedocs.io/en/latest/index.html`

μm fluxes than stars with similar luminosities. To quantify this comparison, we followed a similar procedure as in Testi et al. (2016) based on a statistical comparison of the two populations, and analyzed whether the distribution of the $M_{\rm dust}/M_\star$ ratios in the sample of BD disks is consistent with being drawn from the same distribution as for the stars.

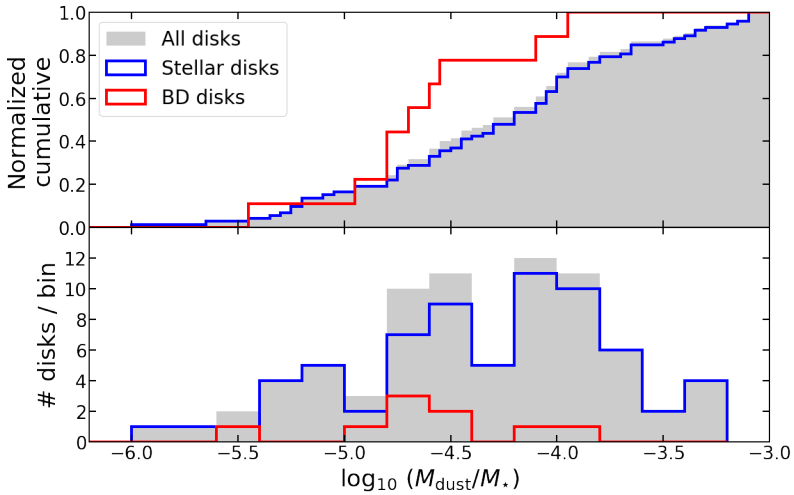

Figure 3.9: Statistical comparison between BD and TTS disks populations in the Lupus star forming region. The histograms (*bottom*) and cumulative (*top*) distributions of the dust mass-stellar mass ratio are shown for both populations. The results summing up both populations are also included (shown as gray). A bin size of 0.2 has been used for the histogram of the populations.

Figure 3.9 shows the cumulative distributions and the histograms of the values of the $M_{\rm dust}/M_\star$ ratios for the Lupus samples. Dust mass of each object is derived following Section 3.4.2, $M_\star$ as described in Section 3.2. The histogram shows that the values of the BD ratios are similar to the stellar population ratios, unlike the Ophiuchus sample in Testi et al. (2016). We performed the Anderson-Darling test[2] to study the null hypothesis that the two samples are drawn from the same underlying population, obtaining a probability of 6% that the BD and stellar disk populations are drawn from the same distribution. Although it is a low percentage, it is below 2σ significance. Moreover, the likelihood increases to $\sim$ 80-90% if we use the dependence of $T_{\rm dust}$ with $L_\star$ from Andrews et al. (2013), and van der Plas et al. (2016). Thus, the data are consistent with the null hypothesis to be correct. Our analysis of the Lupus sample does not show a statistically different fraction of dust mass around BDs as compared to stars. We caution that our sample of VLM stars and BDs in Lupus is very limited and that the results of Testi et al. (2016) were based on highly incomplete and inhomogeneous samples. Further studies with larger and/or unbiased samples are needed to make firm conclusions on this matter.

The result of the previous analysis is also confirmed by inspecting the dependence of $M_{\rm dust}$ on $M_\star$ (Figure 3.10). In Appendix B, this dependence is shown for the other

[2]using `scipy.stats` Python module, `https://docs.scipy.org/doc/scipy/reference/stats.html`

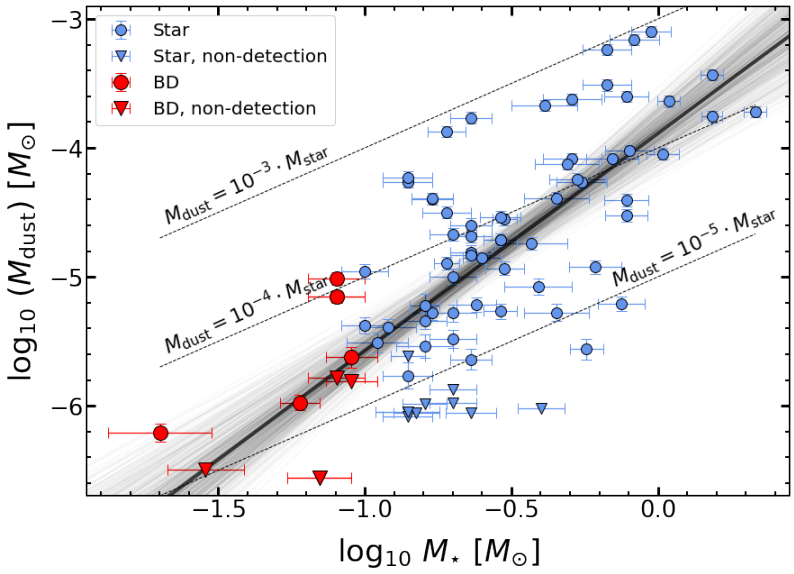

Figure 3.10: Disk dust masses vs. central object mass for the BD (red) and stellar (blue) populations in Lupus. Detected sources from ALMA observations are represented as circles; upper limits of nondetections are shown as triangles. Dust mass uncertainties and upper limits as described in Section 3.4.5. Uncertainties of $M_\star$ are 1σ. Linear regression shown for the entire disk population (stars and BDs).

$T_{\rm dust}$ prescriptions. The linear regression result is consistent with those of Ansdell et al. (2016), and Pascucci et al. (2016) when using the same assumptions of dust opacity and temperature. The slope (α) and intercept (β) for the stellar population are $\alpha = 1.73 \pm 0.25$ and $\beta = -3.88 \pm 0.14$ respectively (inferred using `linmix` package, and including upper limits of ALMA nondetections). As consequence of incorporating the BD population into the fit, there is a substantial reduction of the uncertainty of α and β thanks to the extension of the mass range over one order of magnitude: the slope and intercept become 1.69 ± 0.19 and -3.89 ± 0.13. If we compute a linear regression taking into account only the BD sample, we obtain a slope and intercept that is in agreement with the stellar fit, although the uncertainties in this case are large due to the short range in both axes of the BD population.

Disk size-luminosity relation

The existence of a correlation between the disk luminosity and its size was first shown using pre-ALMA observations (Andrews et al. 2010; Piétu et al. 2014). For the Lupus disk population, this dependence was confirmed in Tazzari et al. (2017) and Andrews et al. (2018b). In Figure 3.11, we show the updated relation for the Lupus disk population, including the seven new measurements from this paper (one BD disk and six disks around stars). The linear regression shown in the figure is obtained for the stellar disk population, excluding the upper limits of the disks with poorly constrained sizes.

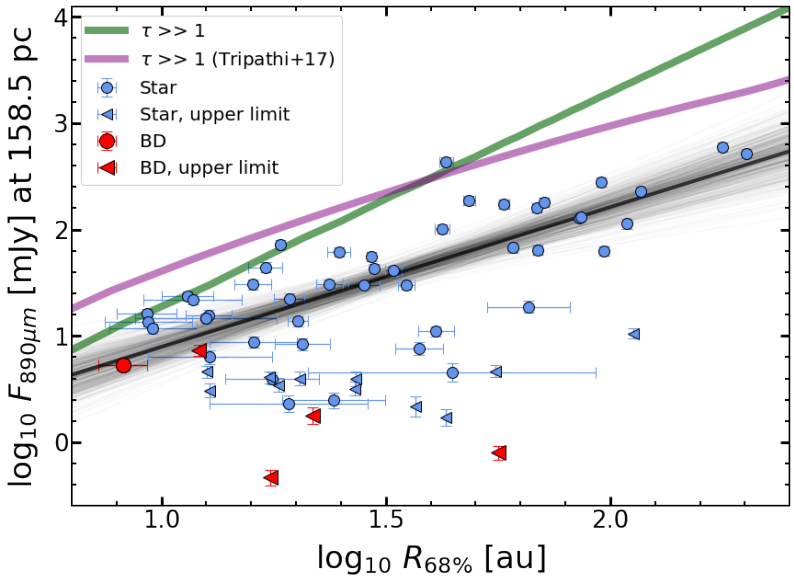

Figure 3.11: ALMA 890 μm fluxes, scaled to a common distance vs. observed size ($R_{68\%}$, see text), for stars (blue) and BDs (red) in the Lupus star forming region. Upper limits of disk sizes that could not be determined accurately from our disk modeling methodology are shown as triangles, they represent the 95% confidence level of the disk size. $R_{68\%}$ error bars account for 1σ from the mean value, flux error bars are associated to the 10% flux calibration uncertainty.

The BD disk with well constrained $R_{68\%}$ (J154518.5-342125) is in very good agreement with the relation for stars. The result suggests that this BD disk is a scaled-down equivalent of the very extended disks around stars that show substructure. Nevertheless, since its central object mass is near the BD/VLM boundary, this result might not be representative of the full BD population. Higher-angular-resolution observations of the BD population are needed in order to obtain reliable estimates of their sizes. The estimated size upper limits of the other BD disks provide limited constraints on the relation. The compactness of the BD disks might be indicative that BD disks follow the size–luminosity relation of stars, as suggested by Hendler et al. (2017) from SED fitting of disk observations, and also from the results for ρ-Ophiuchus of Testi et al. (2016). If these objects were to follow the same relation as stars, their $R_{68\%}$ would range between 1 and 10 au.

There is now evidence of optically thick emission in the inner ($\lesssim$ 50 au) regions of disks around stars (Huang et al. 2018; Liu 2019; Zhu et al. 2019). Likewise, BD disks in Lupus might be optically thick, as suggested by their compact continuum emission. In Figure 3.11, we show two optically thick (optical depth $\tau >> 1$) fiducial models, the first one (green) assuming a constant $T_{\rm dust}$ of 20 K, and a second model (purple) with radial dependence of $T_{\rm dust}[{\rm K}] \approx 30 \cdot (\frac{L_\star}{L_\odot})^{0.25} \cdot (\frac{R}{10})^{-0.5}$ (Andrews et al. 2013). The emission of these models is described by $I_\nu(R) = \mathcal{F} B_\nu(T_{\rm dust})$, where $\mathcal{F}$ is a filling factor that describes the fraction of the disk emission distribution that is optically thin: $\mathcal{F} = 1$ if the disk emission

is optically thick, $0 < \mathcal{F} < 1$ for a partially optically thick disk (analogous to Tripathi et al. 2017; Andrews et al. 2018b). The optically thick curves in the figure are built considering a set of disks with increasing outer size. Objects laying on the line are compatible with being fully optically thick. Additionally, in optically thick disks, the inferred $R_{68\%}$ trace the location of large grains rather than the physical outer radius of the disk (Rosotti et al. 2019).

The only BD with determined dust disk size (J154518.5-342125) lays below both fiducial models. Its dust emission can be understood as optically thin with a fraction of the disk emission distribution being optically thick. If its disk emission is partially optically thin, a portion of dust is not observed, thus the inferred dust mass is underestimated. The upper limits of the remaining BD disks are far below the optically thick models, although their exact positions in the $R_{68\%}$-$F_{890\mu m}$ are unknown.

Correlation between $\dot{M}_{\rm acc}$ and $M_{\rm dust}$

A linear correlation between mass accretion rate onto the central object ($\dot{M}_{\rm acc}$) and the disk mass is expected if disks evolve viscously (e.g., Dullemond et al. 2006; Natta et al. 2007; Lodato et al. 2017). Observational evidence for this correlation was first reported by Manara et al. (2016b) for the Lupus disks, and Mulders et al. (2017) in the Chamaeleon I region.

The $\dot{M}_{\rm acc}$-$M_{\rm dust}$ relation for Lupus disks is shown in Figure 3.12. The x-axis of the figure is an estimate of the total disk mass based on our derivation of the disk dust mass and assuming a gas-to-dust ratio of 100. The $\dot{M}_{\rm acc}$ and its uncertainty is taken from the X-Shooter observations presented by Alcalá et al. (2014, 2017). The accretion rate values have been recomputed with the new accretion luminosities that correspond to the parallaxes from Gaia DR2. One BD disk (SONYC-Lup3-10) was not characterized from X-Shooter observations. Although the H_α emission line is known (Mužić et al. 2014), we have excluded this BD from the analysis in order to have a fully homogeneous sample for our statistical study.

The linear regression for the stellar population in Figure 3.12 has been obtained excluding BDs (due to the different BD disks behavior compared to stellar disks, demonstration below), nondetections from ALMA, upper limits of $\dot{M}_{\rm acc}$, and subluminous sources. The resulting slope is $\alpha = 0.69 \pm 0.14$, while the intercept is $\beta = -7.26 \pm 0.36$. When using the same assumptions of dust temperatures and opacities, the linear regression is consistent with the results presented in Manara et al. (2016b). Brown dwarfs have systematically lower accretion rates than stars for the same disk mass. This is also seen in the relation between the more directly observed properties (in Appendix D), and is independent of the considered prescription of the dust temperature (results using other prescriptions in Appendix B).

We inspected the $M_{\rm disk}/\dot{M}_{\rm acc}$ ratio for the Lupus disk population to confirm or deny this trend. This ratio can be understood as the accretion depletion timescale (or disk age, as in Jones et al. 2012, see also Rosotti et al. 2017), and provides an estimate of the survival time of the disk, assuming that accretion onto the central object remains constant and that

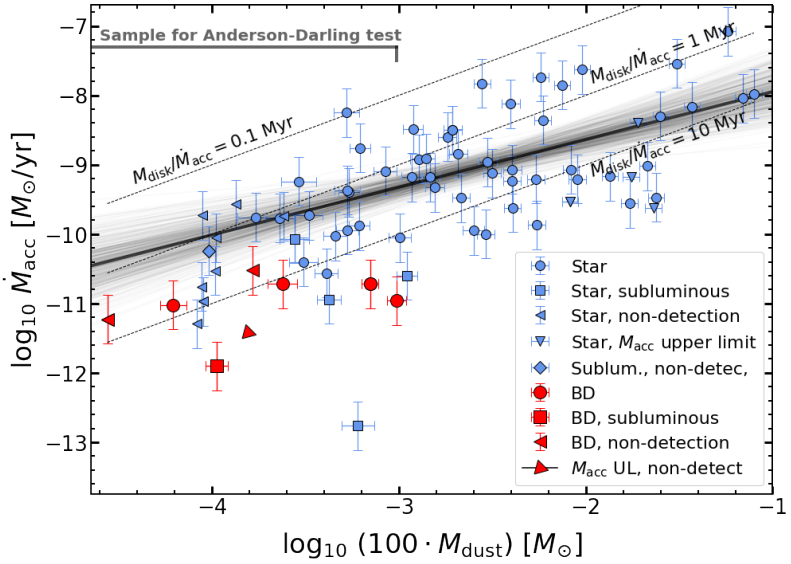

Figure 3.12: Relation between the total disk mass (obtained assuming $\kappa_{890\mu m} = 2$ cm^2 g^{-1}, and $T_{dust} = 20$ K) and the mass accretion rate onto the central object.

accretion is the dominant mechanism for the depletion of the disk. In Figure 3.12, we plot different lines indicating accretion depletion timescales of 0.1, 1, and 10 Myr.

As in Section 3.5.1, we conducted a statistical analysis of the two populations in order to confirm the behavior of the BD disks. We compare the BD population with the subsample of stars with disk masses within the range of the BD disk masses (in other words, all disks with $\log_{10}(M_{disk}) < -3$ in Figure 3.12). This is done in order to remove the more massive disks from the stellar sample, which may accentuate the difference between populations. Subluminous objects and those with upper limits of the $\dot{M}_{acc}$ are excluded from the studied samples. The median value of the central object mass is 0.08 $M_\star$ for the BD sample and 0.19 $M_\star$ for the stellar subsample. The histograms of the accretion depletion timescale and the respective cumulative distributions are shown in Figure 3.13. The Anderson-Darling test confirms that the BD disk population has a significantly larger accretion depletion timescale with respect to the stellar population, with only a 0.6% probability that the BD and stellar disk populations are drawn from the same original distribution. The median value of this timescale for the BD sample is 9.5 Myr, while this timescale is 1.4 Myr for the stellar subsample considered. The results hold when using other prescriptions of the disk dust mass for this test, with even lower probabilities ($\sim 0.05\%$).

The result of the accretion depletion timescale is obtained using the total disk mass, which is estimated assuming that the emission of the dust is optically thin, and that dust mass traces the total disk mass. If (sub-)mm emission of BD disks is optically thick, the disk masses are underestimated, and consequently the accretion depletion timescale is larger than the estimated values. Thus, the difference on the accretion depletion timescale would be even more pronounced if BD disks were optically thick at these wavelengths.

A larger accretion depletion timescale may reflect a difference in the accretion process

Table 3.4: Linear regression results of all the investigated disk property correlations. The values of α and β correspond to the slope and intercept of the linear fit, following the linear relation $\log(Y) = \beta + \alpha \cdot \log(X)$. The dispersion is the standard deviation of the regression in dex. $F_{890\mu m}$ has been scaled to the average distance of the region (158.5 pc).

X-axis	Y-axis	$T_{\rm dust}$ prescription	α	β	Dispersion
$L_\star[L_\odot]$	$F_{890\mu m}$[mJy]	-	1.27 ± 0.13	2.02 ± 0.13	0.60 ± 0.07
$F_{890\mu m}$[mJy]	$L_{\rm acc}[L_\odot]$	-	0.81 ± 0.15	-3.28 ± 0.22	0.68 ± 0.08
$M_\star[M_\odot]$	$M_{\rm dust}[M_\odot]$	Constant (20 K)	1.69 ± 0.19	-3.89 ± 0.13	0.60 ± 0.05
		Andrews et al. (2013)	0.95 ± 0.18	-4.08 ± 0.12	0.57 ± 0.05
		van der Plas et al. (2016)	1.25 ± 0.18	-3.98 ± 0.12	0.58 ± 0.05
$R_{68\%}$[au]	$F_{890\mu m}$[mJy]	-	1.31 ± 0.17	-0.41 ± 0.27	0.41 ± 0.05
$100 \cdot M_{\rm dust}[M_\odot]$	$\dot{M}_{\rm acc}[M_\odot/{\rm yr}]$	Constant (20 K)	0.69 ± 0.14	-7.26 ± 0.36	0.56 ± 0.08
		Andrews et al. (2013)	0.63 ± 0.17	-7.49 ± 0.43	0.64 ± 0.09
		van der Plas et al. (2016)	0.67 ± 0.16	-7.38 ± 0.42	0.62 ± 0.09

of BDs with respect to stars. If viscous evolution models are invoked to explain accretion onto the central star, a weaker accretion would imply a lower α parameter (Shakura & Sunyaev 1973) in BD disks. Since the turbulence in viscous disks depends on α, a lower $\dot{M}_{\rm acc}$ implies a less turbulent disk. Thus, in viscous disks, our result suggests that the α parameter of disks around BDs is lower than around stars (in contrast with the results of Mulders & Dominik 2012), and consequently BD disks would be less turbulent. A bimodal behavior of accretion has been suggested observationally in Alcalá et al. (2017), and Manara et al. (2017), and predicted from theoretical modeling by Vorobyov & Basu (2009); in those studies the two suggested modes were between VLMs ($M_\star < 0.2\ M_\odot$) and more massive stars. When performing a statistical comparison in our sample between the VLM population ($0.1\ M_\odot < M_\star < 0.2\ M_\odot$) and more massive stars, we obtain a likelihood in the Anderson-Darling test of $\sim 9\%$ (averaged over the three different prescriptions of $M_{\rm dust}$ used in this work). Thus, VLM stars might show this behavior as well, but less pronounced, and with much lower statistical significance.

A lower viscosity in disks around BDs/VLM stars compared to disks around more massive stars could be explained with a globally lower ionization rate (e.g., see Mohanty et al. 2005). As a consequence of the general correlation between X-ray and bolometric luminosities, young BDs/VLM stars have slightly lower X-ray luminosities than more massive young low-mass stars (see, e.g., Gregory et al. 2016); this might lead to slightly lower ionization rates in the disks of BDs and VLM objects. Some BD/VLM disks being flatter than disks around more massive stars, which would decrease the irradiation cross-section, could also explain a lower ionization rate (as suggested from SED models and observations by Ercolano et al. 2009; Pascucci et al. 2003; Apai et al. 2004b; Allers et al. 2006). However, there is evidence of disks around BDs being flared (e.g., Natta & Testi 2001; Natta et al. 2002; Furlan et al. 2011), and therefore this last possibility would need more detailed and extended investigation.

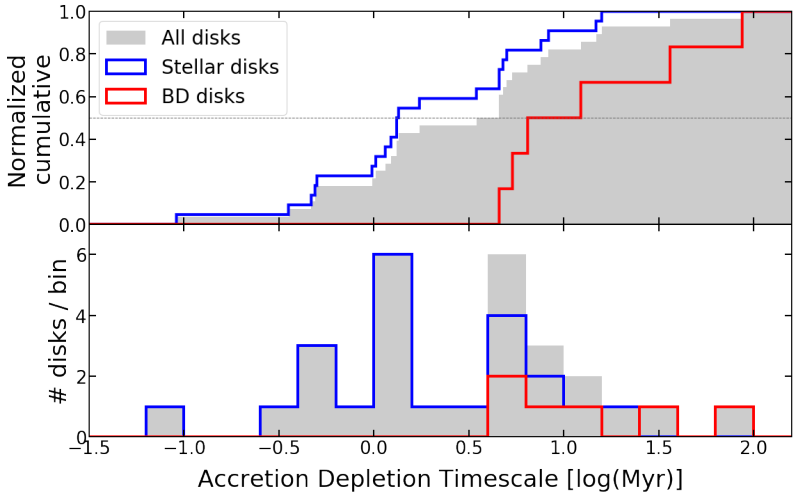

Figure 3.13: Histograms (*bottom*) and cumulative distributions (*top*) of the accretion depletion timescale are shown for both populations (BDs as red, stars as blue). The results summing up both populations are also included (shown as gray).

3.5.2 Planet formation around BDs

The exoplanetary systems recently discovered around BDs and VLMs can be used to study the ability of BDs to form planets. Since the planets hosted by Trappist-1 and Proxima Centauri are most likely of rocky composition, the total planetary mass of these systems can be compared to the estimates of the disk dust mass of the BD disk population in Lupus. The total mass of the seven known planets (Gillon et al. 2017) in Trappist is 4 $M_{\oplus}$ (Wang et al. 2017). Proxima B, the planet hosted by our closest neighbor (Anglada-Escudé et al. 2016), has a minimum mass of 1.3 $M_{\oplus}$. In (Bixel & Apai 2017) the planet mass was predicted to be $1.63^{+1.66}_{-0.72}$ $M_{\oplus}$ with 95% confidence level. The remaining known exoplanets around BDs have estimated masses of at least several times that of Earth. A considerable fraction of them have been detected via microlensing (e.g., Jung et al. 2018), with typically much higher estimated masses. Thus the picture for these planets is analogous to the Trappist-1 planets and Proxima B.

From theoretical predictions of planet formation around BDs via core accretion (Payne & Lodato 2007), disk masses (gas and dust) on the order of a few Jupiter masses are required in order to form Earth-like planets around BDs. Not only do none of the BD disks in Lupus (this paper) and ρ-Oph (Testi et al. 2016) have enough mass available at their current stage to form a planetary system, but even the available mass in solids is smaller than the total planetary mass in Trappist-1. The efficiency with which the available mass is converted into the final planetary rocky cores might be boosted by internal recycling of the disk material, but it is unlikely to reach an efficiency close to unity (Manara et al. 2018a, and references therein). On the other hand, the tentative result from Section 3.5.1 of lower viscosity and ionization rates on BD disks might contribute to the presence of an extended dead zone in the disk, which would boost the planet formation process.

A plausible explanation to alleviate this divergence is that the determination of dust mass from continuum emission flux might be underestimated, as pointed out in Ballering & Eisner (2019). This might be the case if the emission at this wavelength is optically thick; consequently the inferred $M_{\rm dust}$ provides only a lower limit of the disk dust mass. In Fig. 3.11, disks laying on the $\tau >> 1$ fiducial models are consistent with their emission being fully optically thick. The only BD disk with a well-determined size (J154518.5-342125) is below these models. This suggests that the emission of this BD disk is optically thin with small regions of the disk being optically thick. The inferred dust mass of this disk is underestimated by an unknown fraction. This can help to explain the mass difference with exoplanetary systems. Nevertheless, it seems unlikely that partial optically thin emission alone can account for this large difference in solid masses.

A likely possibility is that planets might have already formed at this stage of disk evolution (Greaves & Rice 2010; Najita & Kenyon 2014; Manara et al. 2018a; Dodds et al. 2015). If this is indeed the case, the formation of planetary rocky cores would have occurred within the first million years (considering the estimated ages of Lupus and ρ-Ophiuchus). While direct detection of planets embedded in protoplanetary disks is extremely difficult (see Sanchis et al. 2020a; Johns-Krull et al. 2016), the presence of circumplanetary disks, if confirmed, sets a strong indirect evidence of young planets in these disks (Keppler et al. 2018; Isella et al. 2019; Pérez et al. 2020). Analysis of the gas kinematics can also be used as an indirect method to study embedded planets (Teague et al. 2018; Pinte et al. 2018b). Other indirect indications, such as the existence of gaps, spirals, asymmetries, and dust processing are observed frequently, and suggest that planets might already have formed (e.g., ALMA Partnership et al. 2015b; Zhang et al. 2018; Lodato et al. 2019; Pinilla et al. 2018).

3.6 Conclusions

In this work we presented new Band 7 ALMA observations of five protoplanetary disks around BDs in Lupus. Combined with previous observations, we analyzed the (sub-)mm disk properties of the known population of BDs and VLM objects with infrared excess. From the continuum fluxes and modeling the visibilities, we inferred total dust disk masses and characteristic sizes of the disk population. Due to the extremely compact emission of the BD disks in Lupus, the size determination was only possible on one BD disk, while for the other detected disks we present upper limits on the size.

We updated the relations of $M_\star$-$M_{\rm dust}$, size–luminosity, and $M_{\rm dust}$-$\dot{M}_{\rm acc}$ relations extending them down to the substellar regime. Brown dwarf disks in Lupus follow the relation for stars between stellar mass and dust disk mass. They show no statistical difference from the stellar disk population on the disk mass fraction, however we note the apparent lack of massive BD disks. On the other hand, the accretion depletion timescale (inferred assuming that dust mm and sub-mm continuum emission is a reliable proxy of the total disk mass) of the BD population is significantly longer than for stars (9.5 Myr vs. 1.4 Myr), which in viscously evolving disks may imply a lower α value, possibly linked to a globally lower

ionization rate.

Lastly, we inspected the ability of these objects to form planets, comparing the estimated disk dust masses with the rocky planetary masses in known exoplanetary systems. The estimated disk dust masses around brown dwarfs are very low, suggesting that either these systems are unable to form planets, or more likely, that rocky planetary cores have already formed within the first million years. Optically thick emission in BD disks can alleviate this mass discrepancy.

Chapter 4

Demographics of the gas content in protoplanetary disks

The content of this chapter has been included in:

> *" Measuring the ratio of the gas and dust emission radii of protoplanetary disks in the Lupus star-forming region "*
> **Sanchis, E.**, Testi, L., Natta, A., Facchini, S., Manara, C., Miotello, A., Ercolano, E., Henning, Th., Preibisch, T., Carpenter, J., de Gregorio-Monsalvo, I., Jayawardhana, R., López, C., Mužić, K., Pascucci, I., Santamaría-Miranda, A., van Terwisga, S., and Williams, J., accepted for publication in A&A.

4.1 Introduction

Planets form around stars during their pre-main sequence phase, when still surrounded by a circumstellar disk of gas and dust. Setting observational constraints on the gas and dust properties of these disks is crucial in order to understand what are the ongoing physical processes in the disk. These processes shape the planet formation mechanisms, and ultimately tell us about the disk's ability to form planets (see, e.g., Mordasini et al. 2012).

The advent of the Atacama Large Millimeter/submillimeter Array (ALMA) allowed for a characterization of the dust properties in large populations of disks (e.g., Tazzari et al. 2017; Andrews et al. 2018b; Hendler et al. 2020), based on surveys targeting nearby star-forming regions (Ansdell et al. 2016, 2017; Barenfeld et al. 2016; Pascucci et al. 2016; Cox et al. 2017; Cieza et al. 2018; Cazzoletti et al. 2019; Williams et al. 2019). However, demographic studies of the gas disk properties in these regions are scarcer (e.g., Long et al. 2017; Ansdell et al. 2018; Najita & Bergin 2018; Boyden & Eisner 2020), due to the fewer detections, the difficulty of finding reliable gas tracers (e.g., Miotello et al. 2016, 2017), and frequently, cloud contamination.

A key diagnostic of the evolutionary stage of a disk is its size. Dust and gas evolve differently, thus, we can learn about the undergone physical processes in the disk by study-

ing the relative extent between gas and dust (e.g., Sellek et al. 2020a,b). Initially, the dust grains have sizes below 1 μm and are kinematically coupled to the gas (e.g., Fouchet et al. 2007; Birnstiel et al. 2010). The pressure gradient of a disk, which generally points outward, exerts an additional force that causes gas to orbit in a slightly sub-keplerian speed. Dust grains grow by coagulation, and when large enough –of the order of mm sizes– orbiting grains are no longer supported by the outward pressure force. A frictional force is induced on the large grains, and by angular momentum conservation, a drift inwards that results in piled-up large grains in a compact configuration (e.g., Weidenschilling 1977; Pinilla et al. 2012; Canovas et al. 2016). On the other hand, gas, in viscous disks, spreads out to conserve angular momentum and enable gas close in to accrete onto the star (e.g., Lynden-Bell & Pringle 1974b; Nakamoto & Nakagawa 1994; Hueso & Guillot 2005). In wind-driven accretion models (for a review, see Turner et al. 2014), the gas extent will also be larger than the dust extent: dust still drifts inwards, while the gas extent does not vary significantly. Observations at (sub-)mm wavelengths typically trace the large dust grains (sizes up to cm sizes) decoupled from the gas (Testi et al. 2014; Andrews 2015), hence, disks with undergone dust evolution will appear more extended in gas than in dust continuum from ALMA observations.

A difference in size between the gas and dust content has been confirmed from observations of individual Young Stellar Objects (YSOs; e.g., Isella et al. 2007; Andrews et al. 2012), and thanks to ALMA, also from larger samples (e.g., Ansdell et al. 2018; Boyden & Eisner 2020). Besides the effect of dust evolution, the optical depth difference between dust continuum and gas rotational lines may also contribute to the disparity in the observed gas and dust sizes (e.g., Trapman et al. 2019). While dust thermal emission in the outer disk is optically thin or only partially thick (e.g., Huang et al. 2018), the gas emission is, in general, optically thicker (e.g., Guilloteau & Dutrey 1998). A difference in optical depth implies the dust emission to be fainter than the gas rotational line, thus the emission of the dust outer disk would fall below the sensitivity limit of the instrument at a smaller radius compared to the gas outer emission.

Consequently, identifying the effect that dominates the size ratio is not easy. Trapman et al. (2019) showed that disks with gas/dust size ratios above 4 can only be explained if grain growth and subsequent radial drift has occurred. Such high size ratios between gas and dust have already been observed (Facchini et al. 2019). The existence of pressure bumps can also limit the study of dust evolution based on the gas/dust size ratio. In such scenario, dust grains from the outer disk would only drift inwards down to the bump location. This might result in a larger observed dust size, thus a lower size ratio.

In this work, we expand over the previous study of the gas and dust content in the protoplanetary disk population of Lupus (Ansdell et al. 2018). The gas extent is measured based on emission of ^{12}CO rotational lines at (sub-)mm wavelengths, while the dust extent is obtained from the continuum emission of large grains. The CO emission from these lines is appropriate for the study of the gas extent due to its abundance. These lines are optically thick at low CO column densities (van Dishoeck & Black 1988), allowing CO to self-shield and avoid photodissociation from UV photons. Extremely low CO temperatures (of ~ 20 K) limits the study of gas based on these lines, since CO may freeze out onto the

dust grains' surface, no longer emitting at these rotational lines.

The integrated CO emission is modeled to empirical functions, this allows us to increase the number of disks with characterized CO compared to previous studies. In addition, disks surrounding brown dwarfs (BDs) from more recent observations (Sanchis et al. 2020b) are added to the studied sample. Dust disk sizes are estimated from fitting empirical models in the visibility plane. This manuscript is organized as follows: in Section 4.2 we describe the Lupus disk sample and the observations used; the modeling of the CO and dust continuum emission is presented in Section 4.3; the resulting sizes are summarized in Section 4.4; in Section 4.5, we perform the demographic analysis of the CO and dust sizes, and discuss what the results entail; finally, in Section 4.6, we summarize the main findings of this study.

4.2 Sample selection

The objects studied in this work belong to the Lupus clouds (I-IV), a low-mass Star-Forming Region (SFR) that is part of the Scorpius-Centaurus OB association (Comerón 2008). Lupus is one of the closest SFRs, at a median distance of 158.5 pc (from individual Gaia parallaxes of the Lupus members, Gaia Collaboration et al. 2018). The age of the region is approximately 1-3 Myr (Comerón 2008; Alcalá et al. 2017).

The sample includes young stellar objects with confirmed protoplanetary disks, down to the BD regime (we define as BD systems of spectral type equal or later than M6, and whose central object mass is $< 0.1\ M_{\odot}$). The sources were selected from the catalogs of the clouds (Hughes et al. 1994; Mortier et al. 2011; Merín et al. 2008; Comerón 2008; Dunham et al. 2015; Bustamante et al. 2015; Mužić et al. 2014, 2015), their infrared (IR) excess estimated from *Spitzer* ('Cores to Discs' legacy project, Evans et al. 2009) and 2MASS (Cutri et al. 2003) data. Details on the sample selection for the ALMA surveys are to be found in Ansdell et al. (2016, 2018) for the stellar objects, and Sanchis et al. (2020b) for the BDs. All objects are confirmed members of the Lupus clouds from radial velocity analysis (Frasca et al. 2017). The stellar properties were taken from Alcalá et al. (2014, 2017) and Mužić et al. (2014), while stellar luminosities ($L_{\star}$) and masses ($M_{\star}$) have been recalculated taking into account the distance from the precise Gaia DR2 parallaxes (Gaia Collaboration et al. 2018; Manara et al. 2018b; Alcalá et al. 2019). The stellar mass is obtained from the position in the Hertzsprung–Russell (HR) diagram set by the effective temperature and the updated $L_{\star}$. The stellar mass is primarily interpolated from the pre-main sequence models of Baraffe et al. (2015), which provide accurate estimates of $M_{\star}$ for BDs, M dwarfs and low mass stars up to 1.4 $M_{\odot}$. These models are ideal for our sample, since the great majority of Lupus objects are within this mass range. For the very few objects above 1.4 $M_{\odot}$ (only 3 in the entire Lupus sample) the Siess et al. (2000) models are used instead. The stellar mass uncertainty is obtained from a Monte Carlo procedure as in Alcalá et al. (2017).

Following these criteria, the selected ALMA dataset is composed by 100 protoplanetary disks around YSOs in the Lupus clouds, 9 of which are BDs. However, our analysis concentrates on the 42 disks whose CO and dust radii could be measured.

Table 4.1: Summary of the archival ALMA projects used in this work for the gas and dust modeling.

Obs.	Freq. [GHz]	Ang. resolution [″ × ″]	Sources / Survey name	ALMA Project	References
^{12}CO(2-1)	230.5	$\sim 0.24 \times 0.23$	86, Band 6 Lupus Disk	2015.1.00222.S	Ansdell et al. (2018)
^{12}CO(2-1)	230.5	$\sim 0.26 \times 0.22$	7, Lupus Completion Disk	2016.1.01239.S	van Terwisga et al. (2018)
^{12}CO(2-1)	230.5	$\sim 0.53 \times 0.39$	Sz 82	2013.1.00226.S	Cleeves et al. (2016)
^{12}CO(2-1)	230.5	$\sim 0.25 \times 0.22$	Sz 91	2013.1.01020.S	Canovas et al. (2016)
^{12}CO(3-2)	345.8	$\sim 0.36 \times 0.33$	5, Lupus BD Disks	2017.1.01243.S	Sanchis et al. (2020b)
Cont. B7	~ 335	$\sim 0.34 \times 0.30$	86, Band 7 Lupus Disk	2013.1.00220.S	Ansdell et al. (2016)
Cont. B7	~ 335	$\sim 0.19 \times 0.17$	7, Lupus Completion Disk	2016.1.01239.S	van Terwisga et al. (2018)
Cont. B7	~ 335	$\sim 0.37 \times 0.29$	Sz 82	2013.1.00694.S	Cleeves et al. (2016)
Cont. B7	~ 335	$\sim 0.21 \times 0.15$	Sz 91	2013.1.00663.S	Canovas et al. (2016)
Cont. B7	~ 335	$\sim 0.36 \times 0.34$	5, Lupus BD Disks	2017.1.01243.S	Sanchis et al. (2020b)
Complementary data					
^{12}CO (2-1)	230.5	$\sim 0.10 \times 0.08$	7, DSHARP project	2016.1.00484.L	Andrews et al. (2018a)
Cont. B6	~ 225.4	$\sim 0.27 \times 0.26$	86, Band 6 Lupus Disk	2015.1.00222.S	Ansdell et al. (2018)

4.2.1 Observations

The CO radial extent of the disks is measured from archival ALMA observations covering the ^{12}CO $J = 2 - 1$ rotational line in Band 6 (at 230.538 GHz). For 3 sources, the $J = 3 - 2$ rotational transition in Band 7 (at 345.796 GHz) is used instead. The dust sizes are obtained based on modeling of archival observations of dust continuum in ALMA Band 7 (centered at ~ 0.89 mm). The ^{12}CO channel maps are built after subtracting the continuum and cleaning with a Briggs weighting and robustness = +0.5. In Table 4.1, the details of the line and continuum ALMA observations used in this study are summarized; including information of the ALMA project IDs, the number of Lupus sources targeted at each ALMA project, angular resolution, and the corresponding references that describe the observations and the instrument configuration.

In order to test our method for determining the CO disk radial extent for a few disks in the dataset described above, we have analyzed available ALMA data at higher resolution and better sensitivity. These additional data are part of the DSHARP large program (Andrews et al. 2018a, for a general description of the project; see also the other DSHARP publications, II-X), that also covered the ^{12}CO J = 2-1 rotational transition for all targets. The Lupus disks targeted in DSHARP are: Sz 68 (HT Lup), Sz 71 (GW Lup), Sz 82 (IM Lup), Sz 83 (RU Lup), Sz 114, Sz 129, and MY Lup. Lastly, the continuum dataset of the Band 6 Lupus disk Survey was used to test the dust sizes results between this and previous work (Ansdell et al. 2018).

4.3 Modeling

The methodology employed to measure the gas and dust sizes of the Lupus disk population is described in this Section.

4.3.1 CO modeling

The CO emission of each disk is primarily modeled by fitting the integrated line map to an elliptical Gaussian function in the image plane. For disks in which a Gaussian model does not conveniently describe the observed CO emission, the so-called Nuker profile model (e.g., Lauer et al. 1995; Tripathi et al. 2017) is used instead. We assess the quality of the Gaussian fit by comparing its radii results to those from high angular resolution and sensitivity observations, and by quantifying the residuals between observation and model. This is explained in detail in Section 4.3.1.

This modeling is appropriate for the CO disks characterization due to the low S/N for the bulk of the sample. The integrated map is obtained by summing up all the channels showing emission above noise level around the known position of the object; the range of channels are selected based on visual examination of channel map and spectrum. For the elliptical Gaussian modeling, the `imfit` task from CASA software (McMullin et al. 2007) was used. The task provides the parameter values with uncertainties of the Gaussian fit to the observed emission. The Nuker profile modeling is performed by fitting[1] the azimuthally averaged CO emission to this function, centered at the optimal position from the `imfit` results. The outer edge of the Nuker model is set as the radius in which the azimuthally average profile first reaches zero.

Size definition

The size definition used in this work is the radius enclosing a certain fraction of the total modeled flux, for the CO ($R_{\rm CO}$) and for the dust ($R_{\rm dust}$) components separately. This definition has been recently used to characterize large samples of disks from ALMA observations (e.g., Tazzari et al. 2017; Andrews et al. 2018b; Hendler et al. 2020), and for theoretical modeling of disks (e.g., Rosotti et al. 2019; Trapman et al. 2019, 2020). The fractions considered are the 68, 90 and 95% for easy comparison with previous works. To estimate the CO radii, we first obtain the deprojected model emission profile: from the deconvolved major-axis full-width-half-maximum (FWHM) of the elliptical Gaussian model, or built from the optimal values of the parameters in the Nuker fitting. We then produce the cumulative distribution functions ($f_{\rm cumul}$, following e.g., Eq. A.1 in Sanchis et al. 2020b). The radius (e.g., $R_{68\%}$) is inferred from the expression $f_{\rm cumul}(R_{68\%}) = 0.68 \cdot F_{\rm tot}$, where $F_{\rm tot}$ is the total integrated line emission of the model. For the elliptical Gaussian models, the $R_{68\%}$ can be obtained from the standard deviation (σ) of the Gaussian function:

$$R_{68\%} = \sigma \cdot \sqrt{-2 \cdot \ln(1 - 0.68)} \simeq 1.51 \cdot \sigma, \tag{4.1}$$

[1] using `scipy.optimize` Python module, `https://www.tutorialspoint.com/scipy/scipy_optimize.htm`

The uncertainty of the CO sizes are obtained from the major-axis FWHM error on the Gaussian fits. For the Nuker fitting of CO, the size uncertainties are acquired from a Monte Carlo procedure: 1000 realizations of the free parameters are drawn from a random normal distribution defined by the parameters' optimal values and their standard deviation; from these set of values we build 1000 Nuker models and measure their $R_{68\%}$, $R_{90\%}$, and $R_{95\%}$. Their associated standard deviation are taken as the size uncertainty of the Nuker models.

The method to infer CO sizes of the Lupus disk population differs from the approach in Ansdell et al. (2018). In that work, the CO size was estimated from the curve of growth of keplerian masked moment zero maps. The keplerian masking assumes a physical model in which gas kinematics are described by keplerian rotation. Their moment zero map is built from selected emission on each channel that is expected to come from the disk. We avoid this approach in order to keep our analysis as general as possible, without any assumptions on the disk physics. Additionally, sizes of fainter sources are difficult to measure using the curve of growth, since there is no clear end of the disk emission in the curve of growth. In Section 4.4.1 we compare our sizes to the results of Ansdell et al. (2018).

Lastly, we note that the sizes for 3 BD disks (SSTc2d J154518.5-342125, 2MASS J16085953-3856275 and Lup706) are obtained from the emission of a different line (^{12}CO $J = 3 - 2$). Differences in the measured radii between this line and the ^{12}CO $J = 2 - 1$ line are expected to be negligible, since the two lines are being emitted from essentially the same layer in the disk atmosphere, therefore with almost identical temperatures.

CO size uncertainties, from comparison to the DSHARP survey

The purpose of this Section is to assess the systematic errors of the CO modeling used, and to find a reliable criterion to determine in which cases the CO emission can be modeled to an elliptical Gaussian or to a Nuker profile model instead. To accomplish these goals, we compare the radii of six disks from our sample to the radii from additional ^{12}CO ($J = 2-1$) observations of the same objects at higher angular resolution and sensitivity (DSHARP project, details in Andrews et al. 2018a).

In order to perform this comparison, we need a reliable measurement of the CO disk sizes from the DSHARP data, which are treated as the fiducial sizes of these disks. This is accomplished by interferometric modeling of the ^{12}CO line visibilities: channels with line emission are continuum-subtracted and then spectrally integrated; the resulting visibilities are then modeled by a Nuker profile model. A comprehensive description of this modeling can be found in Appendix E. The resulting sizes are tabulated in Table F.1 of Appendix F, where we summarize the CO sizes using different methodology on the two datasets.

We compare the $R_{68\%}$ from the elliptical Gaussian modeling of the Lupus disk survey with the fiducial sizes from the interferometric modeling of the DSHARP data (Figure F.1, in Appendix E). For all the disks except one, the elliptical Gaussian modeling yields smaller sizes than the fiducial values. One disk (MY Lup) has nearly identical size results between the two datasets, a second disk (Sz 114) has a size deviation below 20%, two other objects (Sz 71 and Sz 129) have $\sim$ 30% difference between the inferred sizes, and the last two sources (Sz 82 and Sz 83) have a discrepancy above 40%. When inspecting the $R_{90\%}$ radii,

the discrepancies are slightly increased, with only three disks with a size deviation below 30%, and discrepancies beyond 40% for the remaining disks.

Several factors might contribute to the difference in the measured sizes. Firstly, the difference in sensitivity between observations can affect the detection of emission in the outermost regions of the disk. In addition, the different angular resolution may also have an impact: in general, the better resolved the disk, the better the size measurement. Another possible cause is the fact of modeling the Lupus disk population in the image plane, while the fiducial sizes are obtained from modeling in the *uv*-plane. Lastly, the size difference could be due to the elliptical Gaussian model not being able to reproduce the true CO emission. To understand the impact of these effects, we study them separately.

The sensitivity difference is tested by using the exact same method to model the two datasets, that is, fitting elliptical Gaussian models to the disk survey and to the DSHARP sets. The results are included in Table F.1 of Appendix F. The measured sizes between the two datasets are very similar, with only $\sim 5\%$ difference. Therefore, sensitivity has a minor effect on the inferred CO sizes of the Lupus disk dataset. The effect of the angular resolution can also be inspected from this comparison. The angular resolution has a stronger effect on smaller disks (i.e., of the order of the beam size). The two smallest disks (Sz 129 and MY Lup) show a slightly larger size difference of $\sim 15\%$ compared to the aforementioned difference of the sample. Although the sample considered is very limited, our results show that resolution effect might be relevant, especially in disks of size of the order of the beam size.

The effect of measuring the CO radial extent from modeling the emission in the image or in the *uv*-plane is investigated by modeling in the two planes the same dataset with the same empirical function (i.e., elliptical Gaussian). For each disk of the DSHARP dataset, we reconstruct the moment zero maps from the line visibilities; the `imfit` task is then used for the Gaussian modeling in the image plane. The interferometric modeling is analogous to the methodology described in Appendix E, but using a Gaussian function instead of the Nuker function. The size results are included in Table F.1. The difference in size is negligible for every disk, 2% on average, thus modeling the emission in the image plane has a negligible effect on the inferred size.

Lastly, we test the accuracy of the Gaussian modeling with respect to the Nuker profile modeling. We compare the interferometric modeling results when fitting the DSHARP data to a Gaussian or a Nuker profile. The results (Table F.1) show a size difference of $\sim 20\%$ on average. Two disks (MY Lup and Sz 129) have size differences below 5%; one disk (Sz 114) has a difference of $\lesssim 15\%$; another disk (GW Lup) has a difference around 30%, and the remaining two disks have differences beyond 40%.

Hence, the Gaussian modeling not reproducing the observed emission of certain objects is the most limiting effect on the CO size determination. It yields accurate CO sizes in several disks, but in other disks (typically those with extended emission) the inferred sizes can differ significantly with respect to the true CO extent. For those disks, the Nuker model is able to describe the extended emission of the disk accurately. In order to determine which CO disks can be described by an elliptical Gaussian model, we developed a criterion that evaluates the quality of the model, based on the amount of residuals (difference between

observed and modeled emission). This criterion is described in detail in Appendix G.

Based on this criterion, the CO emission is fitted to an elliptical Gaussian for those disk models with negligible residuals (i.e., when the quantified residuals are outside the $\mu \pm \sigma$ range of the entire population), otherwise the emission is fitted to a Nuker function.

In summary, our modeling in the image plane typically allows to measure the CO sizes for the Lupus disk sample with an uncertainty $\lesssim 30\%$, based on the comparison with available observations at higher resolution and sensitivity. Due to its simplicity and its ability to reproduce the observed CO emission, we use the elliptical Gaussian modeling for the cases in which the measured $R_{\rm CO}$ is reliable. For CO disks with Gaussian model residuals outside the valid range, the Nuker modeling in the image plane is used instead.

4.3.2 Dust modeling

The dust disks are modeled in the *uv*-plane to an empirical function, the Nuker profile. We refer to Sanchis et al. (2020b) for the detailed description of the interferometric modeling, in which the `Galario` package (Tazzari et al. 2018) was used in combination with a Monte Carlo Markov Chain procedure to model the continuum emission of the BD disks and sources from the Lupus disk completion survey. In the present work, we take the $R_{\rm dust}$ results of Sanchis et al. (2020b) for the 10 disks with detected ^{12}CO, and model the remaining disks of the Lupus population using identical methodology. The dust sizes considered are the radii enclosing the 68, 90, and 95% of the total disk emission, analogous to the size definition of the CO disk.

Performing the modeling in the *uv*-plane may reduce possible uncertainties associated to the image reconstruction process. Nevertheless, we tested the resulting dust sizes when modeling to a Nuker function in the image plane for a number of resolved disks. The results are in very good agreement with the dust sizes obtained from fitting the visibilities (deviation of $\sim$5%). Thus, modeling the continuum emission in the image or in the *uv*-plane does not have a significant impact in the size results. Only for very compact sources, the sizes obtained from the image plane modeling may be affected by the beam.

4.4 Disk size results

4.4.1 CO size results

The CO-disk size results of the Lupus disk population are presented in this Section. We exclude the results from disks with model peak below 3 times the rms of the observed moment zero map, those with maps partially covered by clouds, and disks that belong to binary systems with angular separation below $2''$. The resulting CO disk sizes ($R_{68\%}$) are summarized in Table 4.2. The uncertainties in the table are associated to the fitting method employed. Nevertheless, we warn that the inferred CO sizes may have a discrepancy of $0 \sim 30\%$ with respect to the true CO extent, based on our tests described in Section 4.3.1.

By definition of the Gaussian function, there is a constant relation between the $R_{68\%}$ and the two other radii ($R_{90\%}$, $R_{95\%}$):

$$R_{90\%} \simeq 1.42 \cdot R_{68\%}, \tag{4.2}$$

and

$$R_{95\%} \simeq 1.62 \cdot R_{68\%}, \tag{4.3}$$

The above relations can be used to obtain the $R_{90\%}$ and $R_{95\%}$ radii for the CO Gaussian models. For the disks modeled with the Nuker function, we provide the optimal parameters of the fit in Table H.1 of the Appendix H.

Out of 51 disks detected in CO, three are partially covered by clouds (J15450634-3417378, J15450887-3417333, J16011549-4152351), other three yield models whose S/N is too low (Sz 98, J16085324-3914401, J16095628-3859518), and three belong to close binary systems (Sz 68, Sz 74, Sz 123A). Thus our methodology allowed us to model the emission and size of 42. Three of these CO sizes are provided as upper limits (with tabulated value being the 95% confidence level), since the deconvolved FWHM of their elliptical Gaussian models exhibit a point-like nature. Additionally, two of these objects with CO size upper limits are disks around BDs. Table 4.2 includes a column stating the CO model used to infer the CO sizes (elliptical Gaussian model referred as 'G', Nuker model as 'N'). In Appendix I we include the observed, modeled, and residual CO maps, together with the line spectrum and the modeled intensity profile of every disk with measured CO size. Cloud absorption is seen on the line spectrum for a considerable number of sources. This reduces the integrated flux of the line. However, it should not have significant incidence in the measured CO radii (Ansdell et al. 2018).

Lastly, molecular outflows from ^{12}CO observations have been reported in at least 3 of the tabulated sources based on the dynamical analysis of the CO emission (EX Lup, V1192 Sco, Sz 83; Hales et al. 2018; Santamaría-Miranda et al. 2020; Huang et al. 2020). The outflows of the first two objects are within the reported CO sizes in Table 4.2. Our sizes are obtained by modeling the total integrated emission detected, thus a fraction of the modeled emission does not belong to the disk but to the molecular outflows. Therefore, we consider the inferred CO sizes of EX Lup and V1192 Sco as upper limits. On the other hand, Sz 83 shows a very intricate structure with spirals, jets, and clumps of emission (Herczeg et al. 2005; Ansdell et al. 2018; Andrews et al. 2018a; Huang et al. 2020). We discuss this disk in greater detail in Appendix J, together with other singular systems of the sample. Our CO size reported in Table 4.2 is larger than the keplerian disk size, the surrounding non-keplerian emission, and might contain a fraction of the emission from the spiral arms (Huang et al. 2020). For consistency, we use the CO size measured by our methodology, although we warn that the true value of the CO disk size might differ.

In the left panel of Figure 4.1, we compare our results to the 22 $R^{\rm CO}_{90\%}$ sizes from Ansdell et al. (2018), derived using the curve of growth method on keplerian masked CO maps. The $R^{\rm CO}_{90\%}$ is used for this comparison, since is the only reported size in Ansdell et al. (2018). Due to the different methodology between the two studies, the comparison between the two studies using $R^{\rm CO}_{68\%}$ and $R^{\rm CO}_{95\%}$ might differ from Figure 4.1 due to the difference in

Table 4.2: Results of the CO and dust sizes, following Sections 4.3.1 and 4.3.1. The tabulated distance of objects with uncertain parallax is the mean distance of the Lupus clouds (158.5 pc). Dust mass obtained assuming optically thin emission, with dust optical depth of $\kappa_{890\mu m} = 2$ cm^{2}g^{-1}, and average dust temperature of $T_{\rm dust} = 20$ K.

#	Object	Dist. [pc]	SpT	$T_{\rm eff}$ [K]	$M_\star$ [$M_\odot$]	Model CO	$M_{\rm dust}$ [$M_\oplus$]	$R_{68\%}^{\rm CO}$ [″]	$R_{68\%}^{\rm dust}$ [″]	$R_{90\%}^{\rm dust}$ [″]	$R_{95\%}^{\rm dust}$ [″]	$\frac{R_{68\%}^{\rm CO}}{R_{68\%}^{\rm dust}}$
1	EXLup	157.7	M0	3850	0.53	N	19.1	< 0.70	0.19 ± 0.01	0.23 ± 0.01	0.25 ± 0.01	< 3.7
2	Lup706	158.5	M7.5	2795	0.06	G	0.4	< 0.39	< 0.36	< 0.51	< 0.58	-
3	MYLup	156.6	K0	5100	1.09	G	76.5	0.81 ± 0.10	0.38 ± 0.01	0.51 ± 0.01	0.58 ± 0.02	2.1 ± 0.3
4	RXJ1556.1-3655	158.0	M1	3705	0.49	G	24.8	0.53 ± 0.05	0.19 ± 0.01	0.25 ± 0.01	0.28 ± 0.01	2.8 ± 0.3
5	RYLup	159.1	K2	4900	1.53	N	123.0	1.15 ± 0.10	0.61 ± 0.01	0.80 ± 0.01	0.93 ± 0.03	1.9 ± 0.2
6	Sz65	155.3	K7	4060	0.70	G	27.4	0.76 ± 0.09	0.16 ± 0.01	0.24 ± 0.01	0.28 ± 0.02	4.8 ± 0.6
7	Sz66	157.3	M3	3415	0.29	G	6.5	< 0.61	0.11 ± 0.02	0.16 ± 0.05	0.19 ± 0.08	< 5.7
8	Sz69	154.6	M4.5	3197	0.20	G	7.1	0.56 ± 0.08	< 0.09	< 0.20	< 0.31	> 5.9
9	Sz71	155.9	M1.5	3632	0.41	G	71.2	0.84 ± 0.12	0.45 ± 0.01	0.70 ± 0.01	0.83 ± 0.02	1.9 ± 0.3
10	Sz72	155.9	M2	3560	0.37	G	6.0	0.15 ± 0.05	0.08 ± 0.02	0.12 ± 0.05	0.14 ± 0.07	1.8 ± 0.7
11	Sz73	156.8	K7	4060	0.78	G	13.2	0.48 ± 0.06	0.27 ± 0.04	0.47 ± 0.08	0.55 ± 0.12	1.8 ± 0.3
12	Sz75	151.8	K6	4205	0.80	N	31.9	0.97 ± 0.11	0.12 ± 0.01	0.17 ± 0.01	0.19 ± 0.01	8.0 ± 0.9
13	Sz76	159.5	M4	3270	0.23	G	4.9	0.62 ± 0.06	0.26 ± 0.02	0.41 ± 0.05	0.47 ± 0.08	2.4 ± 0.3
14	Sz77	154.8	K7	4060	0.75	G	2.1	0.17 ± 0.08	< 0.36	< 0.75	< 0.88	> 0.5
15	Sz82	158.4	K5	4350	0.95	N	264.0	3.75 ± 0.67	1.15 ± 0.01	1.64 ± 0.01	1.82 ± 0.01	3.3 ± 0.6
16	Sz83 *	159.6	K7	4060	0.67	N	191.7	1.44 ± 0.13	0.29 ± 0.01	0.39 ± 0.01	0.46 ± 0.01	5.0 ± 0.4
17	Sz84	152.6	M5	3125	0.17	G	13.4	0.89 ± 0.12	0.24 ± 0.01	0.34 ± 0.03	0.40 ± 0.04	3.7 ± 0.5
18	Sz90	160.4	K7	4060	0.78	G	9.9	0.33 ± 0.10	0.12 ± 0.01	0.16 ± 0.03	0.19 ± 0.04	2.7 ± 0.8
19	Sz91	159.1	M1	3705	0.51	N	27.7	1.36 ± 0.10	0.61 ± 0.01	0.00 ± 0.01	0.00 ± 0.01	2.2 ± 0.2
20	Sz96	156.6	M1	3705	0.45	G	1.8	0.15 ± 0.07	< 0.14	< 0.28	< 0.37	> 1.0
21	Sz100	136.9	M5.5	3057	0.14	G	18.1	0.66 ± 0.12	0.26 ± 0.01	0.32 ± 0.01	0.35 ± 0.02	2.5 ± 0.5
22	Sz102	158.5	K2	4900	–	G	6.1	0.33 ± 0.02	0.13 ± 0.01	0.22 ± 0.02	0.27 ± 0.03	2.6 ± 0.2
23	Sz111	158.3	M1	3705	0.51	N	79.3	2.08 ± 0.39	0.44 ± 0.01	0.58 ± 0.01	0.69 ± 0.02	4.7 ± 0.9
24	Sz114	162.2	M4.8	3175	0.19	G	44.8	0.74 ± 0.15	0.25 ± 0.01	0.35 ± 0.01	0.39 ± 0.01	2.9 ± 0.6
25	Sz118	163.9	K5	4350	1.04	G	30.0	0.63 ± 0.14	0.37 ± 0.01	0.44 ± 0.02	0.48 ± 0.04	1.7 ± 0.4
26	Sz129	161.7	K7	4060	0.78	G	83.5	0.76 ± 0.16	0.30 ± 0.01	0.41 ± 0.01	0.46 ± 0.01	2.5 ± 0.5
27	Sz130	160.3	M2	3560	0.39	G	2.8	0.53 ± 0.12	< 0.32	< 0.69	< 0.83	> 1.6
28	Sz131	160.3	M3	3415	0.30	G	3.9	0.56 ± 0.15	0.08 ± 0.02	0.13 ± 0.05	0.16 ± 0.08	7.2 ± 2.8
29	Sz133	153.1	K5	4350	–	G	28.5	0.95 ± 0.11	0.46 ± 0.01	0.68 ± 0.04	0.80 ± 0.07	2.1 ± 0.2
30	J154518.5-342125	151.8	M6.5	2935	0.08	G	2.3	0.17 ± 0.06	0.05 ± 0.01	0.08 ± 0.01	0.09 ± 0.01	3.2 ± 1.2
31	J160002.4-422216	164.2	M4	3270	0.23	G	57.0	1.12 ± 0.13	0.51 ± 0.01	0.71 ± 0.02	0.83 ± 0.05	2.2 ± 0.3
32	J160703.9-391112	158.5	M4.5	3200	0.16	N	2.0	1.04 ± 0.09	0.43 ± 0.08	0.56 ± 0.27	0.65 ± 0.44	2.4 ± 0.5
33	J160830.7-382827	156.1	K2	4900	1.53	N	58.2	1.39 ± 0.13	0.56 ± 0.01	0.67 ± 0.01	0.75 ± 0.03	2.5 ± 0.2
34	J160901.4-392512	164.3	M4	3270	0.23	G	8.3	0.83 ± 0.08	0.47 ± 0.02	0.57 ± 0.04	0.62 ± 0.07	1.8 ± 0.2
35	J160927.0-383628	159.3	M4.5	3200	0.20	G	1.7	0.50 ± 0.09	< 0.36	< 0.67	< 0.80	> 1.4
36	J161029.6-392215	163.2	M4.5	3200	0.20	G	3.4	0.58 ± 0.11	0.23 ± 0.04	0.31 ± 0.12	0.36 ± 0.19	2.5 ± 0.6
37	J161243.8-381503	159.8	M1	3705	0.45	G	13.5	0.30 ± 0.11	0.10 ± 0.01	0.16 ± 0.03	0.19 ± 0.05	3.0 ± 1.1
38	V1094Sco	153.6	K6	4205	0.83	G	230.3	1.93 ± 0.15	1.31 ± 0.01	1.83 ± 0.01	1.96 ± 0.01	1.5 ± 0.1
39	V1192Sco	150.8	M4.5	3197	–	N	0.4	< 0.98	< 0.83	< 0.95	< 0.97	-
40	J16070854-3914075	175.8	M1.8	4000	–	G	50.2	1.36 ± 0.19	0.62 ± 0.01	0.90 ± 0.04	1.06 ± 0.07	2.2 ± 0.3
41	J16081497-3857145	158.5	M5.5	3060	0.10	G	3.7	0.42 ± 0.14	0.13 ± 0.02	0.18 ± 0.05	0.21 ± 0.06	3.2 ± 1.2
42	J16085953-3856275	150.2	M8.5	2600	0.02	G	0.2	< 0.17	< 0.12	< 0.17	< 0.19	-

Notes. * The modeled emission of Sz 83 based on our methodology includes the keplerian emission, non-keplerian extended emission, and part of the spiral structure as reported in Huang et al. (2020). Therefore, the true CO size of the Sz 83 disk might differ from the tabulated value.

methodology. However, the $R_{68\%}^{CO}$, which is the radius used in the discussion section of this paper (Section 4.5), will typically show lower discrepancies, since it is less affected by the low sensitivity on the outermost regions of the disks.

The CO sizes from the two methods are in good agreement for the majority of disks, only one object (Sz 82) has a difference in radius above 30%. This object is the largest CO disk of the Lupus population, this size divergence is likely due to the contrasting approach of the methods. The radius from Ansdell et al. (2018) is inferred from a moment zero map built from selected emission at each channel expected by keplerian rotation of the gas, while in this work there is no assumption on the velocity structure of the observed CO. The Sz 82 disk has an extremely large tail of emission (as seen in the integrated maps of the object, Figure I.4 of Appendix I) that was not captured in the modeling from Ansdell et al. (2018), and explains the large size difference between the two studies. This extended emission was already observed previously (Cleeves et al. 2016; Pinte et al. 2018a). In Appendix J we discuss in detail the Sz 82 disk, together with other singular objects of Lupus population.

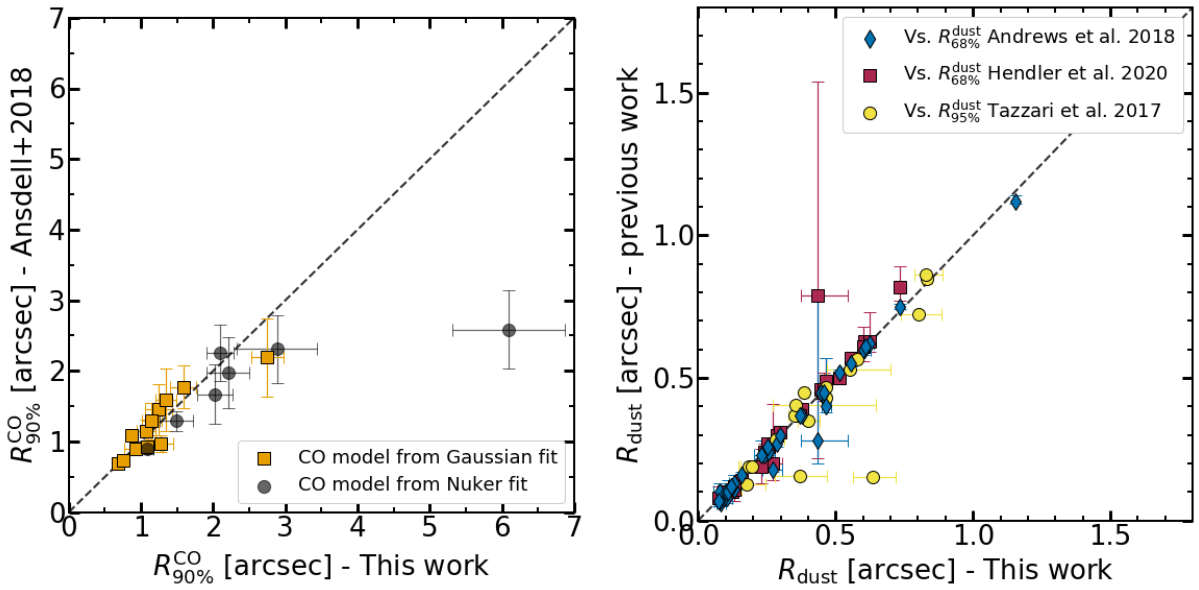

Figure 4.1: Comparison of CO and dust size with previous studies: comparison between the $R_{90\%}^{CO}$ sizes from Ansdell et al. (2018) and the sizes inferred in this work (*left panel*) by fitting an elliptical Gaussian model (orange) or a Nuker function in the azimuthally averaged integrated emission (black); comparison between the R_{dust} sizes from this work and the literature (*right panel*, i.e., Andrews et al. 2018b; Hendler et al. 2020; Tazzari et al. 2017).

4.4.2 Dust size results

The resulting radii from the dust modeling are summarized in Table 4.2, together with uncertainties. For disks in which the dust emission is not appropriately modeled, we

provide upper limits of the sizes, estimated as the 95th percentile of the corresponding size.

The protoplanetary disk sample of the Lupus region have been modeled in various studies (e.g., Tazzari et al. 2017; Andrews et al. 2018b; Hendler et al. 2020) based on the same ALMA Band 7 surveys. Our dust disk results can be directly compared to those from the literature (see right panel in Figure 4.1). In general, the $R_{68\%}^{\rm dust}$ results are in very good agreement with the results of Andrews et al. (2018b) and Hendler et al. (2020), the studies that characterized the dust sizes for a larger sample of Lupus disks. Only five disks have differences above 20% with respect to the $R_{68\%}^{\rm dust}$ from Andrews et al. (2018b). Three of those disks (Sz 66, Sz 72, Sz 131) are marginally resolved in continuum, sizes between the three studies vary between 0.08 to 0.11″. The remaining two are: SSTc2d J160703.9-391112, which has large uncertainties in the three studies, nevertheless, our results are compatible within error bars; and Sz 73, which $R_{68\%}^{\rm dust}$ from our modeling is in good agreement with Hendler et al. (2020). Lastly, when comparing our $R_{95\%}^{\rm dust}$ with the outer radii results for the sub-sample of disks studied in Tazzari et al. (2017), our results are in very good agreement, with only four objects with differences higher than 20%. In this case, the differences in radii might arise due to the modeling approach: instead of an empirical function, Tazzari et al. (2017) fitted the emission to a physical model, which can result in a different model emission profile. Besides, the $R_{95\%}^{\rm dust}$ used for the comparison is expected to have larger uncertainties than $R_{68\%}^{\rm dust}$, since it is more affected by the low signal of the outermost disk.

The dust sizes presented in this work are based on (sub-)mm continuum emission, which typically probes the population of large dust grains at the disk's mid-plane. These sizes are appropriate to constrain dust evolution of the disks. Observations in other wavelengths can be used as well to infer the size of the disks. For instance, scattered-light imaging in Near Infra-Red (NIR) wavelengths probes micron-sizes grains –dynamically more coupled to gas– at the upper atmospheric layers of the disk. Five disks in our sample have been recently observed with VLT/SPHERE (Avenhaus et al. 2018; Garufi et al. 2020). We can compare the extent of the disks in NIR observations to our size results, by taking the outermost radius at which the signal in NIR is detected and our $R_{95\%}$. The sizes from NIR observations are on average $\sim 40\%$ larger than our $R_{95\%}^{\rm dust}$, expected since the smaller grains are more dynamically bound to gas. The NIR sizes are, on the other hand, $\sim 50\%$ smaller than our $R_{95\%}^{\rm CO}$. This comparison is limited due to the very different nature of the observations, the differing definition of the size, and the narrow sample of disks imaged in NIR.

4.4.3 Gas/dust size ratio results

In this and following sections we focus our analysis and discussion on the radii enclosing 68% of the CO and dust fluxes ($R_{68\%}$) instead of $R_{90\%}$ or $R_{95\%}$. This is due to the moderate sensitivity of the observations, which could affect the detection of weak emission, typically in the outermost regions of the disk. This might have an impact in the outer slope of model emission when fitting to a Nuker profile. The $R_{68\%}$ radius is less affected than $R_{90\%}$ and $R_{95\%}$ by the outer slope of the model. Since our dataset is assembled by combining

various surveys with different resolution and sensitivity, we favor the use of the $R_{68\%}$ to reduce this possible effect. We also warn that in the following analysis and figures, the size uncertainties used are the ones derived from the respective method employed. However, CO sizes based on this dataset might have a discrepancy with respect to the true CO size between 0 and $\sim 30\%$, as explained in Section 4.3.1.

In Figure 4.2, we show the histograms and cumulative distributions of the radii ($R_{\rm CO}$ and $R_{\rm dust}$) of all the Lupus disks with measured CO and dust sizes. The radii are obtained for each disk following the methodology described in Section 4.3. A difference between the CO disk and the dust disk sizes becomes apparent from the figure. The Anderson–Darling test[2] yields a $< 0.001\%$ probability that the two radii histograms are drawn by the same parent distribution. There is a selection effect toward larger CO sizes, since it is more difficult to detect and measure CO sizes as small as the dust sizes. Nevertheless, the fraction of disks with measured $R_{\rm dust}$ and unknown $R_{\rm CO}$ is small (around 20% of disks with known $R_{\rm dust}$), thus this effect would not change the observed size difference. This disparity in sizes was already reported in Ansdell et al. (2018) for a smaller sample of the Lupus disk population, and in other SFRs, such as Taurus (Najita & Bergin 2018), and Orion (Boyden & Eisner 2020).

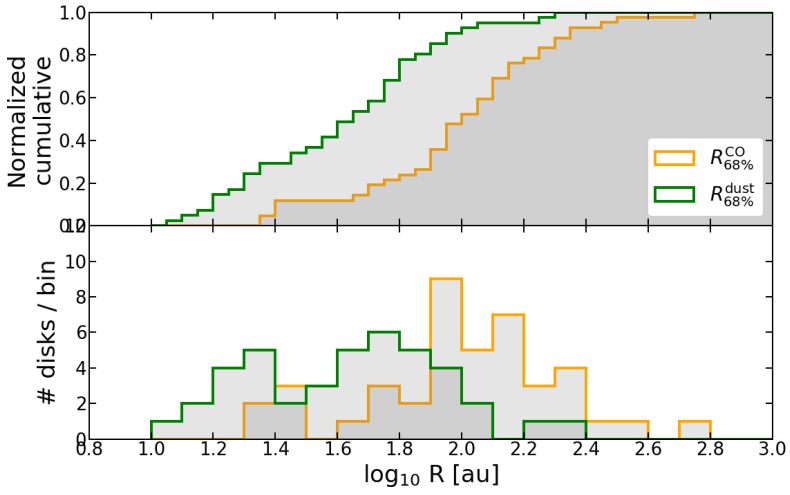

Figure 4.2: Histograms (*bottom*) and cumulative distributions (*top*) of the radii enclosing 68% of the total CO and dust continuum emission for the Lupus disks that have measurements of the two sizes. Upper limits of the $R_{\rm CO}$ and $R_{\rm dust}$ are included in the histograms, their value being the 95% confidence level.

In order to investigate the relative size of CO with respect to the dust continuum, we inspect the ratio between $R_{\rm CO}$ against $R_{\rm dust}$. In Figure 4.3, the radii enclosing 68% of the respective total fluxes are shown, with dashed lines representing the 1, 2, 3, and 4 ratios between CO and dust radii. The median of the $R_{68\%}^{\rm CO}$ / $R_{68\%}^{\rm dust}$ ratio is 2.5, excluding disks with an upper limit value in CO and/or dust size. The dispersion of this sample

[2]using `scipy.stats` Python module, `https://docs.scipy.org/doc/scipy/reference/stats.html`

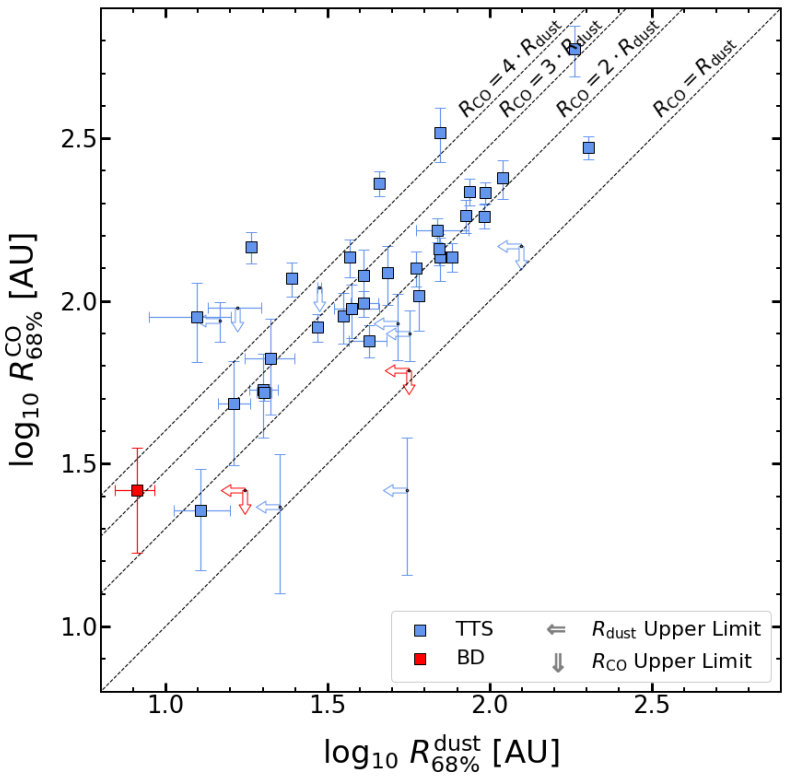

Figure 4.3: Comparison between the $R_{68\%}$ CO and dust emission for the entire disk population.

(considered as the standard deviation of the size ratio sample) is relatively high, of 1.5, raised by the few disks with very high size ratios. The median and dispersion of the size ratio when using the $R_{90\%}$ CO and dust radii are slightly larger, 2.7 and 1.5 respectively. In Appendix J, we describe in more detail disks from singular objects, namely, disks with very high size ratios (J.1 - J.6), the brightest object of the sample (Sz 82, J.7), and the results of disks around BDs and very-low mass stars (J.8). We also note that a few disks with measured sizes are orbiting a component of a binary or multiple system. We have only considered systems with relatively large angular separation between components (> 2 $''$). The impact of binarity and effects such as tidal truncation cannot be constrained based on our limited sample of disks that are part of a multiple system.

The measured size ratios might be even larger on compact objects: Trapman et al. (2019) showed that the measured size ratio is lower than the true value on disks with sizes similar to the beam size. On the other hand, the demographics analysis is affected by a lower completeness of fainter and non-detected CO disks. These disks would likely have small CO/dust size ratios. There is indeed a number of disks with measured $R_{\rm dust}$ but without $R_{\rm CO}$: these disks spread over the entire $M_\star$ range. Therefore, these disks with presumably low size ratio would appear along the full $M_\star$ range.

In the Lupus sample, most of the disks around more massive stars are detected in both

CO and dust and the sizes could be characterized. The completeness level at the low $M_\star$ range of the sample is lower, since disks around less massive objects are generally fainter in continuum and line emission. Therefore, we focus on the solar mass range sub-sample in order to reduce the possible biases due to a lower completeness. In the stellar mass range between 0.7 and 1.1 $M_\odot$, the total number of protoplanetary disks in the Lupus sample considered (Section 4.2) is 10. All of them are detected in ^{12}CO and dust continuum. One source (Sz 68) is excluded from the analysis since is a multiple system with angular separation below 2″. Another object (Sz 77) has an upper limit on the $R_{\rm dust}$. The remaining eight disks have measured radii in ^{12}CO and dust continuum. The size ratio median in this mass range remains 2.5, with a dispersion of 2. If the $R_{90\%}$ sizes are used instead, the median for this sub-sample is 2.6, with a dispersion of 2.2.

The median of the size ratios for the entire sample or the sub-sample considered are higher than the average value of 2 measured in Ansdell et al. (2018). The CO sizes in this work are in good agreement with the 22 measured disk sizes in Ansdell et al. (2018). A possible explanation of this difference is the larger sample of disks with measured sizes (42 disks in this work against 22). If we only consider the same sample of disks from Ansdell et al. (2018) with measured sizes, the size ratio median is again 2.5 (same median if the $R_{90\%}$ radii are used). Thus, the difference with respect the previous study is not due to a larger sample.

Another possible explanation is a difference in the measured dust size. Indeed, the $R_{90\%}^{\rm dust}$ in this work is $\sim 22\%$ shorter than the tabulated sizes in Ansdell et al. (2018). This, in combination with the uncertainty and scatter of the sample, accounts for the observed size ratio difference. This discrepancy in $R_{90\%}^{\rm dust}$ can be due to two main differences between the two studies. Firstly, this work makes use of continuum emission in ALMA Band 7 (~ 0.89 mm), while Ansdell et al. (2018) used the continuum emission in ALMA Band 6 (~ 1.33 mm). The datasets of the two bands differ also in spatial resolution and sensitivity (on average, Band 7 observations with beam size FWHM of 0.″32 and rms of $\sim$0.3 mJy, Band6 with 0.″23 and $\sim$ 0.1mJy). However, the size results in Ansdell et al. (2018) are mostly for bright and relatively large disks, thus sensitivity/resolution should not have a strong effect. The second difference is the method to infer the dust sizes; Nuker profile modeling by fitting the continuum visibilities (this work), and the curve of growth method in the image plane (previous work). In order to understand the origin of this dust size difference, we used the curve of growth method for the Band 6 and Band 7 continuum maps of the disks with measured $R_{90\%}^{\rm dust}$ in Ansdell et al. (2018). In both cases, the sizes match the results from the previous study. The curve of growth sizes from Band 7 are marginally larger than the Band 6 sizes ($\sim 6\%$), this is expected since disks observed in Band 7 are typically brighter, optically thicker, and probe slightly smaller grains (thus less affected by radial drift). These tests indicate that the cause of the size ratio difference between this work and Ansdell et al. (2018) is the method used to infer the dust size, rather than the different ALMA Band considered. The curve of growth method typically overestimates the dust extent. Therefore, we favor the use of our method, which also provides dust sizes that concur with other recent works (e.g., Tazzari et al. 2017; Andrews et al. 2018b; Hendler et al. 2020).

4.5 Discussion

In this section we discuss the physical implications of the CO and dust continuum sizes that we found for the entire Lupus disk population. Additionally, thanks to the significant number of disks with measured CO and dust sizes, we search for possible correlations between the measured size ratio of the sample and various stellar and disk properties.

4.5.1 Disk evolution: Gas size relative to dust size

The relative size between gas and dust is a fundamental property of protoplanetary disks, since it can be linked to evolutionary processes of the disk (e.g., Dutrey et al. 1998; Facchini et al. 2017; Trapman et al. 2019). If the disk has undergone dust evolution (understood as grain growth and subsequent radial drift), the dust emission at (sub-)mm wavelength may appear much more compact than the gas emission. Gas evolution, on the other hand, cannot be constrained based only on the relative gas/dust size: the main two mechanisms of angular momentum transport (viscous evolution, wind-driven accretion) generally cause the gaseous disk to either increase in size or remain similar, thus, the two mechanisms contribute to a large gas/dust size if dust evolution has occurred.

A second major effect that contributes to the observed size divergence between gas and dust is the optical depth. This effect is due to the larger optical depth of the ^{12}CO rotational line with respect to the continuum emission at (sub-)mm wavelengths. This causes the line emission to appear more extended than the optically thinner dust emission. Another way to understand the optical depth effect is by assuming a disk where gas and dust are equally distributed. If the dust emission is optically thin, the $R_{68\%}^{\rm dust}$ would trace the 68% of the total disk mass. But the $R_{68\%}$ of an optically thick line would trace a larger fraction of the total disk mass, since the line emission from the innermost region is hidden due to the optical thickness. Thus, the measured $R_{68\%}^{\rm CO}$ of the optically thick line would necessarily be larger than the $R_{68\%}^{\rm dust}$.

The presence of pressure bumps might also have an influence on the size ratio of a disk. If present, radial drift would stop at the location of the outermost bump, resulting in piled up dust, and likely a ring-like structure. Although very high sensitivity and resolution observations are needed in order to confirm the presence of bumps or rings, most of the Lupus disks targeted on the DSHARP project show rings or enhancements of dust emission (Huang et al. 2018). The existence of bumps might cause dust sizes to be larger, resulting in smaller size ratios. The existence of bumps does not necessarily produce small size ratios; it would ultimately depend on the location of the bump.

As a result, disentangling between dust evolution and optical effect is very difficult: while the optical depth is almost certainly present, the dust evolution does not necessarily occur. Trapman et al. (2019) studied in detail the possible contributions of these and other effects to the gas/dust size ratio based on a large grid of thermo-chemical models (Facchini et al. 2017), and concluded that a size ratio higher than 4 is a clear sign of dust evolution. For disks below this threshold, dust evolution could still have occurred, but specific modeling of each disk is required in order to confirm it. In their study, the same

radius definition as in the present work was used (a fraction of the total observable flux, not a physical radius), and their CO radii were obtained by measuring the flux extent of the same CO line (^{12}CO $J = 2 - 1$), with differences in the CO sizes below 10% when considering the ^{12}CO $J = 3 - 2$ line. Therefore, their findings can be directly applied to our size ratio measurements. The population's mean value of 2.5 that we obtain is far below the ratio threshold of 4 suggested by Trapman et al. (2019), thus radial drift cannot be confirmed as an ubiquitous process of the Lupus disk population. The threshold value of 4 might change slightly with a different setup of the thermo-chemical modeling. In Trapman et al. (2019), the threshold was obtained for a standard disk with a number of assumptions (most significantly, the gas structure being set by a self-similar solution of a viscous accreting disk, and a local gas-to-dust ratio of 100).

The fraction of disks with size ratios above the threshold value of 4 is ∼15% for the entire population (∼13% if we only consider disks whose size ratio uncertainties are strictly above 4). If we examine the 0.7-1.1 $M_{\odot}$ sub-sample, the fraction is marginally higher, 2 out of 9 objects (1 out of 9 if only objects in this mass range with size ratio uncertainties above 4 are considered). These fractions of disks above the threshold remain the same if the $R_{90\%}$ radii are used instead of $R_{68\%}$, for the entire disk population, and for the 0.7-1.1 $M_{\odot}$ sub-sample. Following Trapman et al. (2019) results, these disks with size ratio above the threshold can only be explained if dust evolution took place.

The sources that we identified as having with size ratio above the threshold of 4 are (ordered from higher to lower size ratio): Sz 75, Sz 131, Sz 69, Sz 83, Sz 65, and Sz 111. Although this sub-set of sources is small, the main stellar and disk properties cover relatively wide ranges, for instance, the stellar masses are distributed throughout 0.2 and 0.8 $M_{\odot}$.

In Appendix J, we describe in detail each of these systems with high size ratios. Sz 83, one of the most active sources of the Lupus clouds, might have a lower size ratio when considering the dynamical size based on keplerian motion (Huang et al. 2020). On the other hand, for Sz 69 we only provide a lower bound the size of the dust emission cannot be accurately determined. We did not find any properties or features that these disks might share: specifically, their accretion signatures are ordinary (Alcalá et al. 2017), and only one of them is a known transition disk (Sz 111 disk, van der Marel et al. 2018). Three of these disks belong to wide binary systems, at separations at which tidal truncation effects should not have any incidence.

In summary, ∼ 15-20% of the disk population in Lupus has a disk size ratio greater than 4. This result suggests that a considerable fraction of protoplanetary disks in Lupus have suffered radial drift and dust evolution, which is crucial to form the cores of planets.

4.5.2 Possible correlations between the size ratio and other stellar and disk properties

The large population of disks with characterized CO and dust sizes allows us to search for possible correlations between the CO/dust size ratio and the main stellar and disk

properties. We examined the relation between the size ratio and the stellar mass, the total disk mass, and the dust and CO sizes separately. Figure 4.4 shows the size ratio as a function of each of these properties. The stellar mass and its uncertainty are obtained as explained in Section 4.2, while for the CO and dust sizes and uncertainties, we use the results from the modeling described in Section 4.3 (sizes summarized in Table 4.2). The total disk mass is approximated from the dust disk mass, assuming a gas-to-dust ratio of 100. The dust disk mass is computed assuming that the emission is optically thin and in the Rayleigh-Jeans regime (Beckwith et al. 1990), with an average temperature on the dust mid-plane of 20 K (as in Pascucci et al. 2016; Ansdell et al. 2016, 2018; Sanchis et al. 2020b) and a dust optical depth of $\kappa_{890\mu m} = 2$ cm^{2}g^{-1} (as in Ricci et al. 2014; Testi et al. 2016; Sanchis et al. 2020b). The uncertainty considered for the $M_{\rm dust}$ is the 10% associated to the flux calibrator uncertainty of the ALMA observations. The inferred $M_{\rm dust}$ values of each disk are included in Table 4.2. While this is a big approximation for the disk mass, it is useful in order to have an overall understanding of the available disk mass.

For this examination we make use of the Spearman and Pearson correlation coefficients (similar to the analysis of dust properties' correlations conducted in Hendler et al. 2020). The Spearman test measures the monotonicity of the relationship between two sets of variables (its null hypothesis is that the two sets are monotonically uncorrelated), while the Pearson test evaluates the linear relationship between the two sets (its null hypothesis being that the two sets are linearly uncorrelated). The Pearson test assumes that the two variables are normally distributed. Therefore, we also test the normality of each disk property by performing the Shapiro-Wilk test (Shapiro & Wilk 1965), which null hypothesis is that the set of values is drawn from a normal distribution. The `scipy.stats` Python module[3] is used to perform the aforementioned tests. For each relationship, the tests are performed by excluding all objects with upper limits in the CO size or the dust size. If the p-value of a given test is below 0.05, the null hypothesis of the respective test is rejected.

The results of the tests are summarized in Table 4.3. The size ratio of the sample is not normally distributed since the null hypothesis of the Shapiro-Wilk test is rejected. Therefore we cannot test for linearity between the size ratio and the other properties. However, the Spearman test can be performed independently of the normality of the properties. The relation between the size ratio and the $R_{\rm dust}$ is the only one that rejects the null hypothesis of the Spearman test, that is, it is unlikely that the size ratio and the $R_{\rm dust}$ are monotonically uncorrelated. Additionally, the measured size ratio of compact disks (those with sizes of the order of the beam size) may be lower than the true value due to the beam size (Trapman et al. 2019). In such case, the anti-correlation with $R_{\rm dust}$ might be steeper than what is seen in Figure 4.4. However, this result should be taken with caution, since the Y-axis (the size ratio) is dependent on the X-axis ($R_{\rm dust}$ is the denominator in the size ratio), thus the anti-correlation found could be boosted by this dependence between the two axes. Besides, the test does not take into account uncertainties, which are large in the Y-axis. If the anti-correlation with $R_{\rm dust}$ is true, it would mean that compact dusty disks have higher size ratios than extended dusty disks. And, if we consider Trapman et al.

[3] `https://docs.scipy.org/doc/scipy/reference/stats.html`

Table 4.3: Results of the statistical tests searching for possible correlations between the size ratio and various stellar and disk properties ($M_\star$, $M_{\rm disk}$, $R_{\rm dust}$, and $R_{\rm CO}$). The p-value of each test is included in parenthesis. The first four rows summarize the tests' results when considering the entire population of disks with characterized CO and dust sizes (excluding upper limits); the last four rows show the results when excluding disks with size ratios above 4.

X-axis	Y-axis	Spearman test	Shapiro X-axis	Shapiro Y-axis	Pearson test
$\log_{10} M_\star$ [$M_\odot$]	$R_{\rm CO}/R_{\rm dust}$	Non-monotonic (0.33)	Normal (0.31)	Not normal (4e-5)	-
$\log_{10} M_{\rm disk}$ [$M_\odot$]	$R_{\rm CO}/R_{\rm dust}$	Non-monotonic (0.61)	Normal (0.60)	Not normal (9e-6)	-
$\log_{10} R_{\rm dust}$ [AU]	$R_{\rm CO}/R_{\rm dust}$	Monotonic (0.002)	Normal (0.91)	Not normal (9e-6)	-
$\log_{10} R_{\rm CO}$ [AU]	$R_{\rm CO}/R_{\rm dust}$	Non-monotonic (0.75)	Normal (0.70)	Not normal (9e-6)	-
$\log_{10} M_\star$ [$M_\odot$]	$R_{\rm CO}/R_{\rm dust}$	Non-monotonic (0.06)	Normal (0.36)	Normal (0.39)	Non-linear (0.07)
$\log_{10} M_{\rm disk}$ [$M_\odot$]	$R_{\rm CO}/R_{\rm dust}$	Non-monotonic (0.22)	Normal (0.81)	Normal (0.38)	Non-linear (0.22)
$\log_{10} R_{\rm dust}$ [AU]	$R_{\rm CO}/R_{\rm dust}$	Monotonic (0.008)	Normal (0.93)	Normal (0.38)	Linear (0.025)
$\log_{10} R_{\rm CO}$ [AU]	$R_{\rm CO}/R_{\rm dust}$	Non-monotonic (0.19)	Normal (0.71)	Normal (0.38)	Non-linear (0.53)

(2019) findings, radial drift and dust evolution might be more prominent in these compact dusty disks. The Spearman test found no monotonicity between the size ratio and $R_{\rm CO}$, thus the size ratio is more tightly affected by the dust size than the CO size. For the remaining properties (i.e., stellar and disk masses), no correlations are found.

The results plotted in Figure 4.4 show that disks with very large size ratios (e.g., above the threshold considered) appear along the full range of stellar masses, disk masses and CO sizes. These disks with exceptionally high size ratios may be in a different evolutionary stage compared to the bulk of the disk population. Therefore, we performed the correlation tests but excluding disks with size ratios above the considered threshold of 4. The results of the different tests are summarized in the bottom rows of Table 4.3. Based on the Shapiro test, the size ratio of this sub-sample is normally distributed, thus the Pearson test can be performed. In this sub-sample, the tests yield very low likelihood that the size ratio is uncorrelated with the dust size, analogous to the results for the entire sample. The tests do not confirm possible correlations with the remaining properties, although, the p-value of the Spearman and Pearson's test between the size ratio and the stellar mass are very low (0.06 and 0.07). This result might point towards a possible anti-correlation with $M_\star$; based on Trapman et al. (2019) results, this would tentatively suggest that dust evolution could be more efficient in disks around less massive stars. This is in line with theoretical and observational work that suggested that radial drift is more effective in disks around low-mass stars (Pinilla et al. 2013; Pascucci et al. 2016; Mulders et al. 2015). In order to confirm or refute a tentative anti-correlation with $M_\star$, it is necessary to significantly increase the sample of disks with measured gas and dust sizes.

The results of these statistical tests show a remarkable lack of strong correlations between the size ratio and the investigated properties. The sample of disks with measured size ratios is considerable, and it covers a very wide range of stellar masses, disk masses, dust and CO sizes. And yet, the vast majority of the disks have similar ratios, between

$\sim$ 2 and 4. This denotes that, aside from the small fraction of disks with exceptionally high size ratios, the bulk of the population behaves in a similar manner, independent of its stellar and disk properties. Extending the sample of disks with characterized gas and dust sizes is essential to confirm the results found. In particular, by expanding over other SFRs, the evolution of the size ratio over time can be investigated: this would help us to further constrain the ongoing and/or suffered physical processes and the evolutionary stage of the disks.

4.5.3 CO optical depth

Lastly, we have investigated the CO emission as a function of the CO size, and tried to constrain the temperature of the CO emitting layer. Figure 4.5 shows the modeled CO flux plotted against the CO size for the entire sample. First, we have performed statistical tests (as in Section 4.5.2) searching for possible correlations between the two properties. The Spearman test provides a very low p-value (of 3e-5, obtained by excluding CO size upper limits). Thus its null hypothesis is rejected, and the two properties are monotonically correlated. On the other hand, linearity could not be tested since the CO flux sample is not normally distributed (its p-value from the Shapiro test is < 0.05). The monotonic correlation found is expected due to the optically thick emission of the ^{12}CO lines.

Based on this result, it is also possible to examine the temperature of the CO emitting layer. In Figure 4.5, we have plotted an orange line representing optically thick emission with an average CO temperature ($T_{\rm CO}$) of 30 K. This line is composed by a grid of optically thick emission profiles with constant temperature. These profiles are constant with radius, thus described as $I_{\rm CO}(R) = B_\nu(T_{CO})$, with ν being the frequency of the ^{12}CO ($J = 2-1$) transition line, and $T_{\rm CO} = 30$ K. This $T_{\rm CO}$ is based on the results in Pinte et al. (2018a), where the emission profile of the same CO line (among dust continuum and other transition lines) was studied in detail for the IM Lup disk. The grid of profiles is assembled by taking increasing values of the outer disk edge, in order to cover the entire x-axis and populate the plot. For each profile, we computed the radius enclosing the 68% of the total intensity , and by plotting all the profiles we obtain the orange line.

In the figure, a disk with optically thick emission and an average $T_{\rm CO} = 30$ K would be intersected by this line. Around one third of the sample is crossed by this line when considering their uncertainties in radius. Considering only systems whose errorbars do not cross the line, four disks lay on the left side of the optically thick line: one disk (Sz 72) is among the faintest disks of the sample, and its size uncertainty is large. This source, together with other two objects on the left side (Sz 73, Sz 102) can be explained either by an underestimate of their CO size, by a higher CO temperature, or a combination of both. From the CO emission maps, these disks have a bright compact core of emission (thus, likely warmer than 30 K), and their outer disk emission is either faint or absent. This could happen if the outer emission is fainter than the sensitivity of the observations. For the last source on the left side of the line (EX Lup), the presence of a blueshifted molecular outflow (Hales et al. 2018) makes determination of the CO disk flux and size difficult, thus its exact position in the plot is uncertain.

On the other hand, a considerable fraction of the population appears on the right side of the optically thick line at 30 K (about half of the sample, only considering disks with errorbars not crossing the line). This can be explained by several factors. Firstly, cloud absorption, which can be seen in the line spectrum in a considerable number of disks (see Appendix I) can explain disks on the right side of the line. Absorption from clouds would decrease the total CO emission, while the measured radius would be mostly unaffected (Ansdell et al. 2018). Another possible explanation is that the average CO temperature of some of these disks could be below 30 K, this would be expected in very extended sources, since the regions further from the star are generally colder. Besides, the inclination of the disks might also have an effect. The optically thick line plotted assumes a face-on orientation: if inclined, the emission would appear fainter (the optically thick lines would shift downwards). Nevertheless, the CO fluxes of the Lupus disks shown in Figure 4.5 are corrected accounting for the disk inclination, thus this effect should be minor. Lastly, partially optically thick CO emission in the outer disk can cause the emission to be fainter, thus appearing below the optically thick line.

A second line representing optically thick emission at the typical freeze-out temperature of CO ($T_{\rm CO} = 20$ K) is included in the figure. Eight disks appear on the right side of the 20 K line, taking errorbars into account. These disks are likely explained by a combination of the aforementioned effects that shift the position of the disk to the right side of the line. However, it might be possible that the CO in some regions of these disks is indeed at temperatures lower than the freeze-out temperature, which could be explained by vertical mixing, as suggested in Piétu et al. (2007).

For the case of the three BDs in the sample, their radii are obtained from a different CO transition (^{12}CO 3–2). The optically thick lines of the transition used for the BDs would appear slightly above the drawn lines of Figure 4.5. The only BD with measured size lays within errorbars on the 30 K line.

In conclusion, a monotonic correlation between the CO size and flux is found, as expected from optically thick emission. Our results for the temperature of the CO emitting layer are consistent with a temperature of around 30K as previous studies suggested, albeit a fraction of the sample might have slightly lower average temperatures. However, the exact determination of $T_{\rm CO}$ for the sample or for individual sources is difficult due to the size uncertainties, cloud absorption and other factors that limit this analysis.

4.6 Conclusions

We have investigated the relative extent of gas and dust in a large sample of protoplanetary disks of the Lupus clouds, in order to constrain the evolutionary stage of the disk population. We have assembled the largest sample of protoplanetary disks of the region with characterized CO and dust sizes based on ALMA observations. To infer the gas disk sizes, we have modeled the integrated emission maps of the ^{12}CO ($J = 2-1$) transition line from ALMA Band 6 observations using an elliptical Gaussian function, or a Nuker profile for models with considerable residuals. For the dust modeling, the continuum emission

of large grains (at ∼0.89 mm wavelength) is modeled in the *uv*-plane to a Nuker profile. The radii enclosing 68%, 90%, 95% of the respective total flux, are estimated from the CO and dust models. The CO/dust size ratio ($R_{\rm CO}/R_{\rm dust}$) is then used to investigate the evolutionary stage of the disk population: prominent dust evolution (i.e., grain growth and radial drift) typically produces compact dust emission at these wavelengths, thus high size ratios; gas evolution, on the other hand, cannot be constrained based only on this size ratio.

The median value of the size ratio is 2.5 for the entire population and for a sub-sample with high completeness. 15% of the population show a size ratio above 4 (20% when considering a sub-sample with high completeness), based on thermo-chemical modeling (Facchini et al. 2017; Trapman et al. 2019), such high values can only be explained if grain growth and subsequent radial drift has occurred. These disks with very high size ratios do not show unusual characteristics, and their stellar and disk properties cover wide ranges of the entire population. For the rest of the population, dust evolution cannot be ruled out, but individual thermo-chemical modeling is necessary.

We have searched for possible correlations of the population' size ratio with other stellar and disk properties. Only a tentative monotonic anti-correlation with $R_{\rm dust}$ is suggested by the null hypothesis tests performed. The absence of strong correlations is very significant, the studied sample covers a wide range of stellar and disk properties, and the vast majority of the population has a very similar size ratio (between $\sim$ 2 and 4). This suggests that a large fraction of protoplanetary disks in Lupus behave similarly and may be in a similar evolutionary stage. These results are limited by the optical depth difference between continuum and ^{12}CO ($J = 2 - 1$) line, which can affect each disk's measured size ratio differently, thus hiding their true behavior. Additionally, extending this analysis to the disk population in other SFRs is pivotal to learn about the temporal evolution and the evolutionary stages of protoplanetary disks. Finally, a monotonic correlation between the CO disk flux and size is found. The CO temperature for most of the disks, although difficult to determine accurately, is consistent with previous studies that suggest an average temperature of around 30 K.

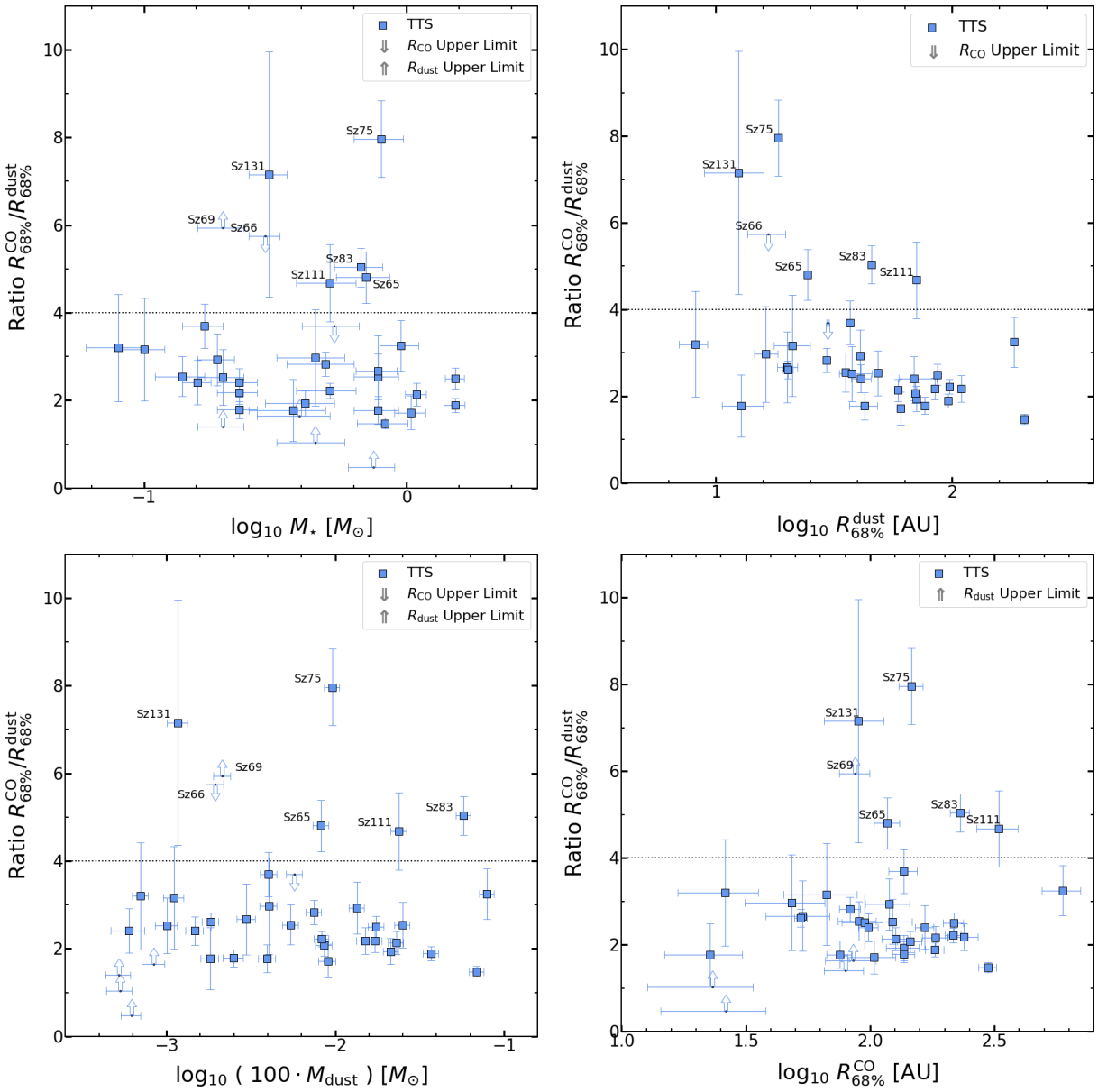

Figure 4.4: Ratio between CO and dust sizes as a function of various stellar and disk properties: as a function of the stellar mass of the central object $M_\star$ (*top left*); as a function of the dust size $R^{\rm dust}_{68\%}$ (*top right*); as a function of the disk mass (*bottom left*), estimated from $M_{\rm dust}$ and assuming a gas-to-dust ratio of 100; as a function of the CO size $R^{\rm CO}_{68\%}$ (*bottom right*). Disks with a size ratio above the horizontal threshold cannot be explained without prominent dust evolution, based on disk evolution models of Trapman et al. (2019).

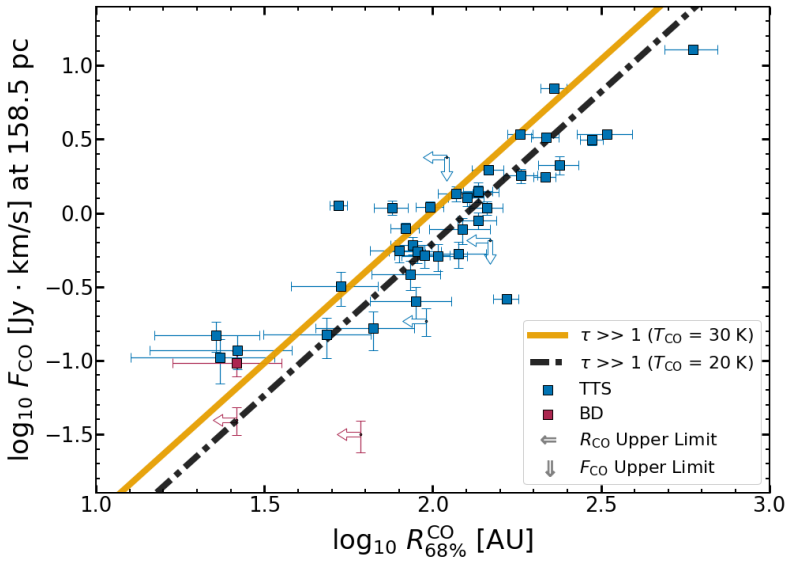

Figure 4.5: Relation between the radius enclosing 68% of the total CO flux (scaled at the median distance of the region, and deprojected with inclination) and the flux enclosed by that radius for the entire Lupus CO disk population. Lines represent optically thick emission of CO with an average temperature of 30 K (orange), and of 20 K (black dash-dotted). Objects with outflows within the measured radius are considered to be upper limits in $F_{\rm CO}$.

Chapter 5

Search for protoplanets

Physical processes such as grain growth and radial drift are critical, not only to understand the evolution of the disk, but also for the formation of the rocky cores of planets. The formation of planets occur before the disk disperses, and there are compelling indications (e.g., mass budget problem, dust evolution in disks, see Chapters 3 and 4) that planet formation might occur in an early phase of the disk lifetime. In this chapter I focus on protoplanetary disks with already formed planets inside. The aim is to address the feasibility of detecting such planets using direct imaging observations.

Finding recently formed planets embedded in disks is of great importance to better understand the planet-disk interaction, which imposes strong effects on both planet and disk. The study of these systems have crucial implications on planet formation, the evolution and the dispersal of the disk.

Direct detection is the only method that unambiguously confirms the presence of a planet, and, besides, it allows for an extensive characterization of the planet. In last years, there has been a vast effort from the community to directly detect young planets embedded in disks. The search is carried out in IR wavelengths, where the peak emission of the planet typically is. Young planets are brighter and, therefore, should be easier to detect in principle. However, the search has turned out to be very difficult. The main limitation when searching for protoplanets embedded in disks, besides the high sensitivity required, is that disk material might partially (or completely) hide the planet. Nevertheless, the recent discovery of two planetary companions within the transition disk of PDS 70 (Keppler et al. 2018; Haffert et al. 2019) serves as an inspiring case to persist on the search of more protoplanets using direct detection methods.

In this chapter, I first discuss the high contrast imaging methods that are used to find protoplanets embedded in disks (Sections 5.1). I then expand on a detactibility model that assesses whether planets within disks can be observable when accounting for the extinction due to the surrounding disk material (Section 5.2). The initial modeling was conducted as part of my Master Thesis, which had a number of open questions and unanswered lines of investigation that I address in this chapter.

5.1 High contrast imaging

Searching for planets from direct imaging requires of very high sensitivity telescopes (typically in the IR) that can detect emission much fainter than the radiation from the central star. One of the main obstacles to detect planetary companions is to distinguish between the planet emission and stellar emission. The later produces artifacts in the image due to scattering with the telescope's aperture, the Earth's atmosphere and other imperfections. In young systems with disks, stellar radiation scattered by small dust grains at the disk atmospheric layers is also detected in these observations. In fact, scattered light observations provide insightful information on the disk structure. Furthermore, the direct detection of protoplanets might be severely limited by extinction due to the presence of disk material along the line-of-sight, which can hide the young planet, even in evolved disks with low surface densities.

A number of techniques – such as coronagraphs, adaptive optics, angular differential imaging (ADI), or polarimetric differential imaging (PDI) – have been developed in order to attenuate the artifacts caused by the stellar radiation, and to boost the faint emission of possible companions.

Coronagraphs are used to mask incoming light from the central star, reducing the diffraction pattern due to the aperture of the telescope caused by the stellar light (Fischer et al. 2014). In a perfect optical system with a circular aperture, the point spread function (PSF) is the Airy pattern; real telescopes have more complicated diffraction patterns. There is a very wide range of coronagraph designs with varying performance and efficiency (Guyon et al. 2006). On the other hand, turbulence of the Earth's atmosphere causes distortions of the incoming wavefront, and, together with imperfections on the mirrors and cameras, generates artifacts on the PSF. These artifacts can be partially corrected by using adaptive optics, which are deformable mirrors that can be adjusted accordingly to compensate for the wavefront distortions.

These atmospheric or instrumental artifacts, generally referred as speckles, can be further minimized with other techniques such as ADI and PDI. The former aims at removing the speckles by convenient subtraction of the PSF pattern, while the later is based on separating non-polarized from polarized light. I will now describe both ADI and PDI observations in more detail.

5.1.1 ADI and PDI techniques

ADI is a PSF calibration technique that highly reduces the PSF quasistatic structure, by keeping the instrument and the telescope optics aligned. A number of images are obtained while keeping this alignment, wherein the PSF structure remains stationary but the field of view rotates. This allows to obtain a reference PSF that is then subtracted from every image. Companions, if present in the field of view, would appear in the PSF-subtracted images (Marois et al. 2004, 2006).

ADI can be used in combination with Spectral Differential Imaging (SDI, Smith 1987; Racine et al. 1999; Sparks & Ford 2002), which consists in obtaining simultaneous images

at contiguous wavelengths where the spectra of star and planet differs significantly (e.g. particular spectral features as the methane absorption band head at $1.6\mu m$, Rosenthal et al. 1996). Observations using the ADI technique, and a combination of ADI and SDI (see Figure 5.1) allowed to detect the first planetary companion of PDS 70 as a point source (Keppler et al. 2018).

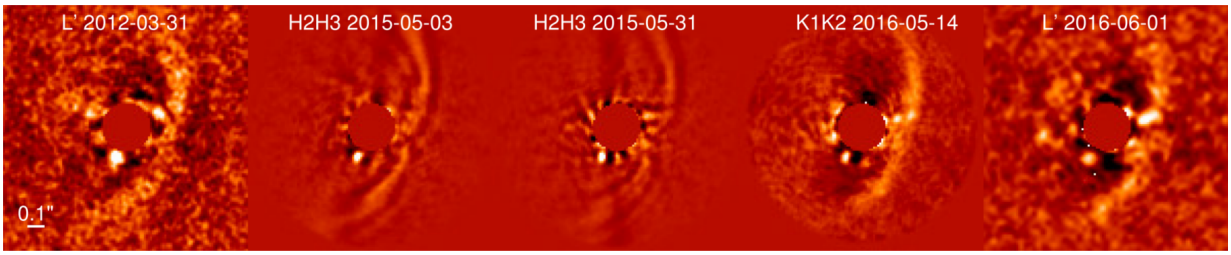

Figure 5.1: Observations of PDS 70 that detected the planetary companion as the point source at the south-east with respect to the central star. In every image, north is up and east is to the left. The images were obtained with: the NICI instrument in the Gemini Observatory in ADI mode (*left image*), VLT/SPHERE in ADI+SDI modes (*three central images*, different bands and observation dates), and VLT/NaCo in ADI mode (*right image*). From Keppler et al. (2018).

The PDI technique is based on the fact that the light radiated by the star is mostly unpolarized, but becomes polarized when is scattered by dust grains (Kuhn et al. 2001). PDI consists of acquiring two simultaneous images that are orthogonally polarized; the non-polarized light, which corresponds to stellar radiation and the speckle structure, is subtracted and only polarized light remains (Apai et al. 2004a). This technique is particularly useful to study protoplanetary disks, since the stellar light scattered by small dust grains in the atmospheric layers of the disk is polarized, thus it is left over after the subtraction of the non-polarized emission. These observations provide valuable information on the disk's vertical structure. PDI can be also used to search for point sources that might be produced by planetary companions.

5.1.2 Present and future observations

There has been substantial effort from the planet formation community aimed at searching for young planets in protoplanetary disks. State-of-the-art instruments, such as the Spectro-Polarimetric High-contrast Exoplanet REsearch (SPHERE) at the VLT or the Gemini Planet Imager (GPI) in the Gemini Observatory, are not only well suited, but have been specifically designed to directly detect planets. Modern instruments typically allow to use several of the aforementioned techniques to reduce stellar emission and boost faint emission of potential planet companions. For instance, VLT/SPHERE includes an adaptive optics system that can be combined with the use of coronagraphs, and allow for ADI or PDI observations in IR wavelengths (from 0.95 to $1.65\mu m$).

Recent efforts searching for planets embedded in disks have targeted nearby and well-known systems such as HL Tau (Testi et al. 2015), TW Hya (Ruane et al. 2017), or HD 163296 (Guidi et al. 2018). Protoplanetary disks with confirmed gaps in their brightness distribution are potentially very good targets to search for protoplanets, since gaps are often explained by orbiting planets that cleared their surrounding disk material. Other observation programs have targeted large samples of systems to search for planetary companions in young nearby stars and to study the structure of protoplanetary disks. Notable surveys conducted with the VLT/SPHERE are the SPHERE High-contrast ImagiNg survey for Exoplanets (SHINE, Chauvin et al. 2017), which has targeted hundreds of stars to characterize known exoplanets and also find new companions, and Disks ARound T Tauri Stars with SPHERE (DARTTS-S, Avenhaus et al. 2018; Garufi et al. 2020), which has performed PDI observations in a number of bright disks to better constrain their vertical structure and the presence of sub-structural features.

In observations searching for planetary companions, it is particularly useful to study the contrast magnitude, which is the relative brightness with respect to the parent star. Contrast curves are often used in these studies, providing information of the sensitivity limit of the instrument used typically as a function of the angular separation with the central star. In Figure 5.2, examples of the contrast curves from observations of HD 163296 (Guidi et al. 2018), and from the SHINE survey (Langlois 2018) are shown. If companions are found in these observations, the contrast magnitude can be used in combination with planetary models to infer the expected mass of the companion. In addition, contrast curves provide upper limits of the planet mass in observations targeting systems with known companions or confirmed gaps but undetected planet emission.

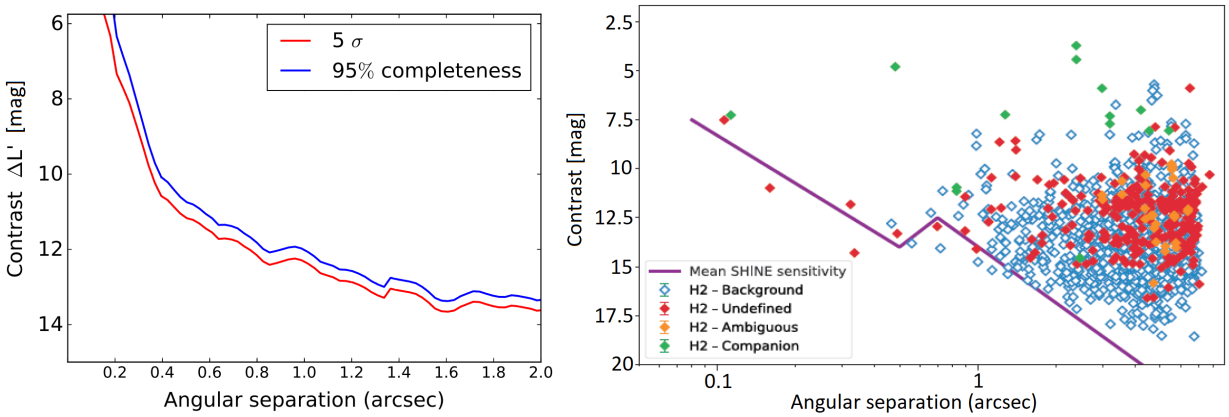

Figure 5.2: Contrast curve (*left panel*) showing the sensitivity limit (red line represents the 5σ level, blue line the 95% completeness) reached targeting HD 163296 with the NIRC2 instrument in the Keck observatory (adapted from Guidi et al. 2018). Contrast curve (*right panel*) of the SHINE survey, showing the mean detection limit and the contrast and angular separation of point sources detected for the observed sample (adapted from Langlois 2018).

These observations illustrate the arduous work that is necessary in order to detect planets that are still embedded in disks. However, the detection of the two planetary

companions in PDS 70 shows that it is indeed feasible to find such protoplanets. Future instrumentation with improved sensitivity and resolution will largely facilitate the task, and will hopefully provide many new detections that would push the field of planet formation to new grounds. In this respect, many hopes are deposited in the James Webb Space Telescope (JWST), which will not only help finding new planets, but greatly contribute in their characterization (e.g., Krist et al. 2007; Greene et al. 2016).

5.2 Detectability of planets embedded in protoplanetary disks

In this section I expand a detectability model that predicts expected magnitudes of planets embedded in disks. The initial study was conducted for my Master Thesis, titled:

> *" Observability of protoplanets embedded in discs using hydrodynamic simulations ",*

with the translated German title:

> *" Beobachtbarkeit der Protoplaneten in zirkumstellare Scheiben über hydrodynamische Simulationen ",*

as part of the Master of Science program in Astrophysics of the Ludwig–Maximilians–Universität. The examination of the Master Thesis took place on September 13th, 2017, with Prof. Dr. Barbara Ercolano as first examiner.

The initial study conducted in my Master Thesis aimed at developing a detectability model of protoplanets embedded in disks, by investigating the planet-disk interaction and estimating the IR extinction due to surrounding disk material.

3D hydrodynamical (HD) simulations with a high-resolution nested grid allowed me to accurately study the planet-disk interaction; three different cases with varying planet masses (1, 2, and $5 M_J$) were considered by performing three independent simulations. Once the planet opened a gap and reached a stationary state, I measured the column density on the planet's line-of-sight. From the column densities, the extinction coefficients in IR wavelengths were estimated by applying analytic extinction curves in the ISM from Cardelli et al. (1989). The total planet flux was assumed as a combination of intrinsic flux, based on early evolutionary models of giant planets (Spiegel & Burrows 2012), and accretion flux, measured from the mass accretion rate onto the planet computed in the simulations (following prescription of Kley 1999; Dürmann & Kley 2015). The expected magnitude of the planets in IR wavelengths could be estimated by applying the measured extinction to the total planet flux. The results from HD simulations can be scaled to

different orbital distances, stellar mass, and surface density at the planet location. This allowed me to apply the detectability model to two real systems, CQ Tau and TW Hya.

This initial study provided important results in order to constrain the detectability in IR of planets embedded in disks. The most massive planet studied ($M_{\rm pl} = 5M_J$) would be detectable in the considered cases, since it clears the surrounding disk very efficiently. On the other hand, the less massive planets ($M_{\rm pl} = 1,\ 2M_J$) would be completely hidden at short wavelengths, but might be observable in favorable conditions at longer wavelengths, due to the assumed extinction curve.

However, crucial aspects that have a large impact on the results were not investigated. First of all, the resolution of the grid in the simulations can have a large effect on the resulting column densities and expected planet magnitudes, especially due to the impact on the potential smoothing and the density stratification near the planet location. The reliability of the HD simulations, particularly the planet-disk interaction and the opening of the gap, is crucial in order to provide a solid detectability model. Furthermore, the prescription of the extinction curve did not account for the known ISM silicate feature around $10\mu m$, and the resulting extinction turned out to be largely underestimated in long wavelengths. Even more important for the results of the model is the composition of the disk, which was not varied in the initial study: the dust composition largely affects the expected opacities, and, consequently, the extinction coefficients. Finally, the model was applied only to two systems to predict planet magnitudes in only one IR band (L-band). The applicability of the model could be largely extended by studying more systems and in additional IR bands. The detectability model can be also used to constrain the planet mass in systems with known planets like PDS 70, and to provide upper limits of unseen planets in systems with confirmed gaps.

As part of my Ph.D., I have addressed the main open questions of the Master Thesis, greatly expanding on crucial aspects of the initial study. The expansion to the initial work provides a much more robust foundation and analysis of the detectability model of protoplanets embedded in disks. Consequently, the largely improved model offers a strong tool to guide future direct imaging observations searching for young planets in protoplanetary disks.

In what follows, I describe the new work conducted during my Ph.D.

The remaining content of this section has been published in:

> *" Detectability of embedded protoplanets from hydrodynamical simulations "*
> **Sanchis, E.**, Picogna, G., Ercolano, E., Testi, L., Rosotti, G., 2020, MNRAS, 492, 3440.

5.2.1 Effects of resolution on the disk-planet interaction

In this section, we investigate the impact that the resolution of the 3D grid has on the column density. For this aim, we have performed new simulations with double resolution

Table 5.1: Set-up parameters of the new simulations, together with the respective column mass densities σ inferred for each simulation. The disk aspect ratio H, defined as $H = h/R$ was set to 0.05 in the simulations. The columns refer to: the α-viscosity parameter for a viscously evolving disk; cell size at planet vicinity, given in Hill radii ($R_{\rm Hill}$) and in planet radii ($R_{\rm pl}$); potential smoothing radius ($d_{\rm rsm}$); accretion radius ($r_{\rm sink}$); and predicted column mass densities. σ is obtained by integrating the density over every cell above the planet except the cells within the $d_{\rm rsm}$. The uncertainty is computed from the dispersion of the σ value in the last 10 orbits. Planet radii are taken from the evolutionary models of giant planets of Spiegel & Burrows (2012).

Run	α	Cell size [$R_{\rm Hill}$]	Cell size [$R_{\rm pl}$]	$d_{\rm rsm}$ [$R_{\rm Hill}$]	$r_{\rm sink}$ [$R_{\rm Hill}$]	σ [g $\cdot$ cm^{-2}]
$1M_{\rm J}$	0.003	0.01	3.7	0.03	0.03	2.7 ± 1.2
$5M_{\rm J}$	0.003	0.01	5.9	0.04-0.05	0.03	0.01 ± 0.01

compared to the original simulations. The impact of the resolution is of high importance in the planet-disk interaction, and specially in the cells closest to the planet, due to the potential smoothing and the prescription used for the accretion onto the planet.

The planet and its atmosphere were not resolved in the original simulations, therefore the first cell is assumed to be the planet outer radius. The vertical density profile shows a sharp peak extending over the cells closest to the planet. This is expected to be a combination of several effects, mainly an artifact of the simulations due to the potential smoothing, which affects every cell within the potential smoothing radius ($d_{\rm rsm}$). However, the possibility that a fraction of the peak might also be the real density stratification of the material at the layers closest to the planet cannot be excluded. Additionally, this over-density is also altered by the accretion radius ($r_{\rm sink}$), and limited by the grid resolution. A fully resolved planet would be necessary to disentangle between the different causes. We have tested whether the extension of the peak is an artifact due to the potential softening and the mentioned resolution limitations. To this aim we have performed 2 additional simulations with doubled resolution over the entire grid. We also decreased both accretion and smoothing radii to 0.03-0.05 $R_{\rm Hill}$. The values of the main parameters for the doubled resolution runs are summarized in Table 5.1.

This test was done for the disks with 1 and 5 $M_{\rm J}$ planets. The grid from the last snapshot of the original simulations were readjusted to the new resolution, and the system is let to evolve until a new steady-state is reached ($\leq$ 15 orbits needed in both cases). The vertical density at the closest cells above the planet for both original and doubled resolution for the 1 $M_{\rm J}$ case are shown in Figure 5.3. The vertical grid-lines represent 0.01 $R_{\rm Hill}$, and the colored lines illustrate the $d_{\rm rsm}$ in both original and doubled resolution runs. The figure shows that the over-density with doubled resolution spans approximately half the original case. This is in accordance with what is expected if the over-density is due to the smoothing within $d_{\rm rsm}$. If one was able to completely remove the potential smoothing

one would only see a peak inside the planet radius, i.e. within the first cell.

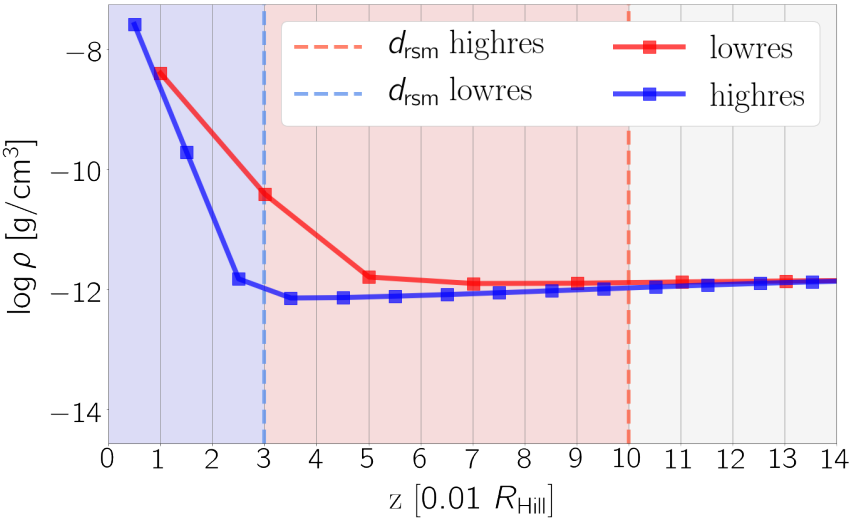

Figure 5.3: Vertical density profile close to the 1 M_{J} planet, comparing the doubled resolution (blue line) to the original case (red). The vertical grid spacing is 0.01 R_{Hill}, equivalent to the cell-size for the doubled resolution run, and half the cell-size of the original run. The red and blue dashed lines represent the smoothing radii for the original and the new run respectively.

From the results of this test, the column mass density σ is considered as the integrated density for all the cells above the smoothing radius. The resulting σ for each of the simulated systems are included in Table 5.1. The uncertainty considered is the dispersion of the column mass density for the last 10 orbits of each simulation. The predicted magnitudes for 1 and 5 M_J planets are derived using the σ values from the doubled resolution runs, since in these cases the planet-disk interaction is represented more accurately. The values for the original and doubled resolution cases are within their respective uncertainty: for a 1 M_J, σ is 2.8 ± 0.9 and 2.7 ± 1.2 g $\cdot$ cm^{-2}, while for the 5 M_J runs the column mass densities were 0.011 ± 0.007 and 0.01 ± 0.01 g $\cdot$ cm^{-2} respectively.

5.2.2 Gap opening analysis

Planets massive enough (typically Jupiter-like planets) can clear their surrounding disk material in only a few orbits (Bryden et al. 1999). The more massive the planet is, the faster the gap carving process is, while less massive planets require of more orbits to clear the material due to its lower potential.

The gap opened by each planet can be compared to disk models to verify the quality of the simulations. We have tested the resulting surface density profiles with an analytical model for gaps in protoplanetary disks, as described in Duffell (2015). An algebraic solution of the gap profiles is presented in that work, together with the derivation of a formula for

the gap depth. The azimuthally averaged surface density radial profiles relative to the unperturbed surface density (Σ_0) for the 1, 2 and 5 M_J simulated planets in a viscous disk are shown in Figure 5.4. The solid lines represent the profiles after a steady-state is reached, and the dashed lines denote the surface density after the first 20 orbits. The predicted gap depths from the model (Duffell 2015, equation 9) are shown in the figure as horizontal dash-dot lines.

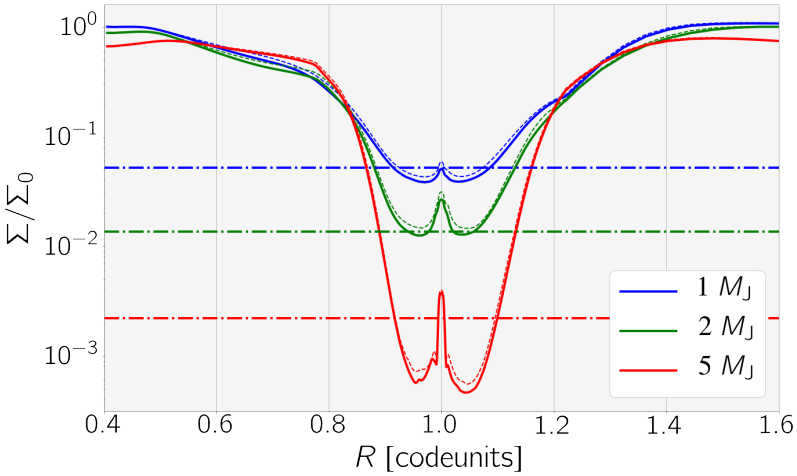

Figure 5.4: Surface density radial profile for 1, 2 and 5 M_J planets after the simulations reach a steady-state, shown as solid lines. The dash-dot lines are the respective predicted gap-depths, derived from an analytical model for gaps in protoplanetary disks (Duffell 2015). The dashed lines represent the surface density after 20 orbits. A value of 1 in radial code units is equivalent to 5.2 AU.

The results for 1 and 2 M_J planets are in very good agreement with the analytical model. The gap for a 5 M_J planet is relatively deeper than the prediction from the model. Nevertheless, the model by Duffell (2015) fails at reproducing the gap profile produced by planets with very high masses, as discussed in that work. Therefore, one can trust the quality of the simulations from the concordance at low planet masses with analytical models.

5.2.3 Prescription of the extinction curve

From the inferred A_V, the extinction coefficients ($A_{\rm band}$) and optical depths ($\tau_{\rm band}$) were initially obtained by using the diffuse ISM extinction curves of Cardelli et al. (1989) for all the IR bands. This produced a significant underestimation of the extinction coefficients in longer wavelengths, and, besides, the original prescription did not consider the important silicate feature around $10\mu m$, which increases the expected extinction at that wavelength.

In the updated study, the prescription of the ISM extinction curve is a combination of the Cardelli et al. (1989) curve, used in the J-, H-, K-bands, and the curves from Chiar & Tielens (2006) for L-, M- and N-bands, since the later curves account for the silicate

feature around $10\mu m$ and provide an accurate determination of the extinction at longer IR wavelengths (namely for L-, M- and N-bands). The main results of extinction and expected planet magnitudes by applying the updated prescription of the extinction curve to the original results are shown in the top sub-panels of Figure 5.5. The silicate feature at $10\mu m$ has indeed a large effect on the extinction coefficients on the 1 and 2 M_J planets, producing much fainter planet emission for these cases.

5.2.4 Effects of dust composition on extinction

In the initial study, ISM composition was considered to estimate the extinction, and it was assumed that mostly small grains were present in the disk atmosphere above the planet. The actual value of extinction largely depends on the dust properties. To investigate the effect of the disk composition, we have evaluated the impact of varying the dust composition and the distribution of grain sizes. The results for the 1 M_J viscously evolving case are shown in bottom panels of Figure 5.5. Besides the ISM composition, two alternative dust models were investigated. First, one model of grains with fractional abundances comparable to the expected in protoplanetary disks mid-plane (Pollack et al. 1994) and grain population with number density $n(a) \propto a^{-3.5}$ (where a is the grain size) between $0.01\mu m < a < 1\mu m$ (Tazzari et al. 2016, for details). Secondly, a dust coagulation model for ice-coated silicate-graphite aggregates (type II grain mixing, see Ormel et al. 2009, 2011) which is applicable to dust in protoplanetary disks (extinction shown is for grain sizes $a \sim 1\mu m$). The results of the ice silicate graphite model are in very good agreement with the ISM extinction used (in M-, and N-bands the diffuse ISM extinction becomes larger). The other model provides similar results in the J-, and H-bands, however, for longer wavelengths extinctions are $\sim$ 2-3 times larger than for the diffuse ISM. Thus, when considering dust with different properties (e.g. composition, size, level of processing), the resulting predicted planet magnitudes may change due to the opacity variations in IR wavelengths.

On the other hand, the extinction is obtained by assuming a gas-to-dust ratio of 100 along the disk. In the atmospheric layers of the disk above the planet, this ratio might be larger due to dust processing and settling. In this regard, the developed detectability model provides a conservative estimate of extinction; the presented results can be interpreted as the worst case scenario.

5.2.5 Search for protoplanets in PDS 70, HL Tau, and HD 163296

The results can be applied to real systems to study the detectability of embedded planets. In what follows, I present the results of the model for the Class II disks of PDS 70, HL Tau, and HD 163296. For the last system, the results are combined with contrast sensitivity limits from previous IR observations (Guidi et al. 2018). This allows to measure planet mass upper limits for the unseen planets that have hypothetically carved the known gaps in this system. The improvement of this revision with respect to the results from (Guidi

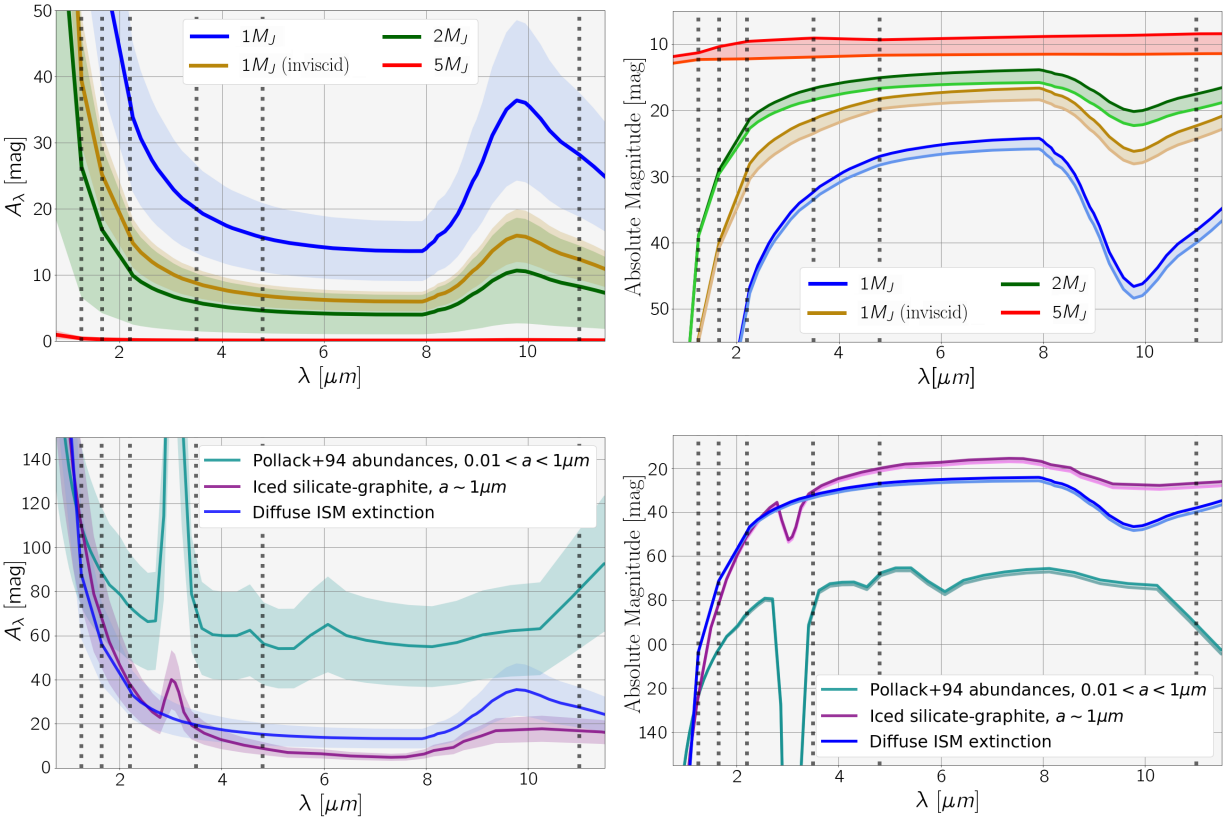

Figure 5.5: Extinction coefficients and expected planet magnitudes in IR as a function of wavelength. Extinction coefficients with uncertainties (*top left*); and predicted magnitudes, shown as an area delimited by the *hot* and *cold* planetary models, for the simulated systems (*top right*). Extinction (*bottom left*) and predicted magnitudes (*bottom right*) of the 1 M_J viscous case using different dust grain models. The results for the various dust models are normalized at A_V. For every panel, the vertical dotted lines represent (from left to right) the central wavelength of J-, H-, K-, L-, M-, and N-bands.

et al. 2018) is the inclusion of the extinction due to the disk material, and the emission from the shocks due to planet accretion.

Additionally, we have also estimated the likelihood of detecting with ALMA the circumplanetary disk (CPD) that surrounds the planets in the simulations. In order to address this question, we computed the fluxes at $890\mu m$ wavelength of the $1M_J$ planet and its respective CPD. The expected planet flux is $\sim 10^{-6}$ mJy, below the ALMA sensitivity limit. For the CPD, simplified to a disk of $1R_{\rm Hill}$ radius centered at the planet and 0.24 $R_{\rm Hill}$ high (i.e. the region around the planet with a disk-shaped over-density), we obtain a dust mass of $M_{\rm dust}^{\rm CPD} \approx 0.003 M_\oplus$, which is comparable to the CPD measurements in PDS 70b (Isella et al. 2019). Assuming a constant CPD temperature of 121 K, the continuum emission in ALMA Band 7 would be 0.07 mJy if emission is assumed to be optically thin, and 0.23

mJy if optically thick. Thus, the CPD of the simulated disk could be detected by ALMA observations with enough sensitivity.

PDS 70

PDS 70 is a member of the Upper Centaurus-Lupus subgroup (at $\sim$ 113 pc, Gaia Collaboration et al. 2018), with a central star of 5.4 Myr and mass 0.76 $M_\odot$ (Müller et al. 2018). It is surrounded by a transition disk with estimated total disk mass of $1 \cdot 10^{-3}$ $M_\odot$. A first companion (PDS 70b) was found combining observations with VLT/SPHERE, VLT/NaCo and Gemini/NICI at various epochs, detected as a point-source in H-, K- and L-bands at a projected averaged separation of 194.7 mas (Keppler et al. 2018). In J-band, PDS 70b could only be marginally detected when collapsing the J- and H-band channels. Due to the high uncertainties, J-band magnitude was not given. Atmospheric modeling of the planet was used to constrain its properties (Müller et al. 2018), with an estimated mass range from 2 to 17M_J.

Recent H_α line observations using VLT/MUSE confirmed a 8σ detection from a second companion (PDS 70c) at 240 mas (Haffert et al. 2019). Dust continuum emission (likely from its CPD) has been also observed (Isella et al. 2019). This second source is very close to an extended disk feature, consequently its photometry should be done with caution. In Mesa et al. (2019), the planetary nature of this companion has been confirmed, and absolute magnitudes in J-, H-, and K-bands could be inferred for two SPHERE epochs. The spectrum in the J-band is very faint, and indistinguishable from the adjacent disk feature, thus the J-band magnitude should be regarded as upper limit. The NaCo L-band map detected emission that is partly covered by the disk, therefore its L-band magnitude should also be taken as an upper limit. Using various atmospheric models, Mesa et al. (2019) constrained the mass PDS 70c to be between 1.9 and 4.4 M_J.

The models were re-scaled using a fiducial surface density of $\Sigma = 12.5$ g $\cdot$ cm^{-2} at 1 AU (taking the unperturbed surface density model with depletion factor $\delta_{disk} = 1$ and gas-to-dust ratio of 100, from Keppler et al. 2018). This corresponds to a surface density scale factor of $\times$0.043 with respect to the simulated disk. From the re-scaling, we obtained contrast curves of planets embedded in the PDS 70 disk with 0.48, 0.95 and 2.38 M_J (Figure 5.6). The results show the effect of a disk with very low surface density: extinction has an incidence in J- and H-bands for 0.95 and 0.48 M_J planets located within $\lesssim$ 40 AU. In the L-band extinction has only a minor effect on the lightest planet model at distances below 20 AU. From the assumed surface density profile, none of the planetary companions would be affected by extinction due to material from the protoplanetary disk in the IR bands.

The observed contrast of the primary companion in three bands is considerably higher than the value for the most massive planet of the models, thus setting a mass lower limit of 2.38 M_J for PDS 70b. The second companion lays on top of the 2.38 M_J model in H-band, and above it in K-band. The redness of this source can explain the difference in the bands contrast. This reddening might be due to material from its own CPD or from the contiguous disk feature. The models are in agreement with the previous mass ranges

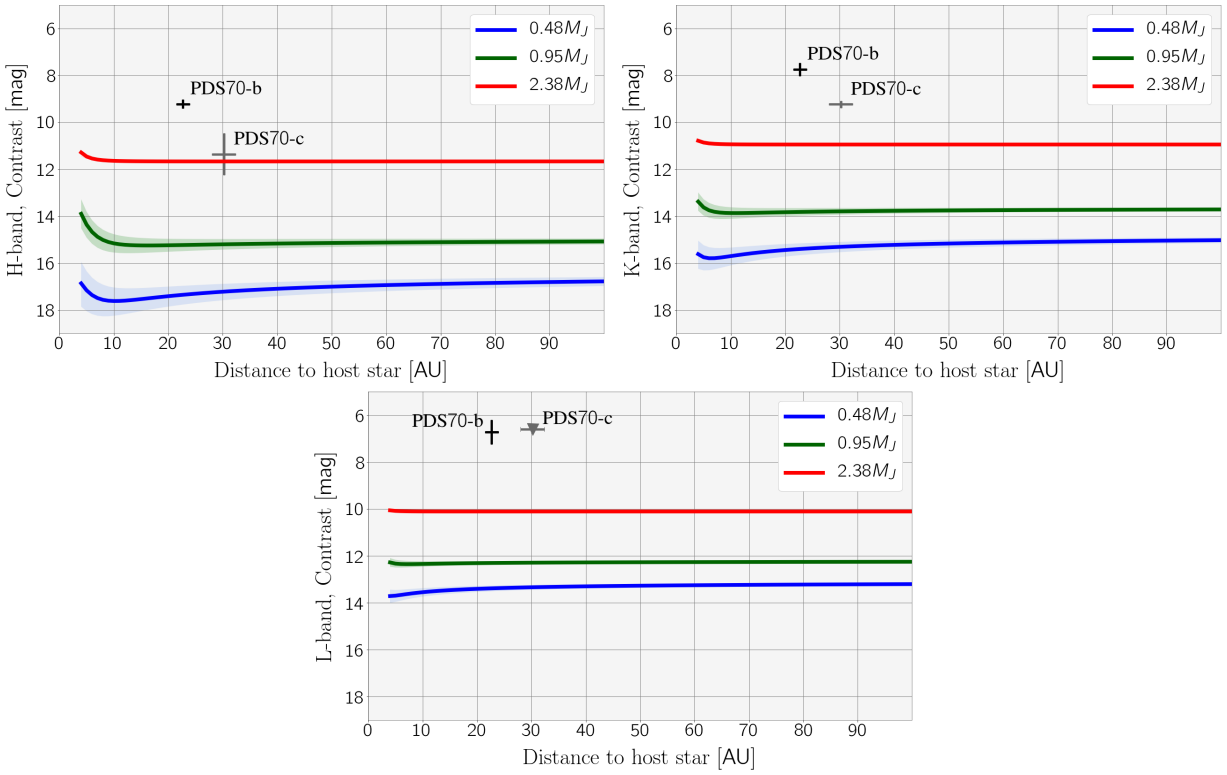

Figure 5.6: Application of the model to planets with 0.48, 0.95 and 2.38 M_J embedded in the PDS 70 disk. The contrast curves shown for H-, K- and L-bands were obtained considering stellar magnitudes of $H = 8.8$ mag, $K = 8.5$ mag and $L = 7.9$ mag (Cutri et al. 2003; Cutri & et al. 2014). The two planetary companions (Keppler et al. 2018; Mesa et al. 2019; Haffert et al. 2019) are shown as black and gray crosses, with the corresponding uncertainties.

estimated for the two companions; further observations and modeling of the disk and their atmospheres are needed to better constrain their masses.

The estimated accretion rates of the companions are of the order of $\sim 10^{-11}\ M_\odot \cdot \mathrm{yr}^{-1}$ (Haffert et al. 2019), thus radiation from accretion shocks near both planets are negligible. From the results, accretion flux would only have an incidence in the modeled IR planet fluxes at distances ~ 5 AU, since accretion rates are expected to be higher due to the scaling. This can be appreciated in the contrast curve of the three planet models in H-band: planets' contrasts decrease at these distances. The effect of the accretion shock's radiation becomes negligible at $\gtrsim 10$ AU.

HL Tau

HL Tau is one of the most extensively studied protoplanetary disks, with several rings and gaps detected in the dust continuum (ALMA Partnership et al. 2015b). It is a young stellar

object of ≤ 1 Myr at around 140 pc to us (Kenyon et al. 2008), with an estimated stellar mass of $\sim 0.7\ M_{\odot}$ (Kenyon & Hartmann 1995; Close et al. 1997). Observations were carried out using the LBTI L/M IR Camera (LMIRcam, Skrutskie et al. 2010; Leisenring et al. 2012), using only one of the two primary mirrors of the LBT telescope. No point-sources were detected. For the normalization of the surface density, we took the inferred gas surface density from CARMA observations (Kwon et al. 2011, 2015) at a fiducial distance of 40 AU, $\Sigma = 34\ \mathrm{g \cdot cm^{-2}}$ (a factor $\times 0.74$ compared to the simulated disk).

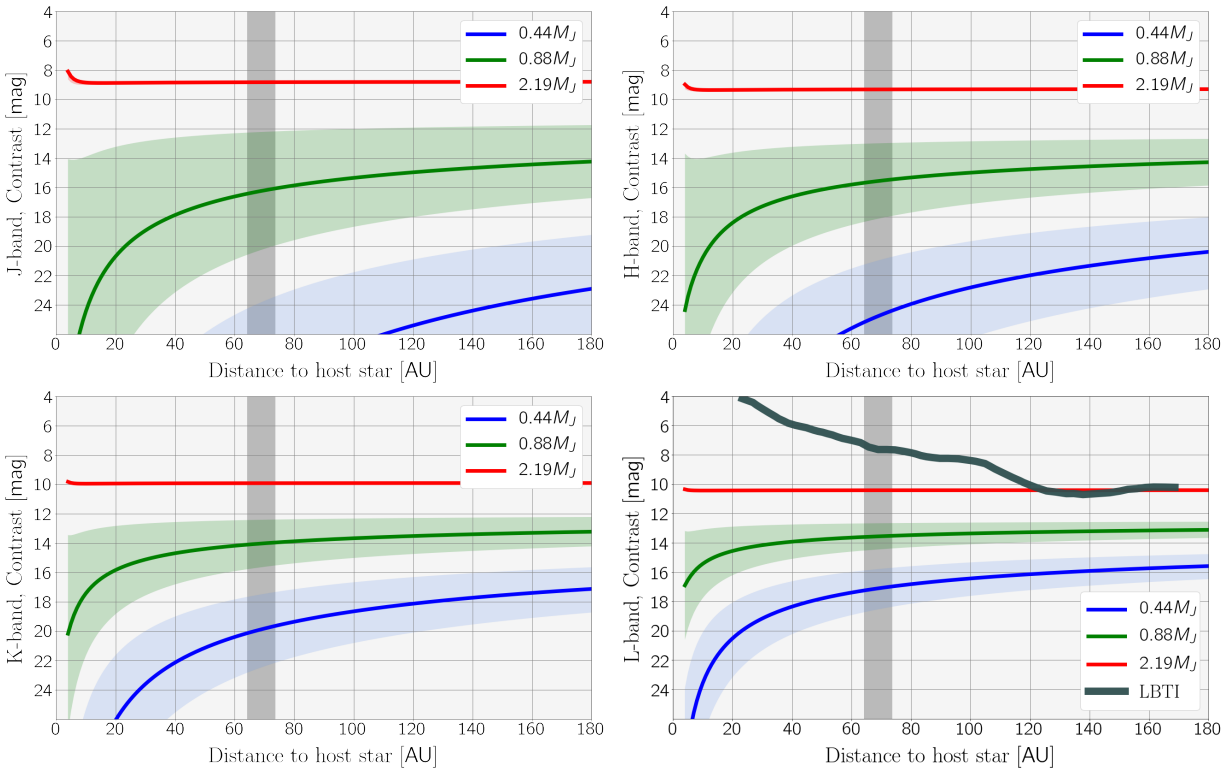

Figure 5.7: Contrast curves in J-, H- K, and L-bands for planets embedded in HL Tau. The results shown in the L-band include the 5σ detection limit of the observation from Testi et al. (2015). The observations were performed using LBTI/LMIRcam. The contrast curves are for planet masses of 0.44, 0.88 and 2.19 M_J. The considered apparent magnitude of the central star was $L = 6.23$ mag (Testi et al. 2015). The colored regions accounts for the uncertainty in the planet contrast. The gray vertical area is delimited by the D5 and D6 rings detected in dust continuum (ALMA Partnership et al. 2015b).

The results for the J-, H- K, and L-bands are shown in Figure 5.7. In the bottom right sub-panel, the contrast limit of the LBTI observation in L-band as a function of the angular separation to the central star is included, together with the derived contrast of the re-scaled models for planets with 0.44, 0.88 and 2.19 M_J. In L-band, a high extinction is predicted for 0.44 and 0.88 M_J along the entire disk, especially at distances $\lesssim 60$ AU; at

that distance, A_L values are 4.27 mag ($A_V = 68.29$ mag) and 1.25 mag ($A_V = 19.98$ mag) for these planets respectively. For planets outer in the disk, the extinction contribution is smaller but still significant: 3.02 mag ($A_V = 48.29$ mag) for 0.44 M_J, and 0.88 mag ($A_V = 14.13$ mag) for 0.88 M_J at 120 AU. These planets are not massive enough to clear the gap efficiently. On the other hand, for the most massive planet (2.19 M_J), extinction is negligible at any distance.

Six gaps were observed in the ALMA continuum observation; following the example as in Testi et al. (2015), within the gap delimited by D5 and D6 rings (marked as gray vertical line) the contrast limit of the instrument does not allow us to constrain the mass of the companion that could be responsible for the gap. Nevertheless, from the inferred contrast curves, extinction would have an incidence in a hypothetical point-source detection only for planet masses $\lesssim 0.88$ M_J.

HD 163296

In Guidi et al. (2018), the HD 163296 disk was studied in the L-band using the same instrument (Keck/NIRC2 vortex coronagraph). The scattered polarized emission in the J-band was also studied with the Gemini Planet Imager in Monnier et al. (2017), detecting a ring with an offset that can be explained by an inclined flared disk. This system has a central star of 2.3 $M_\odot$ (Natta et al. 2004c) and estimated age of ~ 5 Myr (Montesinos et al. 2009). Observations in the dust continuum using ALMA (Isella et al. 2016) confirmed the existence of three gaps at distances of ~ 50, ~ 81 and ~ 136 AU (corrected with the new Gaia distance of 101.5 pc). Kinematical analysis of gas observations suggested the presence of two planets at the second and third gaps (Teague et al. 2018). In Pinte et al. (2018b), HD models showed that a third planet is expected further out. The estimated masses of the three potential planets are 1 M_J (at 83 AU), 1.3 M_J (at 127 AU) and ≈ 2 M_J at (≈ 260 AU). The new DSHARP/ALMA observations confirmed an additional gap at ~ 10 AU (Isella et al. 2018); assuming that this gap is caused by a planet, Zhang et al. (2018) estimated a planet mass between 0.2 and 1.5 M_J from 2D HD simulations.

The L-band high-contrast imaging (Guidi et al. 2018) detected a point-like source at a distance of 67.7 AU with 4.7σ significance. None of the observations in L- or J-band found any point-sources at the gaps observed in the continuum. The models allow to set upper limits for planets at the location of the gaps. A fiducial surface density of $\Sigma = 82.8$ g $\cdot$ cm^{-2} at 40 AU was used (from Isella et al. 2016), corresponding to a factor $\times 1.8$ of the simulated disk, to obtain contrast curves for 1.44, 2.88 and 7.19 M_J (J-, H-, K-, and L-bands in Figure 5.8). In the L-band contrast curve. the innermost gap is within the masked region in the Keck/NIR2 observations, thus a mass upper limit can not be inferred. At the second gap, the model for the most massive planet lays slightly below the detection limit of the observation. A rough extrapolation would yield an upper-limit of 7.6 M_J, slightly below the range provided by Guidi et al. (2018) (8-15 M_J in that work). For the third and fourth gaps, upper limits of 6.7 M_J and 5.5 M_J are obtained from interpolating the models. These values are slightly higher than the upper limits inferred in Guidi et al. (2018) (4.5-6.5 M_J, and 2.5-4 M_J respectively). Taking into account extinction on the contrast of the planets

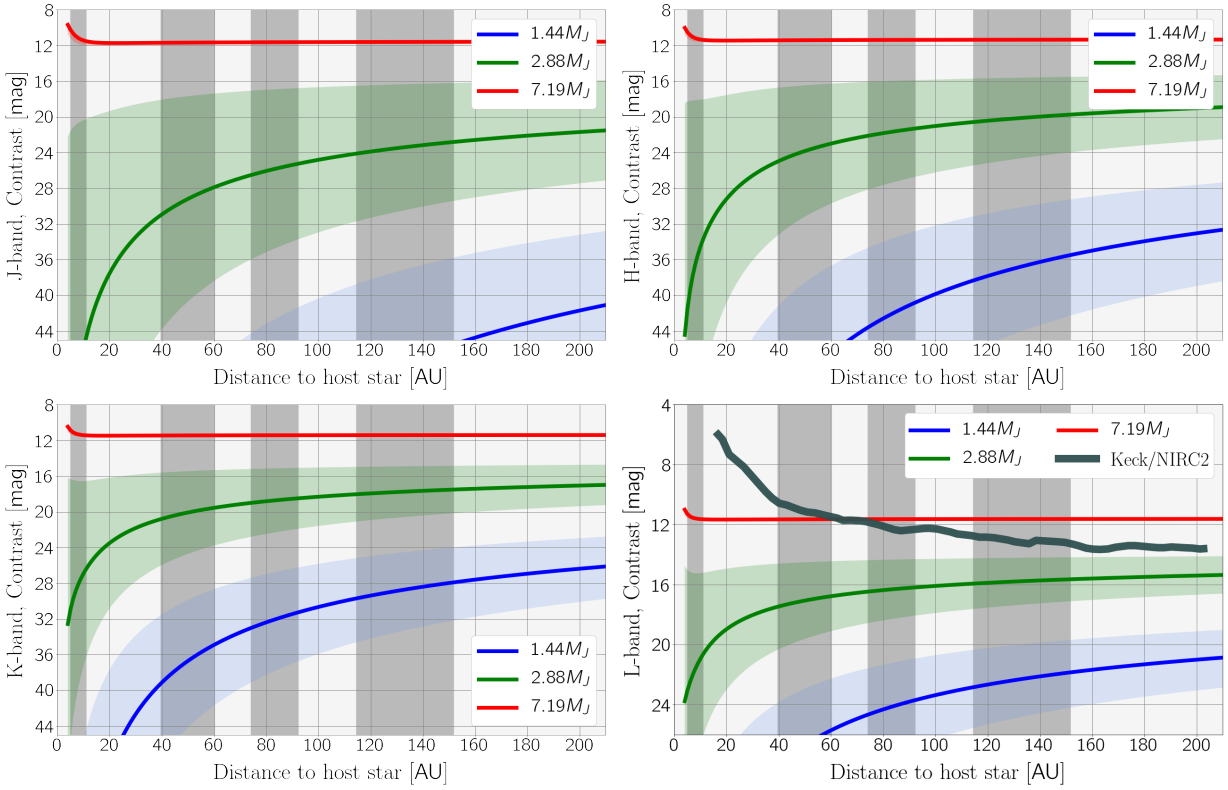

Figure 5.8: Contrast curves in J-, H- K, and L-bands for planets embedded in HD 163296. The results in the L-band include the 5σ detection limits of the observation from Guidi et al. (2018). The observations were performed using Keck/NIRC2. The contrast of planets with 1.44, 2.88 and 7.19 M_J are shown. The apparent magnitude of the central star is $L = 3.7$ mag, inferred from the W1 band in the WISE catalog (Wright et al. 2010). The gray vertical lines account for the gaps observed in Isella et al. (2016, 2018).

increase the inferred upper limits of the non-detected planets. In every gap, extinction does have an important effect for planets with masses lower than the inferred upper limits. Compared to the estimates of Teague et al. (2018) and Pinte et al. (2018b) from indirect analysis, the inferred upper limits are significantly higher; consequently a direct detection of these companions would only be possible improving the detection limit to much higher contrast.

5.2.6 Conclusions

I have expanded on the initial study conducted in my Master Thesis that provided a detectability model for protoplanets that are still embedded in their host disk. The original work presented a number of unanswered points that have been addressed in the present Thesis. A strong effort has been done to understand the impact of the grid resolution on

the density stratification of the planet's atmosphere, and the impact of the dust properties on the expected extinction coefficients. Besides, the detectability model has been largely improved by using an accurate prescription of the extinction curves, and, additionally, by inspecting the reliability of the HD simulations, with a comparison between the results of the simulations and well-established gap-opening models. Moreover, Exploiting properties of locally isothermal disks, the enhanced model is used to study the detectability of planets embedded in the protoplanetary disks around PDS 70, HL Tau, and HD 163296. This allows to apply the model to the two planetary companions of PDS 70, and, on the other hand, to infer upper-limits for planets at the gaps observed in HL Tau and HD 163296. The most important results of the detectability model when applied to real systems like PDS 70, HL Tau, and HD 163296 are:

- Jupiter-like planets embedded in disks with very low unperturbed surface densities (of the order of $\lesssim 1\ \mathrm{g \cdot cm^{-2}}$) have very low extinction coefficients in IR at any distance considered. In PDS 70, extinction has an incidence only for the least massive planet model at distances < 50 AU, more significant at shorter wavelengths.

- In more dense disks like HD 163296, direct detection of companions is unlikely in J-, H-, K-, and N-bands due to the extinction effects. Only the most massive planet from the models would be detectable, since its extinction is negligible.

- Upper limits of the gaps in HD 163296 have been inferred. The values are slightly higher than previous work from the literature due to the effect of extinction. This points out the importance of extinction from the disk material in high-contrast imaging of protoplanetary disks.

The scarcity of detections of planets in direct imaging observations suggests two possible and non-exclusive explanations: planet formation further out in the disk is rare, and/or planets formed at these early stages are still not massive enough ($\lesssim 2\ M_J$) to efficiently carve a gap in the disk, thus it is unlikely to detect the planets in majority of disks based on current instrumentation.

Chapter 6

Conclusions & outlook

In this final chapter I outline the major conclusions and achievements of the Thesis, and provide research pathways as continuation of the work conducted here that will greatly benefit the planet formation and exoplanetary fields.

The understanding on the disk evolution processes that constrain planet formation and the dispersal of the disk has, prior to this work, focused on a handful of sources, and in most cases, with an heterogeneous set of observations of dust and gas. These studies lack of an homogeneous and solid demographic approach to understand the true behaviour of dust, gas, and physical processes that govern the evolution of the disk.

In this Thesis, I have performed a demographic study of dust and gas disk properties in the large and highly complete population of disks in the Lupus region. The sample is assembled from several surveys conducted with ALMA targeting disks of the region. The quality of the sample allows to highly reduce uncertainties and errors associated to mixing observations of different telescopes with very different setups. The large completeness level of the sample provides up to date the most exhaustive demographic study of the true evolution of protoplanetary disks in the region. Furthermore, thanks to the homogeneity of the sample and the manipulation and modeling of the data, this study avoids many of the biases due to the sample selection and modeling.

For each source of the sample, I have modeled the dust continuum emission and the gas emission self-consistently. For the dust component of the disk, I have used continuum observations in ALMA Band 7, centered at $\sim 890\mu m$, while for the gas component of the disks, I have used the ^{12}CO $J = 2 - 1$ rotational line in Band 6 (for 3 sources, I used the $J = 3-2$ rotational transition in Band 7). Among other disk properties, the disk mass, the brightness distribution and the extent of the dust continuum and CO are obtained thanks to the interferometric modeling applied to the dataset. Relationships between the dust mass and other properties were investigated for the entire sample and down to the substellar regime, thanks to the new observations of disks around BDs analized in Chapter 3. The $M_\star$-$M_{\rm dust}$ relationship for stars is followed by objects in the substellar regime, while the BDs of the population are statistically different from the stellar population when investigating the $M_{\rm dust}$-$M_{\rm acc}$ relationship, indicative of a longer time depletion scale on these very low mass objects. The total dust mass in disks around BDs and VLMs confirm a discrepancy

with the mass needed to form known exoplanetary systems such as Trappist-1 and Proxima B. This result suggests that either the very low mass objects are unable to form planetary systems, or more plausible, that the cores of the planets might have already formed at the time when the disks were observed.

The modeling of the gas content allowed me to measure the extent of the emission. The relative extent between the gas and dust is a crucial property that is directly linked to the evolutionary stage of the disk, and in particular to the dust evolution (i.e., grain growth and subsequent radial drift). The ratio between the gas and the dust components is expected to be >1 due to the combination of optical effect differences and dust evolution. It is possible to disentangle the two effects in some cases: very large size ratios ($\gtrsim$4) can only be explained if prominent dust evolution has occurred. Around 20% of the total disk sample has such large size ratio, confirming that these disks have undergone grain growth and radial drift. For the remaining disks, dust evolution might have occurred but can only be confirmed with individual and more elaborated analysis of their structure. This is the first study to determine the size ratio for such a large and homogeneous sample of disks within one region, and the main result suggests that at least a fraction of the disk population has suffered dust evolution, which is a crucial step on the formation of planetary cores.

These conclusions are robust thanks to the completeness of the sample and the homogeneity on the methodology employed to model the (sub-)mm emission of the entire population. However, there are a number of research directions to further extend from the achievements accomplished in this Thesis. In this statistical study I have focused on the Lupus star-forming region. It is necessary to broaden the study by applying the same modeling to additional star-forming regions. By studying other regions of different ages, we can greatly improve our understanding on how disk properties evolve as a function of time. Most importantly, by modeling both dust and gas components for the disk population of other regions, we can further constrain dust evolution and when exactly it takes place. This is important to constrain the timescale of planet formation, and by knowing how and when cores form, we can learn about the properties of the resulting planets. Nearby star-forming regions such as ρ-Ophiuchus, Corona Australis, Chamaeleon I, σ-Orionis or Upper Scorpius, with average ages between $\sim$ 1 to 5, are well-suited for the statistical study of the dust and gas extent of the disk population, and have been targeted in recent ALMA surveys.

Further work can also be performed by conducting individual detailed analysis of the disk structure. Due to the large sample of disks that I analyzed, and in order to keep the homogeneity on the handling of the data and the methodology used, more exhaustive modeling of the temperature structure and composition of each disk was not conducted. The results of the demographic study were insufficient to accurately assess dust evolution in an important fraction of the population. Tailored studies of the temperature structure and distribution of gas species and dust for each disk can help disentangling between optical depth and dust evolution effects that cause the gas/dust size ratio to be > 1.

On the second line of investigation that I have conducted in this Thesis, I have deepened on the study of the detectability of already formed protoplanets embedded in a disk. In

such scenario, the young planet might be partially (or completely) extincted by surrounding disk material. This investigation has paramount implications on planet detection and protoplanetary disks. By detecting planets embedded in disks, it is possible to greatly constrain the timescale of planet formation, and to understand how the planet-disk interaction shapes the dispersal of the disk and the final properties and features of the newborn planet. In this extension of an initial study that I performed in my Master Thesis, I have studied key aspects that have an important effect on the expected extinction of the planet in IR, such as the dust composition of the disk and the grid resolution of the simulations. I have also improved the prescription used to infer the extinction coefficients in IR wavelengths. These aspects allow for a more robust detectability model and for a enhancement of its scope and applicability. I have then applied the model to observations of well-known disks, such as PDS 70, HL Tau and HD 163296, constraining the mass of the possible planetary companions. The main results suggest that the direct detection of young planets in disks is limited to very specific cases, where the planet mass is very large ($M_{\rm pl} \gtrsim 5\ M_J$), the disk surface density is extremely low, and preferably, the planet is far from the central star.

This modeling offers manifold opportunities for future research. On the observational side, the results are crucial to guide future observations trying to directly detect planets in protoplanetary disks. The study is very timely due to the proximity of the launch and start of operation of the James Webb Space Telescope (JWST), which will allow for very high contrast observations, and potentially the detection of planets with very faint expected magnitudes in the IR. On the theoretical side, this study can be extended by improving on the grid resolution in the planet vicinity (until the planet is fully resolved), by extending the physics of the simulations (e.g., properly computing the magnetic field for each cell and snapshot), or by measuring the column densities at different inclinations of the disk.

The last years have set astounding discoveries that confirm how much the fields of protoplanetary disks and exoplanet detection have progressed, but also, how much there is still to understand. This Thesis sets important results and pathways on how the true population of protoplanetary disks can be studied in order to understand their evolution and their ability to form planets. Additionally, this Thesis proves how difficult and sensitive to many effects the direct detection of planets within disks is.

Appendix A

Tests comparing $R_{68\%}$ and $R_{95\%}$

We computed the radii enclosing 68% ($R_{68\%}$) and 95% ($R_{95\%}$) for different models fitting a disk with high S/N and well resolved continuum emission in order to test which radius is better as the characteristic size of the disk. Additionally, we demonstrate that the Gaussian function can be used to describe the interferometric data of moderate-angular-resolution observations. For the calculation of these radii we build the cumulative flux as a function of radius:

$$f_{\rm cumul}(R) = 2\pi \cdot \int_0^R I_\nu(R') \cdot R' \cdot {\rm d}R', \tag{A.1}$$

which gives us the flux contained within the radius R. Therefore, $R_{68\%}$ and $R_{95\%}$ are obtained from $f_{\rm cumul}(R_{68\%}) = 0.68 \cdot F_{\rm tot}$ and $f_{\rm cumul}(R_{95\%}) = 0.95 \cdot F_{\rm tot}$. The total disk flux density $F_{\rm tot}$ is one of the free parameters of our fit and is obtained from its PDF. We build the PDFs of the derived radii: the median value of each distribution is used as the inferred value for each radius.

The resulting radii using three empirical models (Gaussian function, Nuker function, and broken power-law) and one physical model (two-layer approximation) were used to fit RXJ1556.1-3655 disk; the results are shown in Figure A.1. The values of $R_{68\%}$ for the various models are found in the range [29.3, 30.1] au, while the values of $R_{95\%}$ are found to be within [40.5, 47.4] au.

These results show that the difference of $R_{68\%}$ between different models is negligible (thus the value of $R_{68\%}$ is independent of the model used to fit our data) and for the $R_{95\%}$ the values may differ and indeed be considerable. This is in accordance with Tripathi et al. (2017), and is a consequence of the low sensitivity of larger scales; thus the noise makes the fitting of the visibilities uncertain. Therefore, the $R_{68\%}$ is favored over the $R_{95\%}$ as the most reliable size definition, since the differences between models are negligible. On the other hand, this test also shows that the Gaussian function is a reliable model to describe emission of moderate-angular-resolution observations, since the $R_{68\%}$ obtained from the Gaussian model is in perfect agreement with the value inferred using other empirical models.

We also tested the quality of our disk size results by performing additional fits of disks around stars in Lupus that were already characterized in Andrews et al. (2018b). The comparison between the inferred radii with the radii presented in Andrews et al. (2018b)

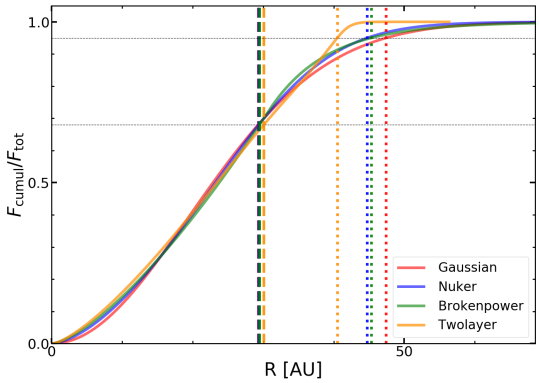

Figure A.1: Normalized cumulative fluxes of various fits used to model the interferometric visibilities of RXJ1556.1-3655 disk, used for the size determination. The results are shown for the following models: a Gaussian distribution as in Equation 3.2 (illustrated in red), the Nuker profile from Equation 3.1 (blue), a broken power-law (green), and for the two-layeräpproximation physical model to describe the disk (orange). The radii enclosing 68% and 95% of the total flux for each model are shown as dashed and dotted lines respectively.

is shown in Figure A.2; the disk size values are indeed in very good agreement. Therefore, the combination of the disk size results of the new disks modeled in this work and the disks modeled in Andrews et al. (2018b) can be done adequately for the demographic analysis in Section 3.5.1.

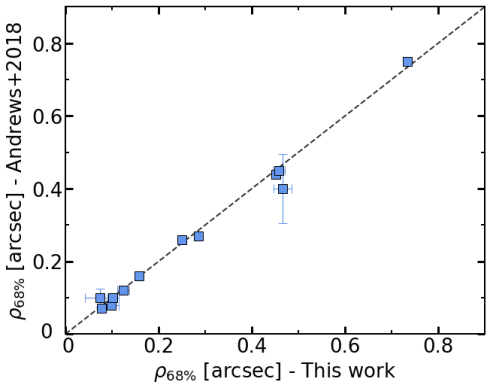

Figure A.2: Comparison of the characteristic size between this work and Andrews et al. (2018b). For this comparison we followed the modeling described in Section 3.4 and fitted the interferometric data of a random subset of Lupus disks that were previously analyzed in Andrews et al. (2018b). The dashed line represents the 1:1 ratio of the radii values.

Appendix B

Disk properties relations using other dust temperature prescriptions

The demographic analysis comparing BD and stellar disks for the relations between disk properties was investigated for various prescriptions of the dust temperature of the disk. The results shown along Section 3.5 in the text are obtained assuming a constant $T_{\rm dust}$ of 20 K. Here we show the disk properties relations for other dust temperature dependence with stellar luminosity. The prescription from Andrews et al. (2013) was designed for disks around central objects of $L_\star \in [0.1, 100]$ $L_\odot$; the one from van der Plas et al. (2016) is more suitable for very low-mass objects (VLMs and BDs).

B.1 Dust temperature from Andrews et al. (2013)

B.2 Dust temperature from van der Plas et al. (2016)

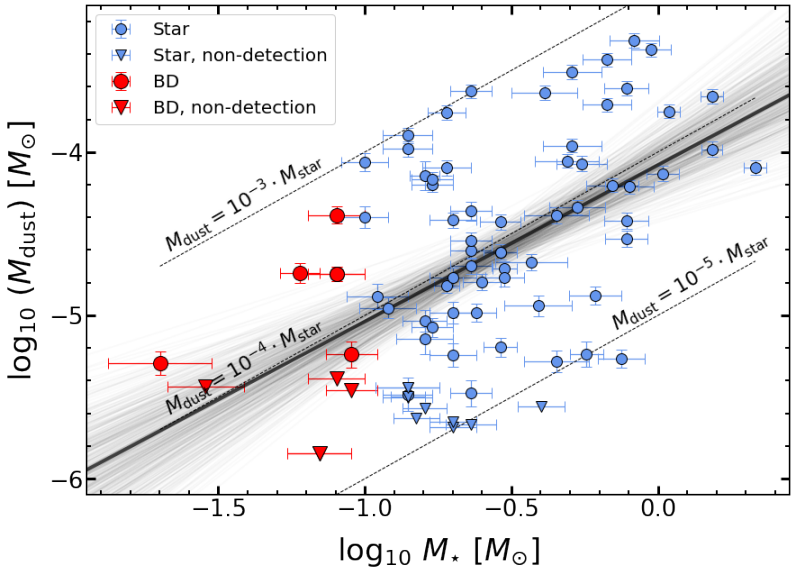

Figure B.1: Relation between the stellar mass and the dust disk mass for the BD and stellar populations in Lupus, using the dust temperature dependence with stellar luminosity from Andrews et al. (2013).

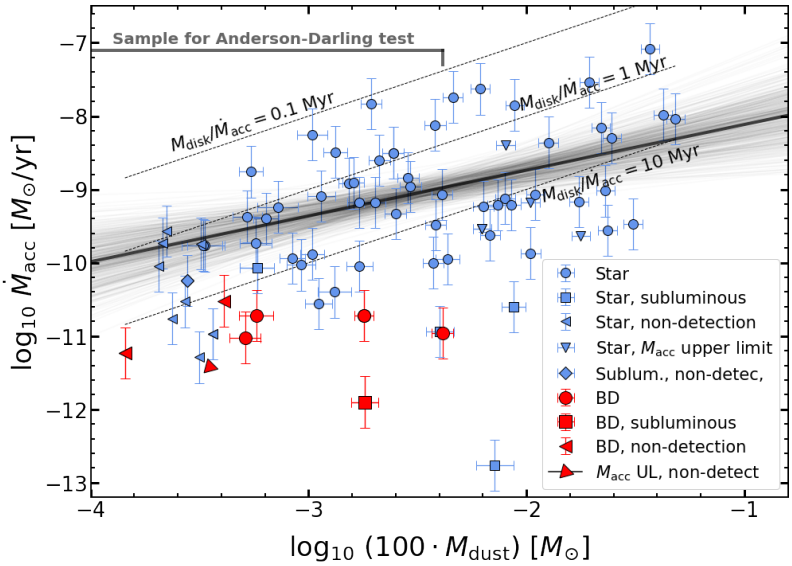

Figure B.2: Relation between the inferred disk mass of the source and the mass accretion rate onto the central object, using the dust temperature dependence with stellar luminosity from Andrews et al. (2013), and assuming a gas-to-dust ratio of 100.

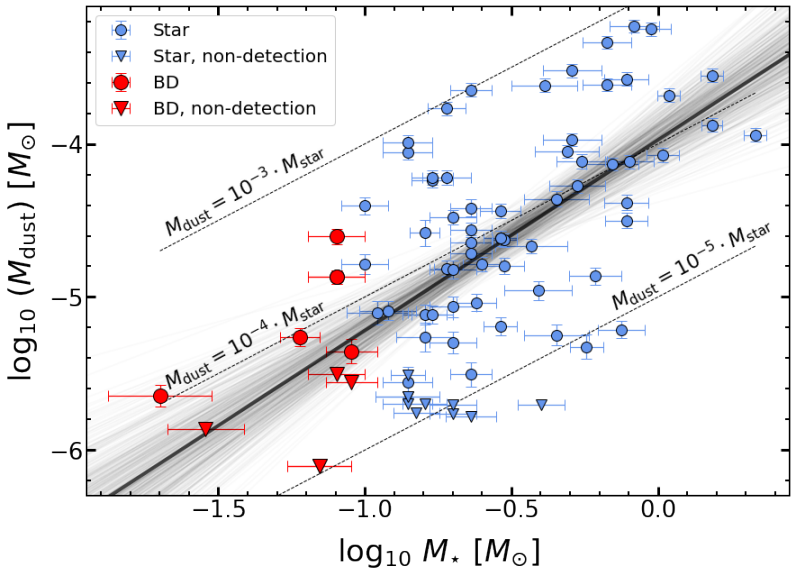

Figure B.3: Relation between the stellar mass and the dust disk masses for the BD and stellar populations in Lupus, using the dust temperature dependence with stellar luminosity from van der Plas et al. (2016).

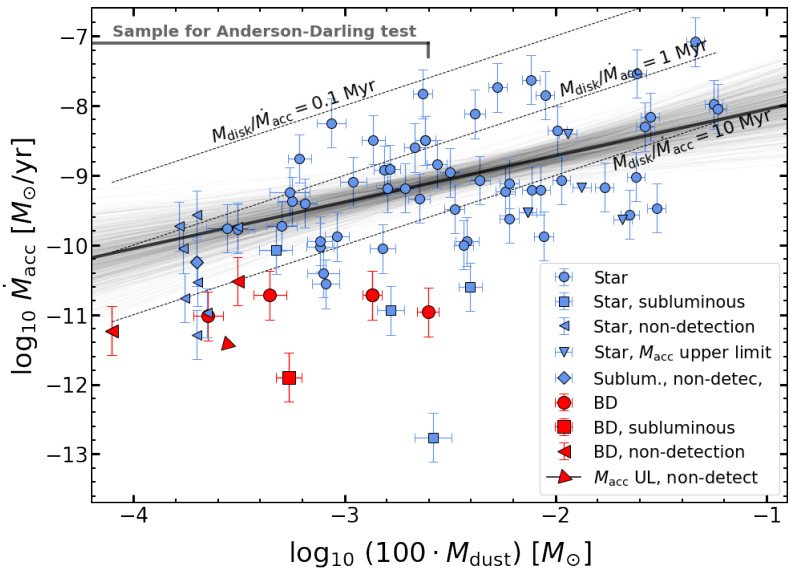

Figure B.4: Relation between the inferred disk mass of the source and the mass accretion rate onto the central object, using the dust temperature dependence with stellar luminosity from van der Plas et al. (2016), and assuming a gas-to-dust ratio of 100.

Appendix C

Results from fits in the continuum

The results of the interferometric modeling for the disks that could be characterized in radius are included in this section. The plots shown for each fitted disk are: (top left) the corner figure composed of the 1D and 2D histograms of the parameter investigation, (top right) the model and observed visibilities (real and imaginary part as a function of Kλ), (center right) the modeled brightness profile with its respective cumulative distribution, (bottom) and the observed, modeled and residuals reconstruction in the imaginary plane from the interferometric analysis. Detailed description of the panels can be found in the captions of Figures 3.3, 3.4, 3.5, and 3.7.

C.1 Results for Sz 102

C.2 Results for V 1094 Sco

C.3 Results for GQ Lup

C.4 Results for Sz 76

C.5 Results for RXJ 1556.1-3655

C.6 Results for EX Lup

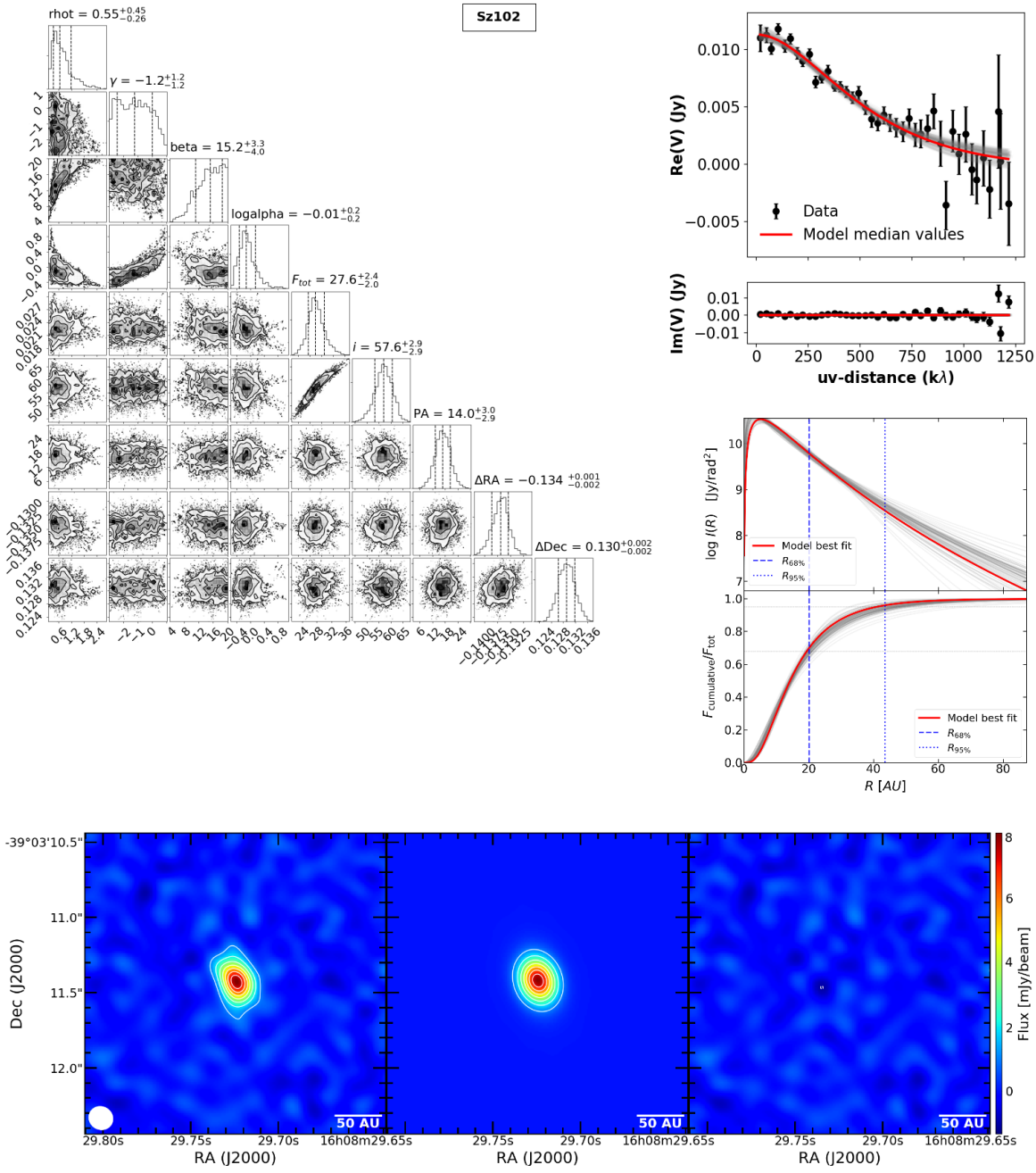

Figure C.1: Modeling results of the Sz 102 disk from ALMA observations. A Nuker profile is fitted to the continuum emission distribution of the disk in the *uv*-plane. The panels show: the real and imaginary part of the observed and modeled visibilities, the 1D and 2D histograms of the Nuker model free parameters, the brightness emission and cumulative distributions, the $R_{68\%}$ and $R_{95\%}$ radii, and the fit results in the image plane.

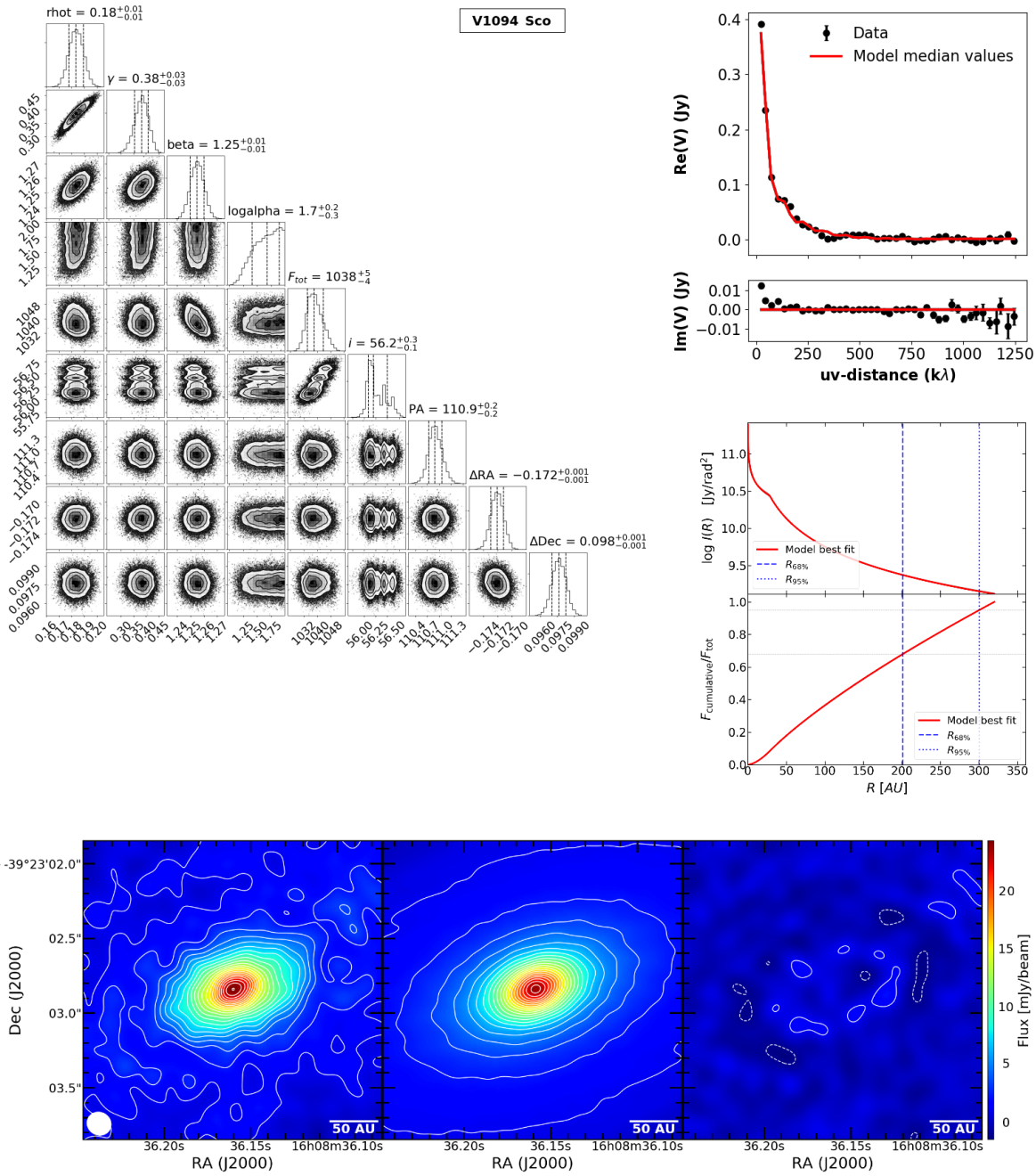

Figure C.2: Modeling results of the V 1094 Sco disk from ALMA observations. A Nuker profile is fitted to the continuum emission distribution of the disk in the *uv*-plane. The panels show: the real and imaginary part of the observed and modeled visibilities, the 1D and 2D histograms of the Nuker model free parameters, the brightness emission and cumulative distributions, the $R_{68\%}$ and $R_{95\%}$ radii, and the fit results in the image plane. The very extended emission of V1094 Sco was studied in detail in van Terwisga et al. (2018), and fitted with a more detailed function. For a comprehensive characterization of this disk we refer to that work. Nevertheless, our fit using the Nuker profile allows us to infer a characteristic radius consistent with the rest of the Lupus disk population.

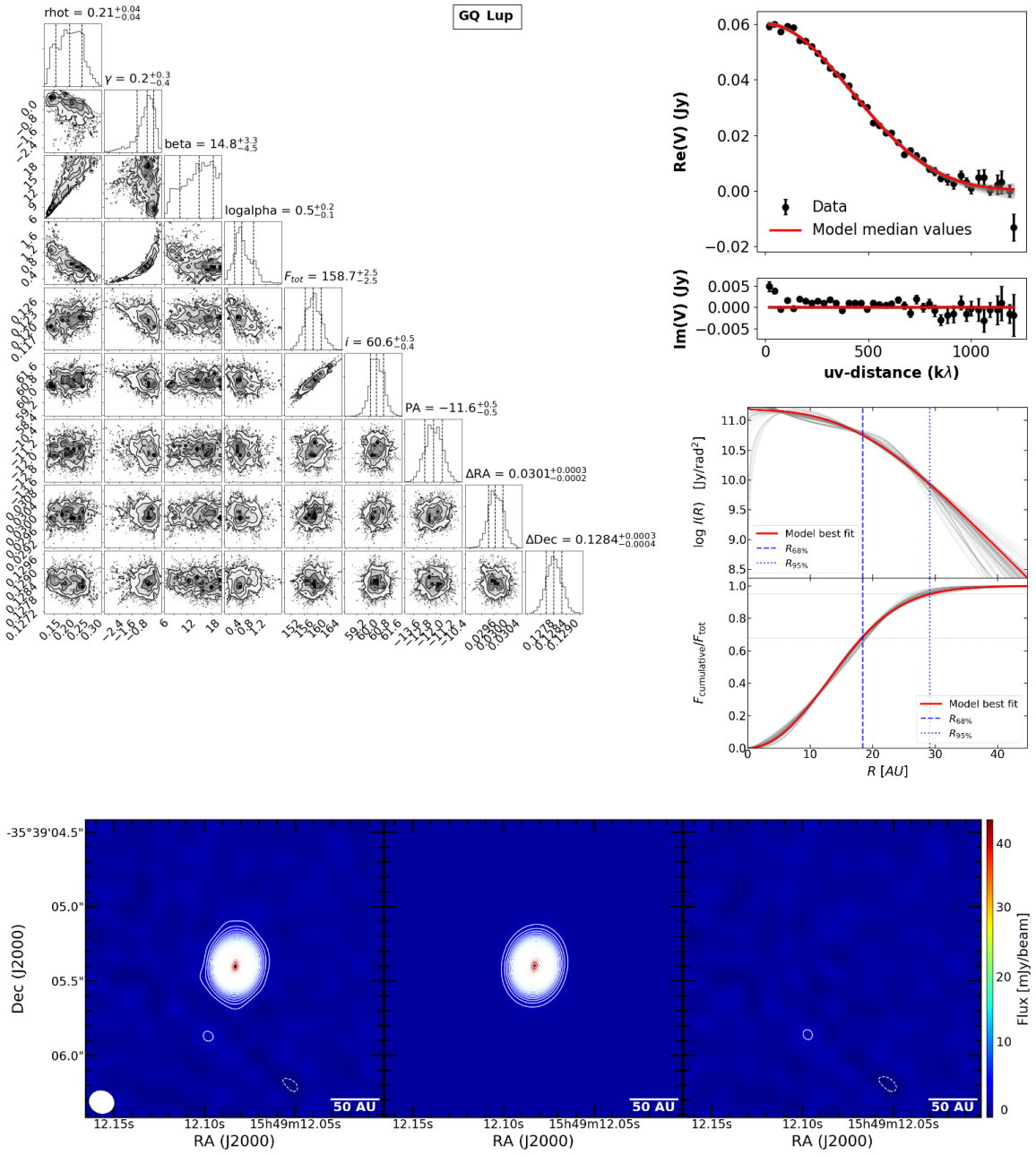

Figure C.3: Modeling results of the GQ Lup disk from ALMA observations. A Nuker profile is fitted to the continuum emission distribution of the disk in the *uv*-plane. The panels show: the real and imaginary part of the observed and modeled visibilities, the 1D and 2D histograms of the Nuker model free parameters, the brightness emission and cumulative distributions, the $R_{68\%}$ and $R_{95\%}$ radii, and the fit results in the image plane.

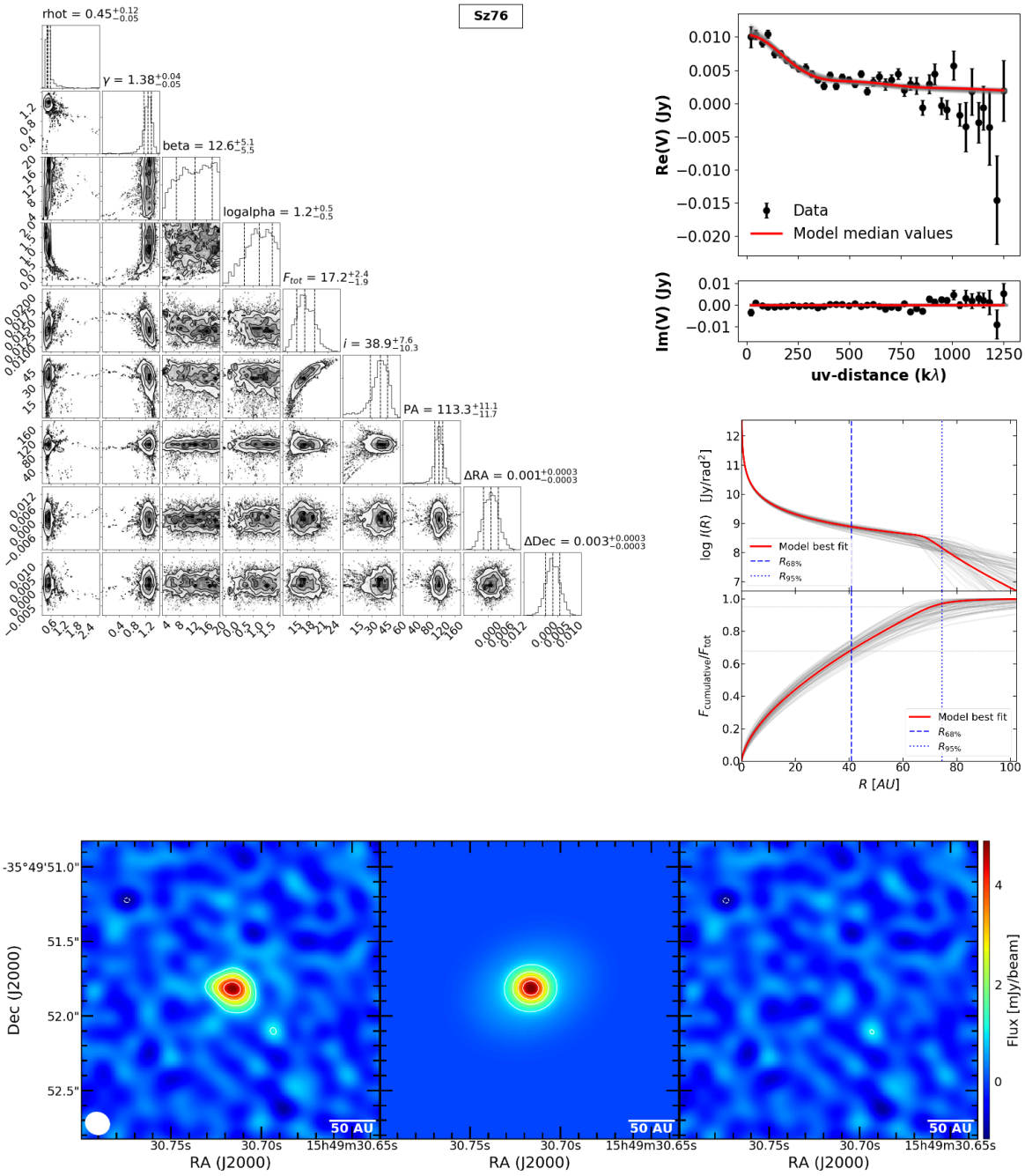

Figure C.4: Modeling results of the Sz 76 disk from ALMA observations. A Nuker profile is fitted to the continuum emission distribution of the disk in the *uv*-plane. The panels show: the real and imaginary part of the observed and modeled visibilities, the 1D and 2D histograms of the Nuker model free parameters, the brightness emission and cumulative distributions, the $R_{68\%}$ and $R_{95\%}$ radii, and the fit results in the image plane.

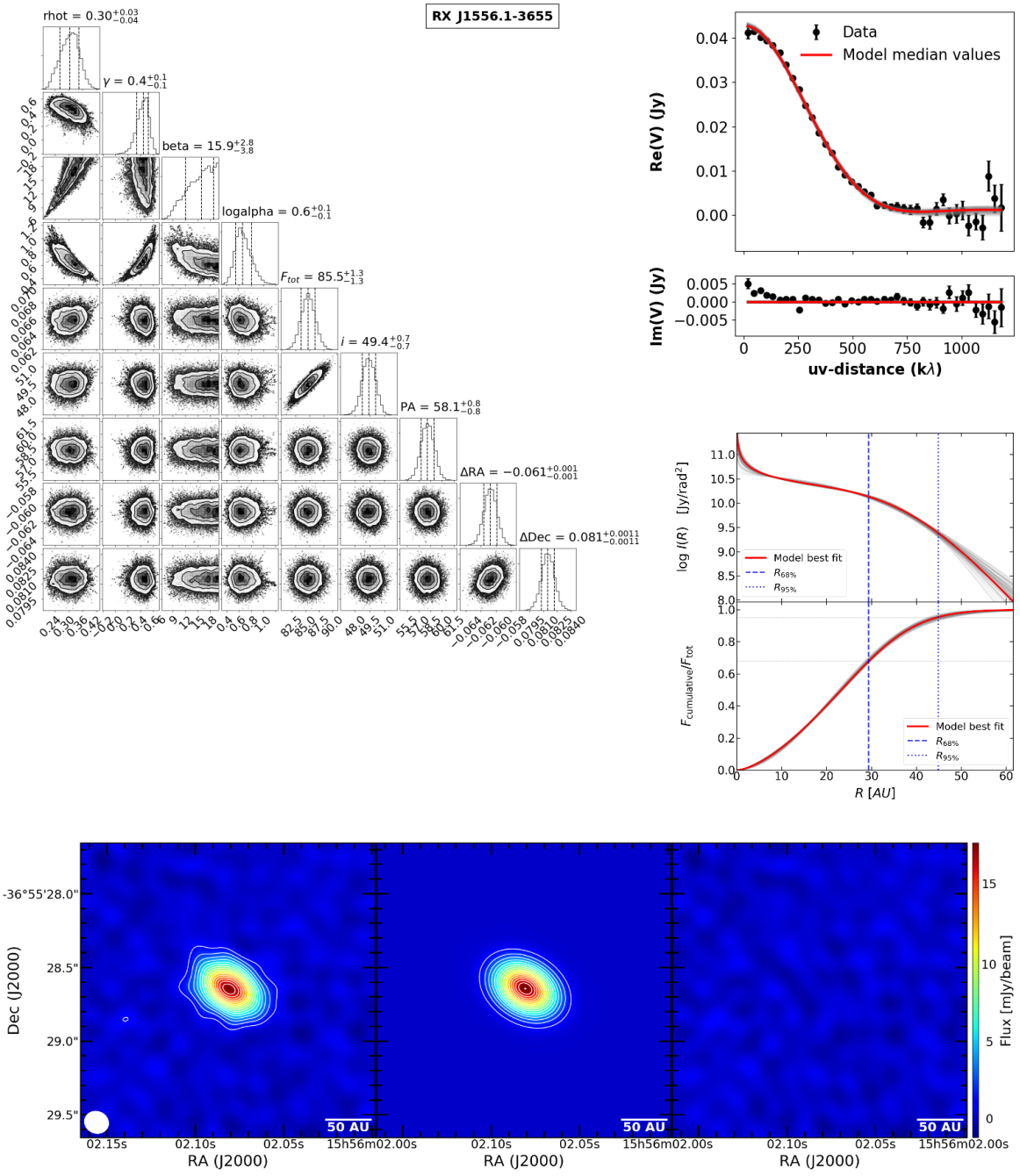

Figure C.5: Modeling results of the RXJ 1556.1-3655 disk from ALMA observations. A Nuker profile is fitted to the continuum emission distribution of the disk in the *uv*-plane. The panels show: the real and imaginary part of the observed and modeled visibilities, the 1D and 2D histograms of the Nuker model free parameters, the brightness emission and cumulative distributions, the $R_{68\%}$ and $R_{95\%}$ radii, and the fit results in the image plane.

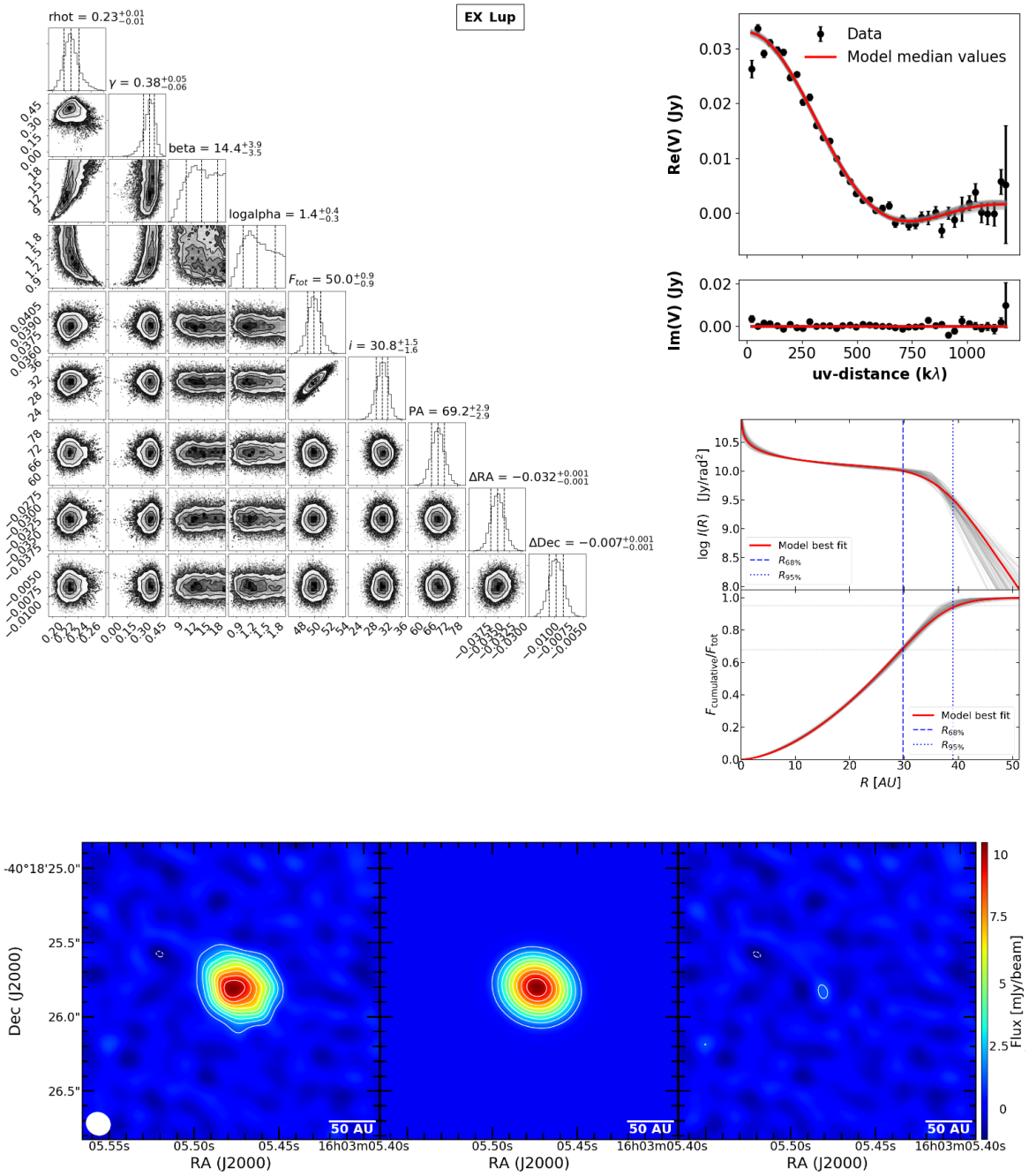

Figure C.6: Modeling results of the EX Lup disk from ALMA observations. A Nuker profile is fitted to the continuum emission distribution of the disk in the *uv*-plane. The panels show: the real and imaginary part of the observed and modeled visibilities, the 1D and 2D histograms of the Nuker model free parameters, the brightness emission and cumulative distributions, the $R_{68\%}$ and $R_{95\%}$ radii, and the fit results in the image plane.

Appendix D

Accretion luminosity versus scaled continuum flux

We inspected the relation between accretion luminosity and continuum flux (scaled to 158.5 pc, the average distance to Lupus region) for the BD and stellar disks population. The demographic analysis is analogous to the different relations studied in Section 3.5. The accretion luminosity used is inferred from X-Shooter observations (Alcalá et al. 2014, 2017) and corrected with the parallaxes from Gaia Collaboration et al. (2018); continuum flux at 890 μm is obtained from ALMA observations in Band 7 (Ansdell et al. 2016, , also this work). The relation is shown in Figure D.1. Red datapoints represent the BD population, while blue datapoints indicate the stellar disks. The linear regression of the stellar population is shown in the figure, it has been obtained excluding nondetections and subluminous sources.

The stellar relation seems to poorly describe the behavior of the BD disk population. In order to verify this result, we built the histograms of the distance to the linear regression of the two populations (Figure D.2), and performed the Anderson-Darling test comparing the BD and stellar populations. This test gives a 0.02% probability that the BD and the stellar disk populations are drawn from the same distribution. Therefore, the difference of accretion between BD and stars is statistically significant based on observed quantities only.

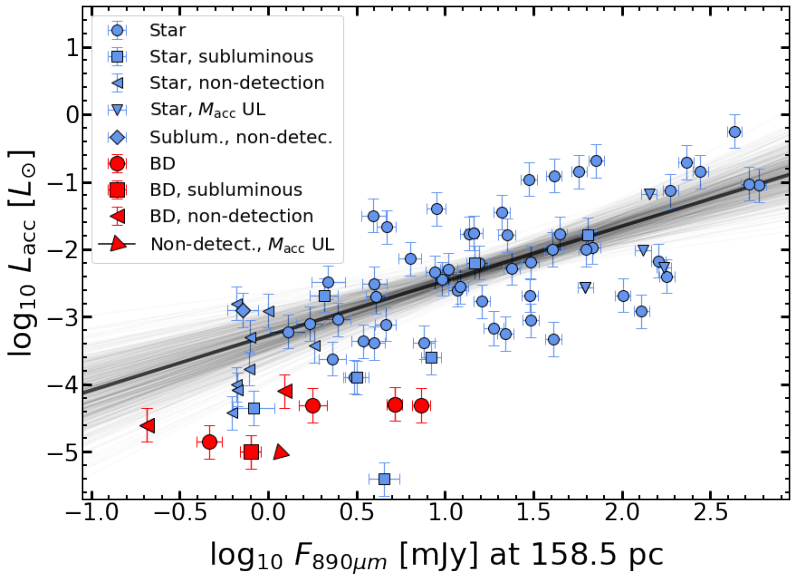

Figure D.1: Relation between the accretion luminosity and the continuum flux of the disk (scaled to the average distance of Lupus). These are the observables used to infer the mass accretion rate and the disk mass as discussed in Section 3.5.

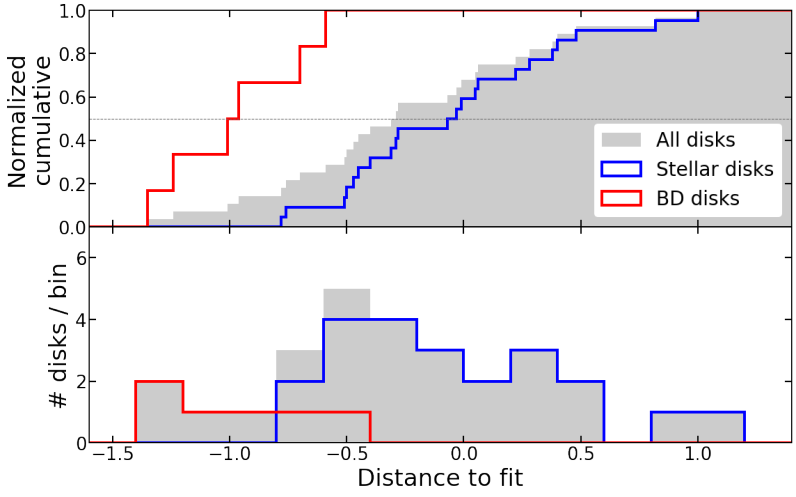

Figure D.2: Histogram of the ratio between accretion luminosity and continuum flux of the disk (scaled to the average distance of Lupus).

Appendix E

Interferometric modeling of line emission from DSHARP

While analysis in the image plane gives a first order insightful information of the emission, fitting the observations in the *uv*-plane provides the most robust method to characterize the disk emission. By working in the *uv*-plane, we avoid systematic errors from the image reconstruction process (e.g., dependency on the weighting, and masking applied during this process).

In recent work, interferometric modeling allowed to characterize dust continuum in large samples of disks from ALMA observations (e.g., Tazzari et al. 2017; Tripathi et al. 2017; Andrews et al. 2018b; Sanchis et al. 2020b). We explore this methodology to model the line emission.

The interferometric modeling of the gas can be accomplished by integrating all channels that show disk emission after the continuum is subtracted. This is analogous (but in the Fourier space) to the moment zero map in which all the channel maps are summed up. The resulting visibilities are then modeled to an empirical emission function, analogous to the interferometric modeling of dust continuum conducted in Sanchis et al. (2020b).

Gas line emission can be modeled using any preferred empirical function, in this work we used the Nuker function (see Tripathi et al. 2017, for details of this function) fitted in the *uv*-plane as the fiducial CO sizes of these objects. The advantage of using this profile resides in independently fitting the inner and outer slopes of the disk emission. In Section 4.3.1 we also test the interferometric modeling by fitting a Gaussian function (as Equation 2 in Sanchis et al. 2020b). This methodology assumes a axi-symmetric emission of the disk, thus substructure or asymmetries are not modeled. Nevertheless, the size determination is not affected by the presence of substructure. More elaborated functions that account for these second order features can be used on the interferometric modeling described here.

The `Galario` package (Tazzari et al. 2018) is used to convert the empirical model into synthetic visibilities, and to compute the χ^2 between observed and synthetic visibilities. In addition, the affine invariant Markov Chain Monte Carlo method from Goodman & Weare (2010) is also used (via the `emcee` package Foreman-Mackey et al. 2013) to investigate

the parameter space, optimizing for models with the lowest χ^2. This is done for 200 independent walkers for thousands of steps. After a number of steps the values of the free parameters converge to those that provide the best fit between synthetic and observed visibilities. Due to expensive computation time required to model the large set of visibilities from DSHARP observations, baselines > 1000 $k\lambda$ are excluded from the fit.

As an example, in the following figures of this Appendix we present the results of the interferometric modeling of the Sz 71 CO disk fitted to a Nuker model. The fitting tool converges to the models with lowest χ^2. In Figure E.1, we show the fit of the visibilities: real and imaginary part of observed and synthetic (for the model with lowest χ^2) visibilities as a function of baseline. Once the fitting tool has converged, the subsequent Markov Chain

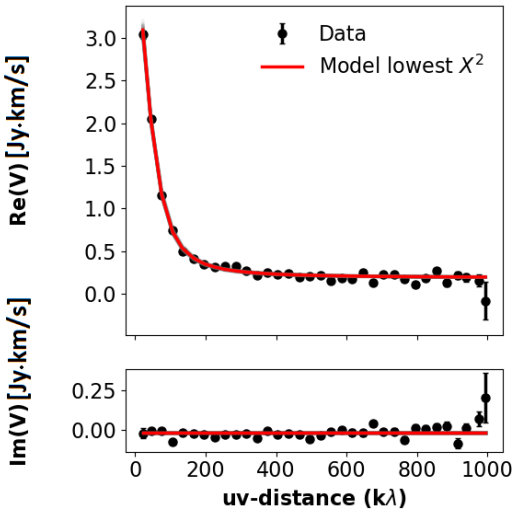

Figure E.1: Observed and model visibilities of Sz 71 CO emission, plotted as real (*top*) and imaginary (*bottom*) parts as a function of the baseline (in kλ). The data from the observations are plotted as black data points with error bars, the model with the lowest χ^2 is shown as solid red curve, and a random set of converged models from the parameter space investigation are drawn as gray curves (mostly covered by the lowest χ^2 model). This figure was made with the `uvplot` Python package (Tazzari 2017).

Monte Carlo method (MCMC) chains store the values of the parameters that fit best to the observed visibilities. Histograms of the free parameters are build from these chains. The median of each parameter histogram are taken as the best value of the parameter, and the 16th and 84th percentiles are used as lower and upper uncertainties. The 1D and 2D histograms between model parameters are plotted in Figure E.2.

Additionally, in order to have an idea of the quality of the interferometric modeling, we show the observed, modeled and residual moment zero maps of CO reconstructed from the visibilities in Figure E.3. In order to visualize the differences between the Nuker modeling and the Gaussian modeling in the *uv*-plane, we also include the reconstructed maps of the Gaussian fit in Figure E.3.

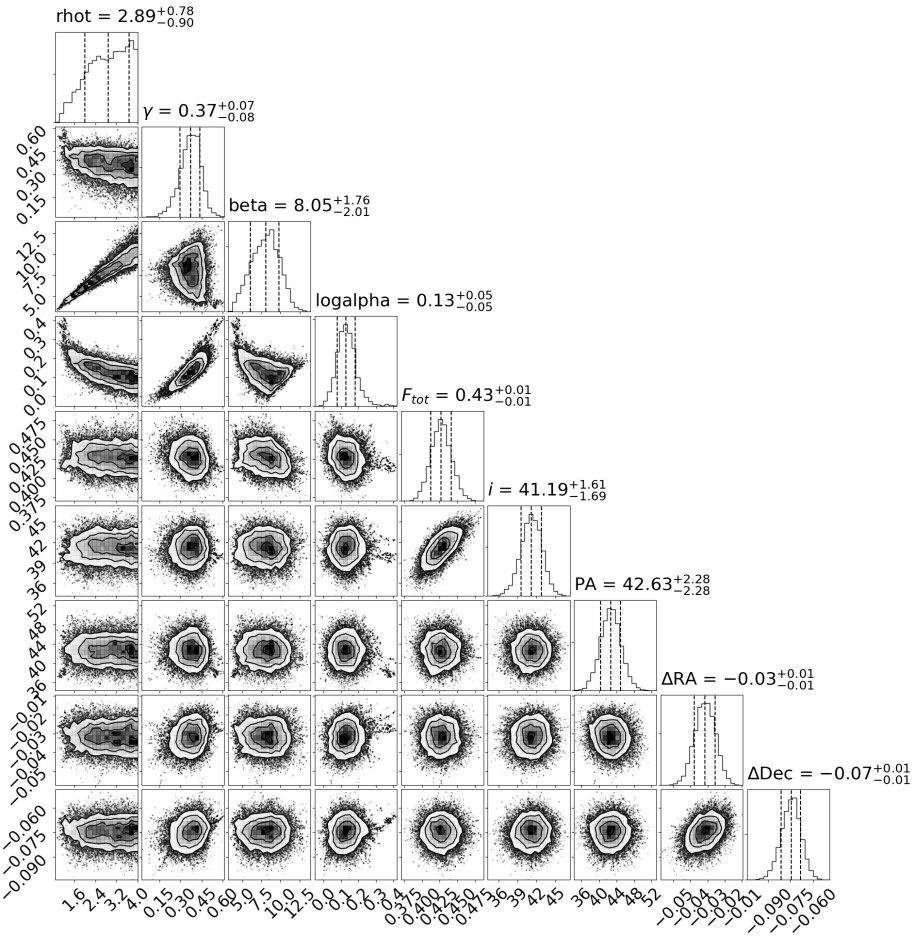

Figure E.2: Corner plot of the Nuker fitting of the observed CO visibilities. The top sub-panels show the histograms of the free parameters from the MCMC chains. The remaining sub-panels show the 2-dimensional histograms between pairs of parameters.

The cumulative distribution function ($f_{\rm cumul}$) for each model is built from the converged chains. From the cumulative distribution, we estimate the $R_{68\%}$, $R_{90\%}$, and $R_{95\%}$ CO radii of each model, and build histograms of each radius. The main value and lower/upper uncertainties of each radius are the median, 16th/84th percentiles of the respective histograms. The cumulative distribution and mean radii values for the modeled CO disk of Sz 71 are shown in Figure E.4.

The CO radii results from the interferometric modeling (fitting a Nuker and a Gaussian function) of all the DSHARP disks can be found in Table F.1 of Appendix F. The Sz 68 CO disk was excluded from the interferometric modeling since it is part of a multiple system that is unresolved in the Lupus disk survey. Additionally, the CO integrated emission from the DSHARP survey is irregular; its shape does not resemble a smooth disk.

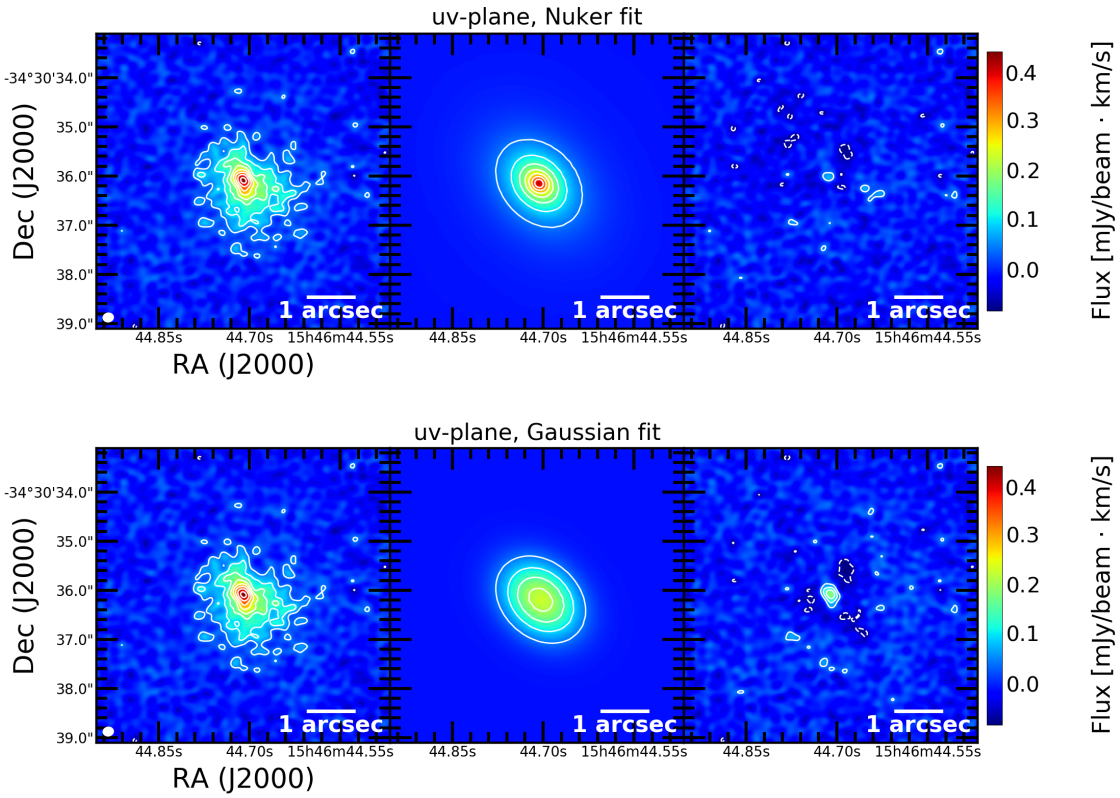

Figure E.3: Reconstructed moment zero maps from fitting in the *uv*-plane the observed CO emission around GW Lup (Sz 71) using a Nuker profile model (*top panels*) and an elliptical Gaussian function (*bottom panels*). For each model, the sub-panels represent the observed (*left*), modeled (*center*) and residual (*right*) reconstructed CO maps.

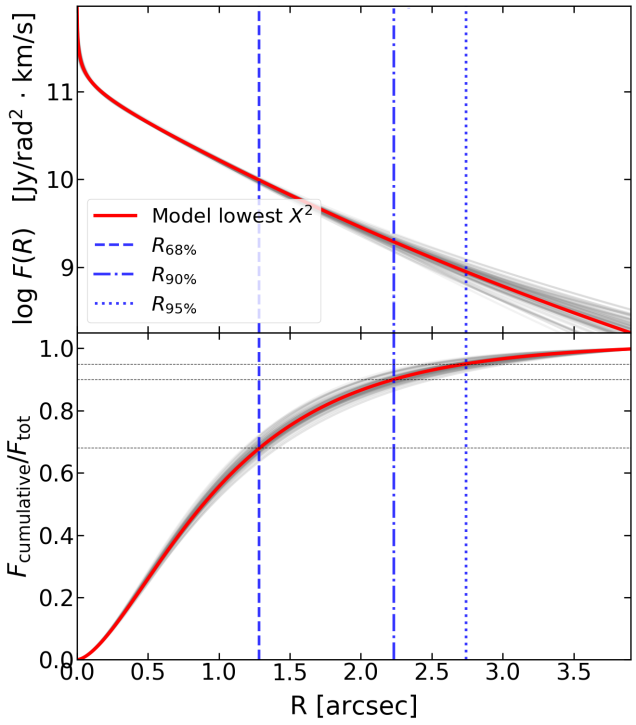

Figure E.4: Radial brightness profile (*top panel*) and the associated cumulative flux (*bottom panel*) modeled for the CO emission of Sz 71 fitted to a Nuker profile. The emission distribution of the model with lowest χ^2 from the fit is drawn as red, while a subset of converged models are shown as thin gray curves.

Appendix F

Results of CO sizes using different methodology

In this Appendix we summarize the CO radii obtained by different modeling (Table F.1) for the two datasets (Lupus disk survey, and DSHARP project). The different models considered are: the interferometric modeling of the DSHARP visibilities fitting Nuker and Gaussian functions, and the elliptical Gaussian modeling in the image plane for the two datasets, and the Nuker fit in the image plane for the lower sensitivity and resolution dataset. These results are used to assess the systematic uncertainties of the modeling described in Section 4.3.1. Lastly, in Figure F.1, we compare CO radii obtained from the elliptical Gaussian modeling in the image plane of the lower sensitivity dataset (as described in Section 4.3.1) with the CO radii from the interferometric fit of a Nuker modeling of the DSHARP data (explained in Section E) for the same objects. The radii based on the interferometric modeling of the DSHARP data are considered as the fiducial CO sizes of the disks. This comparison is used in Section 4.3.1 to assess the quality of the elliptical Gaussian modeling.

Table F.1: CO radii of protoplanetary disks in Lupus observed in the DSHARP survey, inferred from modeling in the image and in the *uv*-plane, using two different datasets (Lupus disk survey, and DSHARP observations).

	Lupus disk survey						*DSHARP survey*					
	image Gaussian		*image Nuker*				*image Gaussian*		*uv-pl. Gaussian*		*uv-pl. Nuker*	
Object	$R_{68\%}$ [']	$R_{68\%}$ [']	$R_{90\%}$ [']	$R_{95\%}$ [']			$R_{68\%}$ [']		$R_{68\%}$ [']		$R_{90\%}$ [']	$R_{95\%}$ [']
MY Lup	0.81 ± 0.10	0.85 ± 0.07	1.22 ± 0.10	1.35 ± 0.11			0.81 ± 0.02		$0.81^{+0.01}_{-0.01}$		$1.12^{+0.03}_{-0.03}$	$1.27^{+0.04}_{-0.04}$
Sz 71	0.87 ± 0.13	0.97 ± 0.10	1.39 ± 0.19	1.51 ± 0.22			0.89 ± 0.03		$0.88^{+0.02}_{-0.02}$		$2.23^{+0.10}_{-0.10}$	$2.74^{+0.12}_{-0.13}$
Sz 82	2.14 ± 0.06	3.75 ± 0.67	6.09 ± 0.78	6.98 ± 0.76			2.52 ± 0.04		$2.64^{+0.01}_{-0.01}$		$5.45^{+0.01}_{-0.02}$	$6.01^{+0.01}_{-0.01}$
Sz 83	0.69 ± 0.04	1.44 ± 0.13	2.18 ± 0.21	2.38 ± 0.23			0.76 ± 0.03		$0.71^{+0.01}_{-0.01}$		$2.43^{+0.04}_{-0.04}$	$3.01^{+0.03}_{-0.04}$
Sz 114	0.74 ± 0.15	0.86 ± 0.08	1.09 ± 0.10	1.15 ± 0.11			0.79 ± 0.04		$0.79^{+0.02}_{-0.02}$		$1.33^{+0.06}_{-0.05}$	$1.53^{+0.07}_{-0.07}$
Sz 129	0.76 ± 0.16	0.75 ± 0.06	0.99 ± 0.09	1.05 ± 0.10			0.60 ± 0.02		$0.58^{+0.01}_{-0.01}$		$0.83^{+0.04}_{-0.03}$	$0.94^{+0.08}_{-0.04}$

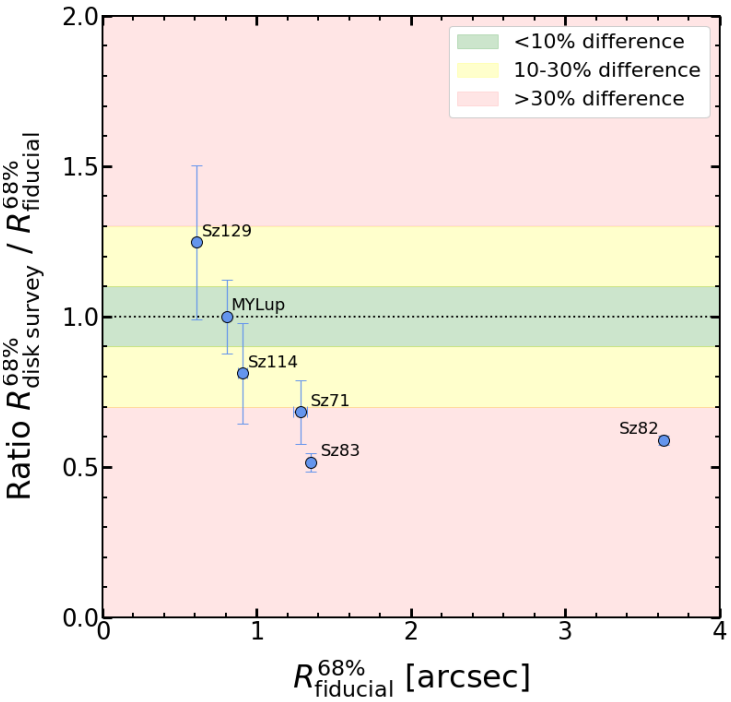

Figure F.1: Comparison between the CO radial extent of objects with two datasets (Lupus disk survey and DSHARP project). The Y-axis shows the ratio between the radius from the Lupus disk survey (obtained by fitting an elliptical Gaussian model in the moment zero map) divided by the fiducial radius of the CO disk. The fiducial CO size is considered as the size inferred from the DSHARP dataset by interferometric fitting of the line visibilities with a Nuker model (interferometric modeling described in Appendix E). The X-axis represents the fiducial size to ease the comparison. The colored regions indicate disks with a divergence in sizes below 10% (green region), between and 10 and 30% (yellow), and greater than 30% (red).

Appendix G

Criterion to model CO in the image plane based on the residuals

The residuals are quantified as the sum of emission enclosed by the inferred $R_{68\%}$ and centered at the elliptical Gaussian centroid in the residual map. Absolute values are used to account for negative residuals. This quantity is also computed on the observed moment zero map centered on the object, and on an emission-free region of the sky (averaged over four random locations in the background). Two quantities are used as the criteria for the quality of the fit: the residuals over background fraction $\frac{\sum|F_{\rm res}|}{\sum|F_{\rm BG}|}$, and the difference between residuals and background over the observed disk emission $\frac{\sum|F_{\rm res}|-\sum|F_{\rm BG}|}{\sum|F_{\rm disk}|}$. A value of 1 in the first quantity means that the residuals of the model are indistinguishable from the background emission. The second quantity gives an idea of what is the fraction of residuals over the observed disk emission; in this case, a 0 value represents a perfect model. These quantities are used together with the size ratio between the model and the fiducial size of each disk to evaluate the quality of each model. The results for elliptical Gaussian models are shown in the two sub-panels of Figure G.1, for those disks in which we have the two (moderate and high resolution) datasets. The red lines in both panels represent the median (μ), and $\mu \pm \sigma$ for the entire Lupus CO disks sample of the respective quantity. For both quantities, the four disks within the region delimited by the $\mu \pm \sigma$ region (Sz 71, Sz 114, Sz 129, and MY Lup) have all a size divergence with the fiducial CO size between 0% and $\sim 30\%$. On the other hand, Sz 82 and Sz 83 fall clearly outside; these disks show a larger divergence in size, both $> 40\%$ difference respect to the fiducial size.

From this analysis, elliptical Gaussian modeling of disks with residuals within the $\mu \pm \sigma$ range of the sample (as in Figure G.1) provide CO sizes with an accuracy between 0 to $\sim 30\%$. Gaussian models of disks with residuals outside the valid range can differ more than 40% with respect to the fiducial value. Therefore, for disks with residuals outside the $\mu \pm \sigma$, their CO emission should not be modeled with a Gaussian function, and instead is modeled by fitting their integrated maps with a Nuker profile (as described in Section 4.3.1). We also tested the quality of the sizes inferred from the Nuker profile modeling in the image plane. The size ratio between the Nuker model in the image plane and the fiducial model

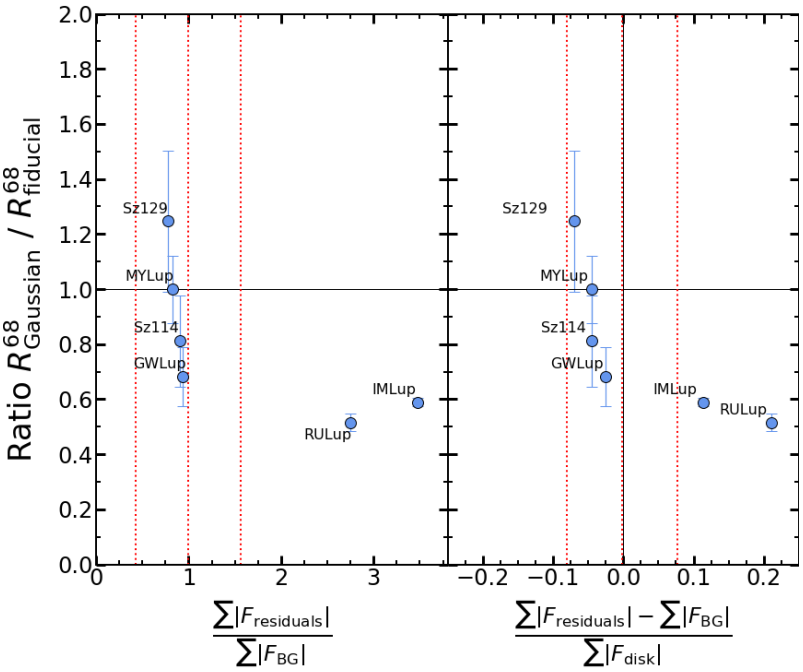

Figure G.1: CO size ratio compared to the residuals from the elliptical Gaussian modeling for the 6 disks with two datasets available. The fiducial radii are the sizes obtained from the interferometric modeling of the visibilities from the DSHARP dataset, following the methodology described in Appendix E. Size ratio as a function of residuals over background fraction (criterion 1; *left panel*). Size ratio vs. the difference between residuals and background over the observed disk emission (criterion 2; *right panel*). Central red line represents the median value of the entire Lupus sample, left and right vertical lines are the $\mu \pm \sigma$ values.

is represented as a function of the Nuker model residuals in Figure G.2. The results show that the inferred radii are in better agreement with the fiducial sizes than the Gaussian modeling. The size difference is found to be $\sim 0 - 30\%$ for every disk, and this remains true for the three radii ($R_{68\%}$, $R_{90\%}$, and $R_{95\%}$).

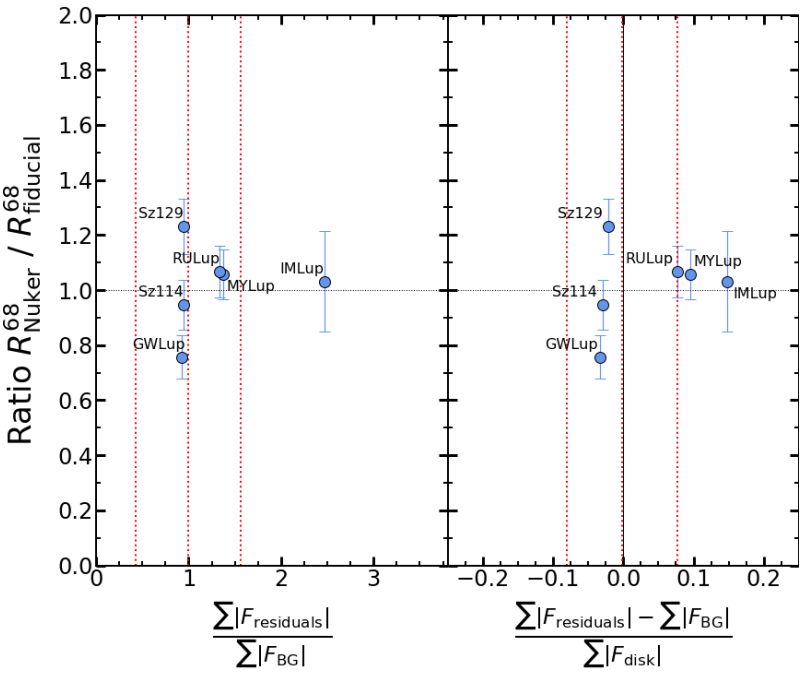

Figure G.2: Residuals criteria for the Nuker modeling of the 6 disks with two datasets available. The fiducial radii are the sizes obtained from the interferometric modeling of the visibilities from the DSHARP dataset, following the methodology described in Appendix E. Size ratio as a function of residuals over background fraction (criterion 1; *Left panel*). Size ratio vs. the difference between residuals and background over the observed disk emission (criterion 2; *right panel*). Red vertical lines identical to the ones in Figure G.1.

Appendix H

Best fit parameters for CO disks modeled with a Nuker function

Table H.1: Optimal parameters of the Nuker model used to fit the CO integrated emission of several sources from the full Lupus sample, based on the criteria described in Appendix G. The modeling of the integrated line emission is performed following the methodology from Section 4.3.1. The parameters of the Nuker function are: the transition radius ρ_t, the inner and outer slopes γ and β, the smoothing parameter α, and the integrated total flux $F_{\rm tot}$. An additional parameter ($\rho_{\rm end}$) is the outermost radius of the model, set to coincide with the radial distance at which the azimuthally averaged line emission reaches a zero value.

#	Object	ρ_t [″]	γ [-]	β [-]	α [-]	$F_{\rm tot}$ [mJy/beam]	$\rho_{\rm end}$ [″]
1	EXLup	1.20 ± 0.15	-0.09 ± 0.01	6.86 ± 0.63	1.23 ± 0.04	296 ± 1	1.4
2	RYLup	0.37 ± 0.01	-0.01 ± 0.01	2.38 ± 0.05	2.25 ± 0.08	952 ± 9	2.7
3	Sz75	0.58 ± 0.02	0.10 ± 0.01	2.83 ± 0.10	2.61 ± 0.09	448 ± 3	1.9
4	Sz82	6.93 ± 1.42	-0.10 ± 0.01	6.21 ± 0.74	0.93 ± 0.03	2824 ± 14	8.2
5	Sz83	0.20 ± 0.01	0.01 ± 0.01	1.58 ± 0.02	2.33 ± 0.11	748 ± 7	2.6
6	Sz91	0.38 ± 0.01	0.01 ± 0.01	1.99 ± 0.04	2.00 ± 0.07	268 ± 2	2.5
7	Sz111	0.22 ± 0.01	0.06 ± 0.01	1.23 ± 0.01	6.49 ± 0.44	598 ± 4	3.2
8	V1192Sco	0.31 ± 0.01	-0.14 ± 0.01	1.96 ± 0.05	3.42 ± 0.21	141 ± 1	1.8
9	J160703.9	0.71 ± 0.01	0.07 ± 0.01	2.38 ± 0.08	10.00 ± 1.33	139 ± 1	1.7
10	J160830.7	0.53 ± 0.01	-0.07 ± 0.01	2.22 ± 0.02	3.03 ± 0.06	1187 ± 4	2.7

Appendix I

Observed, model and residual CO maps of the Lupus disk population

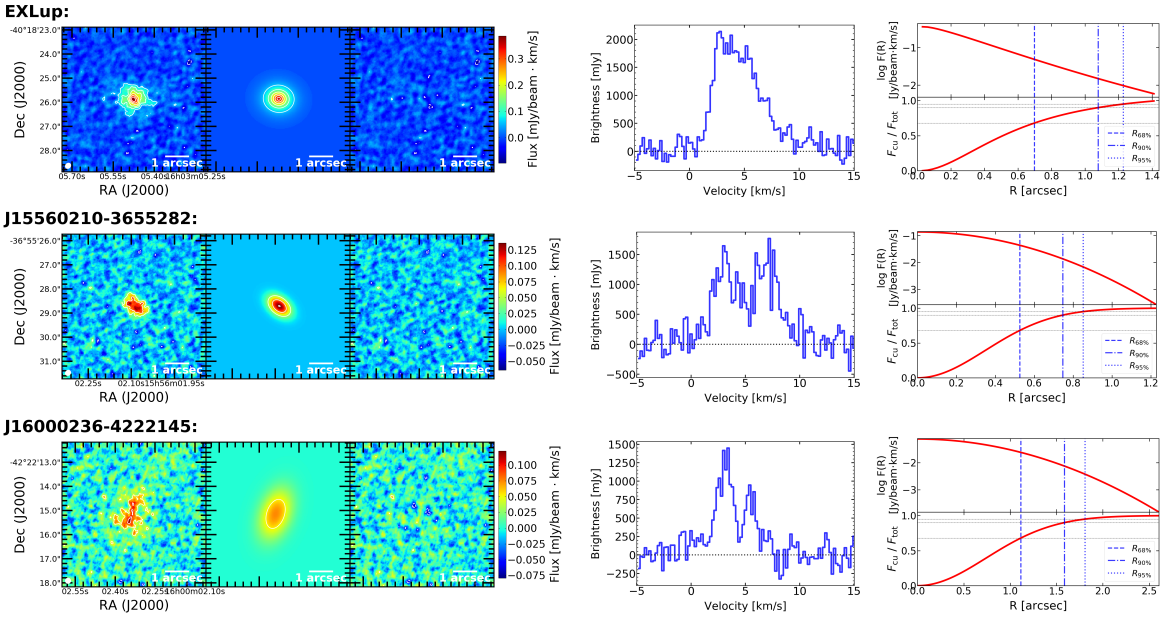

Figure I.1: Results of the CO modeling for every disk with measured CO size, following the methodology described in Section 4.3.1. For each disk, the first three sub-panels show the observed, model and residual CO moment zero maps; solid (dashed) line contours are drawn at increasing (decreasing) 3σ intervals. The forth sub-panel represents the integrated spectrum enclosed by the $R_{68\%}^{\rm CO}$. Last sub-panel shows the radial brightness profile and the respective cumulative distribution of the CO model.

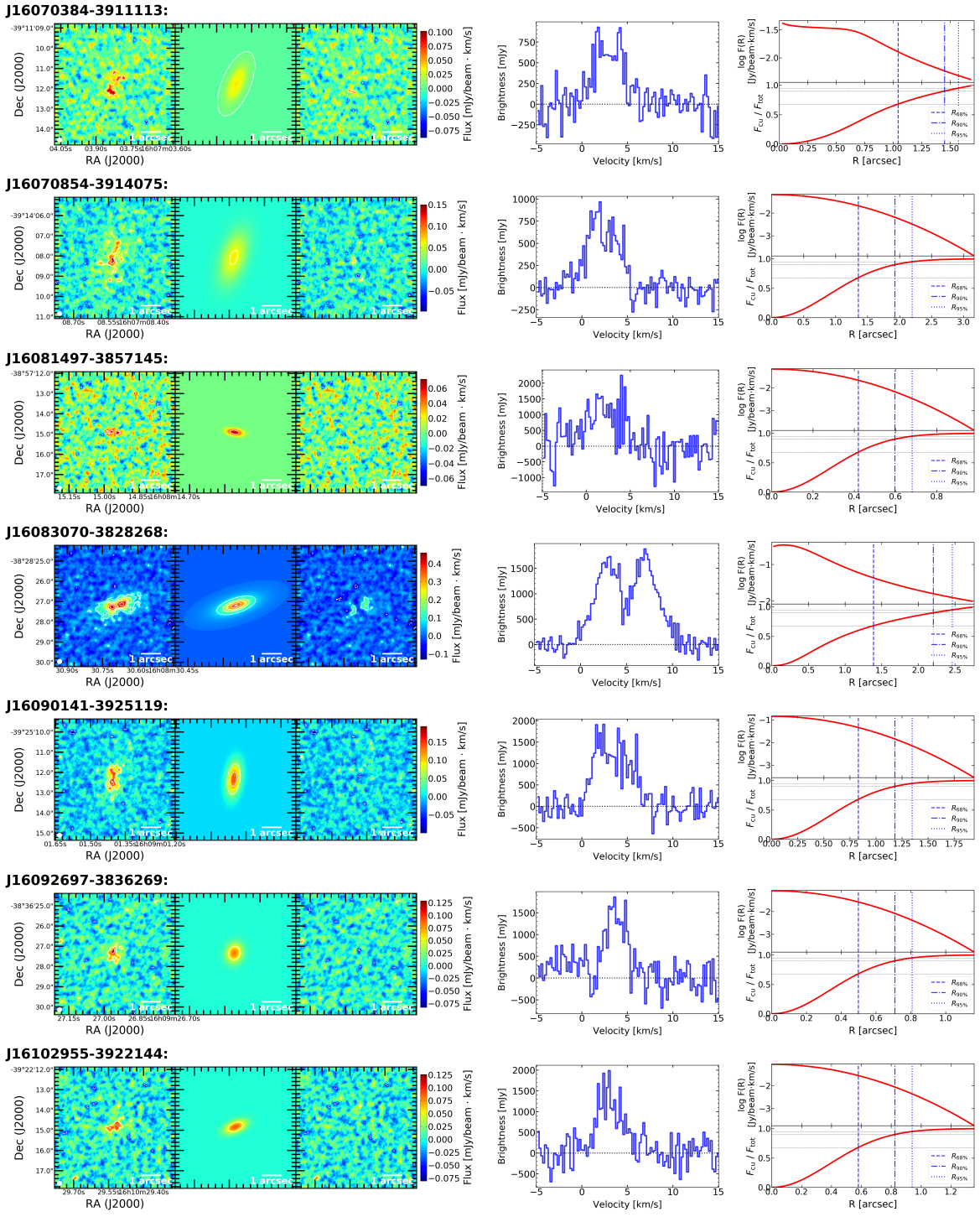

Figure I.2: Results of the CO modeling for every disk with measured CO size, following the methodology described in Section 4.3.1. For each disk, the first three sub-panels show the observed, model and residual CO moment zero maps; solid (dashed) line contours are drawn at increasing (decreasing) 3σ intervals. The forth sub-panel represents the integrated spectrum enclosed by the $R_{68\%}^{\rm CO}$. Last sub-panel shows the radial brightness profile and the respective cumulative distribution of the CO model.

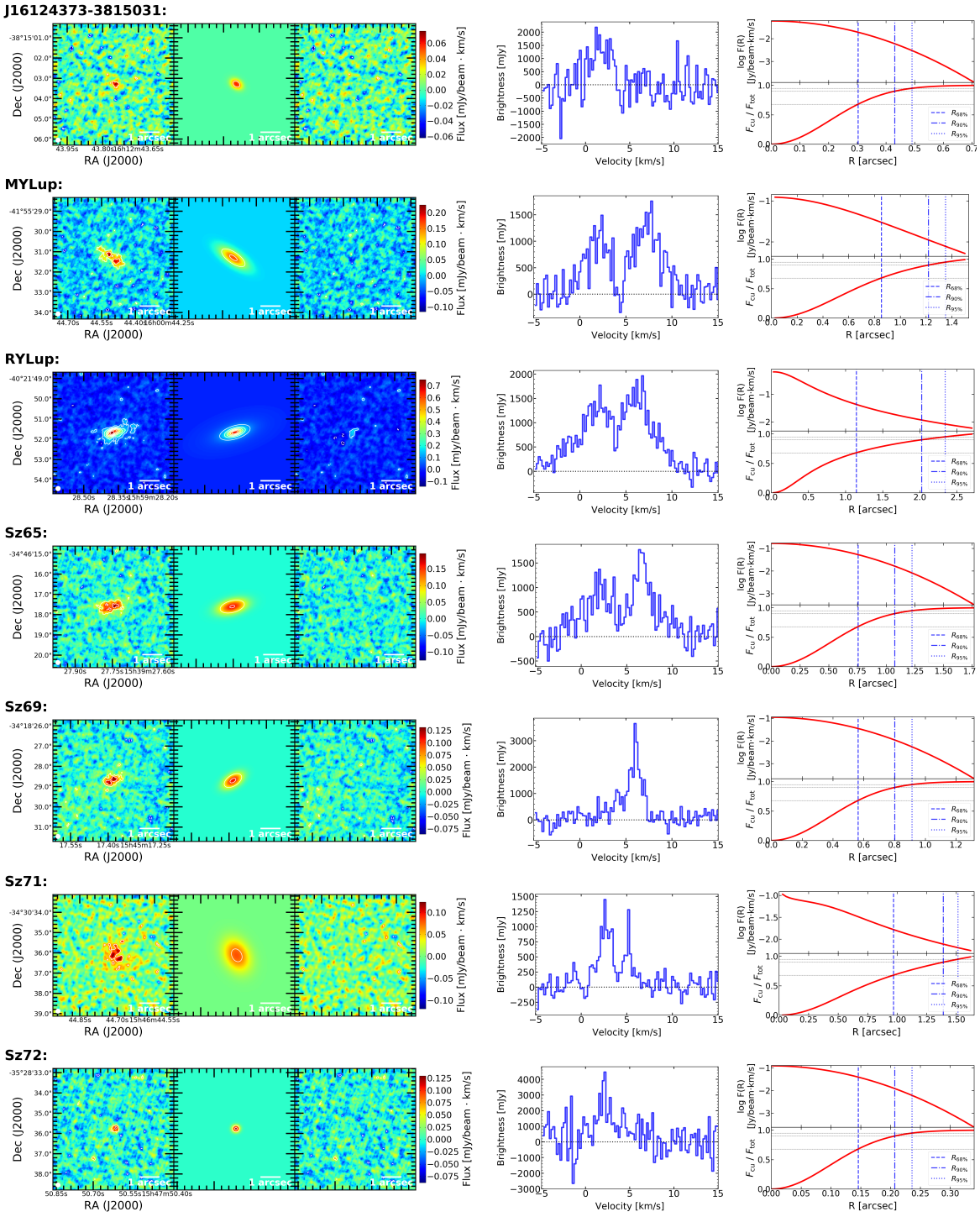

Figure I.3: Results of the CO modeling for every disk with measured CO size, following the methodology described in Section 4.3.1. For each disk, the first three sub-panels show the observed, model and residual CO moment zero maps; solid (dashed) line contours are drawn at increasing (decreasing) 3σ intervals. The forth sub-panel represents the integrated spectrum enclosed by the $R_{68\%}^{\rm CO}$ of the source. Last sub-panel shows the radial brightness profile and the respective cumulative distribution of the CO model.

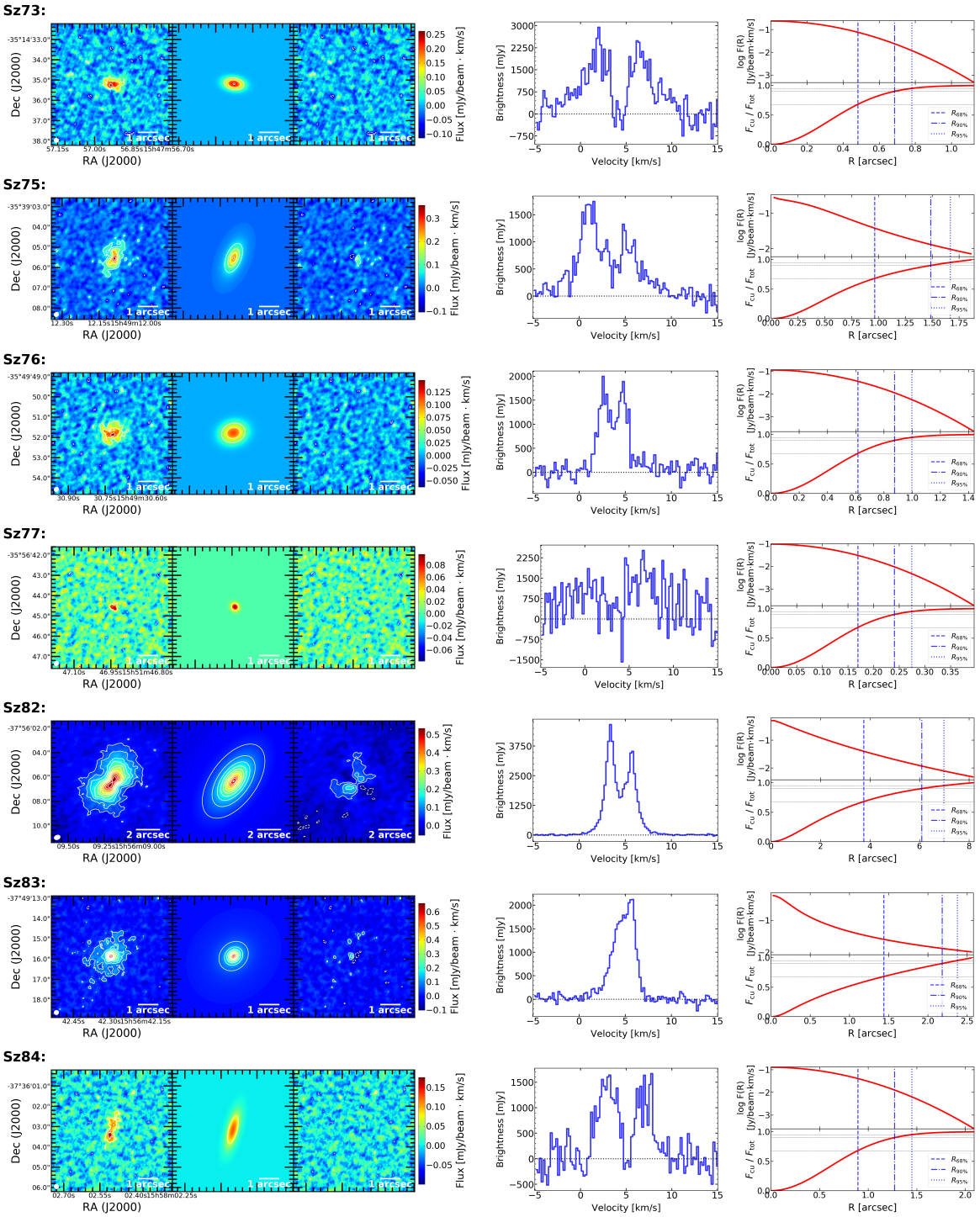

Figure I.4: Results of the CO modeling for every disk with measured CO size, following the methodology described in Section 4.3.1. For each disk, the first three sub-panels show the observed, model and residual CO moment zero maps; solid (dashed) line contours are drawn at increasing (decreasing) 3σ intervals. The forth sub-panel represents the integrated spectrum enclosed by the $R_{68\%}^{\rm CO}$ of the source. Last sub-panel shows the radial brightness profile and the respective cumulative distribution of the CO model.

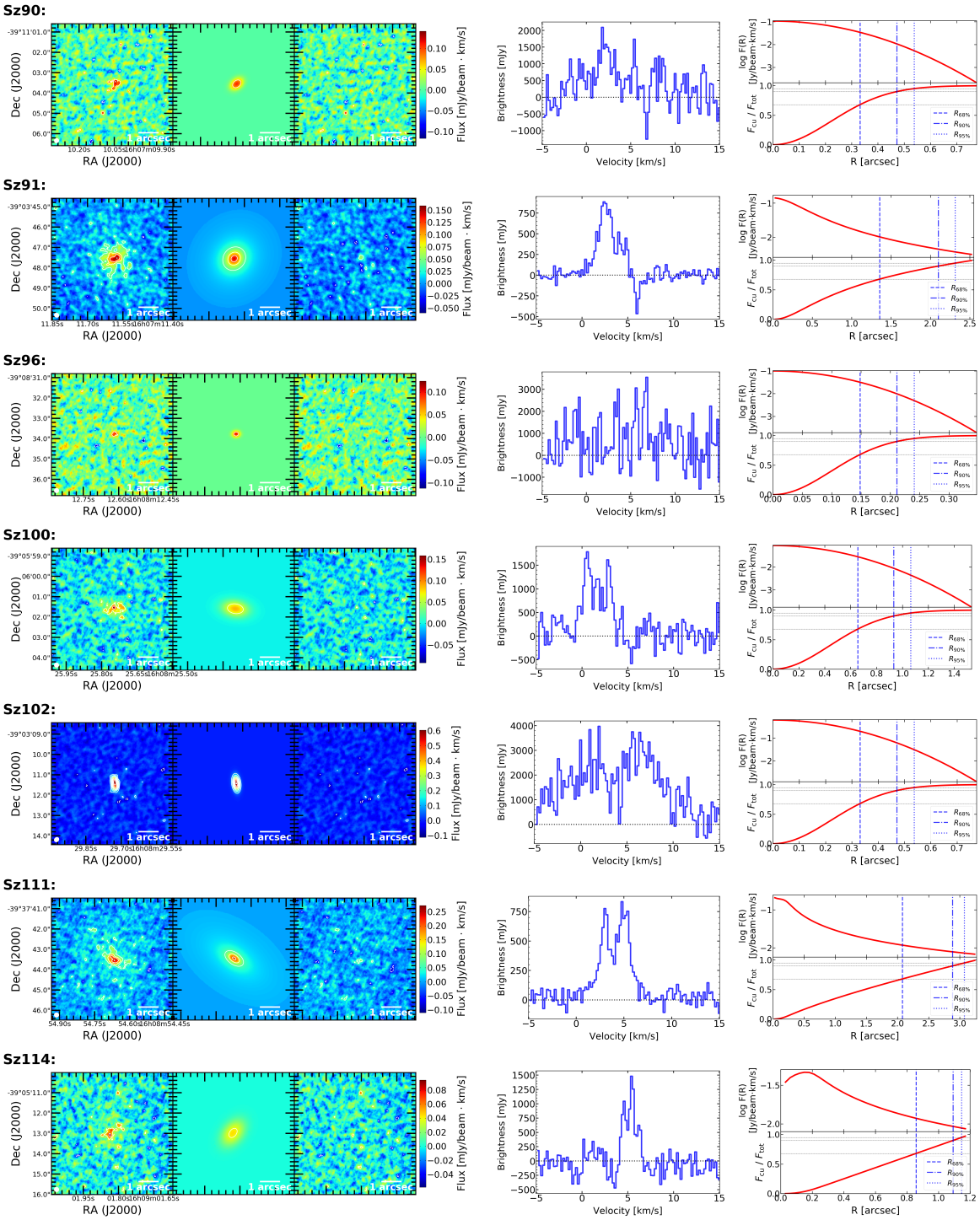

Figure I.5: Results of the CO modeling for every disk with measured CO size, following the methodology described in Section 4.3.1. For each disk, the first three sub-panels show the observed, model and residual CO moment zero maps; solid (dashed) line contours are drawn at increasing (decreasing) 3σ intervals. The forth sub-panel represents the integrated spectrum enclosed by the $R_{68\%}^{\rm CO}$ of the source. Last sub-panel shows the radial brightness profile and the respective cumulative distribution of the CO model.

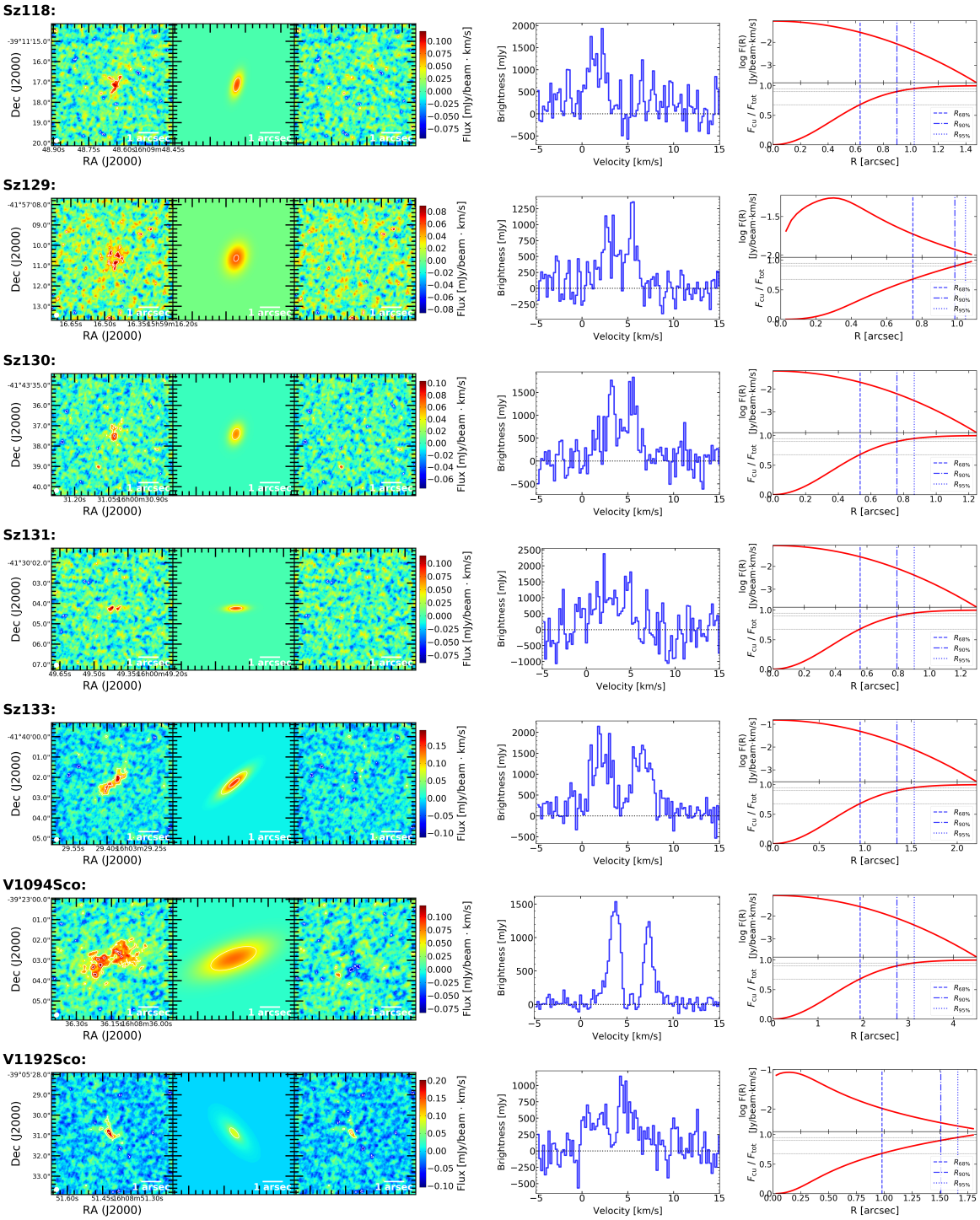

Figure I.6: Results of the CO modeling for every disk with measured CO size, following the methodology described in Section 4.3.1. For each disk, the first three sub-panels show the observed, model and residual CO moment zero maps; solid (dashed) line contours are drawn at increasing (decreasing) 3σ intervals. The forth sub-panel represents the integrated spectrum enclosed by the $R_{68\%}^{\rm CO}$ of the source. Last sub-panel shows the radial brightness profile and the respective cumulative distribution of the CO model.

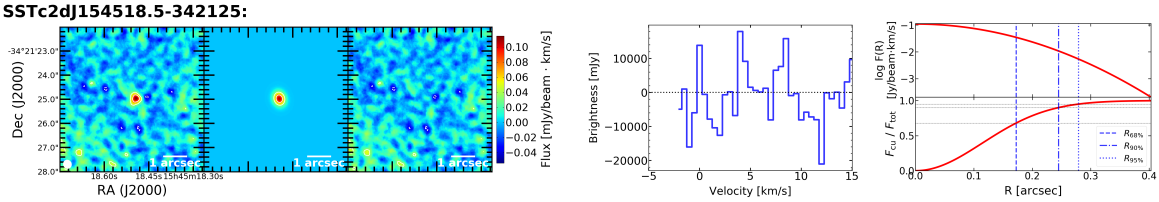

Figure I.7: Results of the CO modeling for every disk with measured CO size, following the methodology described in Section 4.3.1. For each disk, the first three sub-panels show the observed, model and residual CO moment zero maps; solid (dashed) line contours are drawn at increasing (decreasing) 3σ intervals. The forth sub-panel represents the integrated spectrum enclosed by the $R_{68\%}^{\rm CO}$ of the source. Last sub-panel shows the radial brightness profile and the respective cumulative distribution of the CO model.

Appendix J

Singular disks in Lupus

In this Section we discuss unusual systems in the Lupus sample, namely, outliers of the size ratio distribution, or those with particular known features.

J.1 Sz 75

The Sz 75 system (or GQ Lup) has a central star of 0.8 $M_{\odot}$, a sub-stellar companion at an angular separation of $\sim 0.7''$ (Neuhäuser et al. 2005) of uncertain mass (likely in the BD regime, Seifahrt et al. 2007; Neuhäuser et al. 2008; Lavigne et al. 2009), and a second companion candidate at $16''$ of ~ 0.15 $M_{\odot}$ that is likely gravitationally bound to the central object (Alcalá et al. 2020). The first companion is within the pointing of the ALMA observations, but no ^{12}CO or continuum emission is detected around it. The second companion candidate falls outside the ALMA pointing, however, its disk is detected in archival *HST* and *WISE* data (Lazzoni et al. 2020).

The disk of the central star has the largest size-ratio of the entire Lupus population (size ratio of ~ 8). Previous ALMA observations (MacGregor et al. 2017; Long et al. 2020), yielded consistent results of the ^{12}CO (3-2) and dust continuum extent. The compact continuum emission together with the large size ratio confirms that radial drift has been particularly efficient in the disk around the central star. Whether the presence of companions has boosted the radial drift process is unknown, follow-up studies on this system are needed in order to address this question.

The CO disk around the central star (with $R_{95\%}^{\rm CO} = 1.7''$) extents beyond the deprojected distance between central star and the sub-stellar companion, considering the companion's orbital inclination to be $\sim 60^{\circ}$ as suggested by Schwarz et al. (2016a). This is contrary to expected tidal truncation effects (e.g., Martin & Lubow 2011; Bate 2018), possibly due to the sub-stellar nature of this companion. Additionally, the CO channel maps do not show any distortion due to the presence of the sub-stellar object.

The formation mechanism of the system is unclear. A possible scenario, suggested by Alcalá et al. (2020), is that the central star and the second companion might be formed by fragmentation of a turbulent core. Likewise, the formation of the primary companion is

uncertain (MacGregor et al. 2017): if due to fragmentation of the circumprimary disk, it would result in a relatively massive disk around the sub-stellar companion; while formation close the the central star and posterior scattering outwards is a less favored explanation (Bryan et al. 2016).

J.2 Sz 83

This source (also known as RU Lup) is one of the most active young stars of the Lupus clouds (Comerón 2008). The CO/dust size ratio measured is very large (of $\simeq 5$). However, the result should be taken with caution, since the structure of this disk is highly complex, with outflows, jets and mild cloud contamination (Herczeg et al. 2005; Ansdell et al. 2018; Andrews et al. 2018a).

Recent high angular resolution observations of the ^{12}CO, ^{13}CO, C^{18}CO and DCO$^+$ lines showed an intricate structure of the gas in this system, with a central keplerian disk, an extended diffuse emission, spiral arms, and various 'clumps' of emission (Huang et al. 2020). The CO size reported in that work distinguishes between a keplerian disk of $\sim 0.75''$, non-keplerian CO emission of $\sim 1.6''$, spiral structure up to $\sim 6''$, and 'clumps' further out. Although they did not report values of $R_{68\%}$, our $R_{95\%}$ is slightly larger than the non-keplerian emission reported in (Huang et al. 2020). Since our measurement considers any detected emission (from the ^{12}CO $J = 2 - 1$ line observed from the ALMA Band 6 Lupus disk survey), our size is likely accounting part of the spiral structure.

However, the difference between the gas and the dust size is expected to be large, based on the recent studies of the system (e.g., Huang et al. 2020), and, in addition, our dust size coincides with previous works (e.g., Andrews et al. 2018b; Hendler et al. 2020). For consistency, we use our inferred CO size along this manuscript, but we warn that, due to the complex structure of this system, the true extent of the CO disk might differ with respect our tabulated values.

J.3 Sz 131

This is a single star system (0.3 $M_\odot$ mass), and has as well a very high size ratio ($\sim$ 7.2), although with high uncertainty. The large size ratio is driven by the very compact continuum emission, of only $0.08''$. The high uncertainty is caused by the very faint emission in both ^{12}CO and continuum, resulting in large error bars of the $R_{\rm CO}$ and $R_{\rm dust}$ sizes. Even considering the upper and lower bounds of the dust and CO sizes respectively, the ratio lays above 4, setting a strong evidence for dust evolution and radial drift.

J.4 Sz 111

The Sz 111 system is another single star (of 0.5 $M_\odot$ mass), with a bright disk in both continuum and ^{12}CO. Its size ratio is slightly above the 4 threshold, dominated by the

CO disk extent, which is among the largest CO disks of the Lupus population ($R_{68\%}^{\rm CO} = 2.1 \pm 0.4''$). Due to its extended emission in both CO and dust continuum, this system is a good candidate for future ALMA observations at higher resolution and sensitivity to better constrain the radial drift, and to resolve possible substructures as the aftermath of dust evolution.

J.5 Sz 69

Sz 69 (HW Lup) is part of a wide visual binary together with 2MASS J15451720-3418337, a source in Southwest direction at $\sim 6.6''$ of angular separation (Merín et al. 2008). The second element of the binary is undetected in dust continuum nor in CO.

The dusty disk around Sz 69 is extremely compact and partially unresolved, with a $R_{68\%}^{\rm dust} < 0.09''$. Due to its compact continuum emission, the CO/dust size ratio is particularly high, with a lower bound value of 5.7. Using the dust disk size from Andrews et al. (2018b), the size ratio would be 9.3. Such a high value of the size ratio points towards extremely efficient radial drift. The angular separation between the binary components is larger than the distances at which dynamical interactions would typically alter the circumprimary disk (e.g., Jensen et al. 1996; Bate 2000; Harris et al. 2012). A better characterization of the second source is necessary in order to understand this system in more detail.

J.6 Sz 65

The disk around Sz 65 (0.7 $M_\odot$) has a size ratio of 4.8, it is therefore another disk with ratio above the threshold value of 4. It forms a binary system together with Sz 66 (0.3 $M_\odot$), angular separation of $\sim 6.4''$. The disk around the second component is very faint in both ^{12}CO and dust continuum (with a size ratio of about 2.5), the size of the CO disk could not be constrained due to its compactness.

This is another multiple system in which the primary element has a very large size ratio, this case is particularly appealing since CO and dust are detected in the two components. Observations at higher sensitivity and resolution of the two components will greatly help understanding the level of dust evolution of the two disks. Intriguingly, Sz 65 accretion is weak and considered to be only an upper limit (its excess emission is close to the chromospheric levels, Alcalá et al. 2017), while accretion in Sz 66 is slightly above the known correlation with the continuum flux (see, e.g., Manara et al. 2016b; Alcalá et al. 2017; Sanchis et al. 2020b).

J.7 Sz 82

Sz 82 (IM Lup) is the brightest object of the entire Lupus disk population, both in ^{12}CO and in dust continuum emission. It is therefore among the most studied protoplanetary

disks. This disk is exceptionally large, its azimuthally averaged emission shows a plateau of emission that extents up to $\gtrsim$ 1000 AU. Extensive modeling of several CO lines at scales $<$ 450 was performed in Pinte et al. (2018a), and suggested that UV photo-desorption from the interstellar radiation field could explain the further out CO emission. In Cleeves et al. (2016), they discussed the possible origin of this diffuse emission: it could be the remnant of an envelope, a plausible explanation since the system is young ($\leq$ 1 Myr Mawet et al. 2012); gravitationally captured gas is another viable scenario, since the system has a Bondi radius of $\sim$ 3000 AU, far beyond the diffuse emission extent; foreground emission is less likely since there is an offset between the cloud velocity and the object.

J.8 Brown dwarfs/very low-mass stars

We would like to point out the results in the very low-mass range of the Lupus disk population. For that, we consider only disks orbiting around objects of masses below 0.2 $M_{\odot}$. Several of these objects were targeted in a separate survey (Sanchis et al. 2020b), and are of particular interest since their formation and evolution might differ from disks around more massive stars. Six disks in this mass range have inferred CO and dust sizes (Sz 84, Sz 100, Sz 114, SSTc2d J160703.9-391112, 2MASS J16081497-3857145, and SSTc2d J154518.5-342125). From theoretical modeling of the gas/dust sizes (Trapman et al. 2019), the measured sizes inferred from the emission extent can be affected by the resolution of the observations, and in objects whose emission extent is of the order of the beam size, the size ratios inferred could be lower than the true size ratios.

The median size ratio of disks around very low-mass stars is 3.1 (with a dispersion of 0.4), larger than the mean value of the entire population. If the low resolution/beam size effect is indeed affecting the inferred CO and dust sizes of these compact sources, the true size ratio may be even larger than the observed values. Due to the low number of sources in this range is not yet possible to address whether radial drift in disks around this mass range is more efficient than in disks around more massive stars, as predicted theoretically in Pinilla et al. (2013). It is also worth noting that the only BD in the sample with inferred sizes has a ratio of 3.2, higher than the median of the entire disk population. Due to the faint and compact emission of this source, its size uncertainties are relatively large, thus it is difficult to address the true behavior of this disk. Follow-up observations at higher sensitivity and resolution for this source will allow us to better constrain its gas/dust size ratio.

Bibliography

1989, Astronomical Society of the Pacific Conference Series, Vol. 6, Synthesis imaging in radio astronomy : a collection of lectures from the third NRAO synthesis imaging summer school

1999, Astronomical Society of the Pacific Conference Series, Vol. 180, Synthesis Imaging in Radio Astronomy II

Acke, B., van den Ancker, M. E., & Dullemond, C. P. 2005, Astronomy & Astrophysics, 436, 209

Adachi, I., Hayashi, C., & Nakazawa, K. 1976, Progress of Theoretical Physics, 56, 1756

Adams, F. C., Lada, C. J., & Shu, F. H. 1987, The Astrophysical Journal, 312, 788

Alcalá, J. M., Majidi, F. Z., Desidera, S., et al. 2020, Astronomy & Astrophysics, 635, L1

Alcalá, J. M., Manara, C. F., France, K., et al. 2019, Astronomy & Astrophysics, 629, A108

Alcalá, J. M., Manara, C. F., Natta, A., et al. 2017, Astronomy & Astrophysics, 600, A20

Alcalá, J. M., Natta, A., Manara, C. F., et al. 2014, Astronomy & Astrophysics, 561, A2

Alexander, R., Pascucci, I., Andrews, S., Armitage, P., & Cieza, L. 2014, in Protostars and Planets VI, ed. H. Beuther, R. S. Klessen, C. P. Dullemond, & T. Henning, 475

Allers, K. N., Kessler-Silacci, J. E., Cieza, L. A., & Jaffe, D. T. 2006, The Astrophysical Journal, 644, 364

ALMA Cycle 7 Technical Handbook,. 2019, ALMA Doc. 7.3, ver. 1.1

ALMA Partnership, Brogan, C. L., Pérez, L. M., et al. 2015a, The Astrophysical Journal Letters, 808, L3

ALMA Partnership, Brogan, C. L., Pérez, L. M., et al. 2015b, The Astrophysical Journal Letters, 808, L3

André, P. 2002, in EAS Publications Series, Vol. 3, EAS Publications Series, ed. J. Bouvier & J.-P. Zahn, 1–38

André, P., Bouwman, J., Belloche, A., & Hennebelle, P. 2003, in SFChem 2002: Chemistry as a Diagnostic of Star Formation, ed. C. L. Curry & M. Fich, 127

André, P., Ward-Thompson, D., & Barsony, M. 1993, The Astrophysical Journal, 406, 122

André, P., Ward-Thompson, D., & Barsony, M. 2000, in Protostars and Planets IV, ed. V. Mannings, A. P. Boss, & S. S. Russell, 59

Andrews, S. M. 2015, Publications of the Astronomical Society of the Pacific, 127, 961

Andrews, S. M. 2020, Annual Review of Astronomy and Astrophysics, 58, 483

Andrews, S. M., Huang, J., Pérez, L. M., et al. 2018a, The Astrophysical Journal Letters, 869, L41

Andrews, S. M., Rosenfeld, K. A., Kraus, A. L., & Wilner, D. J. 2013, The Astrophysical Journal, 771, 129

Andrews, S. M., Terrell, M., Tripathi, A., et al. 2018b, The Astrophysical Journal, 865, 157

Andrews, S. M. & Williams, J. P. 2005, The Astrophysical Journal, 631, 1134

Andrews, S. M., Wilner, D., Hughes, M., Qi, C., & Dullemond, C. P. 2010, in Bulletin of the American Astronomical Society, Vol. 42, American Astronomical Society Meeting Abstracts #215, 527

Andrews, S. M., Wilner, D. J., Hughes, A. M., et al. 2012, The Astrophysical Journal, 744, 162

Anglada-Escudé, G., Amado, P. J., Barnes, J., et al. 2016, Nature, 536, 437

Ansdell, M., Williams, J. P., Manara, C. F., et al. 2017, The Astronomical Journal, 153, 240

Ansdell, M., Williams, J. P., Trapman, L., et al. 2018, The Astrophysical Journal, 859, 21

Ansdell, M., Williams, J. P., van der Marel, N., et al. 2016, The Astrophysical Journal, 828, 46

Apai, D., Pascucci, I., Brandner, W., et al. 2004a, Astronomy & Astrophysics, 415, 671

Apai, D., Pascucci, I., Sterzik, M. F., et al. 2004b, Astronomy & Astrophysics, 426, L53

Armitage, P. J. 2011, Annual Review of Astronomy and Astrophysics, 49, 195

Armitage, P. J., Simon, J. B., & Martin, R. G. 2013, The Astrophysical Journal Letters, 778, L14

Avenhaus, H., Quanz, S. P., Garufi, A., et al. 2018, The Astrophysical Journal, 863, 44

Bai, X.-N. & Stone, J. M. 2013, The Astrophysical Journal, 769, 76

Bai, X.-N. & Stone, J. M. 2017, The Astrophysical Journal, 836, 46

Bakos, G. Á., Noyes, R. W., Kovács, G., et al. 2007, The Astrophysical Journal, 656, 552

Balbus, S. A. & Hawley, J. F. 1991, The Astrophysical Journal, 376, 214

Ballering, N. P. & Eisner, J. A. 2019, The Astronomical Journal, 157, 144

Baraffe, I. & Chabrier, G. 2010, Astronomy & Astrophysics, 521, A44

Baraffe, I., Homeier, D., Allard, F., & Chabrier, G. 2015, Astronomy & Astrophysics, 577, A42

Barenfeld, S. A., Carpenter, J. M., Ricci, L., & Isella, A. 2016, The Astrophysical Journal, 827, 142

Basri, G. & Batalha, C. 1990, The Astrophysical Journal, 363, 654

Basri, G. & Bertout, C. 1989, The Astrophysical Journal, 341, 340

Bate, M. R. 2000, Monthly Notices of the Royal Astronomical Society, 314, 33

Bate, M. R. 2018, Monthly Notices of the Royal Astronomical Society, 475, 5618

Beckwith, S. V. W. & Sargent, A. I. 1991, The Astrophysical Journal, 381, 250

Beckwith, S. V. W., Sargent, A. I., Chini, R. S., & Guesten, R. 1990, The Astronomical Journal, 99, 924

Benisty, M., Stolker, T., Pohl, A., et al. 2017, Astronomy & Astrophysics, 597, A42

Berdyugina, S. V., Berdyugin, A. V., Fluri, D. M., & Piirola, V. 2008, The Astrophysical Journal Letters, 673, L83

Bergin, E. A., Cleeves, L. I., Gorti, U., et al. 2013, Nature, 493, 644

Bertout, C., Basri, G., & Bouvier, J. 1988, The Astrophysical Journal, 330, 350

Birnstiel, T., Dullemond, C. P., & Brauer, F. 2010, Astronomy & Astrophysics, 513, A79

Bisschop, S. E., Fraser, H. J., Öberg, K. I., van Dishoeck, E. F., & Schlemmer, S. 2006, Astronomy & Astrophysics, 449, 1297

Bixel, A. & Apai, D. 2017, The Astrophysical Journal Letters, 836, L31

Black, D. C. & Scargle, J. D. 1982, The Astrophysical Journal, 263, 854

Blum, J. & Münch, M. 1993, Icarus, 106, 151

Bonfils, X., Delfosse, X., Udry, S., et al. 2013, Astronomy & Astrophysics, 549, A109

Borucki, W. J., Koch, D., Basri, G., et al. 2010, Science, 327, 977

Boss, A. P. 1997, Science, 276, 1836

Boss, A. P. 1998, The Astrophysical Journal, 503, 923

Boss, A. P. 2000, The Astrophysical Journal Letters, 536, L101

Boyden, R. D. & Eisner, J. A. 2020, The Astrophysical Journal, 894, 74

Bradt, H. 2004, Astronomy Methods: A Physical Approach to Astronomical Observations

Briggs, D. S. 1995, in American Astronomical Society Meeting Abstracts, Vol. 187, American Astronomical Society Meeting Abstracts, 112.02

Bromley, B. C. & Kenyon, S. J. 2011, The Astrophysical Journal, 731, 101

Bryan, M. L., Bowler, B. P., Knutson, H. A., et al. 2016, The Astrophysical Journal, 827, 100

Bryden, G., Chen, X., Lin, D. N. C., Nelson, R. P., & Papaloizou, J. C. B. 1999, The Astrophysical Journal, 514, 344

Burke, C. J., Bryson, S. T., Mullally, F., et al. 2014, The Astrophysical Journal Supplement Series, 210, 19

Burrows, A., Guillot, T., Hubbard, W. B., et al. 2000, The Astrophysical Journal Letters, 534, L97

Burrows, A., Heng, K., & Nampaisarn, T. 2011, The Astrophysical Journal, 736, 47

Burrows, A., Hubeny, I., Budaj, J., & Hubbard, W. B. 2007, The Astrophysical Journal, 661, 502

Bustamante, I., Merín, B., Ribas, Á., et al. 2015, Astronomy & Astrophysics, 578, A23

Cabrit, S., Edwards, S., Strom, S. E., & Strom, K. M. 1990, The Astrophysical Journal, 354, 687

Cameron, P. B., Britton, M. C., & Kulkarni, S. R. 2009, The Astronomical Journal, 137, 83

Campbell, B., Walker, G. A. H., & Yang, S. 1988, The Astrophysical Journal, 331, 902

Canovas, H., Caceres, C., Schreiber, M. R., et al. 2016, Monthly Notices of the Royal Astronomical Society, 458, L29

Canup, R. M. 2004, Icarus, 168, 433

Canup, R. M. & Asphaug, E. 2001, Nature, 412, 708

Cardelli, J. A., Clayton, G. C., & Mathis, J. S. 1989, The Astrophysical Journal, 345, 245

Carmona, A. 2010, Earth Moon and Planets, 106, 71

Carr, J. S. & Najita, J. R. 2008, Science, 319, 1504

Cazzoletti, P., Manara, C. F., Baobab Liu, H., et al. 2019, Astronomy & Astrophysics, 626, A11

Ceccarelli, C., Dominik, C., Lefloch, B., Caselli, P., & Caux, E. 2004, The Astrophysical Journal Letters, 607, L51

Charbonneau, D., Brown, T. M., Latham, D. W., & Mayor, M. 2000, The Astrophysical Journal Letters, 529, L45

Charbonneau, D., Brown, T. M., Noyes, R. W., & Gilliland, R. L. 2002, The Astrophysical Journal, 568, 377

Chauvin, G., Desidera, S., Lagrange, A. M., et al. 2017, in SF2A-2017: Proceedings of the Annual meeting of the French Society of Astronomy and Astrophysics, ed. C. Reylé, P. Di Matteo, F. Herpin, E. Lagadec, A. Lançon, Z. Meliani, & F. Royer, Di

Chauvin, G., Lagrange, A. M., Dumas, C., et al. 2004, Astronomy & Astrophysics, 425, L29

Chiang, E. I. & Goldreich, P. 1997, The Astrophysical Journal, 490, 368

Chiar, J. E. & Tielens, A. G. G. M. 2006, The Astrophysical Journal, 637, 774

Chwolson, O. 1924, Astronomische Nachrichten, 221, 329

Cieza, L. A., Ruíz-Rodríguez, D., Perez, S., et al. 2018, Monthly Notices of the Royal Astronomical Society, 474, 4347

Clarke, C. J., Gendrin, A., & Sotomayor, M. 2001, Monthly Notices of the Royal Astronomical Society, 328, 485

Cleeves, L. I., Öberg, K. I., Wilner, D. J., et al. 2016, The Astrophysical Journal, 832, 110

Close, L. M., Roddier, F., J. Northcott, M., Roddier, C., & Elon Graves, J. 1997, The Astrophysical Journal, 478, 766

Cohen, M. 1983, The Astrophysical Journal Letters, 270, L69

Collier Cameron, A., Bouchy, F., Hébrard, G., et al. 2007, Monthly Notices of the Royal Astronomical Society, 375, 951

Comerón, F. 2008, The Lupus Clouds, ed. B. Reipurth, 295

Comeron, F., Rieke, G. H., Claes, P., Torra, J., & Laureijs, R. J. 1998, Astronomy & Astrophysics, 335, 522

Cox, E. G., Harris, R. J., Looney, L. W., et al. 2017, The Astrophysical Journal, 851, 83

Cutri, R. M. & et al. 2014, VizieR Online Data Catalog, 2328

Cutri, R. M., Skrutskie, M. F., van Dyk, S., et al. 2003, 2MASS All Sky Catalog of point sources.

Daemgen, S., Natta, A., Scholz, A., et al. 2016, Astronomy & Astrophysics, 594, A83

Dartois, E., Dutrey, A., & Guilloteau, S. 2003, Astronomy & Astrophysics, 399, 773

Di Stefano, R., Berndtsson, J., Urquhart, R., et al. 2020, arXiv e-prints, arXiv:2009.08987

Dodds, P., Greaves, J. S., Scholz, A., et al. 2015, Monthly Notices of the Royal Astronomical Society, 447, 722

Dominik, C. 2015, in European Physical Journal Web of Conferences, Vol. 102, European Physical Journal Web of Conferences, 00002

Doyle, L. R., Carter, J. A., Fabrycky, D. C., et al. 2011, Science, 333, 1602

Dubrulle, B., Morfill, G., & Sterzik, M. 1995, Icarus, 114, 237

Duffell, P. C. 2015, The Astrophysical Journal, 806, 182

Dullemond, C. P. & Dominik, C. 2005, Astronomy & Astrophysics, 434, 971

Dullemond, C. P., Dominik, C., & Natta, A. 2001, The Astrophysical Journal, 560, 957

Dullemond, C. P. & Monnier, J. D. 2010, Annual Review of Astronomy and Astrophysics, 48, 205

Dullemond, C. P., Natta, A., & Testi, L. 2006, The Astrophysical Journal, 645, L69

Dumusque, X., Pepe, F., Lovis, C., et al. 2012, Nature, 491, 207

Dunham, M. M., Allen, L. E., Evans, Neal J., I., et al. 2015, The Astrophysical Journal Supplement Series, 220, 11

Dürmann, C. & Kley, W. 2015, Astronomy & Astrophysics, 574, A52

Dutrey, A., Guilloteau, S., & Guelin, M. 1997, Astronomy & Astrophysics, 317, L55

Dutrey, A., Guilloteau, S., Prato, L., et al. 1998, Astronomy & Astrophysics, 338, L63

Dutrey, A., Guilloteau, S., & Simon, M. 1994, Astronomy & Astrophysics, 286, 149

Dutrey, A., Henning, T., Guilloteau, S., et al. 2007, Astronomy & Astrophysics, 464, 615

Edwards, S., Cabrit, S., Strom, S. E., et al. 1987, The Astrophysical Journal, 321, 473

Einstein, A. 1936, Science, 84, 506

Eisner, J. A., Arce, H. G., Ballering, N. P., et al. 2018, The Astrophysical Journal, 860, 77

Elsasser, H. & Staude, H. J. 1978, Astronomy & Astrophysics, 70, L3

Ercolano, B., Clarke, C. J., & Robitaille, T. P. 2009, Monthly Notices of the Royal Astronomical Society, 394, L141

Ercolano, B. & Pascucci, I. 2017, Royal Society Open Science, 4, 170114

Evans, Neal J., I., Dunham, M. M., Jørgensen, J. K., et al. 2009, The Astrophysical Journal Supplement Series, 181, 321

Facchini, S., Birnstiel, T., Bruderer, S., & van Dishoeck, E. F. 2017, Astronomy & Astrophysics, 605, A16

Facchini, S., van Dishoeck, E. F., Manara, C. F., et al. 2019, Astronomy & Astrophysics, 626, L2

Fischer, D. A., Howard, A. W., Laughlin, G. P., et al. 2014, in Protostars and Planets VI, ed. H. Beuther, R. S. Klessen, C. P. Dullemond, & T. Henning, 715

Foreman-Mackey, D., Hogg, D. W., Lang, D., & Goodman, J. 2013, Publications of the Astronomical Society of the Pacific, 125, 306

Forgan, D. & Rice, K. 2013, Monthly Notices of the Royal Astronomical Society, 432, 3168

Fouchet, L., Maddison, S. T., Gonzalez, J. F., & Murray, J. R. 2007, Astronomy & Astrophysics, 474, 1037

Frasca, A., Biazzo, K., Alcalá, J. M., et al. 2017, Astronomy & Astrophysics, 602, A33

Fromang, S. & Nelson, R. P. 2009, Astronomy & Astrophysics, 496, 597

Furlan, E., Luhman, K. L., Espaillat, C., et al. 2011, The Astrophysical Journal Supplement Series, 195, 3

Furlan, E., Watson, D. M., McClure, M. K., et al. 2009, The Astrophysical Journal, 703, 1964

Gaia Collaboration, Brown, A. G. A., Vallenari, A., et al. 2018, Astronomy & Astrophysics, 616, A1

Garufi, A., Avenhaus, H., Pérez, S., et al. 2020, Astronomy & Astrophysics, 633, A82

Gatewood, G. 1976, Icarus, 27, 1

Gaudi, B. S., Christiansen, J. L., & Meyer, M. R. 2020, arXiv e-prints, arXiv:2011.04703

Gillon, M., Triaud, A. H. M. J., Demory, B.-O., et al. 2017, Nature, 542, 456

Goldreich, P. & Ward, W. R. 1973, The Astrophysical Journal, 183, 1051

Goodman, J. & Weare, J. 2010, Communications in Applied Mathematics and Computational Science, Vol. 5, No. 1, p. 65-80, 2010, 5, 65

Gorti, U., Liseau, R., Sándor, Z., & Clarke, C. 2016, Space Science Reviews, 205, 125

Gould, A. & Loeb, A. 1992, The Astrophysical Journal, 396, 104

Greaves, J. S. & Rice, W. K. M. 2010, Monthly Notices of the Royal Astronomical Society, 407, 1981

Greene, T. P., Line, M. R., Montero, C., et al. 2016, The Astrophysical Journal, 817, 17

Gregory, S. G., Adams, F. C., & Davies, C. L. 2016, Monthly Notices of the Royal Astronomical Society, 457, 3836

Griest, K. & Safizadeh, N. 1998, The Astrophysical Journal, 500, 37

Güdel, M. 2007, Living Reviews in Solar Physics, 4, 3

Güdel, M., Lahuis, F., Briggs, K. R., et al. 2010, Astronomy & Astrophysics, 519, A113

Guidi, G., Ruane, G., Williams, J. P., et al. 2018, Monthly Notices of the Royal Astronomical Society, 479, 1505

Guillot, T., Santos, N. C., Pont, F., et al. 2006, Astronomy & Astrophysics, 453, L21

Guilloteau, S. & Dutrey, A. 1998, Astronomy & Astrophysics, 339, 467

Guilloteau, S., Dutrey, A., Piétu, V., & Boehler, Y. 2011, Astronomy & Astrophysics, 529, A105

Guyon, O., Pluzhnik, E. A., Kuchner, M. J., Collins, B., & Ridgway, S. T. 2006, The Astrophysical Journal Supplement Series, 167, 81

Haffert, S. Y., Bohn, A. J., de Boer, J., et al. 2019, Nature Astronomy, 3, 749

Hales, A. S., Pérez, S., Saito, M., et al. 2018, The Astrophysical Journal, 859, 111

Harris, R. J., Andrews, S. M., Wilner, D. J., & Kraus, A. L. 2012, The Astrophysical Journal, 751, 115

Harsono, D., Bruderer, S., & van Dishoeck, E. F. 2015, Astronomy & Astrophysics, 582, A41

Hartmann, L., Calvet, N., Gullbring, E., & D'Alessio, P. 1998, The Astrophysical Journal, 495, 385

Hartmann, L., Herczeg, G., & Calvet, N. 2016, Annual Review of Astronomy and Astrophysics, 54, 135

Hartmann, L. & Kenyon, S. J. 1985, The Astrophysical Journal, 299, 462

Hendler, N., Pascucci, I., Pinilla, P., et al. 2020, The Astrophysical Journal, 895, 126

Hendler, N. P., Mulders, G. D., Pascucci, I., et al. 2017, The Astrophysical Journal, 841, 116

Henning, T., Semenov, D., Guilloteau, S., et al. 2010, The Astrophysical Journal, 714, 1511

Henning, T. & Stognienko, R. 1996, Astronomy & Astrophysics, 311, 291

Henry, G. W., Marcy, G. W., Butler, R. P., & Vogt, S. S. 2000, The Astrophysical Journal Letters, 529, L41

Herbig, G. H. 1960, The Astrophysical Journal Supplement Series, 4, 337

Herbig, G. H. 1962, Advances in Astronomy and Astrophysics, 1, 47

Herczeg, G. J., Linsky, J. L., Walter, F. M., Gahm, G. F., & Johns-Krull, C. M. 2006, The Astrophysical Journal Supplement Series, 165, 256

Herczeg, G. J., Walter, F. M., Linsky, J. L., et al. 2005, The Astronomical Journal, 129, 2777

Högbom, J. A. 1974, Astronomy and Astrophysics Supplement, 15, 417

Howard, A. W., Marcy, G. W., Bryson, S. T., et al. 2012, The Astrophysical Journal Supplement Series, 201, 15

Huang, J., Andrews, S. M., Dullemond, C. P., et al. 2018, The Astrophysical Journal, 869, L42

Huang, J., Andrews, S. M., Öberg, K. I., et al. 2020, The Astrophysical Journal, 898, 140

Hubickyj, O., Bodenheimer, P., & Lissauer, J. J. 2005, Icarus, 179, 415

Hueso, R. & Guillot, T. 2005, Astronomy & Astrophysics, 442, 703

Hughes, J., Hartigan, P., Krautter, J., & Kelemen, J. 1994, The Astronomical Journal, 108, 1071

Isella, A., Benisty, M., Teague, R., et al. 2019, The Astrophysical Journal Letters, 879, L25

Isella, A., Guidi, G., Testi, L., et al. 2016, Physical Review Letters, 117, 251101

Isella, A., Huang, J., Andrews, S. M., et al. 2018, The Astrophysical Journal Letters, 869, L49

Isella, A., Testi, L., Natta, A., et al. 2007, Astronomy & Astrophysics, 469, 213

Izidoro, A., Ogihara, M., Raymond, S. N., et al. 2017, Monthly Notices of the Royal Astronomical Society, 470, 1750

Jayawardhana, R., Mohanty, S., & Basri, G. 2003, The Astrophysical Journal, 592, 282

Jensen, E. L. N., Mathieu, R. D., & Fuller, G. A. 1996, The Astrophysical Journal, 458, 312

Johansen, A. & Lambrechts, M. 2017, Annual Review of Earth and Planetary Sciences, 45, 359

Johansen, A., Mac Low, M.-M., Lacerda, P., & Bizzarro, M. 2015, Science Advances, 1, 1500109

Johns-Krull, C. M., McLane, J. N., Prato, L., et al. 2016, The Astrophysical Journal, 826, 206

Jones, M. G., Pringle, J. E., & Alexander, R. D. 2012, Monthly Notices of the Royal Astronomical Society, 419, 925

Joy, A. H. 1945, The Astrophysical Journal, 102, 168

Joy, A. H. 1949, The Astrophysical Journal, 110, 424

Jung, Y. K., Udalski, A., Gould, A., et al. 2018, The Astronomical Journal, 155, 219

Kant, I. 1755, Allgemeine Naturgeschichte und Theorie des Himmels

Kelly, B. C. 2007, The Astrophysical Journal, 665, 1489

Kenyon, S. J., Gómez, M., & Whitney, B. A. 2008, Low Mass Star Formation in the Taurus-Auriga Clouds, ed. B. Reipurth, 405

Kenyon, S. J. & Hartmann, L. 1987, The Astrophysical Journal, 323, 714

Kenyon, S. J. & Hartmann, L. 1995, The Astrophysical Journal Supplement Series, 101, 117

Keppler, M., Benisty, M., Müller, A., et al. 2018, Astronomy & Astrophysics, 617, A44

Klein, R., Apai, D., Pascucci, I., Henning, T., & Waters, L. B. F. M. 2003, The Astrophysical Journal Letters, 593, L57

Kley, W. 1999, Monthly Notices of the Royal Astronomical Society, 303, 696

Kley, W. & Nelson, R. P. 2012, Annual Review of Astronomy and Astrophysics, 50, 211

Koerner, D. W., Sargent, A. I., & Beckwith, S. V. W. 1993, Icarus, 106, 2

Kratter, K. & Lodato, G. 2016, Annual Review of Astronomy and Astrophysics, 54, 271

Kratter, K. M. & Matzner, C. D. 2006, Monthly Notices of the Royal Astronomical Society, 373, 1563

Kratter, K. M., Matzner, C. D., Krumholz, M. R., & Klein, R. I. 2010, The Astrophysical Journal, 708, 1585

Krist, J. E., Beichman, C. A., Trauger, J. T., et al. 2007, in Society of Photo-Optical Instrumentation Engineers (SPIE) Conference Series, Vol. 6693, Techniques and Instrumentation for Detection of Exoplanets III, ed. D. R. Coulter, 66930H

Kuhn, J. R., Potter, D., & Parise, B. 2001, The Astrophysical Journal Letters, 553, L189

Kuzuhara, M., Tamura, M., Kudo, T., et al. 2013, The Astrophysical Journal, 774, 11

Kwon, W., Looney, L. W., & Mundy, L. G. 2011, The Astrophysical Journal, 741, 3

Kwon, W., Looney, L. W., Mundy, L. G., & Welch, W. J. 2015, The Astrophysical Journal, 808, 102

Lada, C. J. 1985, Annual Review of Astronomy and Astrophysics, 23, 267

Lada, C. J. 1987, in Star Forming Regions, ed. M. Peimbert & J. Jugaku, Vol. 115, 1

Lada, C. J. & Wilking, B. A. 1984, The Astrophysical Journal, 287, 610

Lafrenière, D., Jayawardhana, R., & van Kerkwijk, M. H. 2010, The Astrophysical Journal, 719, 497

Lagrange, A. M., Bonnefoy, M., Chauvin, G., et al. 2010, Science, 329, 57

Lahuis, F., van Dishoeck, E. F., Boogert, A. C. A., et al. 2006, The Astrophysical Journal Letters, 636, L145

Lambrechts, M. & Johansen, A. 2012, Astronomy & Astrophysics, 544, A32

Lambrechts, M. & Johansen, A. 2014, Astronomy & Astrophysics, 572, A107

Langlois, M. 2018, in European Planetary Science Congress, EPSC2018–500

Laplace, P. S. 1796

Latham, D. W., Mazeh, T., Stefanik, R. P., Mayor, M., & Burki, G. 1989, Nature, 339, 38

Lauer, T. R., Ajhar, E. A., Byun, Y.-I., et al. 1995, The Astronomical Journal, 110, 2622

Lavigne, J.-F., Doyon, R., Lafrenière, D., Marois, C., & Barman, T. 2009, The Astrophysical Journal, 704, 1098

Lazorenko, P. F. & Lazorenko, G. A. 2004, Astronomy & Astrophysics, 427, 1127

Lazzoni, C., Gratton, R., Alcalá, J. M., et al. 2020, Astronomy & Astrophysics, 635, L11

Leisenring, J., Skrutskie, M., Hinz, P., et al. 2012, in Proceedings of the SPIE, Vol. 8446, Ground-based and Airborne Instrumentation for Astronomy IV, 84464F

Lissauer, J. J. 1987, Icarus, 69, 249

Lissauer, J. J. 1993, Annual Review of Astronomy and Astrophysics, 31, 129

Lithwick, Y., Xie, J., & Wu, Y. 2012, The Astrophysical Journal, 761, 122

Liu, H. B. 2019, The Astrophysical Journal Letters, 877, L22

Lodato, G., Dipierro, G., Ragusa, E., et al. 2019, Monthly Notices of the Royal Astronomical Society, 486, 453

Lodato, G., Scardoni, C. E., Manara, C. F., & Testi, L. 2017, Monthly Notices of the Royal Astronomical Society, 472, 4700

Long, D. E., Zhang, K., Teague, R., & Bergin, E. A. 2020, The Astrophysical Journal Letters, 895, L46

Long, F., Herczeg, G. J., Harsono, D., et al. 2019, The Astrophysical Journal, 882, 49

Long, F., Herczeg, G. J., Pascucci, I., et al. 2017, The Astrophysical Journal, 844, 99

Lovis, C. & Fischer, D. 2010, Radial Velocity Techniques for Exoplanets, ed. S. Seager, 27–53

Luhman, K. L. 2012, Annual Review of Astronomy and Astrophysics, 50, 65

Lynden-Bell, D. & Pringle, J. E. 1974a, Monthly Notices of the Royal Astronomical Society, 168, 603

Lynden-Bell, D. & Pringle, J. E. 1974b, Monthly Notices of the Royal Astronomical Society, 168, 603

Lyot, B. 1939, Monthly Notices of the Royal Astronomical Society, 99, 580

MacGregor, M. A., Wilner, D. J., Czekala, I., et al. 2017, The Astrophysical Journal, 835, 17

Manara, C. F., Fedele, D., Herczeg, G. J., & Teixeira, P. S. 2016a, Astronomy & Astrophysics, 585, A136

Manara, C. F., Morbidelli, A., & Guillot, T. 2018a, Astronomy & Astrophysics, 618, L3

Manara, C. F., Prusti, T., Comeron, F., et al. 2018b, Astronomy & Astrophysics, 615, L1

Manara, C. F., Rosotti, G., Testi, L., et al. 2016b, Astronomy & Astrophysics, 591, L3

Manara, C. F., Tazzari, M., Long, F., et al. 2019, Astronomy & Astrophysics, 628, A95

Manara, C. F., Testi, L., Herczeg, G. J., et al. 2017, Astronomy & Astrophysics, 604, A127

Mao, S. & Paczynski, B. 1991, The Astrophysical Journal Letters, 374, L37

Markiewicz, W. J., Mizuno, H., & Voelk, H. J. 1991, Astronomy & Astrophysics, 242, 286

Marois, C., Lafrenière, D., Doyon, R., Macintosh, B., & Nadeau, D. 2006, The Astrophysical Journal, 641, 556

Marois, C., Racine, R., Doyon, R., Lafrenière, D., & Nadeau, D. 2004, The Astrophysical Journal Letters, 615, L61

Martin, R. G. & Lubow, S. H. 2011, Monthly Notices of the Royal Astronomical Society, 413, 1447

Maury, A. 2011, in EAS Publications Series, Vol. 51, EAS Publications Series, ed. C. Charbonnel & T. Montmerle, 191–209

Maury, A. J., André, P., Testi, L., et al. 2019, Astronomy & Astrophysics, 621, A76

Mawet, D., Absil, O., Montagnier, G., et al. 2012, Astronomy & Astrophysics, 544, A131

Mayer, L., Quinn, T., Wadsley, J., & Stadel, J. 2002, Science, 298, 1756

McCaughrean, M. J. & O'dell, C. R. 1996, The Astronomical Journal, 111, 1977

McKee, C. F. & Ostriker, E. C. 2007, Annual Review of Astronomy and Astrophysics, 45, 565

McMullin, J. P., Waters, B., Schiebel, D., Young, W., & Golap, K. 2007, in Astronomical Society of the Pacific Conference Series, Vol. 376, Astronomical Data Analysis Software and Systems XVI, ed. R. A. Shaw, F. Hill, & D. J. Bell, 127

Mendoza V., E. E. 1966, The Astrophysical Journal, 143, 1010

Mendoza V., E. E. 1968, The Astrophysical Journal, 151, 977

Merín, B., Jørgensen, J., Spezzi, L., et al. 2008, The Astrophysical Journal Supplement Series, 177, 551

Meru, F. & Bate, M. R. 2011, Monthly Notices of the Royal Astronomical Society, 410, 559

Mesa, D., Keppler, M., Cantalloube, F., et al. 2019, Astronomy & Astrophysics, 632, A25

Millan-Gabet, R., Malbet, F., Akeson, R., et al. 2007, in Protostars and Planets V, ed. B. Reipurth, D. Jewitt, & K. Keil, 539

Miller, K. A. & Stone, J. M. 2000, The Astrophysical Journal, 534, 398

Miotello, A., van Dishoeck, E. F., Kama, M., & Bruderer, S. 2016, Astronomy & Astrophysics, 594, A85

Miotello, A., van Dishoeck, E. F., Williams, J. P., et al. 2017, Astronomy & Astrophysics, 599, A113

Mohanty, S., Jayawardhana, R., & Basri, G. 2005, The Astrophysical Journal, 626, 498

Monnier, J. D., Harries, T. J., Aarnio, A., et al. 2017, The Astrophysical Journal, 838, 20

Montesinos, B., Eiroa, C., Mora, A., & Merín, B. 2009, Astronomy & Astrophysics, 495, 901

Morbidelli, A., Lambrechts, M., Jacobson, S., & Bitsch, B. 2015, Icarus, 258, 418

Mordasini, C., Alibert, Y., Benz, W., Klahr, H., & Henning, T. 2012, Astronomy & Astrophysics, 541, A97

Mordasini, C., Alibert, Y., Klahr, H., & Benz, W. 2011, in European Physical Journal Web of Conferences, Vol. 11, European Physical Journal Web of Conferences, 04001

Mortier, A., Oliveira, I., & van Dishoeck, E. F. 2011, Monthly Notices of the Royal Astronomical Society, 418, 1194

Mulders, G. D. & Dominik, C. 2012, Astronomy & Astrophysics, 539, A9

Mulders, G. D., Pascucci, I., & Apai, D. 2015, The Astrophysical Journal, 814, 130

Mulders, G. D., Pascucci, I., Manara, C. F., et al. 2017, The Astrophysical Journal, 847, 31

Müller, A., Keppler, M., Henning, T., et al. 2018, Astronomy & Astrophysics, 617, L2

Mužić, K., Scholz, A., Geers, V. C., & Jayawardhana, R. 2015, The Astrophysical Journal, 810, 159

Mužić, K., Scholz, A., Geers, V. C., Jayawardhana, R., & López Martí, B. 2014, The Astrophysical Journal, 785, 159

Muzerolle, J., Hillenbrand, L., Calvet, N., Briceño, C., & Hartmann, L. 2003, The Astrophysical Journal, 592, 266

Muzerolle, J., Luhman, K. L., Briceño, C., Hartmann, L., & Calvet, N. 2005, The Astrophysical Journal, 625, 906

Najita, J. R. & Bergin, E. A. 2018, The Astrophysical Journal, 864, 168

Najita, J. R., Carr, J. S., Glassgold, A. E., & Valenti, J. A. 2007, in Protostars and Planets V, ed. B. Reipurth, D. Jewitt, & K. Keil, 507

Najita, J. R. & Kenyon, S. J. 2014, Monthly Notices of the Royal Astronomical Society, 445, 3315

Nakamoto, T. & Nakagawa, Y. 1994, The Astrophysical Journal, 421, 640

Natta, A. & Testi, L. 2001, Astronomy & Astrophysics, 376, L22

Natta, A., Testi, L., Calvet, N., et al. 2007, in Protostars and Planets V, ed. B. Reipurth, D. Jewitt, & K. Keil, 767

Natta, A., Testi, L., Comerón, F., et al. 2002, Astronomy & Astrophysics, 393, 597

Natta, A., Testi, L., Muzerolle, J., et al. 2004a, Astronomy & Astrophysics, 424, 603

Natta, A., Testi, L., Neri, R., Shepherd, D. S., & Wilner, D. J. 2004b, Astronomy & Astrophysics, 416, 179

Natta, A., Testi, L., Neri, R., Shepherd, D. S., & Wilner, D. J. 2004c, Astronomy & Astrophysics, 416, 179

Nayakshin, S. 2010, Monthly Notices of the Royal Astronomical Society, 408, L36

Neuhäuser, R., Guenther, E. W., Wuchterl, G., et al. 2005, Astronomy & Astrophysics, 435, L13

Neuhäuser, R., Mugrauer, M., Seifahrt, A., Schmidt, T. O. B., & Vogt, N. 2008, Astronomy & Astrophysics, 484, 281

Observing with ALMA – A Primer,. 2019, ALMA Doc. 7.1, ver. 1

O'dell, C. R., Wen, Z., & Hu, X. 1993, The Astrophysical Journal, 410, 696

Ormel, C. W. & Cuzzi, J. N. 2007, Astronomy & Astrophysics, 466, 413

Ormel, C. W. & Klahr, H. H. 2010, Astronomy & Astrophysics, 520, A43

Ormel, C. W., Min, M., Tielens, A. G. G. M., Dominik, C., & Paszun, D. 2011, Astronomy & Astrophysics, 532, A43

Ormel, C. W., Paszun, D., Dominik, C., & Tielens, A. G. G. M. 2009, Astronomy & Astrophysics, 502, 845

Pascucci, I., Apai, D., Henning, T., & Dullemond, C. P. 2003, The Astrophysical Journal Letters, 590, L111

Pascucci, I., Testi, L., Herczeg, G. J., et al. 2016, The Astrophysical Journal, 831, 125

Payne, M. J. & Lodato, G. 2007, Monthly Notices of the Royal Astronomical Society, 381, 1597

Pérez, S., Casassus, S., Hales, A., et al. 2020, The Astrophysical Journal Letters, 889, L24

Pierens, A. & Nelson, R. P. 2008, Astronomy & Astrophysics, 482, 333

Piétu, V., Dutrey, A., & Guilloteau, S. 2007, Astronomy & Astrophysics, 467, 163

Piétu, V., Guilloteau, S., Di Folco, E., Dutrey, A., & Boehler, Y. 2014, Astronomy & Astrophysics, 564, A95

Pinilla, P., Benisty, M., & Birnstiel, T. 2012, Astronomy & Astrophysics, 545, A81

Pinilla, P., Birnstiel, T., Benisty, M., et al. 2013, Astronomy & Astrophysics, 554, A95

Pinilla, P., Natta, A., Manara, C. F., et al. 2018, Astronomy & Astrophysics, 615, A95

Pinte, C., Ménard, F., Duchêne, G., et al. 2018a, Astronomy & Astrophysics, 609, A47

Pinte, C., Price, D. J., Ménard, F., et al. 2018b, The Astrophysical Journal Letters, 860, L13

Pollack, J. B., Hollenbach, D., Beckwith, S., et al. 1994, The Astrophysical Journal, 421, 615

Pollack, J. B., Hubickyj, O., Bodenheimer, P., et al. 1996, Icarus, 124, 62

Racine, R., Walker, G. A. H., Nadeau, D., Doyon, R., & Marois, C. 1999, Publications of the Astronomical Society of the Pacific, 111, 587

Raymond, S. N. & Morbidelli, A. 2020, arXiv e-prints, arXiv:2002.05756

Ricci, L., Testi, L., Natta, A., & Brooks, K. J. 2010a, Astronomy & Astrophysics, 521, A66

Ricci, L., Testi, L., Natta, A., et al. 2010b, Astronomy & Astrophysics, 512, A15

Ricci, L., Testi, L., Natta, A., et al. 2014, The Astrophysical Journal, 791, 20

Rosenthal, E. D., Gurwell, M. A., & Ho, P. T. P. 1996, Nature, 384, 243

Rosotti, G. P., Clarke, C. J., Manara, C. F., & Facchini, S. 2017, Monthly Notices of the Royal Astronomical Society, 468, 1631

Rosotti, G. P., Tazzari, M., Booth, R. A., et al. 2019, Monthly Notices of the Royal Astronomical Society, 486, 4829

Ruane, G., Mawet, D., Kastner, J., et al. 2017, The Astronomical Journal, 154, 73

Safronov, V. S. 1969, Evoliutsiia doplanetnogo oblaka.

Sanchis, E., Picogna, G., Ercolano, B., Testi, L., & Rosotti, G. 2020a, Monthly Notices of the Royal Astronomical Society, 492, 3440

Sanchis, E., Testi, L., Natta, A., et al. 2020b, Astronomy & Astrophysics, 633, A114

Santamaría-Miranda, A., de Gregorio-Monsalvo, I., Huélamo, N., et al. 2020, Astronomy & Astrophysics, 640, A13

Sargent, A. I. & Beckwith, S. 1987, The Astrophysical Journal, 323, 294

Scholz, A. 2008, Reviews in Modern Astronomy, 20, 357

Scholz, A. & Eislöffel, J. 2004, Astronomy & Astrophysics, 419, 249

Schwarz, H., Ginski, C., de Kok, R. J., et al. 2016a, Astronomy & Astrophysics, 593, A74

Schwarz, K. R., Bergin, E. A., Cleeves, L. I., et al. 2016b, The Astrophysical Journal, 823, 91

Seifahrt, A., Neuhäuser, R., & Hauschildt, P. H. 2007, Astronomy & Astrophysics, 463, 309

Sellek, A. D., Booth, R. A., & Clarke, C. J. 2020a, Monthly Notices of the Royal Astronomical Society, 498, 2845

Sellek, A. D., Booth, R. A., & Clarke, C. J. 2020b, Monthly Notices of the Royal Astronomical Society, 492, 1279

Shakura, N. I. & Sunyaev, R. A. 1973, Astronomy & Astrophysics, 500, 33

Shao, M. & Colavita, M. M. 1992, Annual Review of Astronomy and Astrophysics, 30, 457

Shapiro, S. S. & Wilk, M. B. 1965, Biometrika, 52, 591

Shu, F., Najita, J., Ostriker, E., et al. 1994, The Astrophysical Journal, 429, 781

Shu, F. H. 1977, The Astrophysical Journal, 214, 488

Siess, L., Dufour, E., & Forestini, M. 2000, Astronomy & Astrophysics, 358, 593

Simon, J. B., Armitage, P. J., Li, R., & Youdin, A. N. 2016, The Astrophysical Journal, 822, 55

Simon, J. B., Armitage, P. J., Youdin, A. N., & Li, R. 2017, The Astrophysical Journal Letters, 847, L12

Skrutskie, M. F., Jones, T., Hinz, P., et al. 2010, in Proceedings of the SPIE, Vol. 7735, Ground-based and Airborne Instrumentation for Astronomy III, 77353H

Smith, W. H. 1987, Publications of the Astronomical Society of the Pacific, 99, 1344

Sonnhalter, C., Preibisch, T., & Yorke, H. W. 1995, Astronomy & Astrophysics, 299, 545

Sparks, W. B. & Ford, H. C. 2002, The Astrophysical Journal, 578, 543

Spiegel, D. S. & Burrows, A. 2012, The Astrophysical Journal, 745, 174

Stahler, S. W. & Palla, F. 2004, The Formation of Stars

Stamatellos, D. & Whitworth, A. P. 2009, Monthly Notices of the Royal Astronomical Society, 400, 1563

Strom, K. M., Strom, S. E., & Yost, J. 1971, The Astrophysical Journal, 165, 479

Tazzari, M. 2017, mtazzari/uvplot: v0.1.1

Tazzari, M., Beaujean, F., & Testi, L. 2018, Monthly Notices of the Royal Astronomical Society, 476, 4527

Tazzari, M., Testi, L., Ercolano, B., et al. 2016, Astronomy & Astrophysics, 588, A53

Tazzari, M., Testi, L., Natta, A., et al. 2017, Astronomy & Astrophysics, 606, A88

Teague, R., Bae, J., Bergin, E. A., Birnstiel, T., & Foreman-Mackey, D. 2018, The Astrophysical Journal Letters, 860, L12

Terebey, S., Shu, F. H., & Cassen, P. 1984, The Astrophysical Journal, 286, 529

Terquem, C. & Papaloizou, J. C. B. 2007, The Astrophysical Journal, 654, 1110

Testi, L., Birnstiel, T., Ricci, L., et al. 2014, in Protostars and Planets VI, ed. H. Beuther, R. S. Klessen, C. P. Dullemond, & T. Henning, 339

Testi, L., Natta, A., Scholz, A., et al. 2016, Astronomy & Astrophysics, 593, A111

Testi, L., Natta, A., Shepherd, D. S., & Wilner, D. J. 2003, Astronomy & Astrophysics, 403, 323

Testi, L., Skemer, A., Henning, T., et al. 2015, The Astrophysical Journal Letters, 812, L38

Thamm, E., Steinacker, J., & Henning, T. 1994, Astronomy & Astrophysics, 287, 493

Thi, W. F., van Zadelhoff, G. J., & van Dishoeck, E. F. 2004, Astronomy & Astrophysics, 425, 955

Todorov, K., Luhman, K. L., & McLeod, K. K. 2010, The Astrophysical Journal Letters, 714, L84

Toomre, A. 1964, The Astrophysical Journal, 139, 1217

Trapman, L., Ansdell, M., Hogerheijde, M. R., et al. 2020, Astronomy & Astrophysics, 638, A38

Trapman, L., Facchini, S., Hogerheijde, M. R., van Dishoeck, E. F., & Bruderer, S. 2019, Astronomy & Astrophysics, 629, A79

Tripathi, A., Andrews, S. M., Birnstiel, T., & Wilner, D. J. 2017, The Astrophysical Journal, 845, 44

Turner, N. J., Fromang, S., Gammie, C., et al. 2014, in Protostars and Planets VI, ed. H. Beuther, R. S. Klessen, C. P. Dullemond, & T. Henning, 411

Tychoniec, Ł., Manara, C. F., Rosotti, G. P., et al. 2020, Astronomy & Astrophysics, 640, A19

Ubeira Gabellini, M. G., Miotello, A., Facchini, S., et al. 2019, Monthly Notices of the Royal Astronomical Society, 486, 4638

Uchida, Y. & Shibata, K. 1984, Publications of the Astronomical Society of Japan, 36, 105

van der Marel, N., Williams, J. P., Ansdell, M., et al. 2018, The Astrophysical Journal, 854, 177

van der Plas, G., Ménard, F., Ward-Duong, K., et al. 2016, The Astrophysical Journal, 819, 102

van Dishoeck, E. F. & Black, J. H. 1988, The Astrophysical Journal, 334, 771

van Terwisga, S. E., van Dishoeck, E. F., Ansdell, M., et al. 2018, Astronomy & Astrophysics, 616, A88

van Terwisga, S. E., van Dishoeck, E. F., Cazzoletti, P., et al. 2019, Astronomy & Astrophysics, 623, A150

van Zadelhoff, G. J., van Dishoeck, E. F., Thi, W. F., & Blake, G. A. 2001, Astronomy & Astrophysics, 377, 566

Voelk, H. J., Jones, F. C., Morfill, G. E., & Roeser, S. 1980, Astronomy & Astrophysics, 85, 316

Vorobyov, E. I. & Basu, S. 2009, The Astrophysical Journal, 703, 922

Vrba, F. J., Schmidt, G. D., & Hintzen, P. M. 1979, The Astrophysical Journal, 227, 185

Wang, S., Wu, D.-H., Barclay, T., & Laughlin, G. P. 2017, arXiv e-prints, arXiv:1704.04290

Ward-Duong, K., Patience, J., Bulger, J., et al. 2018, The Astronomical Journal, 155, 54

Watson, A. M., Stapelfeldt, K. R., Wood, K., & Ménard, F. 2007, in Protostars and Planets V, ed. B. Reipurth, D. Jewitt, & K. Keil, 523

Weidenschilling, S. J. 1977, Monthly Notices of the Royal Astronomical Society, 180, 57

Werner, M. W., Roellig, T. L., Low, F. J., et al. 2004, The Astrophysical Journal Supplement Series, 154, 1

Wetherill, G. W. 1992, Icarus, 100, 307

Whelan, E. T., Ray, T. P., Bacciotti, F., et al. 2005, Nature, 435, 652

Whipple, F. L. 1972, in From Plasma to Planet, ed. A. Elvius, 211

Whitworth, A. & Summers, D. 1985, Monthly Notices of the Royal Astronomical Society, 214, 1

Williams, J. P. 2012, Meteoritics and Planetary Science, 47, 1915

Williams, J. P. & Best, W. M. J. 2014, The Astrophysical Journal, 788, 59

Williams, J. P., Cieza, L., Hales, A., et al. 2019, The Astrophysical Journal Letters, 875, L9

Windmark, F., Birnstiel, T., Güttler, C., et al. 2012, Astronomy & Astrophysics, 540, A73

Winn, J. N. & Fabrycky, D. C. 2015, Annual Review of Astronomy and Astrophysics, 53, 409

Wölfer, L., Facchini, S., Kurtovic, N. T., et al. 2020, arXiv e-prints, arXiv:2012.04680

Wolszczan, A. & Frail, D. A. 1992, Nature, 355, 145

Wright, E. L., Eisenhardt, P. R. M., Mainzer, A. K., et al. 2010, The Astronomical Journal, 140, 1868

Yorke, H. W., Bodenheimer, P., & Laughlin, G. 1993, The Astrophysical Journal, 411, 274

Youdin, A. N. & Goodman, J. 2005, The Astrophysical Journal, 620, 459

Zhang, S., Zhu, Z., Huang, J., et al. 2018, The Astrophysical Journal, 869, L47

Zhu, Z., Zhang, S., Jiang, Y.-F., et al. 2019, The Astrophysical Journal, 877, L18

Danksagung

I would like to thank my main supervisor, Leonardo, for his support and care during all these years. He has taught me so many things from science and life. And, even with his schedule packed with work obligations, he always found time and put all the effort on guiding me through the best possible path.

Likewise, I'm also very grateful to Antonella, Carlo, Anna and Stefano, for their patience, honesty and help to develop and improve my scientific work. Of course, I'll always be very grateful to Barbara, she is not only a great researcher and lecturer, but besides, she motivates everyone around her, and offered the best help and opportunities to me and every student. I would also like to thank to the two Giovannis, and specially to GP, because of all the help, kindness, and effort that he always gives. Also, to all the people and students from ESO, the Star and Planet Formation group, and the people from the USM.

I will always thank Heather for her affection and support during all these years. We have gone through a lot of great times, some other more difficult, but together we will always thrive.

Also huge thanks to all my family and friends. To my parents, Juan, Carmen, Yachan, Carlos, Juanito and Carlitos for being always there and help me with everything. Also to all my friends, specially from Valencia, Berlin and Munich: to José Manuel, Fernando, Quique, Alejandro, Miguel, Manu, Mesi, Rodilla, José Ignacio, Memo, Joseph, Michele, Apo, and many others. Thanks for all the experiences we have lived together, the good times, the bad times, and all what is still to come.